The laser-as-detector approach exploiting mid-infrared emitting interband cascade lasers: A potential for spectroscopy and communication applications

Herdt, Andreas

(2020)

The laser-as-detector approach exploiting mid-infrared emitting interband cascade lasers: A potential for spectroscopy and communication applications

Zur Erlangung des Grades eines Doktors der Naturwissenschaften (Dr. rer. nat.)
genehmigte Dissertation von Andreas Herdt geboren in Wetzlar
Tag der Einreichung: 13.10.2020, Tag der Prüfung: 09.12.2020

1. Gutachten: Prof. Dr. Wolfgang Elsäßer
2. Gutachten: Prof. Dr. Thomas Walther
Darmstadt

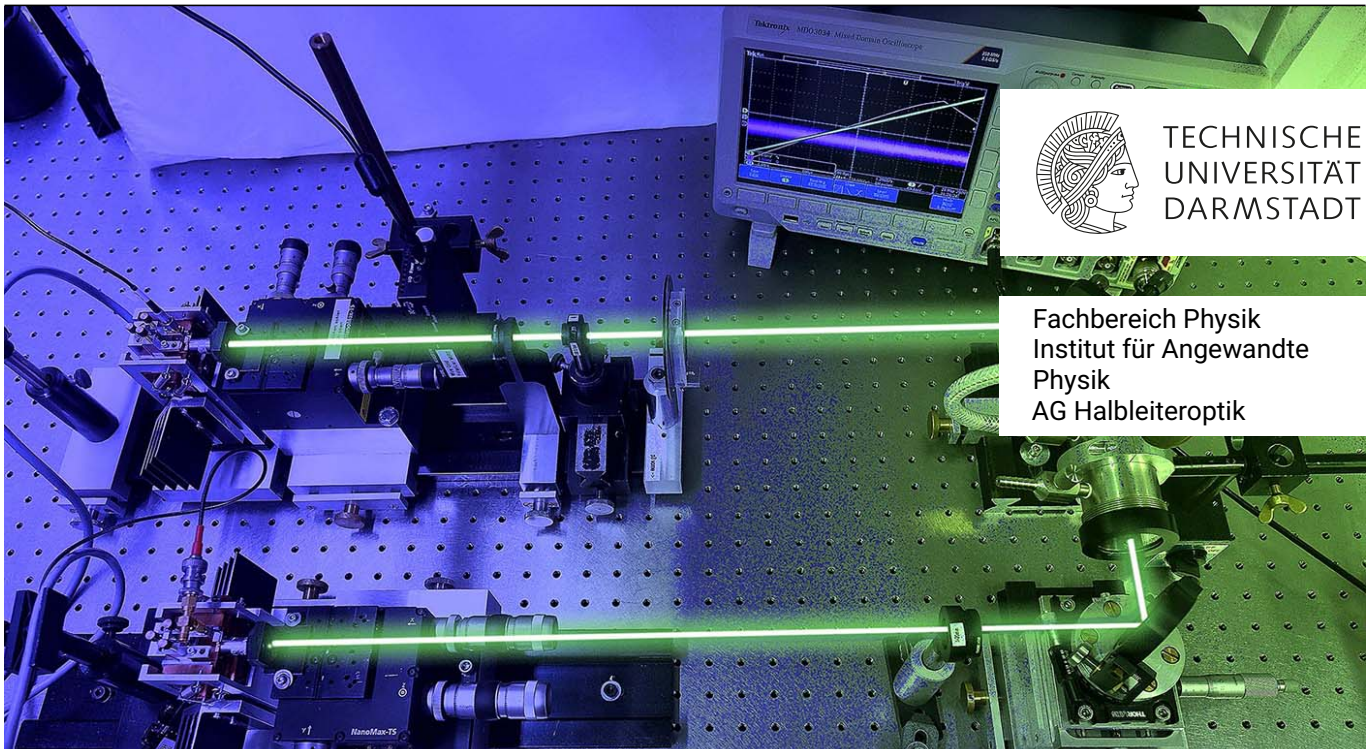

TECHNISCHE UNIVERSITÄT DARMSTADT

Fachbereich Physik
Institut für Angewandte Physik
AG Halbleiteroptik

The laser-as-detector approach exploiting mid-infrared emitting interband cascade lasers: A potential for spectroscopy and communication applications

Doctoral thesis by Andreas Herdt

1. Review: Prof. Dr. Wolfgang Elsäßer
2. Review: Prof. Dr. Thomas Walther

Date of submission: 13.10.2020
Date of thesis defense: 09.12.2020

Darmstadt

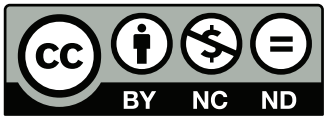

"Alle madri, perchè l'essere in due comincia da loro."

Erri de Luca

Erklärungen laut Promotionsordnung

§8 Abs. 1 lit. c PromO

Ich versichere hiermit, dass die elektronische Version meiner Dissertation mit der schriftlichen Version übereinstimmt.

§8 Abs. 1 lit. d PromO

Ich versichere hiermit, dass zu einem vorherigen Zeitpunkt noch keine Promotion versucht wurde. In diesem Fall sind nähere Angaben über Zeitpunkt, Hochschule, Dissertationsthema und Ergebnis dieses Versuchs mitzuteilen.

§9 Abs. 1 PromO

Ich versichere hiermit, dass die vorliegende Dissertation selbstständig und nur unter Verwendung der angegebenen Quellen verfasst wurde.

§9 Abs. 2 PromO

Die Arbeit hat bisher noch nicht zu Prüfungszwecken gedient.

Darmstadt, 13.10.2020

A. Herdt

Abstract

Interband-Kaskaden-Laser sind außergewöhnlich vielfältig einsetzbare, Hochtechnologiehalbleiterlaser. Sie stellen die neueste Generation von Halbleiterlasern dar, die Strahlung im mittelinfraroten Wellenlängenbereich erzeugen und werden daher bevorzugt in Spektroskopie und Freistrahlkommunikationsapparaten als kohärente Lichtquellen eingesetzt. In dieser Arbeit wurden Sie eingesetzt um den Laser-als-Detektor Ansatz zu evaluieren. Der Laser-als-Detektor Ansatz ist eine bekannte, aber wenig eingesetzte Technik, die es ermöglicht auf externe optische Detektionseinheiten zu verzichten. Dabei wird ein Halbleiterlaser selber als Detektor genutzt, trotzdem er wie gewöhnlich in Betrieb ist. Das Prinzip beruht dabei darauf, dass externe optische Störungen die Ladungsträger im Interbandkaskadenlaser verändern und sich dementsprechend in Spannungsänderungen manifestieren. Mit Hilfe des Laser-als-Detektor Ansatzes werden anschließend zwei Spektroskopie-Sensoren aufgebaut und deren Detektionslimit anhand von Methanabsorptionslinien evaluiert. Danach wird der Laser-als-Detektor Ansatz ausgenutzt, um einen Freistrahlkommunikationsapparat ohne zusätzliche Detektoren aufzubauen.

Abstract

Interband cascade lasers are exceptionally versatile, high-tech semiconductor lasers. They represent the latest generation of semiconductor lasers that generate radiation in the mid-infrared wavelength domain and are therefore preferred as coherent light sources in spectroscopy and free-space-communication setups. In this thesis they are used to evaluate the so-called laser-as-detector approach. The laser-as-detector approach is a well-known but little used technique that allows dispensing external optical detection units. A semiconductor laser itself is used as a detector, even though it is operating as usual. The principle is based on the fact that external optical perturbation change the charge carrier density in the interband-cascade-laser and manifest themselves accordingly in changes of the terminal voltage. Using the laser-as-detector approach, two spectroscopic methane sensors are then set up and their detection limits are evaluated. The laser-as-detector approach is then used to build a free-space-communication communication device without any detector.

List of Abbreviations

ICL interband-cascade-laser

IDL interband-diode-laser

QCL quantum-cascade-laser

SCL semiconductor-laser

QW quantum well

LAD laser-as-detector

OFN optical frequency noise

LEF linewidth enhancement factor

SNR signal to noise ratio

OFD optical frequency detuning

UV ultra-violet

VIS visible

NIR near-infrared

MIR mid-infrared

FIR far-infrared

arb. u. arbitrary units

NLDS nonlinear dynamic systems

DDE delay-differential equation

LFF low-frequency fluctuations

OIL optical injection locking

LBW locking bandwidth

SVEA slowly varying envelope approximation

FTIR Fourier-transform-infrared

QWIP quantum-well infrared photodetector

MCT mercury cadmium telluride

ESA electrical spectrum analyzer

OSCI oscilloscope

ISO optical isolator

NDF neutral density filter

POL polarizer

NPBS non-polarizing beam splitter

DC direct current

AC alternating current

HITRAN high-resolution transmission molecular absorption

LAS laser absorption spectroscopy

TDLAS tunable diode laser absorption spectroscopy

SMLAS selfmixing laser absorption spectroscopy

ILLAS injection locking laser absorption spectroscopy

ppmv parts per million by volume

FSO free space optics

CLS compound laser state

QKD quantum key distribution

Contents

1 Introduction

"A Solution Seeking a Problem."

Theodore H. Maiman - about his invention of the laser

Sixty years ago, in May 1960, not even his developer Theodore H. Maiman could have imagined that his newly developed light source - the Laser - would become the most important component of a myriad of optical systems that would revolutionize nothing less than our everyday lives [1, 2]. Today, communication technology based on lasers represents the backbone of the global Internet[3], they significantly facilitate the production of computer chips and smartphones, monitor our environment [4], are even used to scan our groceries[5] and enable future technologies such as autonomous driving [6] and countless other technologies. Not only in consumers and industrial applications, but especially in fundamental research, the invention of the laser contributed to countless new findings because it is a precise, if not the most precise measuring tool in physics. It can be concluded that without the invention of the laser, the world and the understanding of physics would be a different place today. All these applications rely on the extraordinary coherence properties of laser light, the extremely monochromatic emission and highly directional beam properties. These outstanding properties are the result of the special way in which the light is generated, the so-called stimulated emission. That is why the name laser refers to the method of light generation. Laser is an abbreviation for ***light amplification by stimulated emission of radiation***.

The semiconductor laser (SCL) is a laser source superior to other sources of coherent light in numerous aspects. Indeed only two years after the invention of the first laser - in 1962 - the SCL had been introduced independently by research groups at General Electric in Schenectady, IBM TJ Watson Center in Yorktown Heights, at General Electric in Syracuse and at the MIT Lincoln Laboratory in Boston (Cambridge)[7–10]. The outstanding fact is that SCLs combine all important elements of a laser - the active medium, the pump and the resonator - in a single miniaturized electro-optical component[11]. Indeed the typical size of this active element is in the impressively small range of $100\,\mu\mathrm{m} \times 1000\,\mu\mathrm{m} \times 100\,\mu\mathrm{m}$ or even smaller. The cross section of a SCL is comparable to the diameter of a human hair.
Not only its tiny size makes SCLs incredibly versatile. Another exceptional feature is the possibility to pump the laser electronically and that only with a very low voltage, which usually does not exceed $5\,\mathrm{V}$. Therefore, it can be easily packaged with other types of low-power

electronic elements or semiconductor devices onto electronic circuits or can also be integrated into full photonic integrated circuits (PICs)[12, 13]. These remarkable advantages make SCLs indispensable for research and technology in the 21st century. Already today, SCLs cover numerous wavelength ranges from THz [14] to UV [15]. To achieve this broad coverage, especially in the mid-infrared (MIR) domain, many tough challenges had to be mastered, such that efficient semiconductor-based sources for coherent light provide the necessary optical gain in that spectral domain. Even despite the substantial investments into development of coherent mid infared (MIR) emitters back in the 70s, no room-temperature operating source had been developed for the MIR and also the THz region. Still these laser emitters for that spectral range - mainly lead-salt diodes and CO2 lasers - remained bulky, inefficient, toxic or required cryogenic cooling and were at the same time quite expensive. All that changed with the development of the semiconductor-based Quantum Cascade laser (QCL) in 1994 [16] by Jerome Faist, following a theoretical concept developed by Kazarinov and Suris from the early 70s [17]. The enabling technology to manufacture QCLs was the development of the Molecular Beam Epitaxy in 1975 by Cho[18]. Since then it was possible to grow very thin layers of different semiconductor material onto each other allowing to create quantum-confined states in the conduction-band and valence-band of the semiconductor materials. QCLs, in contrast to common diode SCLs, are based on the emission of photons in QCLs due to unipolar transitions of electrons between energy states **within** the conduction band. These are often referred to as intersubband transitions and are created by the previously described quantum confinement. The idea of a cascading structure finally led to a total optical gain, which was high enough for MIR emission. First realizations of QCLs resulted in an output wavelength of $4.26\,\mu\mathrm{m}$ [19], whereas modern InAs/AlSb or InGaAs/AlGaAs/GaAs devices are recently available all over the MIR domain starting from $2.63\,\mu\mathrm{m}$ and breaking the barrier to the THz region reaching up to impressive $355\,\mu\mathrm{m}$[20–26].

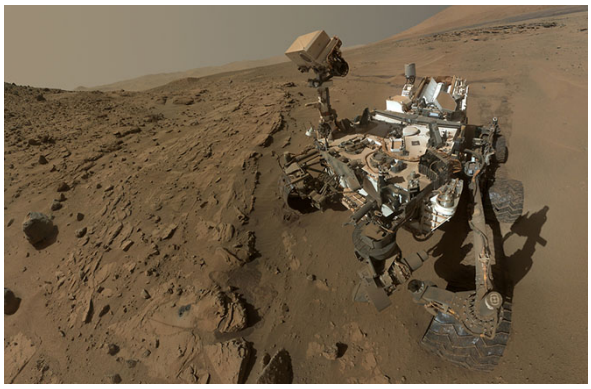

Figure 1.1: "Selfie" of NASAs Mars-rover Curiosity, which uses an ICL-based methane detector. Picture credits: NASA, JPL-Caltech, MSSS.

A second even more promising semiconductor-based concept of MIR emitting lasers was also introduced in 1994 - the interband cascade laser (ICL) [27], but was barely noticed. The main idea was to create a hybrid of conventional diode lasers, that generate photons via recombination between conduction and valence band, but utilize the cascaded structure of intersubband-based QCLs for enhanced optical gain. It took only three years for the first experimental realization of an ICL, which was reported in 1997 by Lin et al. [28] emitting at a wavelength of $3.8\,\mu\mathrm{m}$, however at cryogenic temperatures. Since QCL-research and technology grew significantly faster than ICL-technology, ICLs remained unnoticed for a long period of time. However, many efforts finally led to ICL continuous wave-operation at room temperature in 2008 [29] at a MIR wavelength of $3.75\,\mu\mathrm{m}$. In the following years ICLs have proven to be an impressively efficient MIR source for many application

areas[30, 31]. They are especially attractive when very low power consumption is required[32], because unlike to QCLs, the voltage and current requirements are minimal. Hence, ICLs are increasingly viewed as the laser-of-choice for portable MIR laser based applications in the spectral range between $3\,\mu m$ and $6\,\mu m$ [33]. This advantage finally led to the most famous application of an ICL, which was the deployment in the methane detector of the NASA Curiosity-rover (see Fig. 1.1) quantifying a mean methane-abundance of $0.69(25)\,\mathrm{ppbv}$ in the martian atmosphere[34].

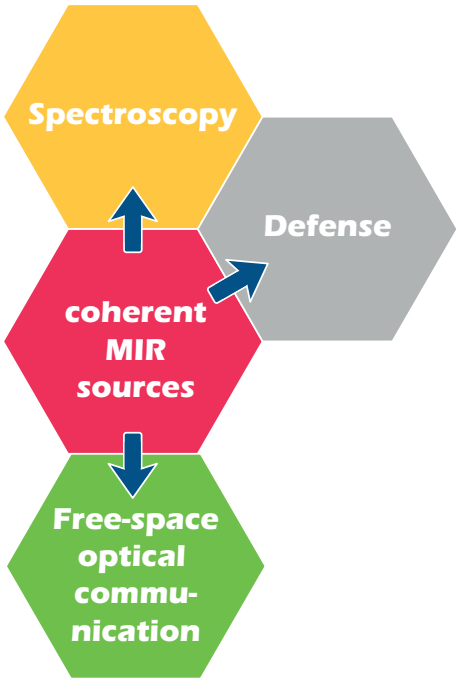

Figure 1.2: Application areas for coherent MIR-sources.

The MIR spectral range is interesting because it offers many opportunities for numerous areas of application including spectroscopy, which are schematically visualized in Fig. 1.2.

> *"Look here, I have succeeded at last in fetching some gold from the sun."*
>
> ***Gustav Kirchhoff***

On the one hand, many fundamental gas-molecules like methane have their specific fingerprint region in the MIR wavelength domain enabling high-precision spectroscopic determination of gas concentrations with a previously unattained precision. Spectroscopic measurements are needed when it comes to the determination of species composition and concentration of an unknown substance. In fact, spectroscopy goes back to Joseph von Fraunhofer[1], who investigated dark lines in the spectrum of the sun in 1817[35]. But it took until 1860, when G. Kirchhoff and R. Bunsen succeeded to find a connection between chemical ingredients and the characteristic absorption spectrum - absorption spectroscopy was born[36]. In fact today many types of spectrometers utilize QCLs and ICLs for MIR gas-detection, because they provide superior precision in trace gas detection. Some examples are the diagnosis of diseases [37, 38], monitoring of exhaust emissions of combustion processes in factories, motor vehicles or pipelines [39, 40], chemical analyses [41, 42], even the detection of explosives to prevent terrorist attacks [43] or general investigations of the earth's atmosphere [44, 45]. A second area, where coherent MIR sources offer great performance are defense and countermeasure systems [46]. We don't cover them in this thesis.

Another extraordinary property of the MIR spectral domain is its highly transparent optical

[1] since 1824 *Ritter von Fraunhofer*

window in the atmosphere. Therefore, MIR sources recently experienced renewed interest for free-space optical (FSO) communication. Indeed, MIR based FSO communication setups with data-rates up to $70\,\mathrm{Mbit\,s^{-1}}$, have for example been demonstrated with ICLs in 2010 [47]. With QCL, transmissions at Gigabit speeds have also already been reported both at room temperature[48] and cryogenic temperatures with a free-space television link application [49].

Still, the most serious challenge of all MIR-based applications is the lack of efficient detectors. Detectors in that spectral domain are bulky, inefficient and/or slow and usually have to be cooled well below room temperature requiring high maintenance. Fast-photodetection in the MIR domain is, according to the current state-of-the-art, only applicable with Quantum Well Infrared Photodetectors (QWIP) [50]. Unfortunately, QWIPs are usually very selective regarding the detectable spectrum and are way more expensive than simple but noisy pyroelectrical detectors. However, the latter are not as sensitive as commonly used mercury-cadmium-telluride (MCT) detectors, which are impressively sensitive, but require a sophisticated cooling mechanism and commercially available devices have not been able to detect electrical frequencies of MIR light higher than $2.12\,\mathrm{GHz}$[51]. Only the military company Raytheon has developed MCT-detectors with detection bandwidth up to $3\,\mathrm{GHz}$.

To overcome these limitations, we employ the so-called laser-as-detector (LAD) approach. It is only little known that a laser that is actually in operation can also be used as a detector. The laser-as-detector approach goes back to the 1980s, when it was shown that voltage changes can be observed when SCL were optically perturbed by their own feedback [52–54]. The central objective of this thesis is to tackle the challenge of unsatisfying MIR detection sensors by reviving the exceptionally performant laser-as-detector concept. Thus, the goal is find a measure, which is linearly connected to the injection strength of the radiation to be detected. Secondly, we want to prove the performance of this approach in two ICL based spectroscopy setups as well as a surprisingly simple free-space optical communication system with enhanced privacy.

> "*I accept chaos, I'm not sure whether it accepts me.*"
>
> ***Bob Dylan (Nobel awardee)***

The laser-as-detector approach is extraordinarily delicate, because its principle is a result of the nonlinear answer to an external optical perturbation. Even a small optical injection in the laser cavity can be amplified rapidly and disturbs the laser to such a degree that it can ultimately lead to non-deterministic output. Therefore, lasers are usually shielded from external optical perturbations via special optical components, so-called optical isolators. In this thesis we not only **accept** these nonlinear effects, our goal is to use them together with the laser-as-detector approach as a powerful tool. Indeed, it is known that semiconductors lasers are the most responsive laser type to external optical perturbations due to a low facet reflectivity and high gain, a fact which we will use to our advantage. Numerous phenomena of nonlinear effects can be found in semiconductor lasers, which we summarize in Chapter 3. For our applications we utilize three different, but well-known methods to generate an external optical perturbation

causing nonlinear effects. The methods are optical feedback, optical injection locking and mutual coupling. Our experimental goal here is threefold:

Initially, we want to deploy the laser-as-detector approach for a detector-free spectroscopy experiment based on an ICL subjected to feedback, which is discussed in Section 4.6. The key idea here is that a small amount of absorption within the feedback path affects the feedback strength, which will result in a change of the ICLs terminal voltage itself and therefore can be accessed easily.

Secondly, this idea is transferred to a setup with unidirectional optical injection. Most importantly we use here the nonlinear effect of optical injection locking, where a laser locks on the wavelength of the injected radiation[55], which occurs when the injected wavelength is close to that of the original wavelength. It is known that optical injection locking provides greater change of the ICLs terminal voltage compared to simple feedback. Thus, we exploit this larger nonlinear answer and therefore we achieve a significantly better signal-to-noise ratio than the first experimental demonstration. In accordance with [56] we demonstrate that it can be assumed that this spectroscopic technique could amplify the signal and lower the detection limit. The evaluation will be carried out it Section 4.7.

Lastly, this thesis closes with a discussion of a bidirectional coupling setup, where we realized a surprisingly simple and innovative mid-infrared private communication scheme without any additional optical detectors (see Section 5.2). The key idea here is that a change in one of the two ICLs causes a change of the terminal voltage in the second ICL coupled to it and vice versa. Data can then be transferred utilizing so-called compound laser states [57]. A private transmission is established, because changes only occur locally in the voltage and do not manifest themselves in the optical field of the coupled lasers.

Structure of the thesis

Following the aforementioned strategy, the thesis is divided into four chapters. First, basic properties of the solitary operating ICLs are characterized. This is followed by the central chapter, where we discuss the laser-as-detector approach in ICLs subjected to three kinds of external optical perturbation experimentally and theoretically. The laser-as-detector approach is finally used as a powerful tool to enable and enhance the applications of spectroscopy and free-space optical communication, which are discussed in chapters 3 and 4, respectively. A schematic diagram depicting the logical connections between the chapters of this thesis is visualized in Fig. 1.3. Altogether, the thesis represents the most comprehensive characterization of the laser-as-detector approach and exploits it to simultaneously evaluate two very promising application scenarios by introducing new measurement techniques without the requirement of an additional optical detector, dramatically reducing the number of optical components.

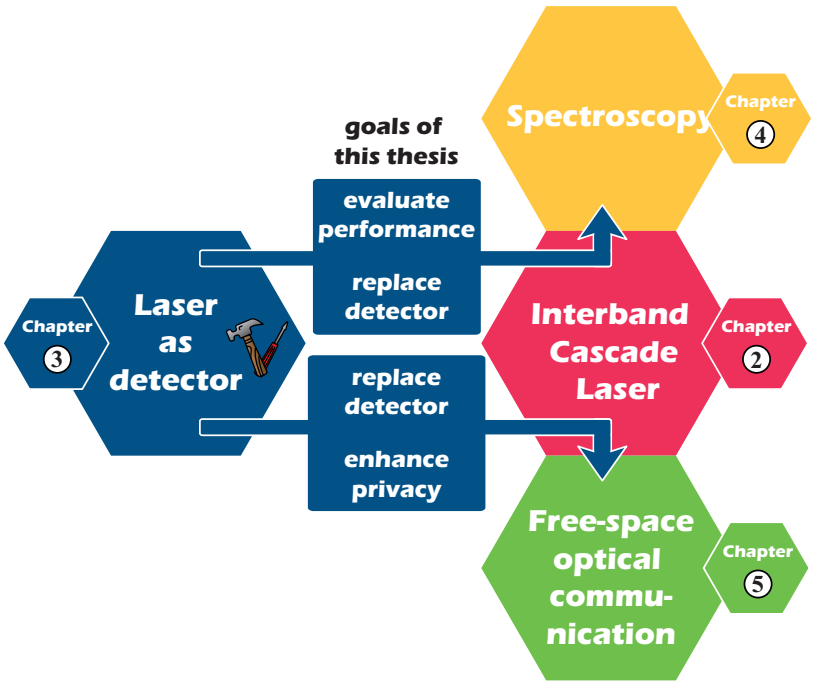

Figure 1.3: Schematic diagram depicting the logical connections between the chapters of this thesis.

2 Mid-infrared-emitting Interband Cascade Lasers

The mid-infrared (MIR) wavelength domain is a spectral domain of electromagnetic radiation between $3\,\mu m$ and $50\,\mu m$. It is arranged between the near-infrared wavelength domain and the far-infrared domain as illustrated in Fig. 2.1.

Figure 2.1: The classification of the electromagnetic spectrum from ultraviolet (UV), over visible (VIS), near-infrared (NIR), mid-infrared (MIR) to far-infrared (FIR) according to ISO 20473:2007.

Well-known sources for incoherent MIR emission are so-called blackbody emitters, which emit thermal radiation. Thermal radiation is the emission of electromagnetic radiation from all objects with a temperature greater than absolute zero. It reflects the conversion of thermal energy into electromagnetic energy. The description of the spectrum of blackbody radiation $S(\lambda, T)$, which depends solely on the object's temperature T is given by Planck's radiation law

$$S(\lambda, T) = \frac{2hc^2}{\lambda^5}\left(\exp\left(\frac{hc}{\lambda k_B T}\right) - 1\right)^{-1}, \quad (2.1)$$

with h the Planck-constant, λ the wavlength, c the speed of light and k_B the Boltzmann constant [58]. Six example spectra of blackbody radiation spectra are shown in Fig. 2.2 for selected temperatures.

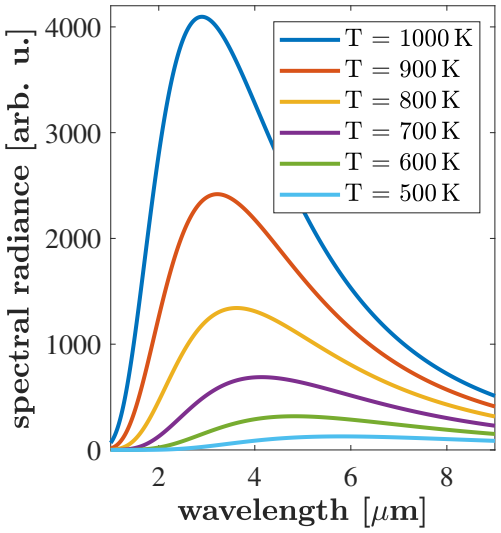

Figure 2.2: Family of blackbody radiation spectra for selected temperatures. Simulated according to Eq. (2.1).

2.1 Application areas of MIR light

The field of application of MIR light is exceptionally diverse. Application areas range from molecular spectroscopy serving medical, industrial and environmental purposes, via optical communication networks to military applications such as countermeasures.

Molecular spectroscopy

The field of molecular spectroscopy is by far the most relevant of these three areas. As a result of the structure of the energy levels and the associated optical transitions, many molecules will absorb light of a specific wavelength, which resembles exactly the energy difference of the energy levels. The simplest solution to detect the presence of a sample molecule can therefore be assessed by illuminating the medium and directly observing the optical transmission spectrum [44]. Each molecule possesses a so-called fingerprint region, which refers to the spectral domain, where molecules shows their most significant and unique absorption lines. Many fundamental trace gas molecules like methane or carbon dioxide have their fingerprint region in the MIR. A selection of the gases spectral fingerprints is in illustrated in Fig. 2.3. The result is that the absorption spectroscopy sensors deployed in the MIR wavelength range enable unrivalled high precision and thus low detection limits.

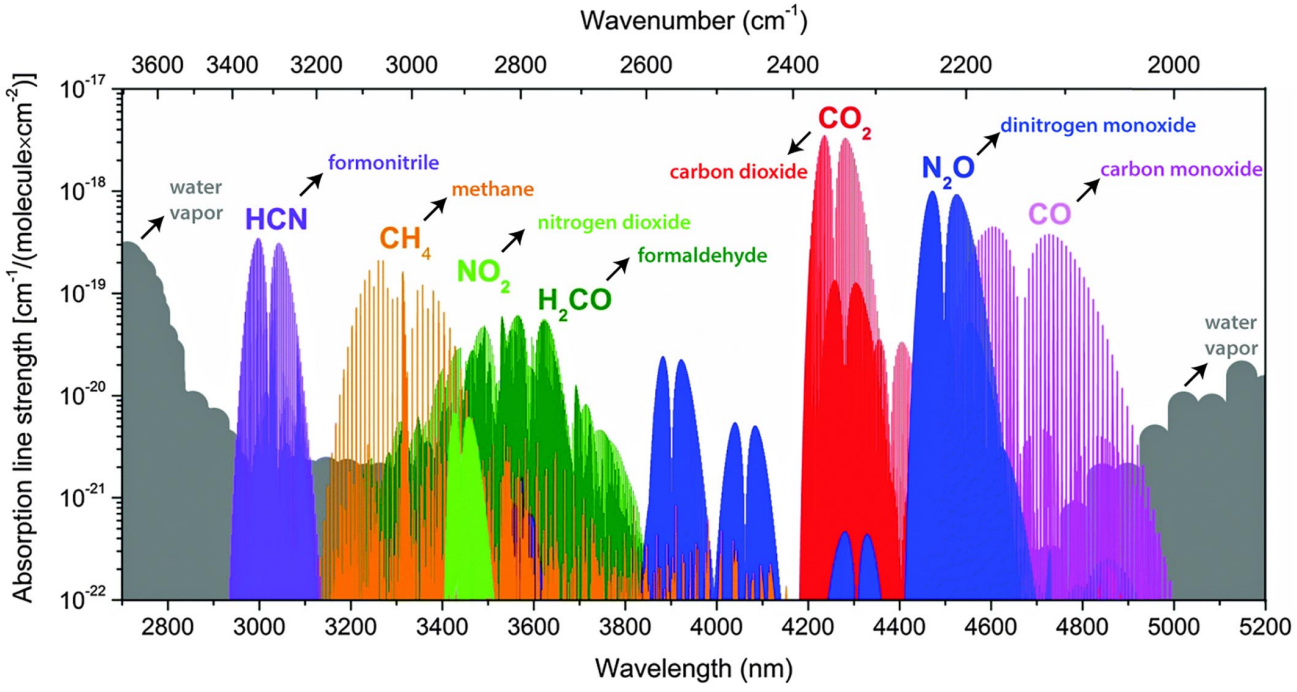

Figure 2.3: Absorption spectra of a selection of trace gases in the wavelength domain from $2.7\,\mu m$ to $5.2\,\mu m$. The figure has been adapted from [59] and the molecular line data are taken from the HITRAN 2012 database [60].

Spectroscopic sensors for the MIR domain for example are used for the control of combustion processes [40] e.g. for detection of nictric oxides in exhaust emissions [61], which have recently played the central role in the Diesel-scandal[62]. Other application areas of MIR spectroscopy include environmental monitoring[63], which can help to improve climate models. Because of the low detection limit MIR based sensors are also used for detection of explosives[64]. MIR based spectroscopy also offers opportunities for clinical purposes. Absorption lines in the MIR wavelength domain enable the identification and quantification of trace gases in human breath for medical uses[38, 65]. Unusual concentrations of these molecules can be associated with a large number of diseases [66]. Compared to other medical state-of-the-art sensors, those sensors provide superior sensitivity, offer selective detection and enable real-time determination of biomarkers such as carbon monoxide, ethane, formaldehyde, nitric oxides and many more [67]. This enables a person-specific diagnosis in real time and a fast personalized treatment, which offers great perspectives for modern medicine [68].

Atmospheric transmission

Beside the presence of many trace gas absorption lines, the MIR domain also offers atmospheric windows in which the absorption is relatively low. The atmospheric transmission spectrum is mainly determined by the absorption of water vapor. It is visualized in Fig. 2.4 showing that one window spans from $3\,\mu\mathrm{m}$ to $5\,\mu\mathrm{m}$ and another one from $8\,\mu\mathrm{m}$ to $14\,\mu\mathrm{m}$. Another advantage of the MIR wavelength domain is that at the same time beam distortion is lower compared to shorter wavelengths. Known distortion mechanisms on the propagation path include beam spreading, beam wandering, loss of spatial coherence or scintillation. In this case, the scintillation will be the dominant phenomenon, corresponding to intensity fluctuations of the propagating beam scaling with the wavelength $\lambda^{-\frac{7}{6}}$ [69]. Thus, using longer wavelength can be beneficial for information exchange via the atmospheric channel. Both facts makes the MIR domain to the preferred spectral region for free-space-optical (FSO) communication. And indeed, many MIR based schemes have been developed for FSO information transfer [47, 48, 70].

Defense application

A completely different field of application for MIR light are defense applications. In fact, MIR light sources for the area of countermeasures are well established and practical application systems have been deployed providing protection to a wide number of military platforms[73]. Most of them are used for aircraft protection from heat-seeking missiles[74]. Usually the missiles follow hot sources, such as airplane exhaust nozzles or other warm military vehicle parts, in order to hit their targets. MIR based countermeasure systems built in the vehicle are able to jam these heat-seeking sensors, such that those missiles are deflected and fail to reach the target.

Most of the above described applications benefit or can only be used with coherent and high-brightness MIR light sources. Therefore, the development of coherent MIR sources have been of special interest in the past and manifested itself in numerous approaches.

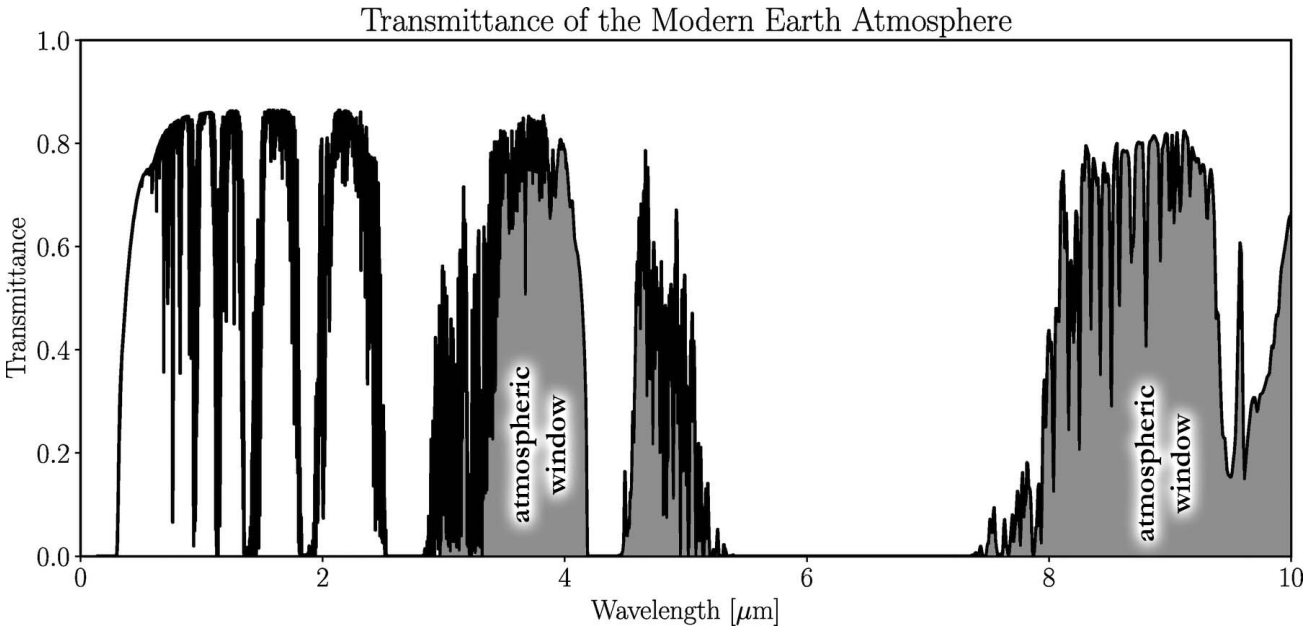

Figure 2.4: Atmospheric transmission spectrum from $0\,\mu m$ to $10\,\mu m$ calculated using the "Spectral Mapping Atmospheric Radiative Transfer" code [71]. The figure is adapted from [72].

2.2 Coherent MIR sources

To address the MIR wavelength domain several coherent light sources have been developed. The first of them to appear were CO_2 and CO lasers [75, 76]. Due to their bulkiness, lack of versatility, and the use of hazardous materials, many of these lasers are less common today than mid-infrared semiconductor lasers. Only applications where very high power is required are still operated by such lasers e.g. welding or metal cutting[75].

For a long time the lead-salt laser diode[77] has been an important source for coherent MIR light. This laser type is, inefficient, the used materials are toxic and furthermore lead-salt lasers are required to be cooled cryogenically. It is obvious, that their deployment is usually not economical in modern applications.

All changed with the invention of the quantum-cascade-laser (QCL) in 1994. It was a revolution for MIR-emitting coherent light sources[19]. The QCL is a semiconductor laser based on unipolar transitions within the conduction band and has quickly replaced many of the aforementioned MIR sources in numerous applications. Although the development of QCL technology was extraordinary steep, an even newer semiconductor laser recently challenged the dominance of the QCL: the interband cascade laser, which is often referred to as ICL [32]. ICLs offer great potential for cost reduction and high efficiency compared to QCLs. In that manner, ICLs became the most appropriate choice for remote gas sensors and FSO communication technology[33].

In this thesis we make use of the ICLs potential and exploit it in the two aforementioned application areas, spectroscopy and FSO. The aim of the thesis is not only to use the ICLs, it is also to reduce the costs of those systems even more by replacing the MIR detector with a secondary ICL exploiting the laser-as-detector approach, which will be discussed in a separate chapter. Because the laser-as-detector approach takes advantage of nonlinearities, it is believed that sensitivity of spectroscopy and performance of communication can be increased.

2.3 Goals of the chapter

We refrain from a detailed discussion of QCLs and ICLs at this point, because it will be addressed later in this chapter in detail. We therefore begin the next section by introducing the operation principle of conventional SCLs and evolve its idea via QCLs enabling finally to describe the operation principle of ICLs. This introduction is followed by investigations of the standard operation parameters and output specifications of our ICL devices. With that we verify the applicability for the aforementioned practical applications. To do so, we present a full characterization of the ICL devices provided through the Greek-German ILLIAS project[1]. The full-characterization also serves as a foundation for further analysis in subsequent chapters and includes

1. a characterization of the relation between light current and voltage (LVI) ,
2. spectral characterization,
3. the measurement of the optical linewidth,
4. the determination of the linewidth enhancement factor,
5. and measurement of the carrier lifetime.

The characterizations are accompanied with a discussion of the measurement techniques and a comparison to other semiconductor laser sources. This chapter closes with a summary of the characterization and is followed by a chapter discussing the mechanisms of the laser-as-detector concept.

[1]The ILLIAS project will be briefly described in 2.8

2.4 Laser operation in conventional Interband Diode Lasers

Common interband diode lasers (IDLs) are based on the recombination of an electron from the conduction band with a hole in the valence band both injected by a pn-junction also known as diode[11]. This so-called *interband* transition led to the specification of the name interband diode lasers.

Figure 2.5 shows the energies of the valence- and conduction band schematically as a function of the position in the most simple case of a biased homojunction diode serving as the active medium. The energies are defined by the energy gap of the semiconductor material E_{Gap} so that $E_{\text{Gap}} \equiv E_C - E_V$, whereas E_{Fe} and E_{Fh} represent the quasi-fermi-levels of the conduction band and valence band, respectively. The energy of the optical transition, depicted with the wavelike arrow, follows the condition $E_C - E_V < \hbar\omega < E_{Fe} - E_{Fh}$. An optical transition can occur spontaneously or can be triggered by a second photon, which is then referred to as *stimulated emission*.

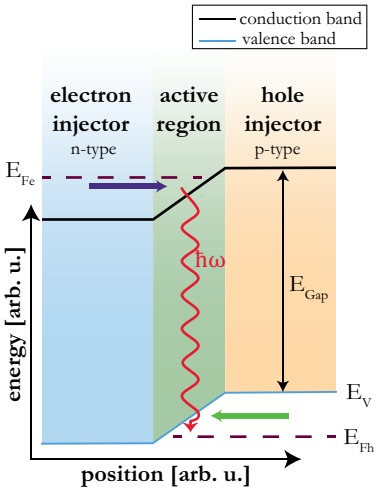

Figure 2.5: Simplfied bandstructure of a common biased semiconductor diode pn-junction, which represents the active medium of a semiconductor laser.

An active medium alone is not sufficient to generate stimulated emission and that's why a resonant cavity is needed. In a given resonant cavity including the active material, only longitudinal optical modes will experience enough amplification for stimulated laser emission. The emitted wavelengths λ_{cavity} supported by the cavity must follow the condition

$$\lambda_{\text{cavity}} = \frac{2n_{\text{SC}}L}{m} \tag{2.2}$$

with m an integer, L the length of the cavity and n_{SC} the refractive index of the semiconductor active material.

A cavity can have many different shapes. The most simple form of a cavity is the Fabry-Perot-resonator. It is realized by two parallel mirrors and the path length of the light L is given by the distance between the two mirrors. In SCLs the mirrors are formed by the cleaved semiconductor material itself. This is result of the relatively high refractive index of the material - for example $n_{\text{GaAs}} \simeq 3.5$ in GaAs - with respect to the refractive index of air $n_{\text{air}} \simeq 1.0$. This refractive index change causes a high internal reflectivity - in case of GaAs of $\sim 27\%$ - creating a photon density high enough for stimulated emission. This is a very advantageous feature, because it means that no additional external optical components are needed to create a cavity.

In a semiconductor laser the gain is usually quite broad and supports many cavity wavelengths. Thus Fabry-Perot-SCLs usually emit many longitudinal modes with a mode spacing of

$\Delta\nu_{\mathrm{L}} = \frac{c}{2n_{\mathrm{SC}}L}$ with c the speed of light. They are usually used if the spectrum of the laser is not crucial to the application, for example when only high brightness matters.

To achieve single-mode emission only o single mode has to be supported by the cavity. One approach is to add a distributed feedback (DFB) grating along the active zone of a common Fabry-Perot-resonator. The grating creates distributed feedback allowing only longitudinal laser modes which interfere constructively, usually only a single mode. The wavelength of these DFB-lasers can be tuned by changing the supported wavelength of the DFB-grating. This can be achieved one the one hand changing the device temperature, which both, changes the DFB-grating length and at the same time the materials refractive index. On the other hand the simplest possible way to achieve wavelength tuning of a DFB-laser is to change the current density. In that case the materials refractive index also changes as well as the devices temperature. Typical applications of DFB-lasers are application where the emission wavelength is important, for example spectroscopy [44, 78] or data communication [79] with wavelength-division-multiplexing[80, 81]. Another way to create single-mode emission is to add distributed-bragg-reflectors(DBR) to the laser facets. DBR reflectors are multi-layer reflectors made out of alternating material combination stacks each with a thickness of exactly $\frac{\lambda}{4}$, where λ is the desired wavelength.

Other types of cavities exit for semiconductor lasers, such as microdisc-resonators [82, 83], ring-resonators [84–86] and many more complex shaped cavities [87, 88]. Beside the longitudinal modes a laser can also exhibit off-axis *transverse optical modes* [89]. The origin of these modes is similar to the longitudinal modes, but is related to the spatial interference of light in the cavity. The transverse modes finally manifest themselves with rather complex beamprofile in the far-field.

Biasing the diode with a certain voltage creates a population inversion of the carriers, i.e. more carriers are in higher energy-states with respect to lower energy states. A population inversion is necessary to provide sufficient carrier-hole pairs for photon generation. This in turn can also be induced by incident photons so that stimulated emission can take place and coherent light is emitted. Semiconductor lasers are superior coherent light sources. They combine all three requirements for laser emission, namely the active medium within a resonant cavity and an optical pump in a single microscopical element.

Since the first demonstration of a working semiconductor laser in 1962, they have been continuously improved and developed. A significant milestone was the invention of lasers based on heterojunctions[90, 91], which again lead to a whole new family of semiconductor lasers. Two special types of semiconductor lasers are described in the next sections, namely the quantum cascade laser and interband cascade laser. They consist of numerous heterojunctions, but utilize different band-structure-architectures than conventional quantum-well lasers to achieve enough optical gain in the MIR wavelength domain. The operation principle of QCLs and ICLs are discussed in the next two sections.

2.5 Quantum Cascade Lasers

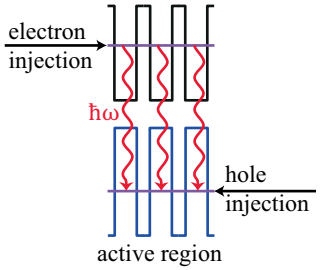

(a) Quantum Well Laser

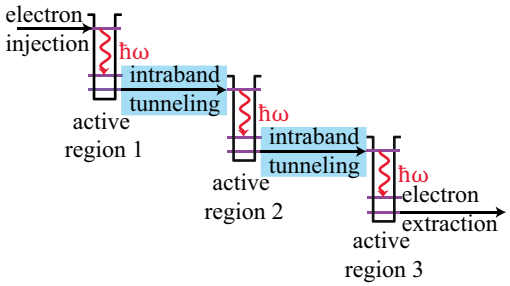

(b) Quantum Cascade Laser

Figure 2.6: Comparision of carrier injection and photon emission in **(a)** a quantum well laser and **(b)** a quantum cascade laser. Black: conduction band, blue: valence band, violet: energy states, red: radiative transitions.

In contrast to IDLs with a quantum well structure (Fig. 2.6a) using type-I band alignments, the emission of photons in QCLs is based on unipolar transitions of electrons between energy states **within** the conduction band (Fig. 2.6b) using type-II band alignments. Those transitions are often referred to as *intraband* or *intersubband transitions*.

A layered sequence of alternating thin semiconductor materials with different bandgaps, forms several quantum wells and mimics a crystal with a periodicity much larger than the atomic one, the so-called *super-lattice* [92, 93]. Due to the well-known effect of quantization, localized electronic energy states for the charge carriers - in this case electrons - arise[19]. But in contrast to the atomic crystal structure, where electronic states are created in terms of bands and bandgaps[94], these electronic states are located *within* the conduction band. The fact that the level of the energy states depend on the width of the semiconductor layers, makes it possible to manufacture transitions with a desired energy, without changing the semiconductor material[95], which is one of the most advantageous property of QCLs. The electronic energy states in the conduction band can have a band structure again, which in the literature is called either minibands or subbands[95]. They arise, when many alternating semiconductor layers with the same width are sequenced, which is visualized in Fig. 2.7. The energy gap between those subbands is then called a minigap. The major challenge in QCL fabrication is the atom layer precision of the epitaxial growth of the alternating semiconductor films with partially only few atom layers thickness together with an extremely high precision as well as development of a suitable waveguide.

Using an appropriate arrangement of layers makes it possible to create a 3-level-laser scheme, where the bandgap between two subbands can be utilized for an optical transition. This is schematically depicted in Fig. 2.8. The optical transition takes place between the 3rd and the 2nd energy state $|3\rangle$ and $|2\rangle$ (wavelike arrow) emitting a photon with the energy $E_3 - E_2 = \hbar\omega$, where ω is the angular frequency of the emitted laser light and $\hbar$ is the reduced Planck constant. Quantum mechanical selection rules restrict the transitions to those, where the electrical field vector is perpendicular to the plane of the quantum films[95, 96].

Thus, QCLs can only emit transversal-magnetic (TM) polarized radiation. Non-radiative transitions between the subbands occur due to electron-phonon-scattering by emitting a longitudinal optical phonon with the energy E_{Ph}, which are depicted with a straight (not undulating) arrow in Fig. 2.8. The phonon emitting transition from the 2nd to the 1st state is significantly faster compared to the optical transition, having a typical relaxation time of a few picoseconds[95]. Thus, it is possible to create a population inversion between the 3rd and 2nd energy state. The transition lifetime of the optical transition is still very small, such that the modal gain of a single active region is insufficient for laser operation. Thus, a repetition of the active stages is required. The number of repetition amounts typically from 20 to 60, which represents a compromise between a high power output and a high precision in the manufacturing process[95]. The electrons finally cascade through this structure of quantum films, which gave the quantum cascade laser its name.

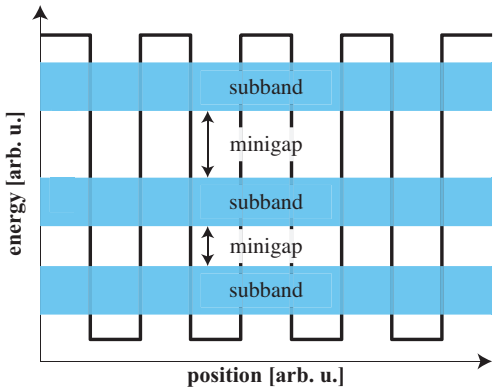

Figure 2.7: Minband and minigap in a superlattice formed by alternating films of semiconductor material with different bandgaps

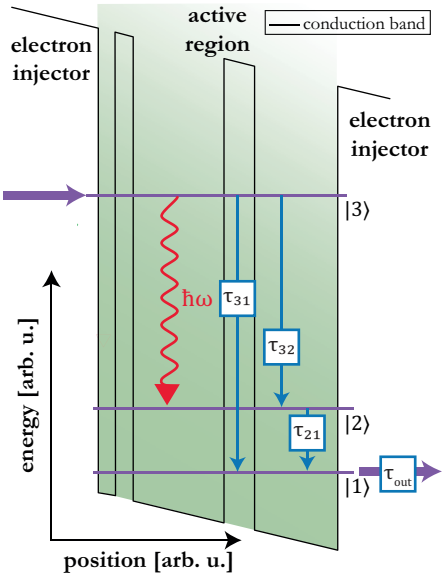

Figure 2.8: Focus on a simplified bandstructure of a QCLs active region with injector stages.

Laser operation in quantum cascade lasers

The cascading structure of QCLs requires regions in between the active media, which transfer the carriers from one active to the next active regions, the so-called injector regions. An injector region[19] and the active region represent one stage of a QCL. But in contrast to the optical active region, where only 3 energy states are manifested, the relaxation stage, which acts also as the injection stage contains a subband structure. To make the carriers pass the electronic structure a voltage perpendicular to the quantum films is applied. Thus, a potential gradient over the whole structure is being provided. Two stages with applied potential gradient are schematically shown in Fig. 2.9.

In the case of a properly applied bias voltage the injector region forms a miniband with a similar energy to state $|3\rangle$ as indicated in Fig 2.9. The injector region itself is made up of multiple quantum films. Its purpose is to inject the electrons into level $|3\rangle$ of the active region and prevent the injection into level $|1\rangle$ and $|2\rangle$. As already described the laser emission occurs in the active region between level $|3\rangle$ and level $|2\rangle$. The population inversion is obtained by a relatively long relaxation time τ_{32} while a fast transition occurs between $|2\rangle$ and level $|1\rangle$ by emitting an optical phonon with a corresponding short relaxation time τ_{21}. Thus $\tau_{32} > \tau_{21}$ holds. Non-radiative transitions from level $|3\rangle$ to level $|2\rangle$ or $|1\rangle$ can happen as well, but they are counterproductive for photon emission. From level $|1\rangle$ the electron is being extracted and relaxes within the subband into the next injector stage and then in the consecutive active region.

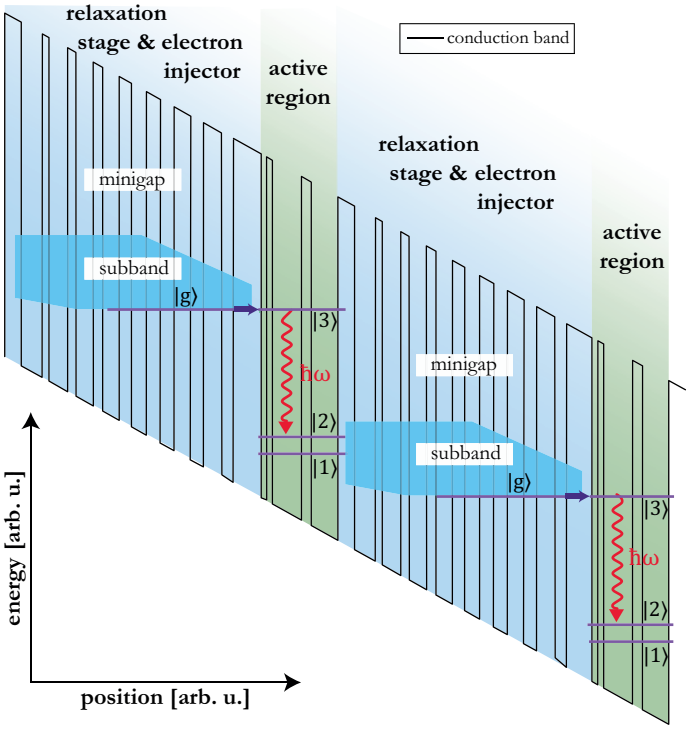

Figure 2.9: Simplified conduction band structure of two stages of a Quantum Cascade Laser. Combined relaxation stage and electron injector (blue), active region (green). Inspired by [97].

2.6 Interband Cascade Lasers

The theoretical concept of interband cascade lasers (Fig. 2.10c) was born in 1994 [27], which was the same year the QCL was technologically realized [16]. The idea was to combine technology from conventional quantum well (QW) diode lasers (Fig. 2.10a), that generate photons via recombination between conduction and valence band, and intersubband-based QCLs (Fig. 2.10b) utilizing their cascaded structure for enhanced gain and carrier recycling.

It took only three years for the first technological realization of an Interband Cascade Laser (ICL) to prove that this hybrid semiconductor laser works. In 1997 an ICL emitting at a wavelength of $3.8\,\mu m$ was reported, but still at cryogenic temperatures [28]. Many efforts in optimizing the band structure [98–102] finally led to cw-operation at room temperature in 2008 [29] at a wavelength of $3.75\,\mu m$. Since then, ICLs became the laser of choice for portable MIR laser applications operating in the spectral range between $3\,\mu m$ and $6\,\mu m$ [33]. With QCLs ICLs share the superior advantage that controlling the thickness of the active regions semiconductor layers during the epitaxial growth process enables precise tailoring of the emission wavelength. However, unlike QCLs, voltage and current requirements are minimal[32]. QCLs are constructed by using at least 30 active stages to overcome its internal optical losses and generate enough optical gain, while ICLs only require 3 to 5 stages resulting in a much lower threshold current density and significant lower voltage. Subsequently, the ICL has proven to be an impressively power-efficient competitive MIR source for many spectroscopy applications [30, 31, 39, 103, 104]. The low power consumption is extremely desirable for battery-powered or ultra low-power sensors, which resulted in the most famous application of an ICL, the employment in the methane detector of the NASA Curiosity-rover. The result was a quantification of a mean methane-abundance of

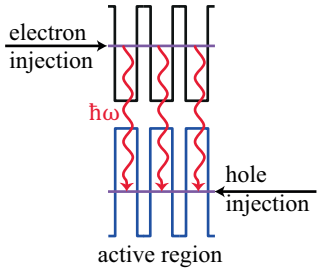

(a) Quantum Well Laser

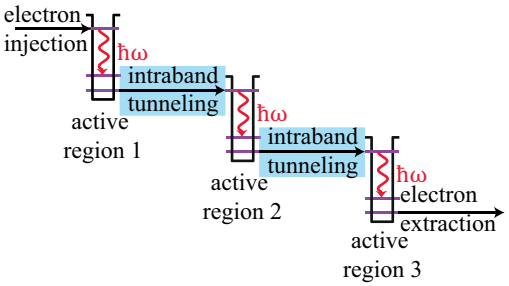

(b) Quantum Cascade Laser

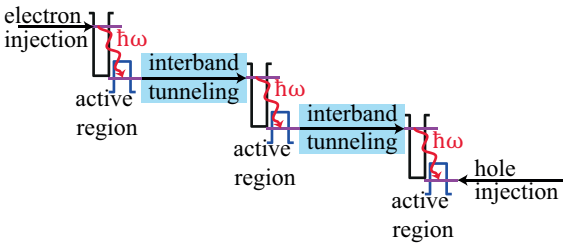

(c) Interband Cascade Laser

Figure 2.10: Comparision of carrier injection and photon emission in **(a)** a quantum well laser, **(b)** a quantum cascade laser and **(c)** an interband cascade laser. Black: conduction band, blue: valence band, violet: energy states, red: radiative transitions.

$0.69(25)\,\mathrm{ppbv}$ (parts per billion by volume) in the martian atmosphere[34], representing the most precise extraterrestrial methane determination that has ever been performed.

Further rapid ICL technology breakthroughs, such as frequency-comb generation and stabilization [105–108] as well as utilization in quartz-enhanced photoacoustic sensors [109, 110], lead to high resolution spectroscopy applications [111] and have the potential to enable more exciting future prospects. Beside spectroscopy ICLs have also been used to exploit the transparency window of the atmosphere in the MIR wavelength domain by acting as data transmitter in a FSO communication link to successfully transfer information with a transmission speed of $70\,\mathrm{Mbit\,s^{-1}}$ [47].

The most recent performance of ICLs includes emission of up to $10.4\,\mu\mathrm{m}$ [112]; others showed operation temperatures of up to $118\,^{\circ}\mathrm{C}$ and multi-mode output powers of more than $900\,\mathrm{mW}$ at room temperature [113]. Single-mode operation has been reported of up to $55\,\mathrm{mW}$ at room temperature for wavelengths around $3.4\,\mathrm{nm}$ [114]. Threshold densities remain significantly lower than that of competitive QCLs with as low as $106\,\mathrm{A\,cm^{-2}}$ at room temperature [33] and wallplug efficiencies of more than 18% [33].

The steep technology progress of ICL fabrication and the previously described impressive specifications attest that it is indeed valid to consider the ICL the laser-of-choice for the MIR wavelength domain. The dominance of the ICL is obtained due to their unique band structure for the realization of the active region.

Interband cascade lasers represent a unique class of semiconductor lasers for coherent MIR emission[32]. The optical transition takes place in a QW structure between conduction and valence band, such as in common MQW lasers, while the QCL concept of a cascading structure is adapted to generate enough gain for coherent emission. Like in QCLs, the active core is a structure of numerous alternating films of semiconductor material usually grown by molecular beam epitaxy (MBE), which ensures a high epitaxial thickness accuracy[115]. The alternating films are assembled to obtain the three building blocks of the ICLs active core

1. the electron injector,
2. the optical active region,
3. the hole injector.

These building blocks are repeatedly connected in series forming the whole active core. An electron can cycle, i.e. cascade, thorough these repetitions, which gave the interband cascade laser its name.

A schematic band-diagram of a typical active region is depicted in Fig. 2.11a and shows the sequence of the building blocks forming one and a half stage of the active core. The electron injector's (blue background) task is to populate the upper laser level of the optical active region (green background) with electrons. To achieve this, its coupled InAs/AlSb QWs band structure is designed to form a subband with a ground state $|g\rangle$ that is aligned with the upper laser level $|2\rangle$ in the case when an external electrical field is applied. The adjacent optical active region can be manufactured with a type-I or type-II band alignment, where the latter shows

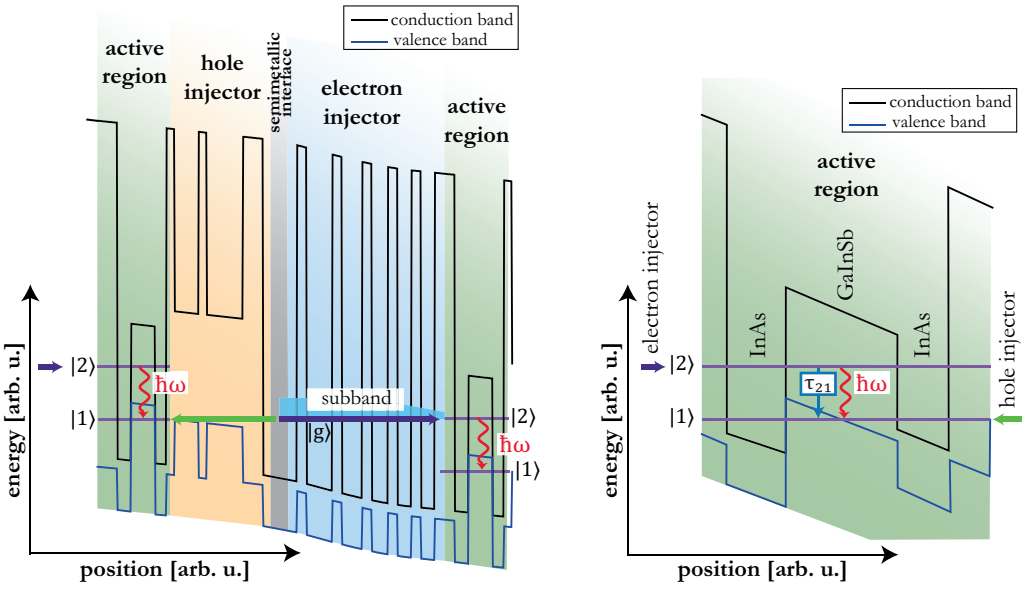

(a) Simplified band structure of a full stage plus a second active region of an Interband Cascade Laser, showing all three ICL building blocks and the semimetallic interface (grey background). The active region bandstructure is highlighted by a green background, the hole injector has a yellow background, while the electron injector is highlighted by a blue background. The electron injectors generate a subband with a ground state $|g\rangle$, which when aligned coincides with the upper laser state $|2\rangle$, when a bias voltage is applied.

(b) Focus on the active region sandwiched between electron and hole injector region. The purple lines show the upper $|2\rangle$ and lower $|1\rangle$ laser state of conduction band and valence band, respectively. The red wavelike arrow depicts the photon radiative transition with energy $\hbar\omega = E_{|2\rangle} - E_{|1\rangle}$.

Figure 2.11: Simplfied band structure of a type-II Interband Cascade Laser (a) and a focus on the active region (b). The band structure has been provided by our project partner nanoplus®.

preferable performance [33]. The "W"-shaped QW is usually constructed by two InAS QWs sandwiching a layer of GaInSb, which is schematically depicted in Fig. 2.11b. The thickness of the two InAs wells defines the energy of the upper laser level and therefore is used to precisely tailor the emission wavelength of the ICL. The "W"-shape ensures maximal spatial overlap of the conduction band (black) and valence band (blue) wavefunctions for the laser transition (wavelike red arrow). To guarantee a population inversion, the typical carrier lifetime of the laser transition τ_e is longer than the timescales the adjacent injectors need to repopulate the laser states. The electron injectors generate a subband with a ground state $|g\rangle$, which when aligned coincides with the upper laser state $|2\rangle$ in the case of an applied bias voltage. The semimetallic interface is marked with a grey background. To hole injector (yellow background in Fig. 2.11a) follows the optical active region and injects holes into the active region by utilizing states in the valence band formed by coupled AlSb/GaSb QWs. An ICL stage finishes with a

hole-injector and the next stage follows with its electron-injector. The connection of hole and electron-injector is designed to mimic a semi-metallic band alignment[116]. Its purpose is to populate hole and electron injector with carriers. Therefore the states in the hole-injector must be in agreement with the subband of the electron injector in the case of an external bias. This kind of carrier recycling has shown to be superior in terms of optical losses with respect to other recycling concepts [114, 117]. Finally, the active core is embedded in two lightly n-doped separate-confinement layers (SCLs) to reduce the waveguide loss.

The optical transitions of carriers within the aforementioned band structure create several photons. The relation between carriers and emitted photons can be described with a rate equation model, which will be discussed in the next section.

2.7 Rate equation model for Interband Cascade Lasers

Lasers in general are appealing dynamical systems . Their physical quantities, i.e. the carrier inversion ΔN or the optical field $\tilde{E}$ and their material polarization P change, when the time progresses. The mathematical formulation to describe the time dependence is deployed by a set of three non-linear rate equations of those quantities. These rate-equations can be derived from the time dependent wave equation of electromagnetic theory

$$\bigtriangledown^2 \mathcal{E} - \frac{1}{c^2}\frac{\partial^2 \epsilon \mathcal{E}}{\partial t^2} = \mu_0 \frac{\partial^2 \epsilon \mathcal{P}}{\partial t^2} \tag{2.3}$$

following the procedure described in [118] and [119]. Here, $\mathcal{E}$ denotes the electrical vector field, $\mathcal{P}$ the polarization vector of matter, ϵ the electric permittivity tensor, c the speed of light in vacuum and μ_0 the magnetic permeability in vacuum. Following [119] and utilizing the plane wave approximation, the rate-equations can finally be described by the so-called Maxwell-Bloch equations:

$$\frac{\mathrm{d}\Delta N\left(t\right)}{\mathrm{d}t} = -\gamma_N \left(\Delta N\left(t\right) - N_0\right) - 2g \cdot \left(\tilde{E}^*\left(t\right) P\left(t\right) - P^*\left(t\right) \tilde{E}\left(t\right)\right), \tag{2.4}$$

$$\frac{\mathrm{d}\tilde{E}\left(t\right)}{\mathrm{d}t} = -\left(i\omega_E + \gamma_E\right) \tilde{E}\left(t\right) + g \cdot P\left(t\right), \tag{2.5}$$

$$\frac{\mathrm{d}P\left(t\right)}{\mathrm{d}t} = -\left(i\omega_P + \gamma_P\right) P\left(t\right) + g \cdot \tilde{E}\left(t\right) \cdot \Delta N\left(t\right), \tag{2.6}$$

where N_0 represents the population inversion in the absence of a laser field. The decay-rate for the electrical field is denoted by γ_E, the decay-rate for the polarization by γ_P and the decay-rate for the inversion by γ_N. The variable g denotes the optical gain, while ω_E and ω_P represent the angular oscillation frequencies of the electrical field and the materials polarization, respectively [119, 120].

To obtain these equations the following assumptions have been made [119]:

- the electrical field is assumed to be a plane wave,
- the optical field is assumed to propagate in only one direction,
- the medium is treated as a homogeneous two-level system,
- only one longitudinal mode is considered,
- the rotating wave approximation (often referred to as RWA) is used and thus fast oscillating terms cancel out,
- losses are continously distributed over the entire cavity,
- no noise terms are considered.

Lasers can be divided into three different classes according to their dynamical properties [121]. The main property determining the dynamics is basically the active laser material. Each material has a specific decay rate of the three physical quantities, the decay-rate for the electrical field γ_E, the polarization γ_P and the inversion γ_N. In the case that one of those decay-rates is much faster than the other ones, it can be adiabatically eliminated and thus reduces the number of rate equations by one.

Class A lasers ($\gamma_P, \gamma_N \gg \gamma_E$) can be described by a single equation for the electrical field and only time-independent solutions exist. A dye laser is a typical class A laser. Class B ($\gamma_P \gg \gamma_N, \gamma_E$) lasers can be described by a two rate equation for the electrical field and the carrier inversion. Class-B lasers provide periodic solutions, where the system can fluctuate between inversion and optical field. A semiconductor laser is a typical class B laser. Class C ($\gamma_P \simeq \gamma_N \simeq \gamma_E$) lasers must be described by a full set of rate equations. Class-C lasers exhibit chaotic dynamics above the so-called second laser threshold. A typical Class C laser is a He-Ne laser operating at a wavelength $3.39\,\mu\mathrm{m}$.

In the case of an ICL these rate equations are quite similar to the rate equations of a conventional IDL [122, 123]. Like it is has been already described above, the dynamics can be modeled by two rate equation for the electrical field $\tilde{E}$ and the carrier inversion ΔN. To include the ICLs cascaded structure in the description, the gain g must be simply multiplied by the number of cascades Z. We obtain

$$\frac{\mathrm{d}\Delta N\left(t\right)}{\mathrm{d}t} = \frac{\zeta J}{qd} - \frac{\Delta N\left(t\right)}{\tau_{\mathrm{eff}}} - g \cdot \Delta N\left(t\right) \cdot \tilde{E}^{*}\tilde{E} + F, \tag{2.7}$$

$$\frac{\mathrm{d}\tilde{E}\left(t\right)}{\mathrm{d}t} = \left(i\omega_{\Delta N_{\mathrm{int}}}\left(\Delta N, \omega\right) + \frac{1}{2}\left(Zg \cdot \Delta N\left(t\right) - \frac{1}{\tau_{\mathrm{ph}}}\right)\right)\tilde{E} + \tfrac{Z}{2}\Delta N \tau_{\mathrm{eff}} + \tilde{E}_{\mathrm{sp}}. \tag{2.8}$$

The parameter Z denotes the number of the cascading stages, q the carrier charge, J the carrier injection current density, d the active layer thickness and ζ the corresponding current injection efficiency, while F and E_{sp} are now Langevin-noise terms following the description of

QCLs[124]. The characteristic times of the system are given by the effective carrier-lifetime is τ_{eff}, as well as the photon lifetime in the laser resonator τ_{ph}[57]. The effective lifetime is composed of the lifetime of Auger-transitions τ_{Aug} and the lifetime of spontaneous emission τ_{e} following

$$\tau_{\text{eff}} \equiv \left(\frac{1}{\tau_{\text{e}}} + \frac{1}{\tau_{\text{Aug}}} \right)^{-1}. \tag{2.9}$$

The angular resonant optical frequency of the cavity mode is described by $\omega_{N_{\text{int}}}(n, \omega)$. Without external light injection $\omega_{\Delta N_{\text{int}}}(\Delta N, \omega)$ can be in a first-order approximation expanded to[54]

$$\omega_{\Delta N_{\text{int}}}(n, \omega) = \omega + \frac{1}{2}\alpha \left(Zg \cdot \Delta N - \frac{1}{\tau_{\text{ph}}} \right), \tag{2.10}$$

where ω is the angular oscillation frequency of the laser without coupling/feedback and α the linewidth enhancement factor (LEF)[125].

In order to simplify the rate equations the ansatz

$$\tilde{E}(t) = E(t) \exp\left(i\left(\omega t + \phi(t)\right)\right) \tag{2.11}$$

can be inserted into Eqn. 2.8, where $E(t)$ represents the slowly varying real field amplitude and $\phi(t)$ the slowly varying real field phase[125]. This step is often referred to as introduction of the slowly varying envelope approximation (SVEA). We find the final rate equations for a solitary ICL to be

$$\frac{\mathrm{d}\Delta N(t)}{\mathrm{d}t} = \frac{\zeta J}{q} - \frac{\Delta N(t)}{\tau_{\text{eff}}} - g \cdot \Delta N(t) \cdot \tilde{E^*}(t)\, \tilde{E}(t) + F, \tag{2.12}$$

$$\frac{\mathrm{d}E(t)}{\mathrm{d}t} = \frac{1}{2} \cdot \left(Zg \cdot \Delta N(t) - \frac{1}{\tau_{\text{ph}}} \right) E(t) + E_{\text{sp}}, \tag{2.13}$$

$$\frac{\mathrm{d}\phi(t)}{\mathrm{d}t} = \frac{1}{2} \cdot \alpha \left(Zg \cdot \Delta N(t) - \frac{1}{\tau_{\text{ph}}} \right) + \phi_{\text{sp}}. \tag{2.14}$$

Here, the orange term describes the injection of charge carriers into the active medium. The terms corresponding to spontaneous emission are highlighted in green, while the in blue highlighted terms correspond to stimulated emission. In other literature the term $\frac{1}{\tau_{\text{ph}}}$ is often referred to as optical loss of the cavity [126, 127]. For a given set of parameters, the state

of a solitary operating ICL at time t is therefore fully determined by the 3 values E, ϕ, ΔN. The described model was developed by us, before [128] was released, yet both are completely consistent. The rate equations will be used in an extended form for modeling the laser under feedback, as well as for simulation of the unidirectionally and bidirectionally coupled laser system. Therefore, it is necessary to reveal most of the above described parameters of our ICLs, which will be covered in the following two sections, where the opto-electrical characterization is described.

2.8 ICL devices - The ILLIAS project

All experimentally utilized ICLs are provided within the framework of the Greek-German ILLIAS-project by the project partner nanoplus®. The aim of this project is to develop a gas sensing platform, which requires no additional detector. With that a measurement principle following [56] shall provide the same or even better detection limit than conventional sensors. Instead to [56], the plan is to utilize ICLs provided by nanoplus®. All ICL devices can be operated at room temperature, they emit in a wavelength region between $3192\,\mathrm{nm}$ to $3450\,\mathrm{nm}$, show output powers up to $20\,\mathrm{mW}$ and need typical bias voltages of $2\,\mathrm{V}$ to $3.5\,\mathrm{V}$, while the threshold current amounts to $15\,\mathrm{mA}$ and $25\,\mathrm{mA}$ depending on the devices temperature. Subsequently, all devices are suitable for spectroscopy of CH_4, which is therefore used as a sample demonstration gas. Some of them also cover spectral lines NO_2, which is the main gas of interest of the ILLIAS-project. Beside the spectroscopy application all devices are well suited for free-space optical communication, because the atmosphere provides an open spectral window within the devices wavelength domain, which can be reviewed in Fig. 2.4. The most important electrical and optical properties are provided by nanoplus and are summarized in Table 2.1, but will be characterized again by us in Section 2.9 for verification reasons.

Figure 2.12: Logo of the Greek-German ILLIAS project

The calculated band structure of one and a half stage of ICL batch 3150 is shown in Fig. 2.13 as an example for all devices. The active region (green) has the typical "W"-QW configuration with a AlSb/InAs/GaInSb/InAs/AlSb layer structure. An adjacent InAs/AlSb super lattice (blue background) acts as the electron injector forming the subband. A hole injector formed by GaSb/AlSb layers follows the active region on the other side. The picture depicted in Fig. 2.14 shows a scanning electron microscope picture of the five cascaded active regions together with the separate-confinement layers of the waver of nanoplus ICL batch 3150.

All c-mount ICLs are mounted on a self-designed copper heatsink shown in Fig. 2.14, which compensates thermal elongation in order to verify a constant distance to the collimation lens (CAD-drawing can be found in Appendix Fig. 6.1). The heatsink can be temperature controlled by a built-in peltier element. In order to prevent water condensation on the mount surface and the laser, the temperature is not set below $12\,^{\circ}\mathrm{C}$. This setup is a versatile mount for laboratory purposes allowing electrical high-frequency connection through the SMA-connectors. Batch 2813 ICLs are mounted within a TO66-Can (visualized in Appendix Fig. 6.2) with an integrated temperature controlling peltier element. This mount is beneficial for in-field applications, because the ICL is protected with respect to the environment and water condensation. The

TO66-Can ICLs are mounted in a special nanoplus heatsink, which provides low-frequency electrical connections for the driver current and the peltier cooling element.

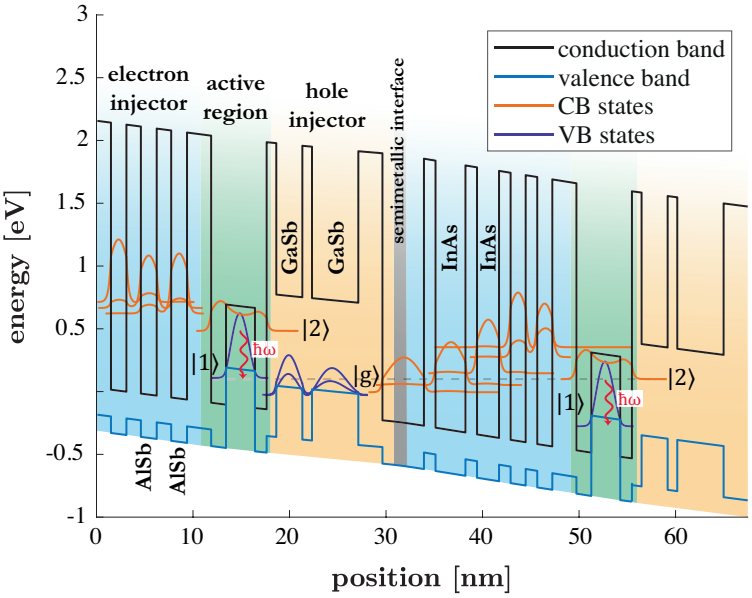

Figure 2.13: Calculated band structure of 1.5 stages of the nanoplus ICL batch 3150. The temperature of material amounts to $300\,\mathrm{K}$ and an applied electrical field strength of $100\,\mathrm{kV\,m^{-1}}$ is suggested. For more information on batch 3150 see Tab 2.1.

2.9 Opto-electrical characterization

With the opto-electrical characterization of the previously introduced devices, we provide an appropriate basis for simulating the lasers with the newly developed rate-equation model introduced in Section 2.7. These simulations will accompany our experimental findings to qualitatively evaluate the laser-as-detector approach in Chapter 3.

In order to quantitatively and qualitatively discuss the laser-as-detector concept the optical output power of each laser and terminal voltage in the free-running operation are of major importance. Changes of the terminal voltage, when the lasers are subjected to external optical perturbation, will be referenced to the values obtained from the determination of the **light-voltage-current** (LVI) **characteristics** in the free-running case.

External optical perturbation scenarios, namely mutual coupling and unidirectional injection locking require two lasers emitting on a close-by wavelength, i.e. their optical frequencies must stay within the so-called locking bandwidth (LBW). The LBW will be comprehensively discussed in Chapter 3 and calculated using the original free-running **optical spectra**. The optical spectrum of each ICL is obtained individually making use of a Fourier-transform-infrared (FTIR)

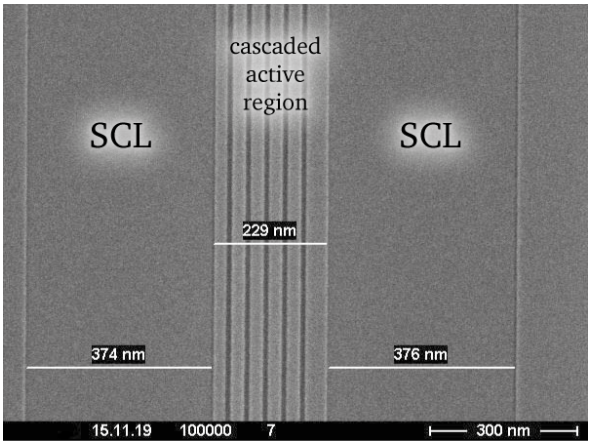

Figure 2.14: Scanning Electron Microscope of the active region and seperate confinement layers of the nanoplus ICL batch 3150. For more information on batch 3150 see Tab 2.1

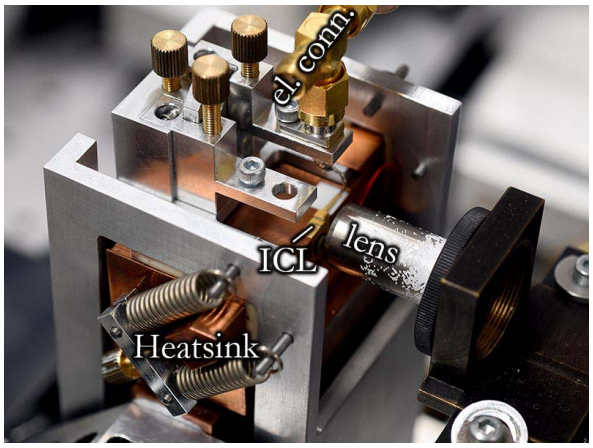

Figure 2.15: ICL mounted on the copper heatsink with tubed lens in front of the facet and electrical connection (el. conn.) to the current driver.

Name	Mount	Type	active stages	ridge length [μm]	Min. temp. [$^{\circ}C$]	Max. temp. [$^{\circ}C$]	Max. current [mA]	max. opt. output power [mW]	Min. wavelength [nm]	Max. wavelength [nm]	Spec. line coverage *species*
2183/10-12	TO66	DFB	6	900	0	40	80	11	3200	3256	CH_4
2183/22-25	TO66	DFB	6	900	5	35	80	10	3192	3245	CH_4
2744/01-16	C-mount	FP	5	900	20	40	90	18	3375	3450	CH_4, NO_2
2744/07-08	C-mount	DFB	5	900	20	45	90	14	3426	3429	CH_4, NO_2
2744/13-25	C-mount	DFB	5	900	20	45	90	10	3429	3432	CH_4, NO_2
3150/07-21	C-mount	DFB	5	900	15	40	90	20	3430	3444	CH_4, NO_2
3150/13-06	C-mount	DFB	5	900	15	40	90	15	3432	3445	CH_4, NO_2
3150/19-06	C-mount	DFB	5	900	15	40	90	17	3431	3445	CH_4, NO_2

Table 2.1: Overview of all used ICLs with properties provided by nanoplus®.ICL 2744/01-16 is not discussed in this thesis.

spectrometer, which enables direct conversion from current to wavelength. This conversion-table can then be utilized for precisely adjusting the wavelength of each laser. With that, it is possible to exactly configure the so-called optical frequency detuning (OFD) $\Delta\nu$ of two lasers in mutual coupling or unidirectional injection locked configuration. The current-to-wavelength calibration is also useful for a quick computation of the lasers wavelength without monitoring it permanently enabling effort-efficient absorption spectroscopy experiments discussed in Chapter 4.

A single mode laser spectrum is never infinitely small and thus "goes" hand in hand with an **optical linewidth**. A small optical linewidth is a crucial parameter for precise laser based spectroscopy measurements, because the recorded spectroscopy signal of many techniques represents a convolution of the absorption-lineshape and laser-lineshape, where the latter is quantified by the optical linewidth. In that manner, the optical linewidth is needed for precise gas-concentration determinations in Chapter 4 allowing accurate curve fitting of the signal to the theoretical reference - the HITRAN database [129]. Unfortunately, the optical linewidth can't be obtained with the wavelength calibration setup, because the FTIRs resolution of $2.25\,\mathrm{GHz}$ is not sufficient. We challenge this by exploiting a technique using the measurement of the **optical-frequency noise** (OFN) to draw conclusion on the optical linewidth following the concept found in [130].

OFN and intensity noise are a result of stochastic processes of stochastically independent events of spontaneous emission. The rate of the spontaneous emission is mainly determined by the carrier-lifetime of the upper laser state, which represents one of the most important parameters for semiconductor lasers. A relatively long **carrier-lifetime** compared to the pumping rate ensures the necessary population inversion for stimulated emission. It also determines the relaxation oscillation frequency. The latter represents one of the most important frequencies in many laser-dynamic determining experiments [131, 132] and limits the performance in many applications [133–135]. We access the carrier lifetime using an electrical small-signal modulation exploiting the frequency dependency of the ICLs impedance following the approach discussed in [136].

The second major dynamic-determining parameter of a lasers is the so-called **linewidth enhancement factor** (LEF), which has already been introduced in Eq. (2.10). The LEF has a remarkable influence on laser-dynamics especially when the device is subjected to optical feedback [137] or is injection-locked to any second laser. It can also found in literature under other designations such as α-Parameter, linewidth broadening factor or Henry-Factor[138]. Since the LEF describes the coupling between electrical field amplitude and electrical field phase of the optical field within the laser, it determines the minimal optical linewidth that can be achieved. The intrinsic Schawlow-Townes linewidth limit [139] is broadened by the factor $(1+\alpha^2)$ [140], where α represents the LEF. A more in-depth description of the LEF can be found in 2.9.4, where we also describe the self-mixing technique we use for its determination.

2.9.1 Light-voltage-current characteristics

The light-voltage-current (LVI) characteristic of each used ICL serves as a reference for measurements, where we compare optical output and voltage changes when they are subjected to an external optical perturbation. To detect the threshold we follow the definition of the threshold by [141]

$$\frac{\mathrm{d}}{\mathrm{d}I}\frac{\mathrm{d}\log(P)}{\mathrm{d}\log(I)} \stackrel{!}{=} 0, \tag{2.15}$$

with optical power P and current I. To experimentally determine the threshold we therefore increase the current of the temperature stabilized laser stepwise and measure the optical power and terminal voltage using the setup depicted in 2.16. For that purpose the signal of the MCT-detector, a Vigo MCT detection unit [2], has been calibrated using a pyroelectrical detector in combination with a Newport 1936-C Powermeter for each measurement. This means, the absolute power measurement relies on the pyroelectrical detector. On the other hand the relative power measurement using the lock-in detection setup in combination with the low-noise MCT-detector assures a high accuracy also for low optical output power enabling a precise threshold determination. This characterization is performed with all devices listed in Table 2.1 and for several heatsink temperatures.

[2] type PVI-4TE-4-1x1-TO8-wAl2O3AR-35 implemented in a Vigo PIP-amplifier

Process of threshold determination by the example of ICL 2744/13-25

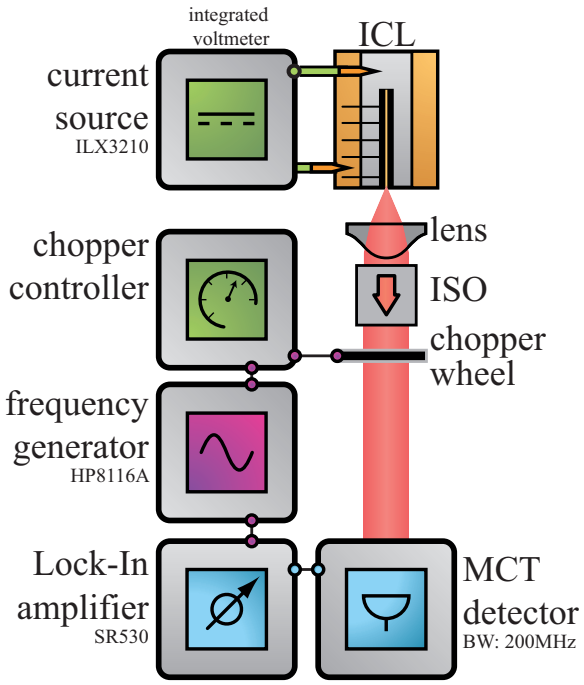

Figure 2.16: Schematic setup for investigation of free-running LVI characteristics using a lock-in detection setup. The isolator (ISO) prevents back reflections from all optical components to be fed back to the ICL, which could eventually lead to undesired unstable emission.

A typical result using the setup in Fig. 2.16 is exemplary visualized in Fig. 2.17 (top), showing the LVI characteristics of ICL 2744/13-25 at $20\,^{\circ}\mathrm{C}$ plotted against a logarithmic current axis. The middle graph shows the optical output power in units of dBm. The bottom graph shows the slope $\frac{\mathrm{d}\log(P/1\,\mathrm{mW})}{\mathrm{d}\log(I/1\,\mathrm{mA})}$. The maximum of latter defines the threshold of the laser according to Eq. (2.15), which in the measurement shown here amounts to $22.85\,\mathrm{mA}$. The threshold is marked with a green dashed vertical line and divides sub-threshold operation (orange) and laser operation (blue). The voltage of ICL 2744/13-25 is also shown in Fig. 2.17 (top) with respect to the driver current. The current-voltage dependency is linked to the devices resistance, which is a result of various electronic device properties, such as the semiconductor material bandgap, the doping as well as the interface roughness between two adjacent semiconductor layers[52]. Usually, ICLs have a higher resistance compared to common IDLs, because each of the 3 to 10 ICL stages introduces new interfaces and band transitions and therefore adds additional resistance resulting in a higher terminal voltage when operating[33]. However, compared to QCLs, the direct competitor, ICLs require significant less bias voltage. QCLs usually require 30 or more stages to minimize the threshold current and therefore usually need bias voltages beyond $9\,\mathrm{V}$[95].

Results of the threshold currents, threshold voltages and maximum optical output power of all DFB-ICL devices are summarized in Table 2.2. For the sake of a good comparison, we only list properties of the devices for the temperature of $20\,^{\circ}\mathrm{C}$, while more detailled information on temperature dependency is visualized in Fig. 2.18, where individual ICLs batches are grouped via a common color family. Batch 2183 ICLs are represented by a blue color, batch 2744 by green and ICLs of batch 3150 by red/yellow. With this color coding it becomes visible, that ICLs of the same batch demonstrate similar output and threshold specifications. Especially batch 3150 ICLs show remarkable similarities in all in Fig. 2.18 visualized properties, which is a first indication that they are good candidates for injection locking and mutual coupling.

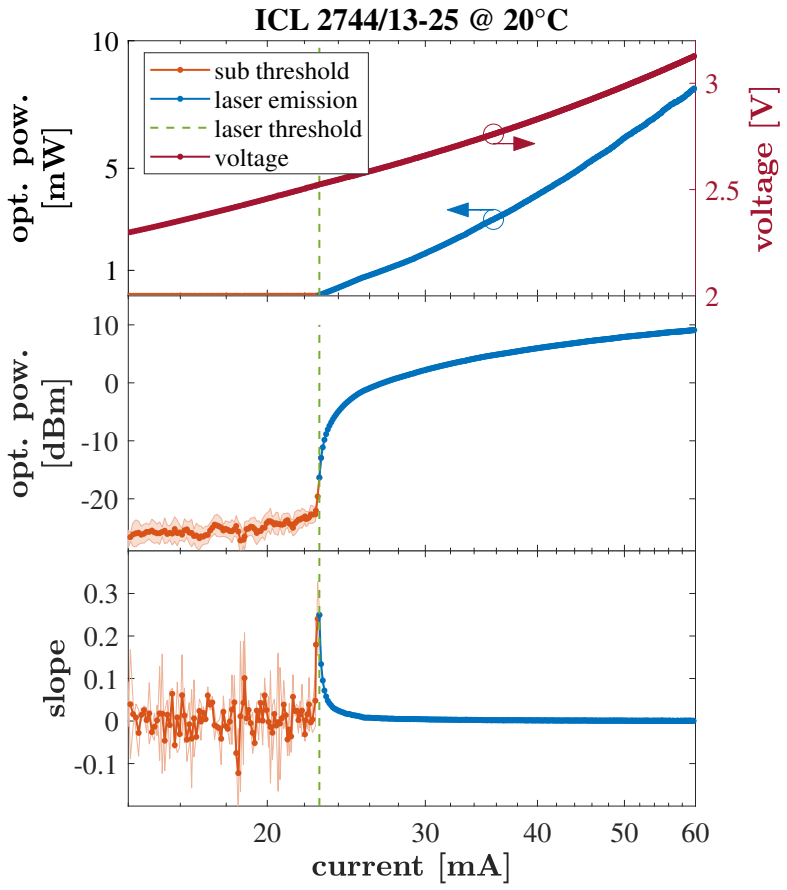

Figure 2.17: Exemplary LVI-characteristic curves for ICL 2744/13-25 with optical output power above threshold in blue with threshold amounting to $22.85\,\mathrm{mA}$ (green), terminal voltage in red and sub-threshold optical output power in orange. Note the logarithmically spaced abscissa. Top: optical output power with ordinate in mW and voltage with secondary ordinate on the right, middle: optical output power with ordinate in dBm and bottom: slope $\frac{\mathrm{d}\log\left(\frac{P}{1\,\mathrm{mW}}\right)}{\mathrm{d}\log\left(\frac{I}{1\,\mathrm{mA}}\right)}$, which is used for threshold detection according the criterion in Eq. (2.15).

Name	**threshold** [mA] @ 20 °C	**terminal voltage** [V] @ threshold	**max. opt. out. power** [mW] @ 20 °C
2183/10-12	22.82	3.26	3.60
2183/22-25	19.98	3.17	4.24
2744/07-08	28.61	2.81	6.04
2744/13-25	22.85	2.56	8.13
3150/07-21	19.47	2.30	11.33
3150/13-06	19.16	2.30	10.47
3150/19-06	19.10	2.30	10.75

Table 2.2: LVI characteristics at $20\,°\mathrm{C}$ of all ICL devices including threshold, voltage at threshold and maximum optical output power all at $20\,°\mathrm{C}$. Note that the maximum optical output power is also determined by the maximum operation current. For batch 2183 ICLs we applied a maximum current of $55\,\mathrm{mA}$ and $65\,\mathrm{mA}$ to batch 2744 and 3150 ICLs.

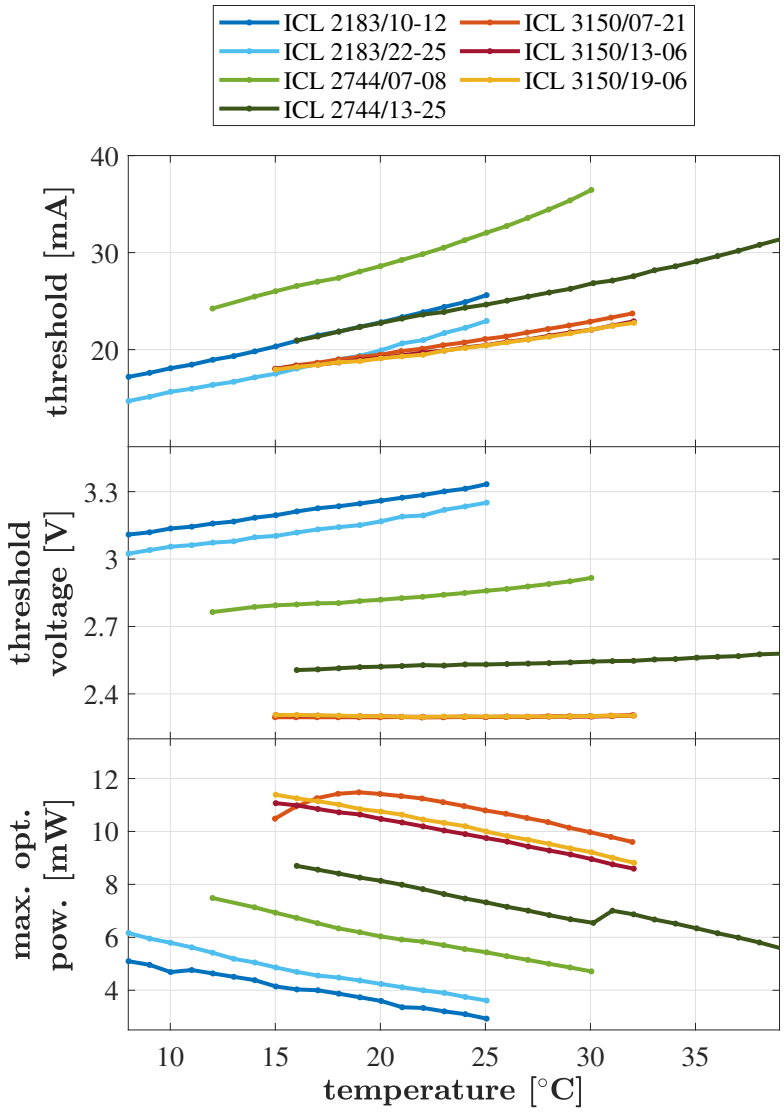

Figure 2.18: Overview of the most important LVI characteristics of all DFB-ICL devices: Threshold (top), terminal voltage at threshold (middle) and maximal optical output power (bottom) of all DFB-ICLs as a function of the heatsink temperature. The individual ICL batches are grouped via color. Batch 2183 ICLs are marked with a blue color, batch 2744 with green and ICLs of batch 3150 are colored in a red/yellow color.

2.9.2 Optical spectra

Generally, the optical spectra serve as a calibration for the driver-current dependency on the optical wavelengths. This calibration e.g. enables the calculation of the optical frequency detuning (OFD) in injection-locked or mutually coupled configuration. On the other hand, it is needed to determine the exact wavelength of the emitter for the purpose of absorption spectroscopy experiments, which are discussed in Chapter 4 and is therefore of utmost importance.

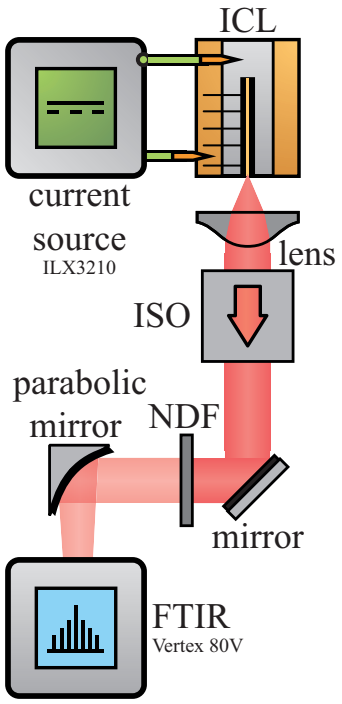

Figure 2.19: Schematic setup for investigation of free-running optical spectra using a Fourier-transform-interferometer. The isolator (ISO) prevents back reflections from all optical components to be fed back to the laser, which may destabilize the emission of the ICL.

The setup for the determination is shown in Fig. 2.19, where the spectrally resolving instrument to measure the spectrum is the Fourier-transform infrared (FTIR) spectrometer *Bruker Vertex 80V*. Its maximum resolution amounts to $0.075\,\mathrm{cm}^{-1}$, which converts to a optical frequency resoultion of $2.25\,\mathrm{GHz}$ or a wavelength resolution of $87\,\mathrm{pm}$ at mean wavelength of $3400\,\mathrm{nm}$. The detector used inside the instrument is either an integrated DigiTect liquid nitrogen cooled MCT detector or the previously described Vigo detection unit [3], which is placed inside the instrument and connected to the data-acquisition of the device.

For each ICL device we initially set current and temperature, then we take a discrete interferogram $I_\mathrm{d}(x)$ with the instrument. Since an infinite range of movement of the moving mirror of the FTIR is impossible, thus infinite samples can not be recorded, we perform a discrete Fourier transformation with the finite interferogram. Therefore we add zeros to the interferogram for artificially increasing the resolution of the calculated spectrum and simultaneously enhancing the signal to noise ratio (SNR) by the factor $\sqrt{2}$. For increasing the SNR the zero-filling factor must be equal or greater than two [142, 143], which means that at least two times as many zeros as the samples of the original interferogram itself must be attached to the original interferogram. A zero-filling-factor of 10 was empirically found to be optimal for SNR improvement and resolution enhancement while maintaining an appropriate computation time. The zero-filled interferogram is now referred to as $I_\mathrm{ZF}(x)$. We calculate each discrete complex spectrum $C_\mathrm{d}(\nu)$ using

[3] PVI-4TE-4-1x1-TO8-wAl2O3AR-35 with Vigo PIP-Amplifier

$$C_{\mathrm{d}}(\nu) = \sum_{n=0}^{N-1} W(x) \cdot I_{\mathrm{ZF}}(x) \exp^{-\frac{2\pi i}{N}\nu n}, \tag{2.16}$$

where N is the number of samples of the zero-filled interferogram following the implementation described in [144]. The term $W(x)$ represents a Blackman-Harris 4-term apodisation-function, which was incorporated in this discrete Fourier-transformation to suppress artificial ripples in the obtained spectrum[145]. We calculate the absolute value of the discrete complex spectrum to obtain the optical spectrum $S(\nu) \equiv |C_{\mathrm{d}}(\nu)|$ and finally convert the optical frequency ν to a wavelength λ. A set of observed spectra of ICL 3150/19-06 temperature-stabilized at $20\,^{\circ}\mathrm{C}$ is shown in Fig. 2.20a for various driver currents (top) as an example for all DFB-ICLs. The spectra show single mode operation beyond the threshold of $19.65\,\mathrm{mA}$. The ICLs wavelength shifts to higher values for increasing currents, which is typical for semiconductors with a DFB grating, because of the increased carrier density and temperature giving rise to a change of the refractive index. A selection of spectra is shown in Fig. 2.20a (bottom) verifying the single mode operation and indicating the aforementioned trend.

In order to empirically describe the influence of current on to the spectrum we apply a 2nd order polynom fit to the obtained spectra. We have chosen a 2nd order polynomial, because it empirically describes the tuning characteristics with appropriate agreement. An example using the spectra of ICL 3150/19-06 temperature-stabilized at $20\,^{\circ}\mathrm{C}$ is shown in Fig. 2.20b, where the measurement is shown in blue and the fit in orange. We calculate the mean tuning rate for ICL 3150/19-06 resulting in $71.8\,\mathrm{pm\,mA^{-1}}$, which we convert to an optical frequency tuning rate of $-1.8\,\mathrm{GHz\,mA^{-1}}$. The first number will be used for spectroscopy experiments in 4 and the latter will be used for frequency detuning determination in Chapters 3 and 5.

To observe injection locking, emission of two ICLs on a close-by wavelength is required. Injection locking occurs when the wavelength difference of both lasers is in the range of $0.5\,\mathrm{nm}$ or below, which can be converted to an OFD of $12\,\mathrm{GHz}$ or below depending on the type of laser [127]. The OFD-range, where locking occurs is referred to as locking bandwidth (LBW). To ensure that two ICL are able to operate on a close-by wavelength, we compare the spectra of two of them. This is exemplary visualized for ICL 3150/19-06 and ICL 3150/07-21 in Fig. 2.21, where we compare the emission wavelengths of ICL 3150/19-06 at $30\,^{\circ}\mathrm{C}$ for a selected range of currents with those of ICL 3150/07-21 for four selected temperatures for the same range of selected currents. We conclude that both lasers are able to operate on the same wavelength at each temperature, solely the driver current has to be adjusted to obtain the desired wavelength. The best case represents ICL 3150/07-21 at $32\,^{\circ}\mathrm{C}$, where wavelengths coincide with those of ICL 3150/19-06 at $30\,^{\circ}\mathrm{C}$ at a very similar current.

This verifies our assumption of the previous findings that batch 3150 ICLs are very good candidates for injection locking and mutual coupling. Since batch 3150 also covers relatively strong absorption lines of methane, the ICLs will be deployed for spectroscopy experiments in injection locking setups found in Chapter 4. Since the atmosphere also provides an open spectral window for batch 3150 ICLs they will be also used for the purpose of the novel approach of

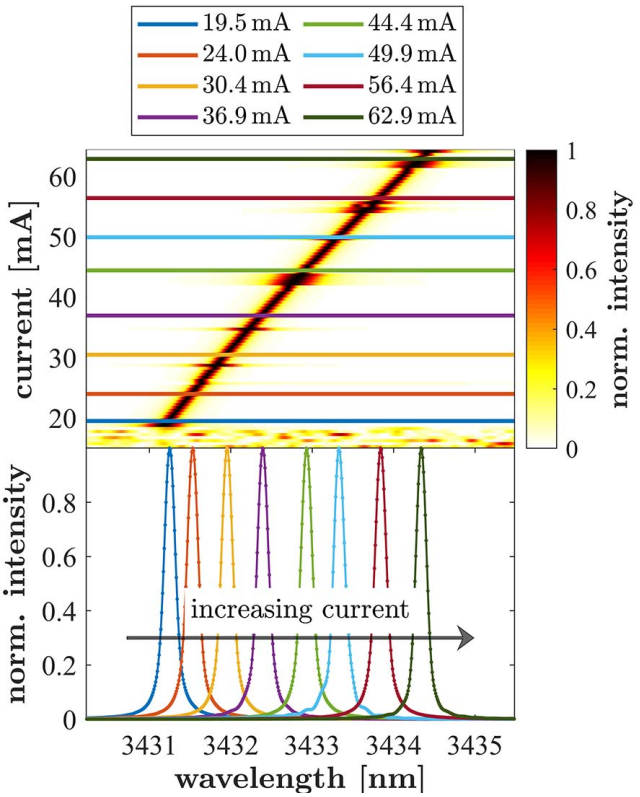

(a) Exemplary spectra of the at 20 °C temperature-stabilized ICL 3150/19-06 for a variety of currents normalized to its maximum (top). The colored cross-sections of the top graph are plotted in the lower graph.

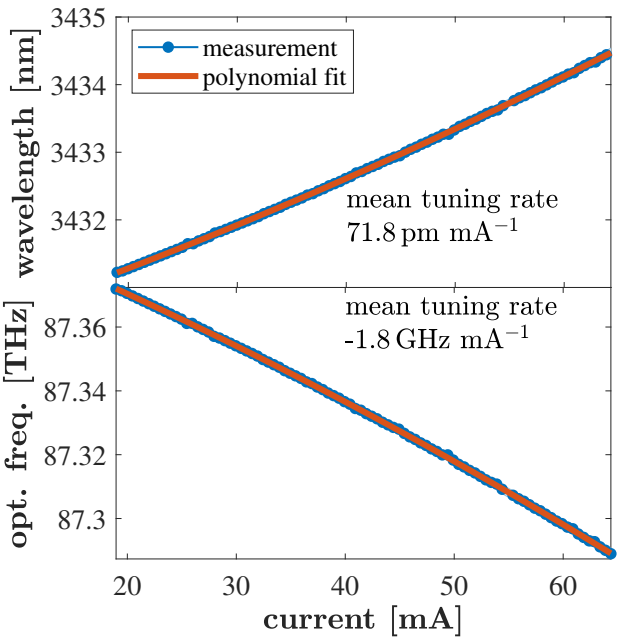

(b) Exemplary positions of the spectral maximum of the temperature-stabilized ICL 3150/19-06 at 20 °C as a function of driver current. The ordinate is displayed in the wavelength domain (top) and in the optical frequency domain (bottom).

Figure 2.20: Spectral analysis of ICL 3150/19-06 at 20 °C.

free-space optical communication with the laser-as-detector concept described in Chapter 5. Generally speaking, batch 3150 ICLs will be used to demonstrate applications. Nevertheless batch 2744 ICLs provide the ability to obtain matched wavelengths of both ICLs. We use 2744 ICLs for the high-frequency electrical characterization in injection locking and mutual coupling mode in Chapter 3 in order to provide a basis for the laser-as-detector approach. Finally, batch 2183 ICLs are also able to operate on matched wavelengths. They are used for basic characterization of the fundamental laser parameters and characterization of the injection locking and mutual-coupling phenomena in order to verify the assumptions of influence of injection strength and coupling phase suggested by the model.

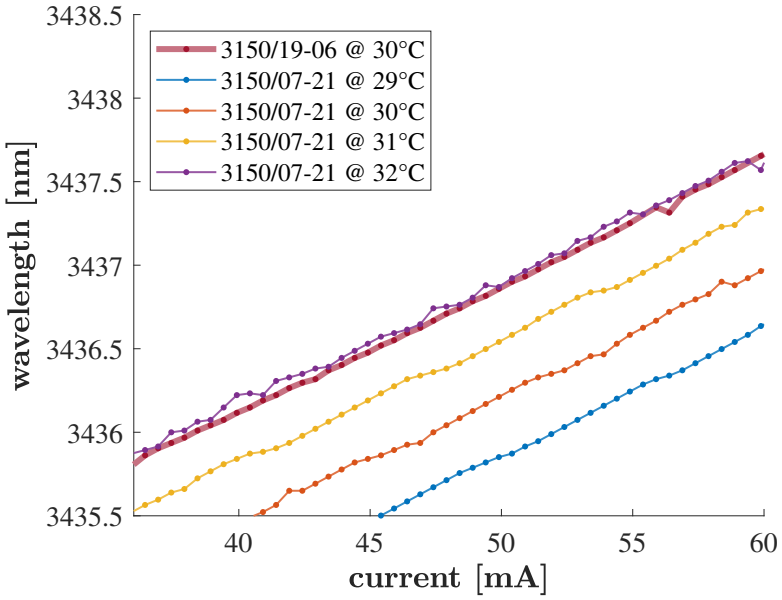

Figure 2.21: Comparison of spectra of ICL 3150/19-06 and 3150/07-21, where the emission wavelengths of ICL 3150/19-06 are plotted as a function of current at 30 °C is compared with the emission wavelengths for various currents of ICL 3150/07-21 for four selected temperatures.

Name	min. wavelength [nm]	max. wavelength [nm]	mode hops
2183/10-12	3212.6	3260.0	1
2183/22-25	3206.5	3245.6	1
2744/07-08	3342.6	3424.0	2
2744/13-25	3339.5	3422.6	1
3150/07-21	3391.5	3438.0	1
3150/13-06	3381.8	3438.2	1
3150/19-06	3381.7	3438.7	1

Table 2.3: Spectral characteristic of the ICL devices.

2.9.3 Optical linewidth

Single mode lasers with a high spectral purity find applications in coherent optical communications, atomic physics and frequency metrology. They also represent the core in the gravitational wave detectors LIGO and VIRGO[146], but high spectral purity lasers are especially needed for high-resolution spectroscopy. In particular, the signal of many spectroscopy techniques including TDLAS is a convolution of the absorption-lineshape and laser-lineshape, where the latter is mainly quantified by the optical linewidth. In that manner, we require the value of the ICLs optical linewidth for precise gas-concentration determinations allowing accurate comparison to spectra generated using the HITRAN database [129]. DFB gratings and distributed bragg reflectors (DBR) have already been implemented for a long time in order to create continuously tunable single-frequency ICLs, but still there are only few reports of the optical linewidth of ICLs[147, 148]. The most recent one [147] reports a narrow sub-MHz linewidth of not more than $372\,\mathrm{kHz}$ and a Schalow-Townes-limited linewidth of not more than $1.6\,\mathrm{kHz}$, which is surprisingly narrow compared to other types of semiconductor lasers[149, 150].

In order to resolve the linewidth of any laser the Fourier-transformation of the first-order auto-correlation-function $\Gamma(\tau)$ of the lasers electrical field $E(t)$ can be utilized using the Wiener-Khintchine-theorem[151]. Due to that fact, techniques to reveal the auto-correlation function are usually used for the linewidth determination including self-homodyne detection[152, 153] and self-mixing-interferometry [154]. Other techniques are the self-heterodyne detection [152, 153], the etalon-method [155–157] or the heterodyne-beating approach [158, 159]. Yet another way to obtain the optical linewidth has been especially established for the MIR wavelength domain[150], because previously described techniques require high precision optical alignment or provide not enough resolution. This technique utilizes the link between OFN and the auto-correlation $\Gamma(\tau)$ [160] and follows the calculation found in [130] for the evaluation of the optical linewidth.

The first order auto-correlation function $\Gamma(\tau)$ of the lasers electrical field $E(t)$ with

$$\tilde{E}(t) = \tilde{E}_0 \exp\left(i\left(2\pi\nu t + \phi(t)\right)\right) \tag{2.17}$$

is defined by

$$\Gamma(\tau) \equiv \left\langle \tilde{E}^*(t)\,\tilde{E}(t+\tau)\right\rangle = \tilde{E}_0^2 \left\langle \exp(i\phi)\right\rangle \cdot \exp\left(i \cdot 2\pi\nu\tau\right), \tag{2.18}$$

where we defined $\phi_\tau \equiv \phi(t+\tau) - \phi(\tau)$. It is the stochastic process of the spontaneous emission and thus the field-phase $\phi(t)$ and hence also ϕ_τ, that will later determine the finite optical linewidth. Since spontaneous emission events are stochastically independent, the probability density of ϕ_τ follows a Gaussian-distribution

$$p(\phi_\tau) = \sqrt{2\pi\left\langle\phi_\tau^2\right\rangle}\exp\left(-\frac{\left\langle\phi_\tau\right\rangle^2}{\left\langle\phi_\tau^2\right\rangle}\right). \tag{2.19}$$

It follows that $\Gamma(\tau)$ is dependent on the mean-quadratic noise $\langle\phi_\tau^2\rangle$ with

$$\Gamma(\tau) = \exp\left(-\frac{1}{2}\left\langle\phi_\tau^2\right\rangle\right) \cdot \exp(i \cdot 2\pi\nu\tau). \tag{2.20}$$

The mean-quadratic phase-noise is according to [160] related to the OFN power spectrum $S_{\text{OFN}}(\nu)$ via

$$\left\langle\phi_\tau^2\right\rangle = \tau^2 \int_{-\infty}^{\infty} \frac{\sin^2(\pi\nu\tau)}{(\pi\nu\tau)^2} S_{\text{OFN}}(\nu)\,\mathrm{d}\nu. \tag{2.21}$$

It can be concluded that $\Gamma(\tau)$ and thus the spectrum and the linewidth are a direct consequence of the OFN power spectrum $S_{\text{OFN}}(\nu)$. According to [130] the OFN can be divided into two regions, where the first part containing low frequencies contributes to the central part of the line shape and thus to the laser linewidth. The second part only affects the wings of the lineshape and thus does not contribute to the linewidth significantly. Both parts are separated by the so-called β-separation line, which is defined as

$$S_\beta(\nu) \equiv 8\frac{\ln(2)\,\nu}{\pi^2}. \tag{2.22}$$

It was shown by [130] that only OFN components with $S(\nu) > S_\beta(\nu)$, which is often referred to as the high modulation index area, contribute to the linewidth. The lineshape then is a Gaussian function whose variance is the sum of the contributions of all that components. Therefore the optical linewidth $\Delta\nu$ can be obtained via the expression

$$\Delta\nu = \sqrt{8 \cdot \ln(2)\, A} \qquad \text{with} \tag{2.23}$$

$$A \equiv \int_{\frac{1}{T}}^{\infty} \Theta\left(S(\nu) - S_\beta(\nu)\right) \cdot S_{\text{OFN}}(\nu)\,\mathrm{d}\nu \tag{2.24}$$

where Θ is the Heaviside-step-function [161] and T is the integration time.

In order reveal the OFN the challenge is converting the fluctuations in the optical frequency to an intensity noise, which then can be directly detected. Therefore, we utilize an absorption line as a discriminator.

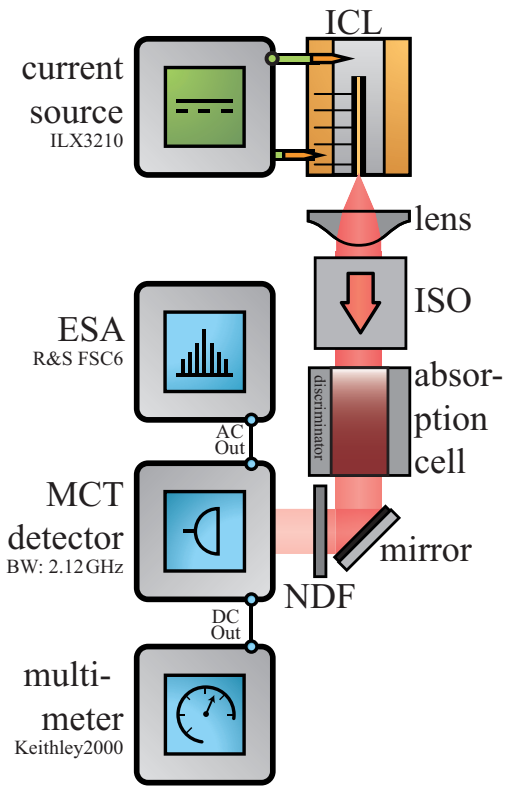

Figure 2.22: Setup for the investigation of the free-running laser linewidth. The optical isolator (ISO) prevents back reflections from all optical components to be fed back to the laser and is followed by an absorption cell filled with methane. An absorption line at $\lambda_{CH4} = 3216.16\,\mathrm{nm}$ acts as a discriminator. The beam illuminates a MCT detector after passing a variable neutral density filter (NDF), which attenuates the beam to avoid detector saturation. The DC-voltage is measured by a multimeter and the AC-part is spectrally resolved and finally recorded by an electrical spectrum analyzer (ESA).

The linear part of an edge of a methane absorption line at $\lambda_{CH4} = 3216.16\,\mathrm{nm}$ [4] is utilized as the discriminator in our setup, which is schematically depicted in Fig. 2.22. The transmission profile observed with the optical detector used for discrimination is therefore shown in Fig. 2.23 (top) with respect to the frequency detuning $\Delta\nu = |\nu_{CH4} - \nu_{ICL}|$, where ν_{ICL} is the optical frequency of the ICL and ν_{CH4} that of the methane absorption line. The abscissa (bottom) is obtained by the findings in Section 2.9.2. For the optimal discrimination the ICL is operated at $45\,\mathrm{mA}$. The applied current translates into an OFD of $0.6\,\mathrm{GHz}$ with respect to the optical frequency of the absorption line. At this point a frequency noise is linearly discriminated to an amplitude noise. The operation point is visualized with an orange circle in Fig. 2.23.

The experimental setup makes use of an electrical spectrum analyzer (ESA), which spectrally resolves the noise of the MCT-detectors electrical AC-signal. The measured electrical spectrum $R_{\mathrm{meas}}(\nu)$ is the sum of the laser intensity noise $R_{\mathrm{int}}(\nu)$, the detector dark noise $R_{\mathrm{det.}}(\nu)$ and the intensity noise induced by the discrimination of the OFN $R_{\mathrm{OFN}}(\nu)$. To get rid of laser intensity noise and detector dark noise from $R_{\mathrm{meas}}(\nu)$, we take a 256 times averaged measurement of the electrical spectrum using the same temperature and current, without discrimination, hence without the gas cell inside the beam. The obtained signal then is $S_{\mathrm{int}}(\nu) + S_{\mathrm{det.}}(\nu)$. With an optical attenuator placed between laser and detector we take care, that the optical power at the detector is the same as in the case, where we have placed the gas cell within the beam.

We subtract the recorded signal to resolve the intensity noise part induced by the discriminated OFN using

[4] The wavelength $3216.16\,\mathrm{nm}$ converts to a optical frequency of $93.2789\,\mathrm{THz}$

$$R_{\text{OFN}}(\nu) = R_{\text{meas}}(\nu) - (R_{\text{int}}(\nu) + R_{\text{det.}}(\nu)). \tag{2.25}$$

To access the spectral density of the OFN $S_{\text{OFN}}(\nu)$ the intensity noise $R_{\text{OFN}}(\nu)$ has to be converted using

$$S_{\text{OFN}}(\nu) = \left(\frac{R_{\text{OFN}}(\nu)}{B_{\text{RBW}} \cdot C}\right)^2, \qquad \text{with} \qquad C \equiv C_{\text{slope}} \cdot \frac{A_{\text{AC}}}{A_{\text{DC}}} \tag{2.26}$$

where we utilized the conversion-coefficient C linking the voltage to a frequency and the resolution bandwidth B_{RBW} of the ESA. The conversion-coefficient C is calculated from the slope C_{slope} of the detector voltage with respect to the $\Delta\nu$ at the yielding $C_{\text{slope}} = 47.4\,\text{mV}\,\text{GHz}^{-1}$. Since the VIGO-AIP detection unit has two outputs, i.e. DC and AC, with different amplification factors A_{DC} and A_{AC}, respectively, the value C_{slope} needs to be corrected by $\frac{A_{\text{AC}}}{A_{\text{DC}}}$.

We finally obtain $S_{\text{OFN}}(\nu)$ and present it in Fig. 2.24 together with the β-separation line. The optical linewidth is then calculated using Eq. (2.24). The integration time T amounts to $1\,\text{ms}$ and is set by the lowest electrical frequency of investigation amounting in our case to $1\,\text{kHz}$.

It is found that the measured linewidth of $\Delta\nu = 582\,\text{kHz}$ of ICL 2183/10-12 is comparable to already known ICL linewidths [147]. In fact the device examined in [147] is also a device from nanoplus. Here, our measurement has been performed chronologically before that publication. The result is still surprisingly narrow, even if it compares to that of the narrow-linewidth QCLs[162]. An explanation could be the quite low flicker noise in our ICLs, thanks to the self-designed ultra-low-noise battery-source in addition to the generally low driver current. The relatively low number of semiconductor layers compared to QCLs, can also lead to more homogeneous carrier-lifetimes through all active regions, resulting in a small linewidth broadening.

The narrow-linewidth finding of our ICL is of utmost importance for high-resolution gas spectroscopy applications utilizing the MIR wavelength domain. It shows that ICLs are at least equal or even better in their spectral operation domain with respect to their competitor, the QCL. The determined optical linewidth will be used in Chapter 4 to precisely evaluate the gas concentration using a fit to a spectrum generated with data from the HITRAN-database.

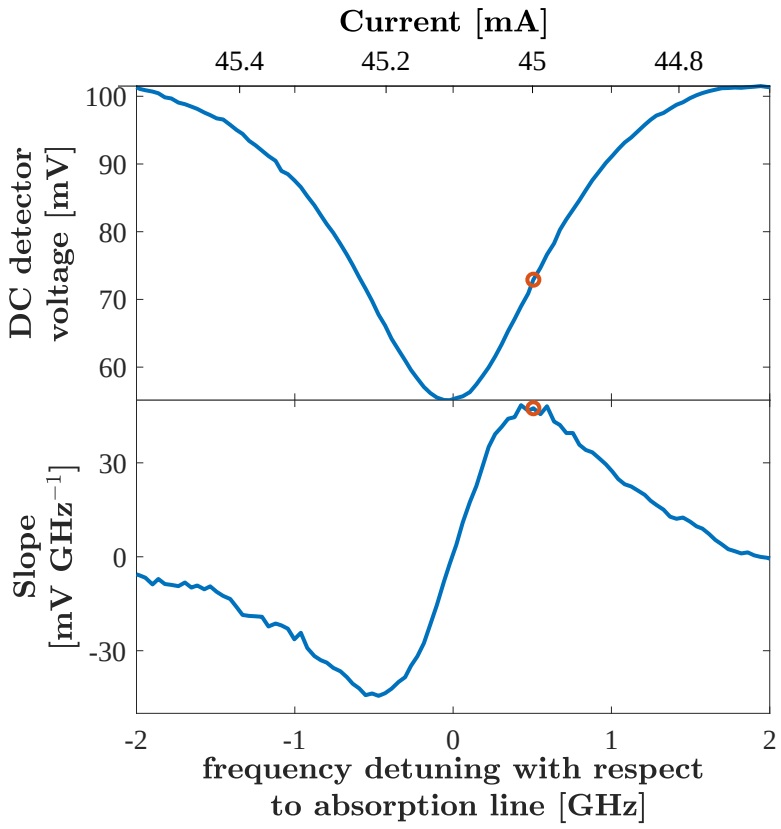

Figure 2.23: Detector signal as a function of the detuning with respect to the absorption lines frequency (top), while the temperature stabilized ICL 2183/10-12 at $20\,^{\circ}\mathrm{C}$ scans across the absorption line, which is used as the discriminator for the OFN and allows finally the linewidth determination. Its slope (bottom) is necessary for the intensity noise to OFN conversion. The orange circle indicates the operation point, i.e. $45\,\mathrm{mA}$, where the lasers wavelength hits the point of the absorption line linear edge, which is optimal for the determination of the OFN.

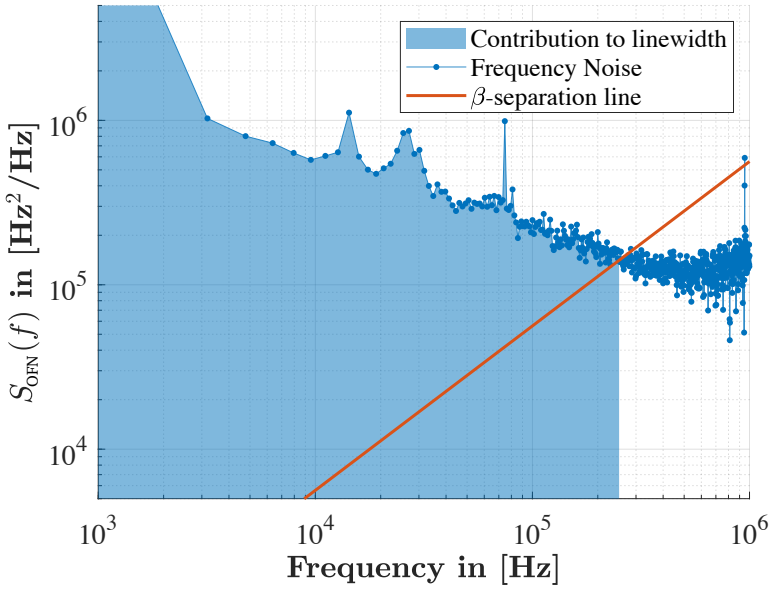

Figure 2.24: OFN spectral density (blue) with beta-separation line (orange) from which a linewidth of $582\,\mathrm{kHz}$ has been calculated according to Eq. (2.23). The transparent blue area shows, which electrical frequencies contribute to the optical linewidth.

2.9.4 Linewidth enhancement factor

The linewidth enhancement factor (LEF) dictates various phenomena such as broadening of the intrinsic optical linewidth or enrichment of the laser dynamics, when the laser is subjected to external light (re-)injection. The reason for that is that the LEF quantifies the coupling between the phase and amplitude of the electrical field, or similarly speaking, the coupling between the gain and the refractive index of a semiconductor laser. This essential parameter of every laser has been introduced in 1967 by Lax [163] and Haug and Haken[164], but initially it was assumed that $\alpha = 0$ for all lasers, because of their symmetric gain profiles. Since its introduction it has been therefore neglected until Henry reintroduced it in 1982, when measurements resulted in LEFs between 2 to 5 for semiconductor laser [140].

The LEF is defined as

$$\alpha \equiv \frac{\partial \chi_R / \partial N}{\partial \chi_I / \partial N} \tag{2.27}$$

with the complex susceptibility $\chi \equiv \chi_R + i\chi_I$ [165]. In semiconductors the susceptibility is described by

$$\chi = -\frac{i}{\hbar\omega\epsilon V}\sum_k |\mu_k|^2 \left(F_{\mathrm{e}k}\left(T\right) + F_{\mathrm{h}k}\left(T\right) - 1\right)\mathcal{L}\left(\omega_k - \nu\right)\left(1 - i\frac{\omega_k - \nu}{\gamma}\right), \tag{2.28}$$

where μ_k is the chemical potential[165]. The Fermi-Dirac distributions of the electrons are denoted by $F_{\mathrm{e}k}\left(T\right)$ and that of holes by $F_{\mathrm{h}k}\left(T\right)$ and are given by

$$F_{ek,hk}\left(T\right) = \left(\exp\left(\frac{\hbar\omega_{ek,hk} - \mu_{ek,hk}}{k_{\mathrm{B}}T}\right) + 1\right)^{-1}, \tag{2.29}$$

where k_{B} is the Boltzmann constant [123]. The term ϵ in Eqn. 2.28 denotes the electric permittivity below threshold, V is volume, where the dipole interaction takes place, γ is the decay rate of the dipole and $\mathcal{L}\left(\omega_k - \nu\right)$ is a function the describing the lineshape, for example a lorentzian or a hyberbolic secant (sech).

The carrier density N depends on the temperature T and is given by the summation over the Fermi-Dirac distribution

$$N = \frac{1}{V}\sum_k F_{\mathrm{e}k}\left(T\right) = \frac{1}{V}\sum_k F_{\mathrm{h}k}\left(T\right) \tag{2.30}$$

The local gain g is connected to the imaginary part of the susceptibility χ_I via

$$g = -\frac{\nu n}{2c}\chi_i \tag{2.31}$$

The refractive index n is connected to the real part of the susceptibility χ_R via

$$\frac{\eta}{n} = \frac{\chi_R}{2}, \tag{2.32}$$

where η is the carrier induced part of the refractive index. This results in

$$\alpha \equiv \frac{\partial\chi_R/\partial N}{\partial\chi_I/\partial N} = -\frac{\nu n}{2c}\frac{\partial\eta/\partial N}{\partial g/\partial N}. \tag{2.33}$$

In other words, the LEF can also be understood as the ratio between derivative of the refractive index η and the derivative of the gain g, both with respect to the carrier density N. This characteristic expression shows that the LEF is not really a fixed constant, but can be more

seen as a multidimensional figure. This has already lead to controversy among researchers manifesting itself in countless reviews and summaries of LEFs determined with several techniques [166–168]. For example quantum dot lasers give results to LEFs differing substantially, when different measurement methods are used [169].

In conclusion, we emphasize that it is only reasonable to specify a value of the LEF by indicating the measurement technique and all external conditions.

Measurement methods to determine the LEF

There are various methods to determine the LEF. The *Hakki-Paoli method* exploits the measurement of gain and refractive index changes (Eqn. 2.33) with respect to the pumping parameter and can only be used for sub-threshold determination of the LEF [170]. Other techniques are the *FM/AM method* as described in [171], or the *Fiber Transfer Function method* [172]. Since the LEF enhances the optical linewidth by a factor $\sqrt{1+\alpha^2}$ compared to the Schawlow-Townes limit [140] the determination of the linewidth, often referred to as the *linewidth method* or the *modified linewidth method* can also be used to obtain the LEF.

A quite different approach to determine the LEF exploits its influence on feedback and injection locking, because the LEF describes the amplitude-phase coupling of the electric field. This influence is manifested in the rate equations of the laser, which have been introduced in Eqs. (2.12) to (2.14) and will be extended and discussed in detail in Section 3.3. In the *optical injection method*, light from a master laser is injected into the slave laser under test. This causes locking of the slave optical frequency to that of the master. This locking is strongly influenced by the LEF showing an asymmetry in the locking region in the case of a non–zero LEF [173].

To obtain the LEF of ICLs via the linewidth method or modified linewidth method, very high effort would be needed. Gratings meeting the resolution requirement are not available for the determination in the mid-infrared. A FTIR could meet that requirement, but a very long travel of the scanning mirror would be needed, which is not applicable. The Hakki-Paoli method is also not suitable, because we want to investigate the LEF above threshold in order to determine the influence of the operation parameters on the LEF. The FM/AM method requires modulation well above the relaxation frequency together with high-bandwidth detection and is not applicable in the MIR wavelength domain, because the lack of fast-diodes. The fiber-transfer function method would require a well characterized fiber, which is also not available in the MIR.

The *self-mixing-method* is based on the self–mixing interferometry according to the Lang-Kobayashi theory [54, 126]. This technique is advantageous, because no optical high-resolution or high-bandwidth measuring instruments are required. At the same time, it is possible to exploit terminal voltage of the laser, so optical detection becomes completely unnecessary [174]. Therefore, this technique is often used for lasers operating in the mid- or far-infrared wavelength domain, where detectors show poor performance or require extraordinary cooling technology [137, 175, 176]. Another great advantage of self–mixing interferometry method is the ability to measure the LEF at operating conditions, i.e. above the threshold, which is not possible with the often applied Hakki-Paoli method. This enables investigation of the

influence of operating parameters on the LEF, which is particularly of great value, because of the LEFs previously mentioned multi-dimensionality. The additional benefit we gain using this method, is its applicability for many different types of semiconductor lasers. Therefore, the method provides a superior possibility for comparison.

The self-mixing method relies on the determination of the so-called interferometric function $F(\phi_{\text{FB}})$. This function describes the impact of the feedback phase ϕ_{FB} on the optical output power P. Referring to [177] the following relations can be applied when the feedback parameter κ is in the weak or moderate feedback regime, i.e. $\kappa < 4.6$:

$$P(\phi_{\text{FB}}) = P_0 (1 + m \cdot F(\phi_{\text{FB}})) \tag{2.34}$$

with

$$F(\phi_{\text{FB}}) \equiv \cos\left(\nu_{\text{FB}}(\phi_{\text{FB}}) \cdot \frac{4\pi L}{c}\right) \tag{2.35}$$

and

$$\phi_{\text{FB}} \equiv \frac{4\pi\nu}{c} \cdot L \tag{2.36}$$

The variable L represents the physical distance between the laser source and a mirror and ν_{FB} results from the transcendental optical phase equation [160, 178]

$$\nu_{\text{FB}}(\phi_{\text{FB}}) = \nu_0 - \frac{\kappa}{\tau_{\text{round}}}\sqrt{1+\alpha^2} \cdot \sin\left(2\pi\nu_{\text{FB}}(\phi_{\text{FB}}) \cdot \frac{2L}{c} + \arctan(\alpha)\right), \tag{2.37}$$

where τ_{round} is the internal round trip time in the laser cavity and α finally describes the value of the LEF. Von Staden showed that in the case of QCLs the LEF is preferably determined in the weak feedback regime ($\kappa < 1$) [174]. No hysteresis jumps of $F(\phi_{\text{FB}})$ occur in this range, which is schematically visualized for $\kappa < 1$ in Fig. 2.25.

In that case the result of the α and κ can be extracted using the analytic solutions of the interferometric function via

$$\alpha = \frac{\Phi_M - \pi}{\Phi_Z - \pi} \tag{2.38}$$

and

$$\kappa = \frac{1}{2}(\Phi_Z - \pi) \cdot \sqrt{1+\alpha^2}, . \tag{2.39}$$

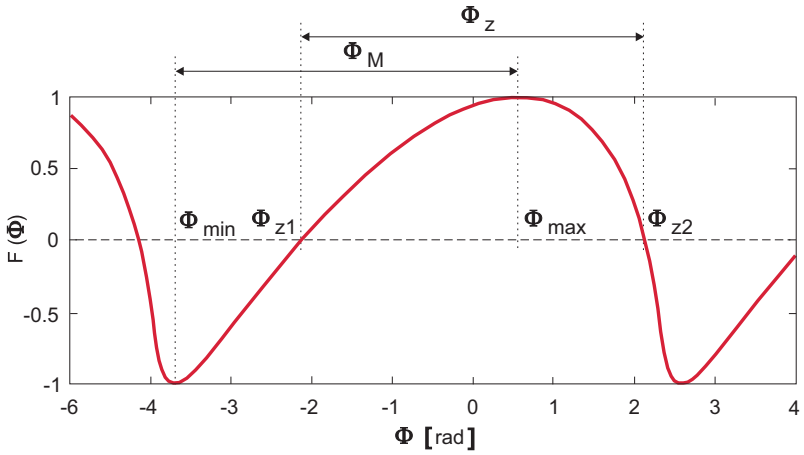

Figure 2.25: Ideal interferometric function $F(\phi_{\mathrm{FB}})$ with an assumed $\alpha = 1.5$ in the weak feedback regime. The marked intervals Φ_{Z} and Φ_{M} are required for the calculation of the LEF.

where Φ_Z is the phase distance between two consecutive zero-crossings of the interferometric function and Φ_M a phase between maximum and minimum.

Experiment

We investigate the influence of current and temperature on the LEF, because in semiconductor lasers both external parameters predominantly affect both gain and refractive index. The laser under test is ICL 2183/10-12. The used setup is schematically shown in Fig. 2.26. The ICL beam is splitted due to a non-polarizing-beam-splitter (NPBS) into one part illuminating the MCT-detector, while the other part of the beam passes two polarizes forming an attenuator. This beam is then being back reflected by the feedback mirror and is finally fed back into the ICL again via the NPBS. The mirror is mounted on a piezo translation stage allowing to control the feedback phase ϕ_{FB} by displacing the mirror. We modulate the stage with a sinusoidal signal at $50\,\mathrm{Hz}$ and use its linear edge for the evaluation of the LEF.

An exemplary normalized terminal-voltage time-trace with marked T_i values is shown in Fig. 2.27, which according to Eq. (2.38) results in $\alpha = 0.384 \pm 0.054$ for this particular measurement. We repeat this measurement for several temperatures and driver currents. The result of this evaluation is depicted in Fig. 2.28 together with feedback coefficient κ as a function of the driver current. We note that κ is well below 1, which is a aforementioned requirement for the evaluation of the LEF. We attribute the variations of the feedback parameter to the wavelength dependent transmission function of the beamsplitter. Figure 2.28 shows that a very low LEF of $0.1 \leq \alpha \leq 0.4$ is found. Still, the visualization confirms that the LEF of ICL 2183/10-12 deviates from the special value zero when biasing the laser above its threshold. Nevertheless, the value can fit into a series of already existing measurements for ICLs biased below threshold, which used the Hakki-Paoli method [179, 180]. There is only a discrepancy

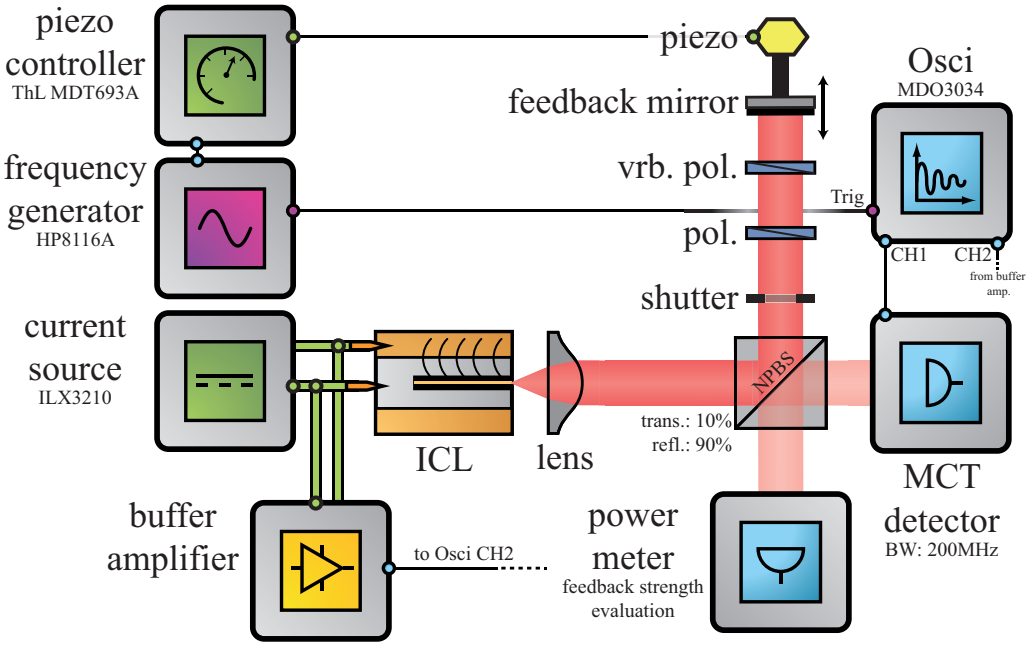

Figure 2.26: Setup for the determination of the LEF with the self-mixing method. The feedback mirror is driven by a piezo-controller, which controls the sinusoidal back-and-forward movement. The combination of rotatable variable polarizer (vrb. pol) and fixed polarizer (pol.) ensures that the feedback parameter κ stays below 1. We can evaluate the amount of feedback using a pyroelectrical detector connected to a calibrated powermeter. We record the time-trace of the optical signal using the MCT-detector just as a reference and save it to the oscilloscopes channel 1 (CH1). For the determination of the LEF we utilize the amplified terminal-voltage time-trace recorded with the oscilloscope at Channel 2 (CH2). The LEF of this particular measurement amounts to 0.384 ± 0.054.

with one experiment that uses the self-mixing method also reported in [179]. In this case, however, the laser differs in its spectral emission curve and shows multimode emission for higher currents, whereas our DFB-ICL predominantly shows single mode emission. A complete classification of our results can be found in Table 2.4, where we also show our result in relation to MQW lasers [181] and QCLs [137, 174, 182].

The determined LEF value is well below those of MQW lasers, but covers a part of the LEFs range of QCLs. It is likely that the active regions properties, namely refractive index and gain of MIR materials cause this low value together with the strong carrier-confinement due to the complex band-structure. The strong influence on the current can be explained by a possible non-linearty of the gain and the refractive index on the carrier density. Indeed many of physical processes such as spectral hole burning [174], carrier heating [183], and gain compression [184] are known as possible candidates for being responsible for these kind of non-linearities. Another issue is that our ICL under test shows two mode emission within a small domain of the investigated currents (gap inbetween shown LEFs). This significantly influence the gain in the current domain, where two mode operation occurs. In Fig. 2.28 we only show LEFs where we

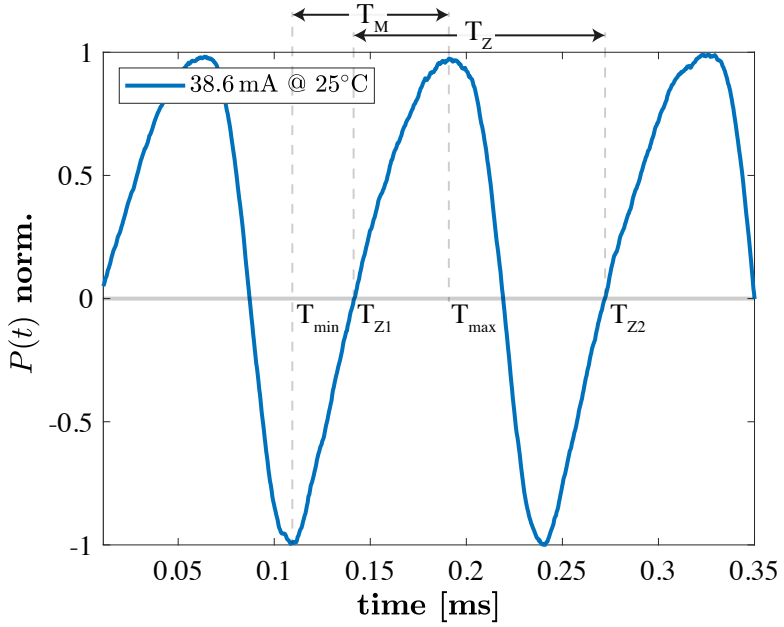

Figure 2.27: Example of normalized and low-pass-filtered terminal-voltage of the self-mixing signal of ICL2183/10-12, which has been temperature-stabilized at $25\,^{\circ}\mathrm{C}$ with an injection current of $38.6\,\mathrm{mA}$. The timetrace is used for the LEF determination using Eqn. 2.38. The corresponding zero-crossings and times of maxima and minima are marked with T_i. These values convert easily to Φ via $\Phi_i = T_i \cdot 2\pi f$, where f is the modulation frequency of the mirror amounting to $50\,\mathrm{Hz}$. The low-pass-filter stopband-frequency amounts to $5\,\mathrm{kHz}$.

type	**LEF**	**method**	**reported in**
GaAs/AlGaAs MQW	$1.5 \leq \alpha \leq 1.7$	Hakki-Paoli	[166, 181]
QCL	$-0.44 \leq \alpha \leq 2.29$	self-mixing	[174]
QCL	$0.8 \leq \alpha \leq 3$	self-mixing	[137]
QCL	$0 \leq \alpha \leq 7.7$	self-mixing	[182]
ICL	0.71	Hakki-Paoli	[180]
ICL	$1.1 \leq \alpha \leq 1.4$	Hakki-Paoli	[179]
ICL	$1.7 \leq \alpha \leq 2.7$	self-mixing	[179]
ICL	$0.1 \leq \alpha \leq 0.4$	self-mixing	**this work**

Table 2.4: Comparison of LEFs of different laser types obtained by different methods.

have verified that the ICL under test emits on only one mode.

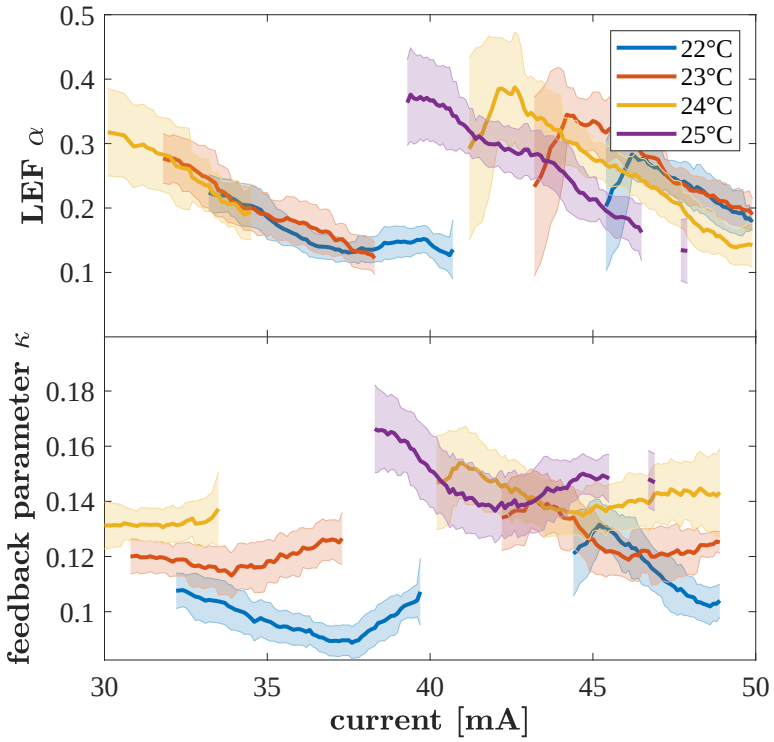

Figure 2.28: LEFs of ICL 2183/10-12 for four different temperatures. We only show LEFs values in current domains where we have verified that the ICL under test emits on only one mode. With that we avoid two-mode self-mixing signals, which can not be utilized for LEF determination with the self-mixing-technique.

Reviewing the collected literature and our experiments, we conclude that ICLs seem to have rather low LEFs. Therefore, it is expected that ICLs are not expected to have rich and complex dynamics, but still show non-linearities when exposed to an external optical perturbation. This could be an advantage for spectroscopic applications and communication methods where non-deterministic dynamic, such as chaos, is a disadvantage. Indeed we exploit the weak non-linearity for spectroscopic measurements in Chapter 4. We also make use of the low LEF in Chapter 5 and define four indistinguishable so-called compound-laser-states that are used in a FSO communication scheme.

We already described in Eq. (2.33) that the LEF is a measure representing the fraction of derivative of the refractive index η with respect carrier density N and the derivative of the

gain g with respect to the carrier density. The next paragraph deals with the determination of the carrier density N with help of measuring the carrier-lifetime τ_e. The latter is also a major parameter of the already described rate equations in Section 2.7 and will be implemented for simulations of the ICL subjected to an optical perturbation.

2.9.5 Carrier lifetime and carrier density

The rate of the spontaneous emission is determined by the carrier-lifetime in the upper laser state[123]. Hence, it represents one of the most important parameters for every semiconductor laser. For stimulated emission a relatively long carrier-lifetime compared to the pumping rate ensures the carrier-density necessary for population inversion. The carrier density N can directly be found by integrating the measured carrier-lifetime τ_e over the current I via

$$N(I) = \frac{1}{e \cdot A \cdot d} \int_0^I \tau_e(I') \, \mathrm{d}I', \tag{2.40}$$

where d is the active layer thickness and A its area, while e represents the elementary charge.

The carrier-lifetime τ_e also mainly determines the lasers dynamic behavior not only in solitary operation, but also in configurations, when the laser is exposed to an external optical perturbation[127]. Its importance is manifested in the rate equations described in Eqs. (2.12) to (2.14). The carrier-lifetime also determines the so-called relaxation oscillation frequency. The relaxation oscillation frequency ν_{RO} is a fundamental frequency found in every laser, whose upper-state lifetime is much longer than the cavity damping time, which is the case for interband transition based lasers like ICLs. When a laser is disturbed during operation its output power does not immediately return to its steady state but executes to oscillations with the frequency ν_{RO}. This frequency limits the applicability of many semiconductor lasers, especially when it comes to fast-modulation or gain-switching [185, 186]. It is given by

$$\nu_{RO} \equiv \frac{1}{2\pi} \sqrt{\frac{\Gamma P_{int}}{\tau_{round} E_{sat.}} - \frac{1}{4} \left(\tau_e^{-1} + \frac{P_{int}}{E_{sat.}} \right)^2}, \tag{2.41}$$

where $E_{sat.}$ is the saturation energy and P_{int} the intracavity power.

Time resolved photoluminescence (TRPL) has conventionally been used to reveal the carrier lifetime τ_e by tracking the decay in photoluminescence intensity as a function of time for different optical pumping densities [187]. The carrier lifetime is then extracted by fitting the data to a exponential decay model. Since carrier lifetimes are usually in the range of nanoseconds for interband transition based lasers [188] or even picoseconds for QCLs [189], optical detectors with a very high-bandwidth are required. Fast photodetection in the MIR

domain is, according to the current state of the art, only applicable with Quantum Well Infrared Photodetector (QWIP) [50]. Unfortunately QWIPs are usually very selective regarding the accepted spectrum and are additionally quite expensive. Therefore, TRPL or the impedance independent technique [190] are not applied in this thesis. Another promising technique, the Hakki-Paoli method [191] does not require a fast detector or relies on an experimentally complex electrical implementation. However this method involves the determination of the gain below the laser threshold and is therefore in our opinion not useful.

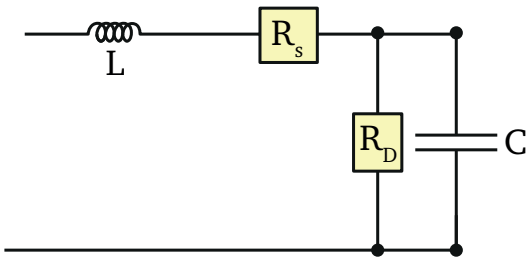

Figure 2.29: Equivalent circuit diagram for a single ICL.

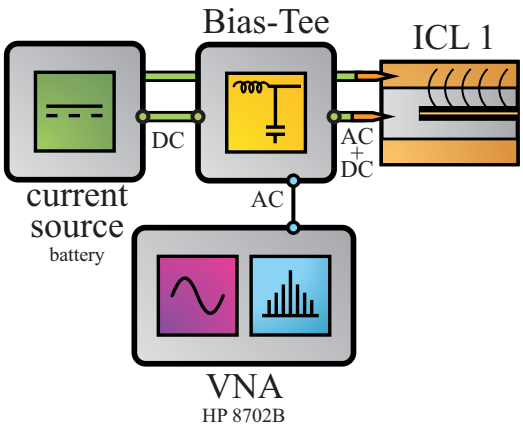

Figure 2.30: Setup for investigation of free-running carrier lifetime of ICL.

We overcome all of these limitations by accessing the carrier-lifetime parameter using a technique relying solely on electrical properties of the device [136]. A combination of this methods with TRPL would additionally increase the quality of the determination [136], but is not possible due to the previously described restrictions. Another advantage of the deployed technique is the relatively high SNR even for low driver currents thus low output powers, where the detectivity of the optical sensor would not be sufficient [192]. Only the measurement of the carrier-lifetime for low driver currents finally enables a true determination of the carrier density using Eq. (2.40).

The basis of this technique is that every weakly-modulated active region of a semiconductor laser can be electrically modeled by an electric RC-circuit, which is schematically depicted in Fig. 2.29. The impedance is a characteristic property for every electric circuit extending the concept of resistance to alternating current (AC) circuits. This complex valued impedance describes the relationship between the amplitudes of the voltage and applied current as well as their phase difference and is typically a function of the AC frequency f. The impedance of a solitary resistance is for example given by $Z_{\mathrm{R}} = R$, an individual inductance is represented $Z_{\mathrm{L}} = i \cdot 2\pi f \cdot L$ and a capacitance by $Z_{\mathrm{C}} = (i \cdot 2\pi f \cdot C)^{-1}$. Here R denotes the ohmic resistance, L the inductivity and C the capacitance. The complex-valued impedance of the RC-circuit of the equivalent circuit diagram depicted in Fig. 2.29 is given by

$$Z(f) = i2\pi f L + R_{\mathrm{s}} + \frac{R_{\mathrm{d}}}{1 + i \cdot 2\pi f \cdot \tau_{\mathrm{e}}} \tag{2.42}$$

The characteristic time τ_e of a RC-circuit, which is in our case given by the carrier-lifetime τ_e, is proportional to the resistance R and the capacitance C. With this knowledge it is possible to extract the lifetime from the device's frequency dependent impedance.

To obtain the impedance we utilize the setup shown in Fig. 2.30. A properly calibrated vector network analyzer (VNA) *HP 8702B* directly measures the impedance using the two-network scattering parameters S_{ij}. However it is not possible to determine the scattering parameters related to transmission, because of the lack of high-frequency optical detectors. Therefore, the device only utilize S_{11} for impedance calculation, where S_{11} is determined from the ratio of reflected to sent in electric signal.

An exemplary result of the real value of impedance $\Re(Z)$ is shown in Fig. 2.31 together with a fit to Eq. (2.42). Here we obtain a value of $5.11\,\mathrm{ns}$ for τ_e.

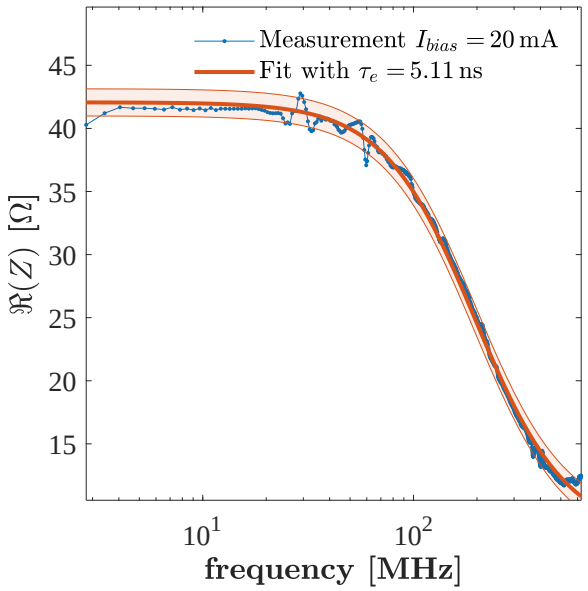

Figure 2.31: Real part of impedance Z of ICL 2183/10-12 driven by a current of $20\,\mathrm{mA}$ at $20\,^\circ\mathrm{C}$ (blue) together with fit to Eq. (2.42) (orange). This particular fit resulted in a carrier-lifetime of $\tau_e = 5.11\,\mathrm{ns}$.

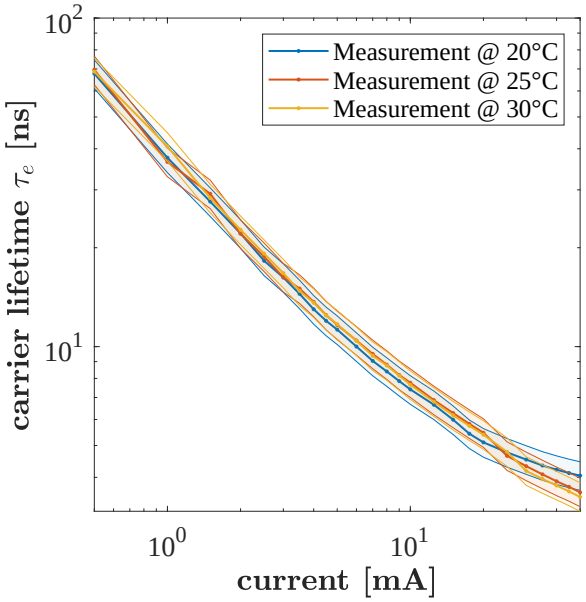

Figure 2.32: Impedance of ICL 2183/10-12 as a function of the current for three selected temperatures.

The measured value is in the order of the magnitude of those for semiconductor lasers that rely on interband transitions to generate light [193, 194] and that of other ICLs [195]. This is no surprise, since architectures of type-II ICL bandstructures do not differ substantially.

In Fig. 2.32 it is not visible that the carrier-lifetime is affected by the temperature. Actually, a reduction is expected with increasing temperatures[136], but our measurements could not

detect any trend. This a result of the small range of the examined temperatures, such that a more extensive measurement series is requested to confirm the predicted trend. On the other hand an inverse relationship between carrier-lifetime and current can be observed. With that it becomes possible to caluclate the carrier density using Eq. (2.40). Assuming a $8\,\mu\mathrm{m}$ wide ridge and taking the length from Table 2.1, the carrier density at threshold ($I_{\mathrm{th}} = 22.82\,\mathrm{mA}$) is found to be $165.7 \times 10^{11}\,/\mathrm{cm}^2$, which is in the expected range [32]. This carrier-density is here related only to the area of the active region A, which is defined by length and width of the ridge and not the volume.

2.10 Conclusion of the chapter

In this chapter, the band structure was used to compare the different concepts for the generation of coherent light in IDLs, QCLs and ICLs. The ICLs under investigation were listed in 2.1 together with their most important electrical, optical and mechanical properties. A rate equation model has been introduced to describe the emission of solitary operating ICLs. A modified version of this will now allow to describe the operation of these lasers when exposed to an optical perturbation. The ICL were characterized in order to determine the most important parameters for the rate equation model, which are summarized in Table 2.5. Our characterization represents one of the most detailed one for ICLs so far. The findings will be used to compare experimental findings of ICLs subjected to an optical perturbation with the later described theoretical model. Since we suggest an application based on a mutually coupled configuration in Chapter 5 and a unidirectional coupled configuration in Chapter 4 two ICLs were investigated with respect to their ability to emit at a similar wavelength, which is a prerequisite for mutual coupling. The characterization thus lays the foundation for qualitatively and quantitatively classification of the phenomena occurring in these two applications.

parameter	value or value range
temperature	0 to $40\,^{\circ}\mathrm{C}$
output power @ $20\,^{\circ}\mathrm{C}$	up to $12.1\,\mathrm{mW}$
operation voltage	up to $3.6\,\mathrm{V}$
driver current	up to $90\,\mathrm{mA}$
wavelength	3206.5 to $3260.0\,\mathrm{nm}$ 3339.5 to $3438.7\,\mathrm{nm}$
optical linewidth	$\approx 582\,\mathrm{kHz}$
LEF	0.1 to 0.4
carrier lifetime above threshold	3.1 to $5.4\,\mathrm{ns}$

Table 2.5: Summary of observed ICL parameters based on all measurement results in this chapter.

"It is the greatest shot of adrenaline to be doing what you have wanted to do so badly. You almost feel like you could fly without the plane."

Charles Lindbergh

3 The laser-as-detector approach in feedback, unidirectional injection and mutual coupling configurations of interband cascade lasers - theory and experiment

In February 1665 Christian Huygens, who was suffering from a mild illness, had to remain in his bed. He watched two pendulum clocks, which he had mounted close to each other on a thin wooden partition in front of his bed like it is sketched in Fig. 3.1. He surprisingly realized that the pendulums synchronized within half an hour [196]. Even when he disturbed the synchronization, the pendulums regained synchronicity after a while [197]. This observation was the first known report of two coupled oscillators.

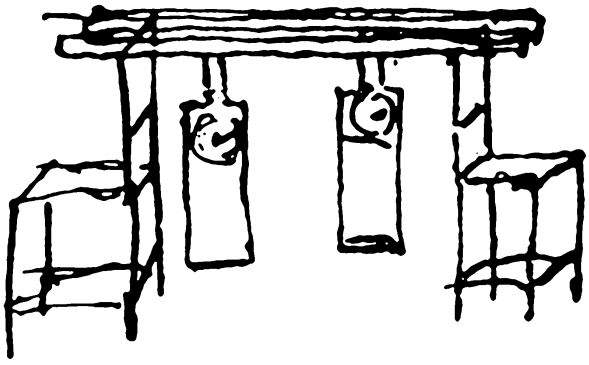

Figure 3.1: Adaption of a sketch, which has been drawn by Christiaan Huygens of an experiment with two coupled clocks. He had mounted them close to each other on a thin wooden partition in front of his bed.

Semiconductor lasers are well-known driven oscillators like the clocks and widely used in telecommunications, spectroscopy and countless more applications. Lasers in general are appealing dynamic systems and like the clocks they become even more interesting when they are subjected to an external optical perturbation. We refer to optical perturbation, when talking about injection of an optical radiation of any origin.

The goal of this chapter is to describe how this optical perturbation can be detected, i.e. how to use the laser as a detector. For this purpose we have to explain which quantities change when an external optical perturbation is applied to the ICL and how they can be extracted.

To characterize an ICL in any configuration, its two physical quantities are used: First, its oscillating optical field and second, its charge carrier inversion. Both change when time progresses. The physical quantities are time-dependent and must be distinguished from constants or time-independent values, which are commonly known as parameters. The mathematical formulation to describe the time dependence of the light-matter interaction in lasers was initially carried out by Haken [198] and is deployed by a set of non-linear rate equations including the parameters as time-independent constants [127]. These rate equation models have been developed for many different types of lasers and especially for a variety of semiconductor lasers. In fact, we have already introduced a model in Section 2.7 for our laser of choice - the Interband Cascade Laser. Not only have we introduced the model, we also experimentally fixed some of its parameters, which we summarized in Section 2.10. While the model provides a very accurate description of the ICLs when operated solitary, it can not describe phenomena that happen when the ICL is subjected to an external optical perturbation. In fact, the sensitivity of SCLs to external optical perturbations is exceptionally delicate. Even a small optical injection into the laser cavity is rapidly amplified and disturbs the balance between optical field and population inversion massively. Sometimes even non-deterministic dynamics can be observed. Dynamic systems of that kind are referred to as nonlinear dynamic systems (NLDS). Indeed, NLDS can not only be found in lasers subjected to external optical perturbation, but occur in numerous other systems e.g. fuild flows [199], coupled clocks and other mechanical pendula [200, 201] and even in the trajectory of Pluto [202]. Biological systems, such as the population of predators and prey [203] but also neurons [204] represent also very interesting NLDS. Even dynamics not related to physics such as economic developments can show a rich nonlinear dynamic[205] as well as computational neural networks [206, 207]. Up to this point it should have become clear that numerous relationships in nature are in fact NLDS.

Nevertheless and coming back, SCLs and ICLs are ideal model systems for studying NLDS and indeed they have been investigated both theoretically and experimentally in countless publications, because

- they can be controlled very well experimentally, especially in terms of their oscillation frequency,
- they can be deployed in many applications, because of their tiny size. It is even possible to implement them easily in photonic-circuits [12, 13, 208],
- they can be manufactured in many different architectures including conventional diode lasers, quantum-well, -dash, or -dot lasers, QCLs, ICLs and many more[11].
- they show strong non-linear answer compared to other laser types, mainly because of their considerably large linewidth enhancement factor[168],
- they show rich and fast dynamics, which on the one hand enables the acquisition of very large amounts of data in a very short time[123, 198], but on the other hand also places special demands on the detection technology,
- they show strong spontaneous emission, whereby strong noise components manifest themselves in the dynamics

- and a rich theoretical background is known [127].

The main reason for the fragile stability in semiconductor lasers is the relation between the refractive index η of the laser, the carrier density n, the laser oscillation frequency Ω and the temperature T, which all change when the laser is subjected to external optical radiation. The model from Lang and Kobayashi [54] proposes a linear relation for that

$$\eta\left(n,\Omega,T\right)=\eta_0+\left.\frac{\partial\eta}{\partial n}\right|_{n=n_0}\cdot\Delta n+\left.\frac{\partial\eta}{\partial\Omega}\right|_{\Omega=\Omega_0}\cdot\Delta\Omega+\left.\frac{\partial\eta}{\partial T}\right|_{T=T_0}\cdot\Delta T. \tag{3.1}$$

The terms η_0, n_0, T_0 and Ω_0 denote the respective reference values, where $\eta_0=\eta\left(n_0,T_0,\Omega_0\right)$. A similar term can be found for the laser diode cavity resonance frequency ω

$$\omega_{N_{\text{int}}}\left(n,\Omega,T\right)=\omega_0-\frac{\omega_0}{\eta_0}\left(\left.\frac{\partial\eta}{\partial n}\right|_{n=n_0}\cdot\Delta n+\left.\frac{\partial\eta}{\partial\Omega}\right|_{\Omega=\Omega_0}\cdot\Delta\Omega+\left.\frac{\partial\eta}{\partial T}\right|_{T=T_0}\cdot\Delta T\right), \tag{3.2}$$

with the reference value ω_0. Assuming that the half width of the spectrum is much broader than the typical laser diode axial mode separation the dependency of Ω, the gain g can be expressed by

$$g\left(n\right)=g_0+\left.\frac{\partial g}{\partial n}\right|_{n=n_0}\cdot\Delta n. \tag{3.3}$$

The impact of the carrier density n on that properties is found to be very strong in semiconductor lasers [54]. In other words, the influence of $\frac{\partial\eta}{\partial n}$ and $\frac{\partial g}{\partial n}$ governs the change in η, g and ω, when external light is injected. It does not surprise, but it's very noteworthy that the fraction of $\frac{\partial\eta}{\partial n}/\frac{\partial g}{\partial n}$ exactly defines the aforementioned LEF, which ultimately verifies that the LEF is one of the key parameters determining the sensitivity of semiconductor lasers to optical perturbation.

With the SCLs extraordinary sensitivity to optical perturbation numerous phenomena of nonlinear dynamics can be observed e.g. regular pulse packages [209], low-frequency flucatuations [210], chaos generation [211], chaos-pass filtering [212], rogue waves [213, 214] as well as square wave emission [215] and many more. A comprehensive study of those phenomena is summarized in [216]. Promising applications of nonlinear dynamics in SCLs include chaos communication [135], chaos-LIDAR[1] [217] and random bit sequence generation [218], as well as countermeasure devices[219] and spectroscopy [220].

[1] LIDAR is an abbrevation for the technique **li**ght **d**etection **a**nd **r**anging

For us the most important nonlinear phenomenon is the effect of optical injection locking (OIL), where a laser locks on the wavelength of an injected coherent radiation[55]. OIL occurs when the injected wavelength is close to the originally emitted wavelength. This scenario can occur in three different configuration of optical perturbation, whereby the literature mainly distinguishes between optical feedback (sometimes called self-mixing), unidirectional injection and mutual coupling [121]. They are schematically depicted in Fig. 3.2. Based on these three scenarios the so-called laser-as-detector approach will be evaluated.

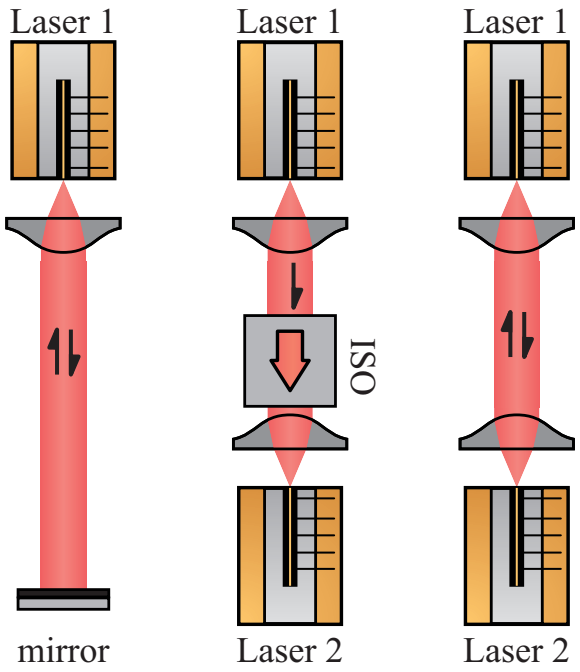

(a) feedback **(b)** unidirectional injection **(c)** bidirectional coupling

Figure 3.2: Schematic comparison of the three kinds of optical perturbations, which can lead to nonlinear dynamics in SCLs.

3.1 Laser-as-detector approach

The change of the carrier density in all types of SCLs, for example caused by optical perturbation, can be detected by analyzing the terminal voltage even when the laser is biased forward, i.e. it operates normally. This technique is generally referred to as the laser-as-detector (LAD) approach. It can be deployed, when conventional photo-detection is not possible or not economical.

The typical technique for photo-detection is based on photo-diodes[221]. This is not always possible for every wavelength domain. Many detectors in the MIR spectral region are bulky, inefficient and/or slow and usually have to be cooled well below room temperature. Fast photodetection in the MIR domain is, according to the current state of the art, only applicable with Quantum Well Infrared Photodetector (QWIP) [50]. Unfortunately QWIPs are usually very selective regarding the accepted spectrum and are additionally quite expensive and not as sensitive as commonly used mercury-cadmium-telluride (HgCdTe or MCT) detectors. The latter are impressively sensitive, but require a sophisticated cooling mechanism and commercially available devices have not been able to detect frequencies higher than $2.12\,\mathrm{GHz}$[51, 222]. The military company Raytheon has already succeeded to develop MCT-detectors with electrical frequencies up to $3\,\mathrm{GHz}$, but they are not available for commercial customers.

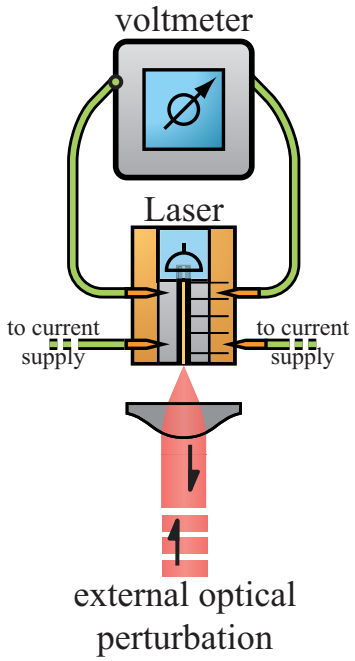

Figure 3.3: Principle of the LAD approach, where the terminal voltage change can be utilized to detect the amount and phase of light.

The decisive advantage of the LAD approach is that the optical setup of many laser based applications even gets much simpler, because no additional optical detector is needed. The LAD approach can also provide high-frequency detection up to the relaxation oscillation frequency, which enables a lot of new applications for example in the MIR spectral region. In that manner, the biggest advantage is that the LAD approach can of course be applied to any other wavelength region, e.g. also for the THz-spectral region, where optical detectors are even rarer than in the MIR domain and photo-detection is more challenging.

The principle of the LAD approach is schematically exemplified in Fig. 3.3. It is based on the inherent coupling of electric and optical field in the semiconductor laser properly described by the rate-equations. Since the ICLs terminal voltage is related to the carrier density, changes in the terminal voltage can be regarded as changes of the optical perturbation.

The relation between terminal voltage and carrier density in semiconductor lasers

According to [52] the terminal voltage changes in semiconductor lasers caused by external optical perturbations can generally be divided into three categories

I. photo-conduction effects,

II. changes in the quasi-Fermi level separation,

III. and the decrease of the current leaking from the p-type active region to the p-type clad layer, which can be neglected here. However, a full explanation can be found in [52].

I. Photo-conduction effects

While in normal operation a forward bias voltage is applied carriers are injected and photons are emitted by recombination, in the reverse biased case electron-hole pairs are generated by absorbing photons with an energy exceeding the bandgap energy E_{gap} in the depletion zone. These are then spatially separated by drifting in different directions due to the diffusion voltage prevailing in the depletion or space-charge zone. This reduces the diffusion voltage, which can be detected in the voltage drop across the semiconductor chip. It has to be considered that the injected radiation generates free carriers not only in the active region, but mostly in its vicinity. The spot of the injected light on the facet will in most of the cases never be the size of the active region, because of lens aberrations and other experimental reasons. Indeed, the fraction of photogenerated carriers in the active region is supposed to be negligible and will not give rise to significant voltage change[52]. Hence, only carriers generated in the part surrounding the active region have to be considered. Absorption of radiation in the parts surrounding the active region can also happen when the laser is operated with forward bias and therefore lowers the resistance of the device. The voltage change ΔU_1 from photoconduction effects is proportional to the injected amount of light S_{inj} via

$$\Delta U_1 = -\Phi\left(I, \lambda\right) \Delta S_{\text{inj}}, \tag{3.4}$$

where $\Phi\left(I, \lambda\right)$ is a positive function of the current I and wavelength of the incident light λ and is characteristic for every laser [52]. Not generally, but it is usually found that $\Phi\left(I, \lambda\right)$ is larger for currents near the laser threshold [223], but is constant for λ within the range of the lasers wavelength. Thus, a voltage change due to photoconduction would manifest itself by a voltage drop, which is mostly independent of λ considering wavelengths close to that of the original lasers wavelength.

II. Changes in the quasi-Fermi level separation

A good approximation for the voltage at a semiconductor junction is given by the differences of the quasi Fermi levels of electrons $E_{\mathrm{F}}^{\mathrm{e}}$ and holes $E_{\mathrm{F}}^{\mathrm{h}}$ and is given by

$$e \cdot U = E_{\mathrm{F}}^{\mathrm{e}} - E_{\mathrm{F}}^{\mathrm{h}} \tag{3.5}$$

with e the elementary charge. A change in the quasi Fermi-level energies therefore results in a voltage change

$$e\Delta U = \Delta E_{\mathrm{F}}^{\mathrm{h,e}} \equiv \Delta E_{\mathrm{F}}^{\mathrm{e}} - \Delta E_{\mathrm{F}}^{\mathrm{h}} \tag{3.6}$$

It is known that the quasi Fermi-levels are related to the carrier density N. It is assumed that the changes due to injection of external light are small compared to the actual carrier density. Thus, we can apply a first order approximation

$$e\Delta U = B\left(N\right)\Delta N \tag{3.7}$$

with

$$B\left(N\right) = \frac{1}{e}\frac{\mathrm{d}E_{\mathrm{F}}^{\mathrm{e}}}{\mathrm{d}N}. \tag{3.8}$$

The relation of electron density and quasi-Fermi-level is

$$N = \frac{1}{2\pi^2\hbar^3}\left(2m_{\mathrm{e}}^*\right)^{\frac{3}{2}} \cdot \int_{E_{\mathrm{cl}}}^{\infty} \frac{\sqrt{E - E_{\mathrm{cl}}}}{\exp\left(\frac{E - E_{\mathrm{F}}^{\mathrm{e}}}{k_{\mathrm{B}}T}\right) + 1}\mathrm{d}E, \tag{3.9}$$

where the assumption was made that N is uniform across the active region. The variable T is the absolute temperature, m_{e}^* is the effective electron mass, k_{B} is the Boltzmann constant, E_{Cl} is the energy at the edge of the conduction band and $\hbar$ is the reduced Planck-constant. It can be seen that $B\left(N\right)$ can not be found in an analytical form, but changes in the carrier density due to an optical injection are indeed small compared to the overall carrier density. Thus, we conclude that in a first order approximation changes in the quasi-Fermi level separation are proportional to the carrier density within the active region. Indeed, it will be seen later that changes in the quasi-Fermi level separation play the dominant role for voltage changes, when optical perturbation is in the same wavelength domain of the affected laser.

III. Decrease of the current leaking from the p-type active region to the p-type clad layer

The final cause that affects the terminal voltage of the laser is reduction of the leakage current from the active p-type area into the p-type cladding layer. This also results from the reduction of the quasi-Fermi level distance already discussed. The series resistance is increased in the p-type cladding layer and thus the terminal voltage. The voltage change ΔU here is again proportional to the changes of carrier density ΔN. A full explanation can be found in [52].

3.2 Goals of the chapter

The three effects of optical perturbation on the terminal voltage mentioned in the previous section form the basis for the LAD approach, which we will evaluate in the chapter. Therefore, we discuss three different scenarios of optical perturbation visualized in Figs. 3.2a to 3.2c successively in the following sections with regard to the applicability of the LAD approach.

We begin with an extension of the rate equation to generally include all three types of optical perturbation (Section 3.3). This extended model is not restricted to ICLs, it was found that it can be utilized for any kind of SCL including QCLs [224], however, then with different characteristic times and a set of different parameters.

Using the LAD approach does not necessarily mean that the voltage change itself is linear to the strength of the optical perturbation, other measures can be linear to the optical perturbation strength as well. Therefore, we first use the theoretical model in order to find two of these measures, namely the so-called modulation index and the so-called locking bandwidth, which are linear with the strength of the optical perturbation and use them in the following experiments.

After discovering that the so-called modulation index is a proper linear measure, we then verify its applicability for the LAD approach by self-mixing experiments in Sections 3.4 and 3.5. The findings in these sections are then exploited later for a detector-free spectroscopy experiment, which will be discussed in Section 4.6. The key idea here is that a small amount of absorption within the feedback path affects the feedback strength, which will result in a change of the carrier density, which is connected to the change in the terminal voltage and therefore can be accessed easily.

This simple idea is transferred to the setup with unidirectional optical injection discussed in Section 3.6. Since optical injection can provide a larger change of the carrier density compared to feedback, it is reasonable that the SNR of the detector-free spectroscopic setup improves. The evaluation of the approach for spectroscopy will be carried out it Section 4.7. Here, in this chapter we present the basis for experiments based on unidirectional injection and address the phenomenon of OIL on the basis of ICLs. We show that in that case the so-called locking bandwidth is a good measure to draw conclusions about the optical perturbation strength.

The chapter finally closes with Section 3.7, where we present a general discussion of ICLs in a bidirectional coupling configuration. With the findings of that, we realize a surprisingly simple and innovative mid-infrared private communication scheme in Section 5.2 without any additional optical detectors. The key idea here is that a change in one of the two ICLs causes a change of the physical quantities in the second ICL coupled to it and vice versa.

3.3 Rate equations with external optical perturbation

A generally utilized way to describe lasers exposed to an optical perturbation of any kind, is to extend the rate equation model by an injection term [225]. Our in Eqs. (2.7) and (2.8) introduced rate equation model can be extended to include externally injected light by the following equations, representing the first-ever rate-equation system for optically injected ICLs

$$\frac{\mathrm{d}\Delta N\left(t\right)}{\mathrm{d}t} = \frac{\zeta J}{qd} - \frac{\Delta N\left(t\right)}{\tau_{\mathrm{eff}}} - g \cdot \Delta N\left(t\right) \cdot \tilde{E}^{*}\tilde{E}, \tag{3.10}$$

$$\frac{\mathrm{d}\tilde{E}\left(t\right)}{\mathrm{d}t} = \left(i\omega_{\Delta N_{\mathrm{int}}}\left(\Delta N, \omega\right) + \frac{1}{2}\left(Zg \cdot \Delta N\left(t\right) - \frac{1}{\tau_{\mathrm{ph}}}\right)\right)\tilde{E} + \kappa_{\mathrm{inj}}\tilde{E}_{\mathrm{ext}}\left(t-\tau\right), \tag{3.11}$$

where we have highlighted the injection terms in **orange** and neglected the noise terms E_{sp} and F_i for simplicity. The complex coupling coefficient κ_{inj} in Eqs. (3.10) and (3.11) describes the influence of coupling between each laser. Following [226] it can be split into the modulus $|\kappa_{\mathrm{inj}}|$ and the argument θ_{inj}

$$\kappa_{\mathrm{inj}} = |\kappa_{\mathrm{inj}}| \exp\left(i\theta_{\mathrm{inj}}\right) \tag{3.12}$$

$$\tag{3.13}$$

with

$$|\kappa_{\mathrm{inj}}| = \frac{\kappa}{\tau_{\mathrm{round}}}, \tag{3.14}$$

$$\theta_{\mathrm{inj}} = \Delta\omega\tau_{\mathrm{round}} + \theta_C. \tag{3.15}$$

The modulus of the coupling coefficient $|\kappa_{\mathrm{inj}}|$ describes the amplitude of the incident electrical field. It is determined by the coupling strength κ and the round-trip time τ_{round} of the laser's cavity. The coupling strength κ takes into account all losses of the injected optical field amplitude from the original source to the laser's cavity. The argument of the coupling coefficient, θ_{inj} shifts the phase of the incident electrical field. It is influenced by the OFD $\Delta\nu \equiv \nu_{\mathrm{ext}} - \nu$, τ_{round} and coupling term θ_C describing all phase shifts of the injected optical field.

With the assumptions in Eq. (2.10) and the SVEA Eq. (2.11) we find the final rate equations for an ICL subjected to an external optical perturbation to be

$$\frac{\mathrm{d}\Delta N(t)}{\mathrm{d}t} = \frac{\zeta J}{q} - \frac{\Delta N(t)}{\tau_{\text{eff}}} - g \cdot \Delta N(t) \cdot E^*(t)\, E(t)\,, \tag{3.16}$$

$$\begin{aligned}\frac{\mathrm{d}E(t)}{\mathrm{d}t} = {} & \frac{1}{2}\left(Zg \cdot \Delta N - \frac{1}{\tau_{\text{ph}}}\right) E(t) \\ & + |\kappa_{\text{inj}}|\, E_{\text{ext}}(t-\tau)\, E(t) \cos\left(\theta_{\text{inj}} + \left(\phi_{\text{ext}}(t-\tau) - \phi(t)\right) + \Delta\omega t - \omega\tau\right)\end{aligned} \tag{3.17}$$

$$\begin{aligned}\frac{\mathrm{d}\phi(t)}{\mathrm{d}t} = {} & \frac{\alpha}{2}\left(Zg \cdot \Delta N - \frac{1}{\tau_{\text{ph}}}\right) \\ & + |\kappa_{\text{inj}}|\, \frac{E_{\text{ext}}(t-\tau)}{E(t)} \sin\left(\theta_{\text{inj}} + \left(\phi_{\text{ext}}(t-\tau) - \phi(t)\right) + \Delta\omega t - \omega\tau\right),\end{aligned} \tag{3.18}$$

where we again divided the optical field into amplitude E and phase ϕ and substituted the OFD $\Delta\nu$ by $(2\pi)^{-1}\Delta\omega$, as well as ν by $(2\pi)^{-1}\omega$.

This advanced model can be used for either describing self-injection, i.e. feedback, unidirectional or bidirectional injection.

1. In the case of feedback for example, the external perturbation is described by the optical field of itself delayed by a time τ, i.e. $E_{\text{ext}}(t) = E(t-\tau)$. Additionally, the OFD is zero: $\Delta\nu = 0$.

2. In case of unidirectionally injected light from an external source, the above equation applies as described.

3. In case of bidirectionally coupled ICLs, the rate equations have to be extended by the complex optical field and the carrier inversion of the second laser. The externally injected optical field of each laser is then the optical field of the other laser delayed by the time $\tau = \frac{L}{c}$, where L denotes the spatial distance between the lasers and c the speed of light.

All three scenarios will be discussed in detail in the next sections, but before we discuss how solutions of the rate equations can be obtained.

3.3.1 Methods to find the solutions of the rate-equations

There are two favored methods to obtain solutions of $E(t)$, $\Delta N(t)$ and $\phi(t)$, the steady-state ansatz and numerical integration.

Steady-state ansatz

The first is usually referred to as steady-state ansatz. In this method it is assumed that $\frac{\mathrm{d}\Delta N(t)}{\mathrm{d}t} = 0$ and $\frac{\mathrm{d}\Delta E(t)}{\mathrm{d}t} = 0$. This method is ideal for determining the optical field and carrier density subjected to optical perturbation, when knowledge of the time-evolution is not required. It instead provides exact solutions for $t \to \infty$ and reveals the underlying physical mechanisms. However, the stability of these steady-states-solutions may change, when parameters of the equations are varied. The parameter values where this happens are referred to as bifurcations and sometimes a conventional calculation of the steady-state-solutions becomes impossible. Here usually a numerical continuation is used to reveal the type of bifurcation [227]. The latter is not the subject of this thesis and is therefore not discussed, but can be conveniently reviewed in [127] or [228].

Numerical integration

The second option is to numerically integrate the rate-equations enabling access to the time-evolution of the physical properties. This can be done e.g. with the Runge–Kutta method[229], the implicite-Euler method or many more integration procedures [230]. The disadvantage of numerical integration is that the rate-equations involve very different time constants. The fastest processes, i.e. the optical-transitions, in our rate-equation system imply the use of a small temporal step size (in our case $100\,\mathrm{fs}$), because otherwise the numerical integration would become unstable. At the same time, much slower processes force an integration over a long time span, resulting in a large number of numerical steps. Thus, a lot of computation power is needed for that option. This can also be beneficial, because numerical integration therefore reveals the dynamics of the system and can show hysteresis just like a real-world system. The numerical integration in this thesis is performed via the first-order exponential integrator method, which we briefly introduce here. A detailed of the method can be found reviewed in [231].

The first-order exponential integrator method Our differential equations are of the form

$$\frac{\mathrm{d}y}{dt} = -Ay\left(t\right) + \zeta\left(y\right), \tag{3.19}$$

where we have a linear term $-Ay\left(t\right)$ and a nonlinear term $\zeta\left(y\right)$. Exponential integrators are constructed by multiplying with $\exp At$ and integrating over the time interval $[t_n, t_n + h]$

$$y_{n+1} = \exp\left(-Ah\right) y_n + \int_0^h \exp\left(-\left(h-\tau\right)A\right) \zeta\left(y\left(t_n+\tau\right)\right) \mathrm{d}\tau. \tag{3.20}$$

This is exact, but the integral can often not be calculated. Thus, by requesting $\zeta\left(y\left(t_n+\tau\right)\right)$ is constant over the whole interval we obtain

$$y_{n+1} = \exp\left(-Ah\right) y_n + A^{-1}\left(1-\exp\left(-Ah\right)\right)\zeta\left(y\left(t_n\right)\right). \tag{3.21}$$

We have chosen this type of solver because it offers a great time stepping capability and high accuracy for sets of so-called stiff differential equations like ours [231, 232].

Deployment of steady-state approach and numerical integration

In this thesis we use the steady-state ansatz to qualitatively describe the detected and observed phenomena, when the ICLs are exposed to an optical perturbation. Numerical integration is then used to quantitatively reproduce the effects of external optical perturbation.

The most crucial parameters we focus on in this thesis are the coupling strength determined by the coupling strength κ, the coupling phase due to delay τ as well as the OFD $\Delta\nu$. The effects of these three parameters on the dynamical phenomena of each optical perturbation scenario will be described in the following sections, where the model provides a proper basis for comparing the experimental results with the theory described here. Considering the LAD approach it should be emphasized again that effects due to optical perturbation also manifest themselves in the carrier density of the ICL - not only in the optical field.

3.4 The demonstration of the laser-as-detector approach in a self-mixing experiment

For a first experimental verification of the LAD approach we utilize the self-mixing-effect. In Fig. 3.2a the principle of optical feedback or in other words reinjecting its own light of the emitting laser itself has already been discussed briefly. Usually, optical feedback into the active medium of the laser is undesirable. SCLs are generally very sensitive to optical feedback and the optical output, i.e. wavelength and power, may become non-deterministic and chaotic. To avoid that special optical elements, so-called optical isolators (ISOs), are implemented in the setup and are usually placed directly in front of the SCLs. On the other hand, many applications such as chaos-lidar[217], chaos-communication [135] or random bit sequence generation [218] exploit chaos generated by semiconductor lasers subjected to feedback. Optical feedback must not necessary lead to chaos, which only occurs when strong feedback is applied. In the case of weak and moderate feedback the laser is very sensitive to the feedback phase, which is determined by the distance between the reflective object and the laser, i.e. the external cavity length. This sensitivity can also be undesirable, because each optical element within the beam reflects a fraction of the incoming light back into the SCL making the output become very

sensitive to mechanical vibrations of these components. This phase-sensitivity can be exploited, because the relation between the changes of optical power and optical frequency due to the change in the feedback phase are well known [54]. In that manner optical feedback can be used to tailor the laser noise[233, 234] or to identify fundamental parameters of a laser like the linewidth enhancement factor (LEF)[174], which we have already described in Section 2.9.4. From an applied perspective there are also many techniques exploiting the effects of weak optical feedback including imaging [235] and spectroscopy [236]. Other techniques based on self-mixing include velocimetry [53] and vibration-sensing [237]. All these applications do not require an additional optical detector, which represents the ultimate goal of the LAD approach.

The procedure developed here is to show that the LAD approach is applicable, by showing that the ICLs output power is strongly correlated with the terminal voltage. We first introduce the theory for ICLs subjected to feedback. Then we demonstrate the correlation experimentally.

3.4.1 Self-mixing theory

In self-mixing experiments the OFD $\Delta\nu$ amounts to 0 . Note that all further equations in this section are restricted to this criterion. With the rate equations described in Eqs. (3.16) to (3.18) stationary lasing conditions can be described and qualitatively understood. Therefore, we set the electrical field $E\left(t\right)$ and population inversion $\Delta N\left(t\right)$ constant:

$$\Delta N\left(t\right) = \Delta N \tag{3.22}$$

$$E\left(t\right) = E. \tag{3.23}$$

Following [238] and [178] we obtain the steady-state solutions

$$E^2 = \frac{\left(\frac{\zeta J}{q} - \frac{N_{\text{th}}}{\tau_{\text{eff}}} - \Delta N_0\right)}{\frac{1}{\tau_{\text{ph}}} + Zg\Delta N_0} \tag{3.24}$$

$$\Delta N_0 = -2\frac{|\kappa_{\text{inj}}|}{Zg}\frac{E_{\text{ext}}}{E}\cos\left(\phi_{\text{FB}}\right) \tag{3.25}$$

and the relation

$$\nu_{\text{FB}}\left(\phi_{\text{FB}}\right) = \nu_0 - |\kappa_{\text{inj}}|\sqrt{1+\alpha^2}\cdot\sin\left(2\pi\nu_{\text{FB}}\left(\phi_{\text{FB}}\right)\cdot\frac{2L}{c} + \arctan\left(\alpha\right)\right), \tag{3.26}$$

with

$$\phi_{\text{FB}} \equiv \frac{4\pi\nu}{c}\cdot L \tag{3.27}$$

and

$$\Delta N = N_{\text{th}} + \Delta N_0 \tag{3.28}$$

The threshold carrier density N_{th} can be easily derived by calculating the steady-state values in the absence of feedback ($\kappa_{\text{inj}} = 0$) yielding

$$\frac{N_{\text{th}}}{\tau_{\text{eff}}} + \frac{|E_0|^2}{\tau_{\text{ph}}} = \frac{\zeta J}{q}. \tag{3.29}$$

Here, E_0 the characteristic optical field of the actual steady state (above threshold). Assuming a linear relation between gain g and current density J the relation

$$Zg \cdot |E_0|^2 = \frac{J}{J_{\text{th}}} - 1 \tag{3.30}$$

holds. Inserting Eqs. (3.29) and (3.30) into Eq. (3.24) and after a few equivalent transformations one can obtain

$$E^2 = |E_0|^2 + |E_0|^2 \cdot 2\tau_{\text{ph}} |\kappa_{\text{inj}}| \frac{J/J_{\text{th}}}{J/J_{\text{th}} - 1} \cos(\phi_{\text{FB}}) \tag{3.31}$$

This equation reveals that the electrical output power $P \equiv E^2$ is a function of $\cos(\phi_{\text{FB}})$. Other literature [137, 160, 174, 223, 236, 239, 240] interprets this relation as

$$P(\phi_{\text{FB}}) = P_0 (1 + m \cdot F(\phi_{\text{FB}})) \tag{3.32}$$

with

$$F(\phi_{\text{FB}}) \equiv \cos\left(\nu_{\text{FB}}(\phi_{\text{FB}}) \cdot \frac{4\pi L}{c}\right) \tag{3.33}$$

with $P_0 \equiv |E_0|^2$. Here $F(\Phi)$ the so-called interferometric function (see before Section 2.9.4), which is 2π-periodic in the feedback phase. The variable $m \equiv \tau_{\text{ph}} |\kappa_{\text{inj}}| \frac{J/J_{\text{th}}}{J/J_{\text{th}}-1}$ denotes the modulation index and amounts typically to a value of $m \approx 10^{-3}$ [239]. It shall be emphasized that the modulation index is proportional to the feedback strength:

$$m \propto |\kappa_{\text{inj}}|. \tag{3.34}$$

A exemplified sketch of the interferometric function is depicted in Fig. 3.4 for four selected ranges of the feedback strength parameter C, which is defined as

$$C \equiv \kappa \cdot b_{\text{inj}} \cdot \sqrt{1+\alpha^2} \tag{3.35}$$

with

$$b_{\text{inj}} \equiv (1 - R_{\text{fac}}) \sqrt{\frac{R_{\text{ext}}}{R_{\text{fac}}}}, \tag{3.36}$$

where R_{fac} denotes the reflectivity of the laser facet and R_{ext} is the reflectivity of the external mirror. When $C > 1$ multistabilites in $F(\phi_{\text{FB}})$ arise. In the case $1 < C < 4.6$, which is referred to as moderate feedback, the function $F(\phi_{\text{FB}})$ becomes three-valued as it is depicted in Fig. 3.4 (bottom left). The asymmetry of $F(\phi_{\text{FB}})$ depends mainly on the LEF. The *weak feedback regime* affiliates for $C < 1$, where only one solution is possible and the *strong feedback regime* for $C > 4.6$, where more complex dynamics can be observed (see before Section 2.9.4).

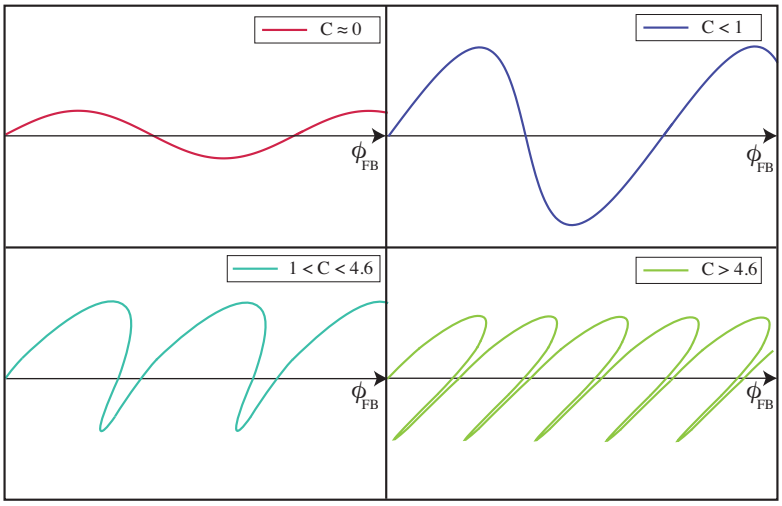

Figure 3.4: Exemplification of the simulated interferometric function $F(\phi_{\text{FB}})$ for four ranges of the C- parameter.

In Section 2.9.4 we have already used the interferometric function for the determination of the LEF utilizing the weak feedback regime $C < 1$. Here, we see what happens if moderate feedback or strong feedback is applied. In the case of strong feedback it can happen that so many solutions exist, that the laser may arbitrarily change between those multistabilities, which we observe as chaos. While increasing the feedback from the moderate to the strong feedback regime usually other types of dynamics are observed before entirely chaotic output is generated [210, 241, 242]. Those fluctuations are called low-frequency fluctuations.

In order to generally avoid multistabilities or even chaos that this theoretical introduction revealed we choose to remain in the weak feedback regime for the LAD approach verification experiment.

3.4.2 Self-mixing experiment

The actual experimental setup is depicted in Fig. 3.5. We utilize ICL 2183/22-25 temperature stabilized at $15\,°C$ for this investigation. The laser beam is divided by a non-polarizing beam splitter (NPBS). One part irritates the detector, while the other part enters the $40\,cm$ long feedback arm. In the feedback arm we place a variable polarizer and a fixed polarizer, which both serve as a continuous attenuator. The fixed polarizer is aligned to the polarization of the laser in order to ensure feedback with the same polarization. The feedback itself is provided by a mirror, which is mounted on a loudspeaker, which has been mechanically isolated from the table to avoid mechanical resonances. Also the sinusoidal movement of the loudspeaker of $584\,Hz$ was chosen to minimize mechanical resonances. The back-reflected beam is sent on a pyro-electrical detector to evaluate the relative feedback strength. The other part reenters the ICL, where it influences the optical output and at the same time alters the terminal voltage. Both the signal of the optical detector and the AC-part of the terminal voltage amplified by $46\,dB$ are recorded with an oscilloscope in Channel 1 and Channel 2 respectively.

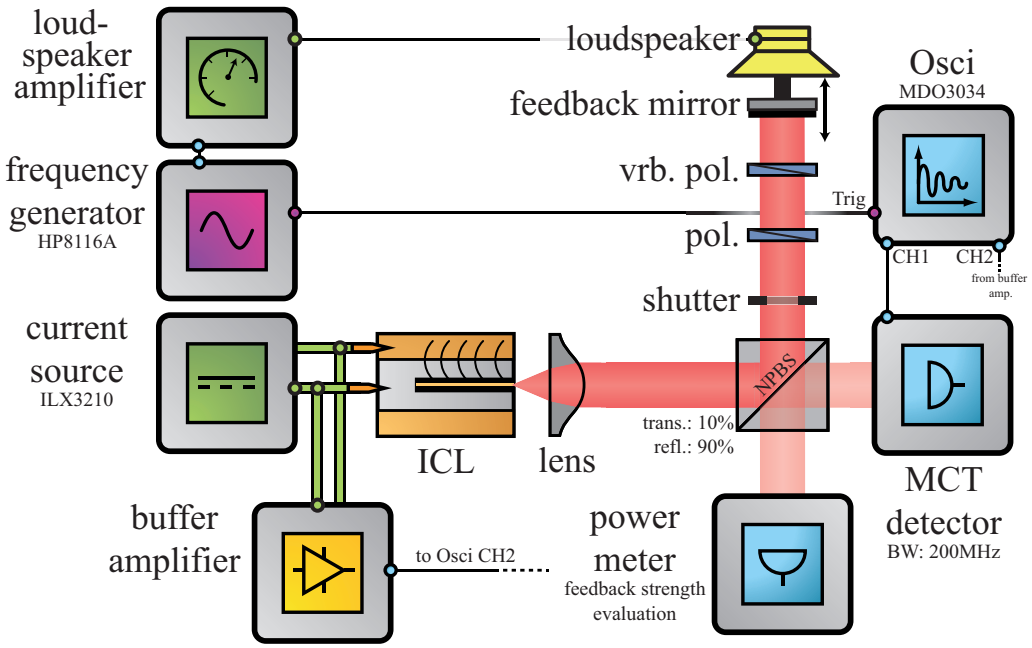

Figure 3.5: Setup to investigate the LAD approach.

An example of obtained time-traces is shown in Fig. 3.6. It can already been seen that both signals show strong correlation. The correlation becomes clearer when plotting the terminal voltage time-trace against the optical detector timetrace, which is shown in Fig. 3.7.

From that we quantify the correlation with the Bravais-Pearson correlation coefficient R_{BP}, which is often referred to as Pearson R, using

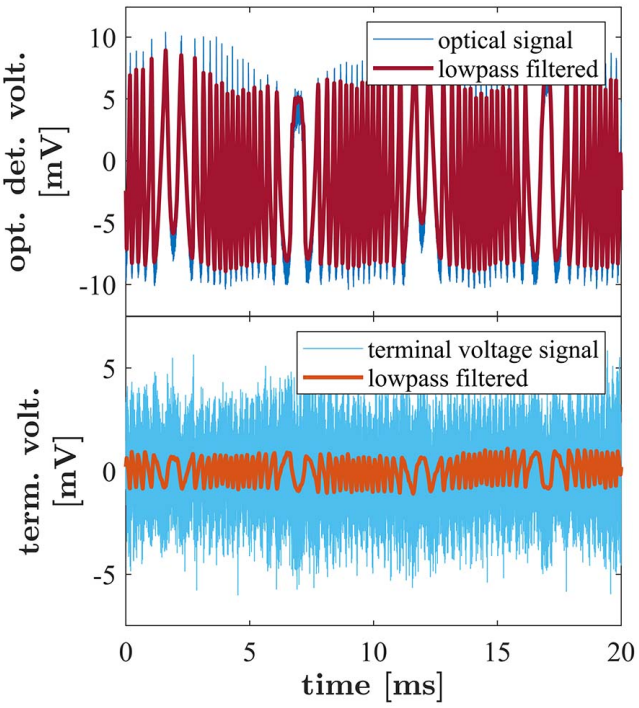

Figure 3.6: Timetraces of the optical detector signal (top) and AC-coupled terminal voltage signal (bottom) and the lowpass filtered traces. The lowpass filter is a Butterworth filter with $10\,\mathrm{kHz}$ stop-band frequency and $90\,\mathrm{dB}$ stopband attenuation.

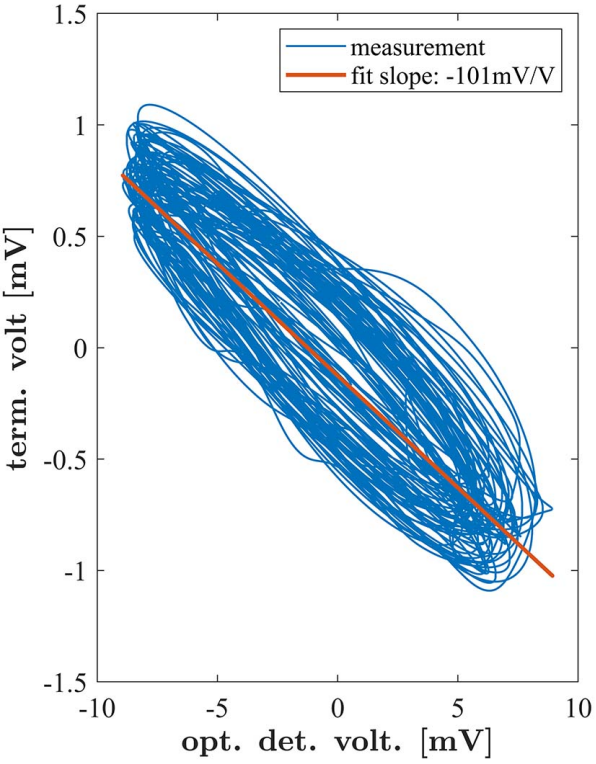

Figure 3.7: Terminal voltage signal vs. optical signal of the LAD approach (blue) and a linear fit (orange) to find a constant conversion factor between both. The data is taken from the lowpass filtered timetraces in Fig. 3.6.

$$R_{\mathrm{BP}} = \frac{\sum_{n=1}^{N}\left(I_n^{\mathrm{opt.}} - \overline{I^{\mathrm{opt.}}}\right)\cdot\left(I_n^{\mathrm{volt.}} - \overline{I^{\mathrm{volt.}}}\right)}{\sum_{n=1}^{N}\left(I_n^{\mathrm{opt.}} - \overline{I^{\mathrm{opt.}}}\right)^2 \sum_{n=1}^{N}\left(I_n^{\mathrm{volt.}} - \overline{I^{\mathrm{volt.}}}.\right)^2}, \tag{3.37}$$

It gives a reliable measure on the confidentiality of the correlation with $-1 < R_{\mathrm{BP}} < 1$ and $R_{\mathrm{BP}} = 1$ representing full correlation and $R_{\mathrm{BP}} = -1$ full anti-correlation[243]. The variable N represents the total number of datapoints, while $\overline{I^{\mathrm{opt.}}}$ and $\overline{I^{\mathrm{volt.}}}$ represent the arithmetic means of all $I^{\mathrm{opt.}}$ and $I^{\mathrm{volt.}}$ respectively.

The evaluation of the Bravais-Pearson correlation coefficient in our case yields $R_{\mathrm{BP}} = -0.803$, demonstrating a good linear relationship between optical signal and terminal voltage,

which is also visualized with the linear fit curve in Fig. 3.7. The curve fitting of that particular measurement results in a conversion factor of $-101\,\mathrm{mV\,V^{-1}}$. For spectroscopy experiments using the self-mixing ansatz and the LAD approach it is required that the conversion factor remains constant for all coupling strengths κ. Otherwise there would lack linearity between optical output power and terminal voltage. We verify this by analyzing the influence of the feedback strength on the conversion factor and the Pearson R, which is visualized in Fig. 3.8.

It is visible that the conversion factor is very roughly constant for increasing feedback strength and the Pearson R stays constant except for small feedback strengths. For very small feedback strength noise dominates the time-traces and thus correlation will reduce. However, it is also clear that the conversion factor in particular does not remain constant for all driver currents (compare the colors in Fig. 3.8).

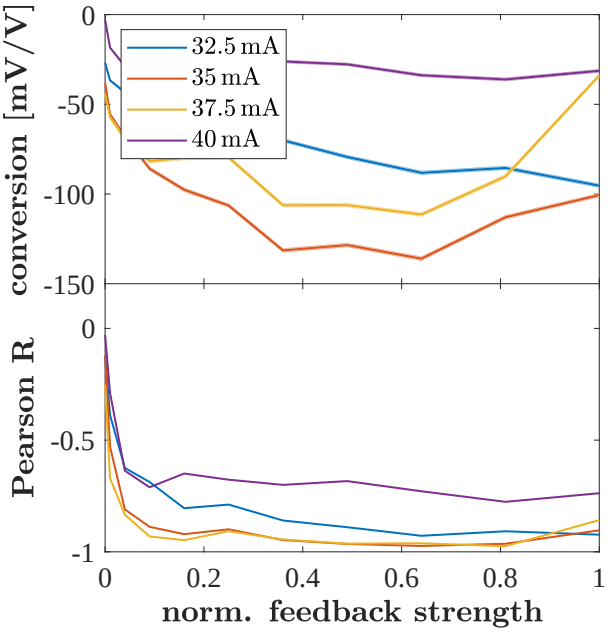

Figure 3.8: Conversion factor and Pearson R as a function of feedback strength for four exemplary currents.

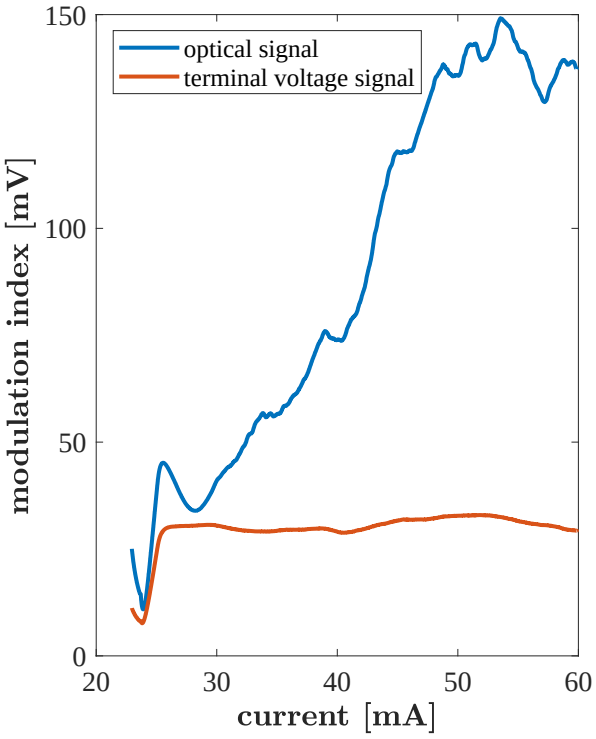

Figure 3.9: Modulation index of the optical and the terminal voltage signal as a function of the driver current.

To analyze the influence of the current on the modulation index we determine the modulation index m [2] both for the low-pass filtered optical signal and the low-pass filtered terminal voltage and visualize them in Fig. 3.9. We find that the modulation index of the optical signal

[2] for the definition of the modulation index m remind Eq. (3.32)

changes with increasing current, which could be caused by defocussing effects due to temperature elongation caused by the current flow. The modulation index of the terminal voltage remains constant for the whole range of currents above the threshold. This is because Eq. (3.25) does not depend on the current and the ratio $\frac{E_{\text{ext.}}}{E}$ stays constant, which is very advantageous for the spectroscopic method based on self-mixing demonstrated later (see Section 4.6). Thanks to the constant modulation index, an additional reference measurement, which is usually necessary for the spectroscopic measurement, is not required and can be replaced by a baseline fitting.

3.4.3 Summary of the section

We find that the LAD approach together with self-mixing proves to be very versatile for later measurements using the modulation index as a measure for the feedback strength. It has been shown that the electrical detection setup is less susceptible to optical perturbation such as stray light or defocussing, but a little more sensitive to electromagnetic disturbances.

We finally conclude that the LAD approach provides an uncomplicated and very cost-effective detection setup for MIR applications significantly facilitating the subsequent experiments, because no additional detector is required. We utilize our findings to perform a spectroscopic technique without an additional optical detector in Section 4.6.

3.5 Dynamical stability of ICLs subjected to optical feedback

In Fig. 3.10 the principle of self-mixing or in other words optical feedback has already been shown. In many cases, optical feedback into the active medium of the laser is undesirable, because the optical output, i.e. wavelength and power, of the laser becomes either instable, non-deterministic or chaotic. Usually optical isolators are aligned to avoid feedback. As described in the introduction of this chapter semiconductor lasers are generally very sensitive to optical feedback. Nevertheless many applications such as chaos-lidar[217], chaos-communication [135] or random bit sequence generation [218] exploit the chaotic output of semiconductor lasers subjected to feedback. Chaos occurs, because the system possesses multiple possible operation states and the laser emission jumps erratically between those states. But optical feedback must not necessary lead to chaos, in fact, chaotic emission only occurs when strong feedback is applied ($C > 4.6$), recall Eq. (3.35) and Section 3.1, where we've already discussed the influence of feedback on a SCL). In the regime

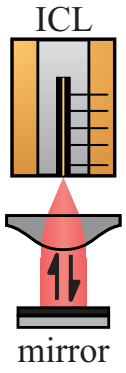

Figure 3.10: Schematical setup of an ICL subjected to optical feedback.

between moderate and strong feedback ($C \simeq 4.6$) several other dynamic patterns can be observed, such as low-frequency-fluctuations or regular-pulse packaging [244]. In that case the jumps between the still large number of possible states is not more erratic, but is somehow regular. In the case of moderate feedback ($1 < C < 4.6$) only three multi-stabilities arise. Here, the lasers optical power and carrier density are very sensitive to the feedback phase, which is determined by the distance between the reflective object and the laser, i.e. the external cavity length. In the moderate feedback regime, the output is stable on these three states, but optical power and carrier density show a hysteresis with respect to the feedback phase. In the weak feedback regime ($C < 1$) only one operation state is possible, which is still influenced by the feedback phase. This can also be undesirable, because each optical element within the beam reflects a fraction of the incoming light making the laser become very sensitive to mechanical vibrations.

However, this deterministic sensitivity can be beneficially exploited, because the relation between the changes of optical power and optical frequency due to the change in the feedback phase are well known [54]. In that manner optical feedback can be used to identify fundamental parameters of a laser like the linewidth enhancement factor (LEF)[174], which we have already described in Section 2.9.4 or manipulate the laser noise[233, 234]. From an applied perspective there are also many techniques to exploit the effects of weak optical feedback including imaging [235] and spectroscopy [236] without the use of an optical detector as well as velocimetry [53] and for vibration-sensors [237]. These techniques are usually referred to as self-mixing experiments.

In this section we discuss which feedback strengths lead to higher dimensional dynamics in ICLs. We shall see that strong feedback is not targeted in the following experiments, because high-dimensional dynamics, since it is non-deterministic, can not provide a proper metric for spectroscopy applications or data transmission purposes. We therefore need to quantitatively separate the three feedback regimes, weak, moderate and strong feedback.

Low-frequency fluctuations (LFFs) occur, when the semiconductor lasers switch between multiple destabilized steady-states (also referred to as destabilized attractors) on a micro- or nanosecond timescale[242]. This phenomena has been demonstrated for the first time by Risch and Voumard[245] and later has been called chaotic itinerancy[241]. LFFs are especially interesting because their frequencies are relatively slow compared to other internal characteristic frequencies such as relaxation oscillations or the cavity roundtrip time and mark the onset of chaotic emission, which we want to avoid. Thus, the minimal feedback strength, where LFFs can be observed marks a hard limit that must not be exceeded in the subsequent applications. Therefore, we determine minimal feedback strength above which higher-dimensional dynamics are observed in this section, which we will avoid in later measurements.

3.5.1 Experimental observation of low-frequency-fluctuations

The setup to investigate the influence of feedback strength on ICLs is a typical self-mixing-setup and depicted in Fig. 3.11.

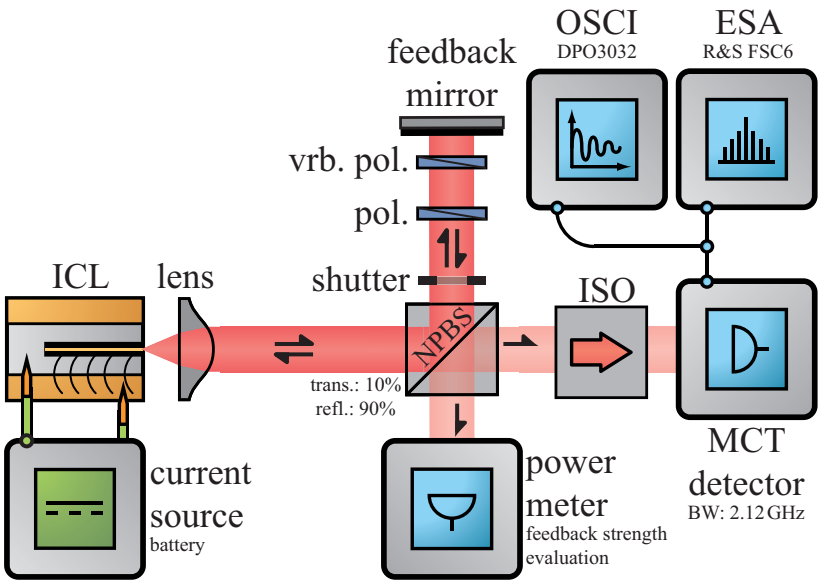

Figure 3.11: Setup to investigate low-frequency-fluctuations in ICLs. The shutter can be closed in order to investigate the system without feedback. Two MIR wiregrid polarizers enable adjusting the feedback strength following the law of Malus.

We utilize ICL 2183/22-25 temperature stabilized at $15\,^{\circ}\mathrm{C}$ for these investigations. The laser beam is divided by a non-polarizing beam splitter (NPBS). One part illuminates the MCT-detector [3], while the other part enters the feedback arm. The MCT-detector is placed behind an optical isolator in order to avoid back-reflections at the facet of the detector. We place a variable polarizer as well as a fixed polarizer in the $2 \times 71\,\mathrm{cm}$ long beam path, which both serve as a continuous attenuator. The fixed polarizer is aligned to the polarization of the laser in order to ensure feedback with the same polarization. The feedback itself is provided by a gold mirror. To avoid reflections from both polarizers, we slightly turn them with respect to the beam. The back-reflected beam simultaneously sent on a pyro-electrical detector to evaluate the relative feedback strength. The other part reenters the ICL, where it influences the optical output. We record the AC-Part of the signal with an oscilloscope and analyze the embedded electrical frequencies with an $6\,\mathrm{GHz}$ electrical spectrum analyzer (Rhode und Schwarz FSC-6). With the shutter in the feedback arm we can obtain a reference measurement without any feedback. We choose this specific feedback length, because it is in the desired range for the spectroscopic sensor.

[3] VIGO PVI-4TE-3.4-0.5x0.5-B-wZnSeAR-35 with an AIP-10k-2G-M4-INT preamplifier

The temporal evolution of the ICL subjected to feedback [4] emitting in a non-stable regime is depicted in Fig. 3.12. The timetraces are characterized by sudden drop-outs followed by a recovery to a more or less stable intensity. This intensity is maintained until the next drop-out occurs. In addition, the RF-spectrum shows a series of equally spaced and strongly broadened peaks, caused by the round trip resonances of the light in the external cavity and the corresponding harmonics. Both findings represent typical indications of low-frequency-fluctuations [210]. The time evolution of a SCL including ICLs emitting in the LFF regime can be explained with the Lang-Kobayashi theory, follwing the steady-state solutions for ICLs subjected to feedback inEqs. (3.16) to (3.18). The ICL switches between multiple destabilized steady-states called attractors. On each destabilized attractor, the emitted power follows an erratic path. In the time inbetween these erratic outputs, the system passes over to another destablized attractor. This naturally happens until the highest-gain has been reached. The feedback finally leads to collision of stable and unstable attractors. This is referred to as crisis making the system descend to a steady-state with a lower gain, which we observe as the characteristic drop-out. This happens over and over again and therefore semi-regular characteristic drop-outs and recovery can be seen[210].

3.5.2 Dynamical stability as a function of the feedback strength

In order to reveal the maximal feedback strength, where the laser emits on a stable state, we operate the laser with a constant current and stepwise increase the feedback strength using the two polarizers. [5] We use the RF-spectra to visualize, at which LFFs start to occur. LFFs manifest themselves with a series of equally spaced and strongly broadened peaks, caused by the round trip resonance in the external cavity and its corresponding harmonics [244].

We find that the relative external feedback strength R_{meas} to obtain high-dimensional dynamic emission amounts to $62.2\,\%$ and is indicated by the green vertical line in Fig. 3.14.

Keeping the high reflection coefficient of the NPBS in mind (specification $90\,\%$) we find, that the threshold feedback strength for the occurence of high-dimensional dynamics is quite high compared to that of other MIR SCL types such as QCLs [213], where typical values of $8.1\,\%$ are observed. This can be explained as a direct result of the very low LEF of the sample ICL compared to other SCL types (compare for Eq. (3.35)). Equation (3.35) verifies that SCLs with low LEF require a higher external reflectivity R_{ext} to obtain coupling strength parameters of $C \geq 4.6$.

Beyond $62.2\,\%$ LFFs occur only for few feedback strengths, that are interrupted by regimes, where no higher-dimensional dynamics can be observed. It was found that this happens when turning the polarizer, which might slightly shift the feedback phase ϕ_{FB}. Above a feedback strength of approx. $75\,\%$ no LFF-dynamics can be observed and the ICL begins operation on

[4] We define the relative feedback strength as the ratio between the actual optical power at the power meter and the maximal detected power at the power meter.

[5] It shall be recalled that a normalized feedback strength of 1 is obtained when both polarizers are aligned to match the polarization of the ICL, i.e. when the maximal possible feedback strength is applied.

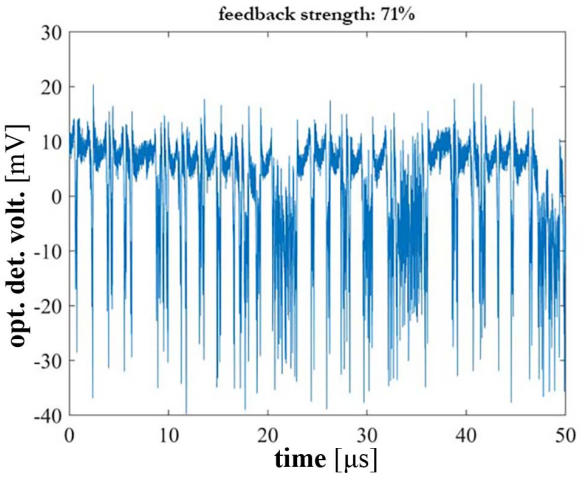

Figure 3.12: Example time evolution of the intensity dynamics of the ICL subjected to optical feedback in the LFF regime (blue). The feedback strength amounts to $71\,\%$

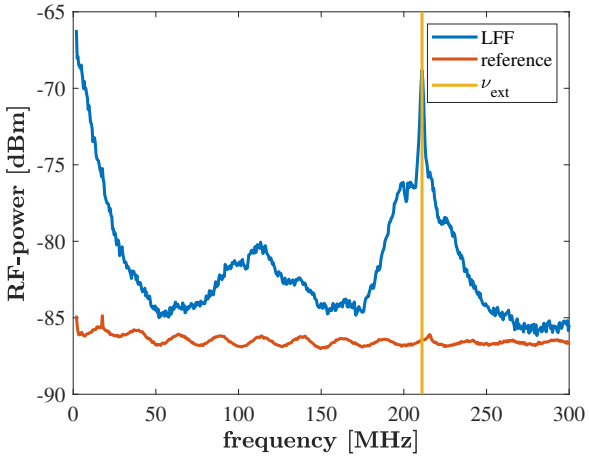

Figure 3.13: Example RF-spectra of the intensity dynamics of the ICL subjected to optical feedback in the LFF regime (blue) and reference (red). The external cavity frequency of $211\,\mathrm{MHz}$, corresponding to an external cavity length of $71\,\mathrm{cm}$ is marked with a vertical yellow line. In this example, where the feedback strength amounts to $71\,\%$ the blue RF-power-spectrum corresponds to the timetrace in Fig. 3.12.

a stable mode again. In analogy to [210] this could mean that beyond that point the systems operates on a so-called high-gain-mode. The evaluation of latter is not within the scope of this thesis and remains open for further investigation.

We conclude that regarding higher-dimensional dynamics, ICLs are quite immune to feedback. This can be mainly explained due to their low LEF. Since we require operation in the weak feedback regime ($C < 1$) for the spectroscopy application based on self-mixing, the finding is quite promising. It means that even relatively strong feedback does not introduce unwanted dynamics that may disturb the measurement. Hence, ICLs represent relatively insensitive MIR SCLs to be used in MIR self-mixing applications.

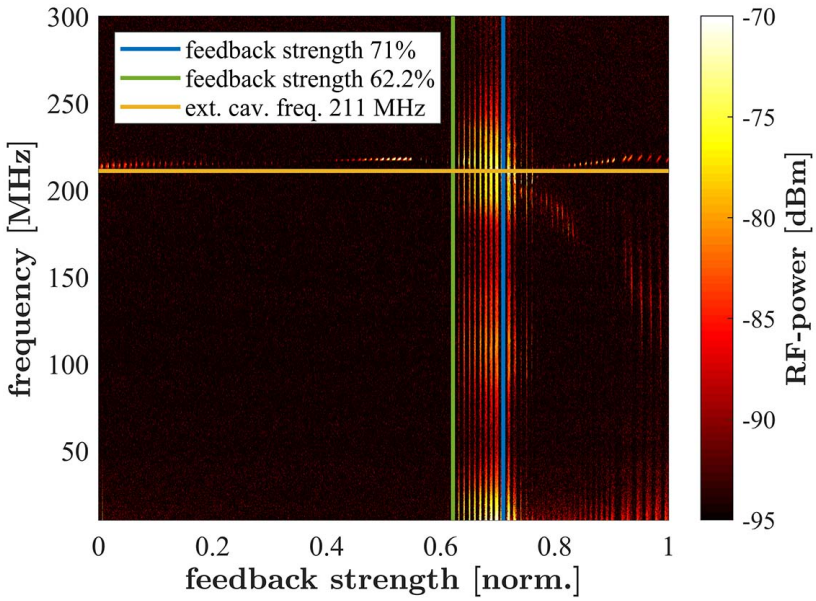

Figure 3.14: RF-power corrected by the reference in the plane of feedback strength and electrical frequency. The blue marked line corresponds to the blue spectrum of Fig. 3.13. The green vertical line marks the minimal feedback strength, where LFFs are observed and the yellow line marks the external cavity frequency of $211\,\mathrm{MHz}$. The driving current amounts to $30.69\,\mathrm{mA}$.

3.6 Evaluation of the laser-as-detector approach for unidirectional injection of coherent light

The investigation of ICLs subjected to feedback provokes the question how the terminal voltage of ICLs react to unidirectional injection of a secondary ICL, which will now be referred to as master. In that case it is possible that light of a different optical frequency is injected. Thus, this section tackles the aforementioned question by a theoretical and experimental analysis of an ICL, the so-called slave, under unidirectional injection by the master. The principle of unidirectional injection, sometimes also referred to as unidirectional coupling, is visualized in Fig. 3.15 with master and slave laser and an optical isolator (ISO) only allowing the light to pass in one direction.

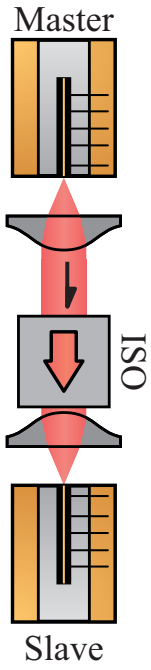

Figure 3.15: Principle of unidirectional injection with master and slave laser and optical isolator (ISO).

In this section, we generally concentrate on the unidirectional injection of coherent light into the slave laser like it is exemplary visualized in Fig. 3.15. Effects caused by the injection of incoherent and broadband light, such as black-body emitters, are not considered here. We also assume that both master and slave are biased above threshold and emit on only one spectral mode, respectively.

For unidirectional injection of monochromatic coherent light, four different scenarios can be distinguished:

1. Injection of light of a wavelength smaller than the slave's wavelength,
2. injection of light of a wavelength longer than the slave's wavelength,
3. injection of light of a very similar wavelength $|\Delta\lambda| \lessapprox 0.5\,\mathrm{nm}$ to $1\,\mathrm{nm}$[6],
4. injection of light of a near, but not very close wavelength $|\Delta\lambda| \gtrapprox 1\,\mathrm{nm}$.

We will later see that the effect in the first two scenarios on the slaves output is negligible and therefore we assume the slave to operate like in solitary mode. We here initially discuss the effects on the optical frequency of the slave laser, while later we describe the effects of scenario 3 and 4 in terms of influence on the terminal-voltage, thus in terms of the applicability of the LAD approach.

[6]The wavelength which are considered to be "very similar" depends on the sample laser. In the case of our sample ICLs "very similar" wavelengths are considered to be approximately $0.5\,\mathrm{nm}$ to $1\,\mathrm{nm}$, depending on the injection strength.

The distance of two lasers wavelength $\Delta\lambda = \lambda_1 - \lambda_2$ is usually converted to the optical frequency detuning (OFD) via

$$\Delta\nu = c\left(\frac{1}{\lambda_1} - \frac{1}{\lambda_2}\right), \tag{3.38}$$

where c is the speed of light and λ_1 is the wavelength of the first and λ_2 the wavelength of the second laser.

Scenario 1: Master wavelength smaller than the slave's wavelength

In the case when light from the master laser at a wavelength smaller than the slave laser is injected into the slave $|\Delta\nu| \gg 1\,\mathrm{nm}$, the photoconduction effect plays the dominant role as discussed in Section 3.1. The external laser injection can thus be seen as a kind of optical pump to the slave laser. Since additional carrier-hole pairs are generated the optical output is amplified with respect to the solitary case. However, terminal voltage and optical power shift only very little when the injection is not extraordinarily strong. Since the change in carrier density also changes the refractive index according to Eq. (3.1), the wavelength of the slave laser will slightly change. When injecting significantly smaller wavelengths into the slave no change of the output can be detected, because the semiconductor material becomes transparent for significantly small wavelengths.

Scenario 2: Master wavelength significantly larger than the slaves wavelength

In the case when the injected wavelength of the laser is larger than that of the slave laser $|\Delta\lambda| \gg 1\,\mathrm{nm}$, none of the previously mentioned effects occur. The radiation will be mainly absorbed directly at the slaves facet and can not enter the whole active region, only generating additional heat. That may generate changes in the refractive index according to Eq. (3.1).

Scenario 3: Very similar wavelengths - optical injection locking

By injecting light from the master at a very similar wavelength $|\Delta\nu| \ll 1\,\mathrm{nm}$ into the slave laser the coupling of the incident optical field $E_{\text{ext}}(t)$ with the slave's optical field $E(t)$ is very strong. A phenomena called optical injection locking (OIL) occurs, which is sometimes only referred to as injection locking. The slave laser's wavelength locks on the master laser's wavelength. This happens when the separation between the optical frequencies of master and slave are in the range of a few gigahertz up to few tens of gigahertz depending on the sample lasers, which we now refer to as locking bandwidth (LBW). In our case the ICLs operate around $3420\,\mathrm{nm}$ and the LBW converts to a locking range in the wavelength domain around $0.5\,\mathrm{nm}$ to $1\,\mathrm{nm}$. The coupling of the two electric fields is sufficiently well described with the rate equations already introduced

in Eqs. (3.16) to (3.18). Here, in contrast to self-mixing we assume $\Delta\nu$ not necessary to be zero. Changes in the optical field inside the slave cavity influences also the quasi-Fermi level separation and therefore the terminal voltage is affected.

Scenario 4: Near, but not very close wavelength

There are two options to achieve OIL. One way is to shift the master laser's optical frequency towards the slave laser's optical frequency, when holding the coupling strength κ constant. When the master laser's optical frequency is near but not yet within the LBW, the optical frequency of the slave laser will be pulled towards that of the master laser. The effect is known as frequency-pulling. The slave laser optical frequency will then lock to the master's at the edge of the LBW. Another way is increasing the coupling strength at fixed optical frequency of the master laser. The optical frequency of the slave laser will initially be pushed away from the masters, but at a certain threshold the slave laser's optical frequency will collapse towards that of the master and lock on that of the master laser [126].

3.6.1 Goals of the section

The objective of the next paragraphs is to create a basis for our precise optical detector-free absorption spectroscopy application utilizing the OIL phenomena in Section 4.7. Therefore, we need to explore the influence of the external injected light onto output and terminal voltage of the slave laser. Thus, our goals for the next sections are fourfold

1. Theoretically discuss the effects of unidirectional injection with focus on the OFD (Subsection 3.6.2).

2. Experimentally verify the model and explore the shape of the optical locking signal and the locking signal in the terminal voltage regarding the optical frequency detuning (OFD) (Subsection 3.6.3)

3. Experimentally investigate the influence of the coupling strength on the carrier density and the optical output power (also discussed in Subsection 3.6.3).

4. Observe the potential for the slave laser to be used in a general LAD application by analyzing the modulation response using the electrical $-3\,\mathrm{dB}$ detection bandwidth of the slave laser as a metric (Subsection 3.6.4).

We close the section with a summary in Subsection 3.6.5.

3.6.2 Theory for unidirectionally injected ICLs

Stationary lasing conditions for the slave ICL can be obtained, when the electrical field amplitude $E_{\text{ext.}}$ in Eq. (3.11) is set constant. Mapping the description in [125] to the case of ICLs, the steady state solutions result in

$$E^2 = \frac{\left(\frac{\zeta J}{q} - \frac{N_{\text{th}}}{\tau_{\text{eff}}} - \Delta N_0\right)}{\frac{1}{\tau_{\text{ph}}} + Zg\Delta N_0} \tag{3.39}$$

$$\Delta N_0 = -2\frac{|\kappa_{\text{inj}}|}{Zg}\frac{E_{\text{ext}}}{E}\cos\left(\phi_{\text{inj}}\right) \tag{3.40}$$

with the relation

$$\nu_{\text{inj}}\left(\phi_{\text{inj}}\right) = \nu_0 - |\kappa_{\text{inj}}|\sqrt{1+\alpha^2}\cdot\sin\left(\phi_{\text{inj}} + \arctan\left(\alpha\right)\right), \tag{3.41}$$

and

$$\Delta N = N_{\text{th}} + \Delta N_0 \tag{3.42}$$

The term N_{th} originates from the solution without injection. Recalling Eq. (3.29), it can implied that

$$\frac{N_{\text{th}}}{\tau_{\text{eff}}} + \frac{|E_0|^2}{\tau_{\text{ph}}} = \frac{\zeta J}{q}. \tag{3.43}$$

The variable N_{th} is the carrier density at threshold and E_0 the characteristic optical field of the steady state (above threshold). ϕ_{inj} is the locked phase of the slave laser relative to that of the master. In the event of frequency locking to the master laser

$$\nu_{\text{inj}}\left(\phi_{\text{inj}}\right) - \nu_0 = \Delta\nu \tag{3.44}$$

applies. Then Eq. (3.41) can be rewritten to

$$\sin\left(\phi_{\text{inj}} + \arctan\left(\alpha\right)\right) = \frac{-\Delta\nu}{|\kappa_{\text{inj}}|\sqrt{1+\alpha^2}} \tag{3.45}$$

Since $-1 \leq \sin\left(\phi_{\text{inj}} + \arctan\left(\alpha\right)\right) \leq 1$ in Eq. (3.45) defines the boundaries of the LBW Ω_{LBW}, which is the OFD domain, where the slave laser's frequency locks to the master laser

frequency. It was found that not all solutions are stable [246] and therefore the OFD must comply with

$$-|\kappa_{\text{inj}}|\sqrt{1+\alpha^2} \leq \Delta\nu \leq |\kappa_{\text{inj}}|\,. \tag{3.46}$$

With that the width of the LBW Ω_{LBW} can be determined by

$$\Omega_{\text{LBW}} = |\kappa_{\text{inj}}| \cdot \left(1+\sqrt{1+\alpha^2}\right) \tag{3.47}$$

Therefore, the LBW depends on the LEF α of the slave laser as well as on the coupling strength $|\kappa_{\text{inj}}| = \dfrac{\kappa}{\tau_{\text{round}}}$. We experimentally verify this relation in the following paragraph.

3.6.3 Influence of injection strength - experiment and comparison with model

We experimentally evaluate the relationship described by Eq. (3.47). Therefore, we utilize the setup, which is schematically depicted in Fig. 3.16. We utilize ICL 2183-22/25 as the master and ICL 2183-10/12 as the slave laser. The experimental operation parameters of both ICLs are summarized in Table 3.1.

Laser	**parameter**	**value**
Master ICL: ICL 2183-22/25	temperature	$29\,°\text{C}$
	mean current	$53.7\,\text{mA}$
	current modulation	$5\,\text{mA}$
	wavelength modulation	$3427.5\,\text{nm}$ to $3428.5\,\text{nm}$
	modulation frequency	$584\,\text{Hz}$
Slave ICL: ICL 2183-10/12	temperature	$20\,°\text{C}$
	current (constant)	$28.1\,\text{mA}$
	wavelength	$3428\,\text{nm}$
	macroscopic distance	$1.5\,\text{m}$
	optical frequency detuning	$-10\,\text{GHz}$ to $10\,\text{GHz}$

Table 3.1: Operation parameters for optical injection locking experiment determining the influence of the injection strength on the locking bandwidth

The time-traces are shown in Fig. 3.17a (top) for the AC-coupled optical signal in terms of detector voltage and in Fig. 3.17b (top) for the by $46\,\text{dB}$ amplified AC-coupled terminal-voltage in a map depiction of OFD and coupling strength. In both figures three example traces are

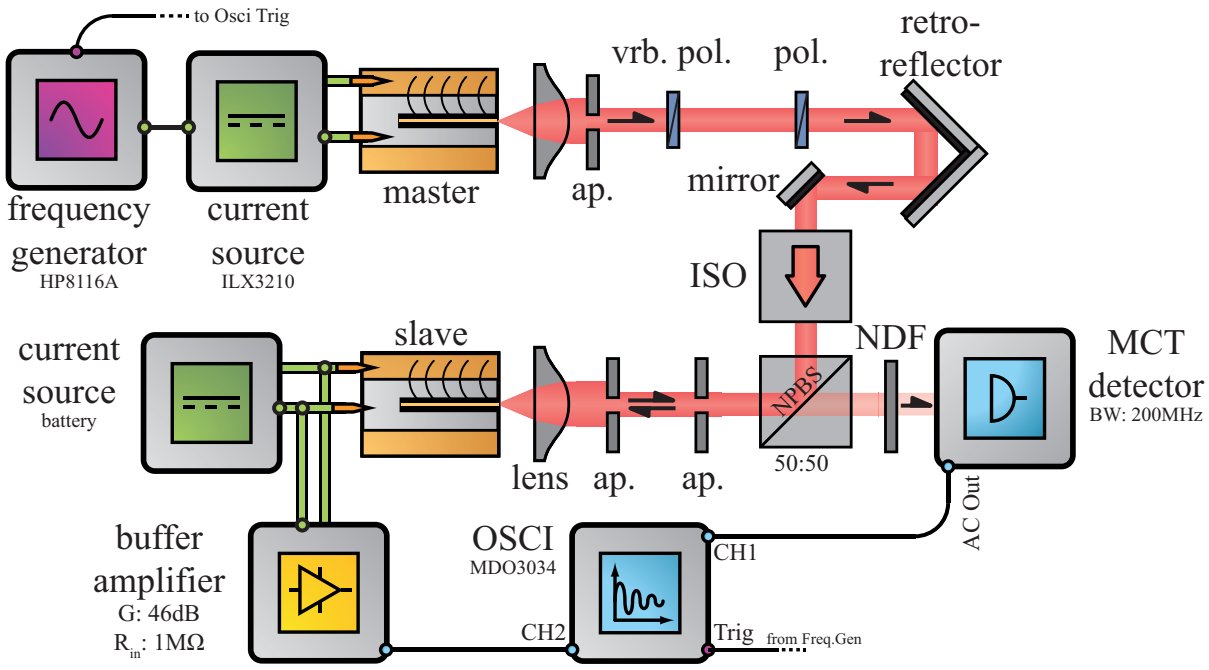

Figure 3.16: Setup for investigation of the influence of coupling strength on terminal voltage and optical output of ICL1 in the unidirectional coupling scenario. The optical setup consists of three apertures (ap.) and 2 lenses, 1 mirror and 1 non-polarizing beam splitter for beam alignment. The variable rotatable polarizer (vrb. pol.) and the polarizer allow continuous attenuation of the coupling strength. The polarizers in front of each ICL also ensure that the incident polarization matches the original polarization of the laser. The optical isolator ensures that the beam can only pass unidirectionally. The non-polarizing beam splitter ensures that the beam of ICL1 is injected into ICL 2, but also allows to investigate the optical power of ICL 2. An neutral density filter (NDF) attenuates the beam of the ICL 2 illuminating the MCT-detector. We record the AC-coupled time traces of the optical power and the by $46\,\mathrm{dB}$ amplified terminal voltage with an oscilloscope.

visualized (bottom), which are marked with a specific color in the map. Since the terminal voltage traces contain noise with high-frequencies components, we added the lowpass filtered signals in purple for better visualization. We determine the lower and upper edges of the LBW using the lowpass filtered terminal voltage timetraces of Fig. 3.17b for each coupling strength. They are displayed as a function of κ in Fig. 3.18a in blue and orange, respectively. The LBW is then calculated by subtracting the distance of the edges, which is then shown in Fig. 3.18b as a function of κ^2. It shall be recalled that κ describes the coupling strength in the electrical field amplitude domain (compare Eq. (3.12)), whereas κ^2 describes the coupling strength in the optical power domain. The latter is more intuitive for the experimenter, since he/she defines his/her coupling strength usually in the power domain.

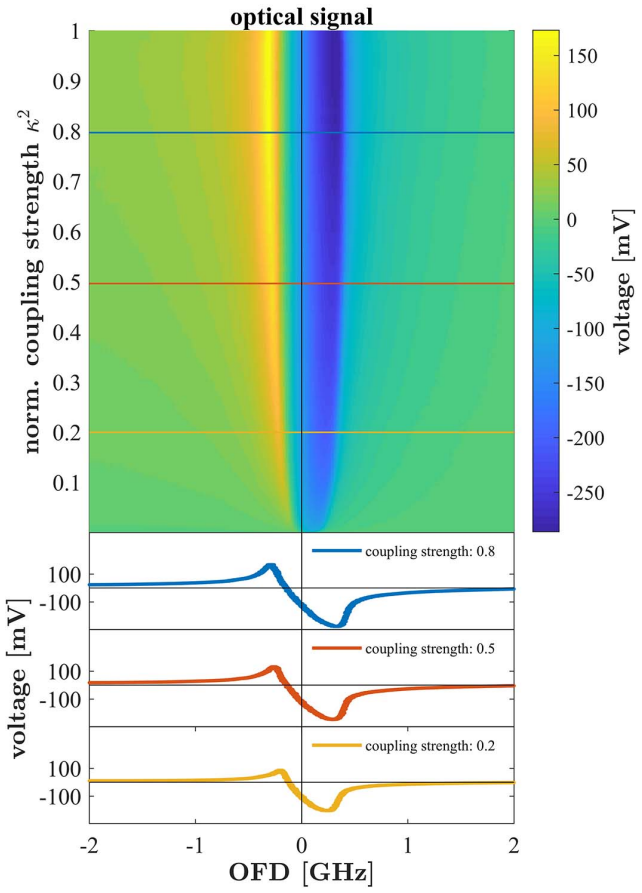

(a) AC-coupled voltage at the optical detector illuminated by the slave laser (proportional to the optical power of the slave laser) in the plane of OFD and coupling strength κ^2 (top), with three example traces with different coupling strenghts marked by different colors (bottom).

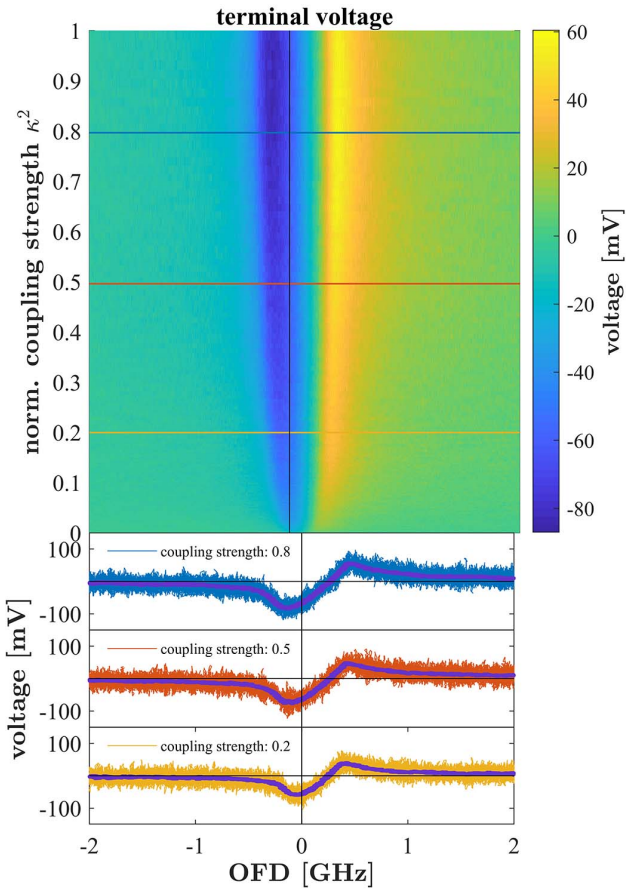

(b) AC-coupled terminal voltage of the slave laser in the plane of OFD and coupling strength κ^2 (top), with three example traces with different coupling strenghts marked by different colors (bottom).

Figure 3.17: (a) Optical and **(b)** terminal voltage signal in the plane of optical frequency detuning (OFD) and coupling strength κ^2 (top), when the optical frequency scanning master ICL is unidirectionally injected into the slave ICL operated with constant bias. Nothe that the coupling strength κ^2 is here described in the power domain. The cross-sections correspond to a normalized coupling strength 0.8 (blue), 0.5 (orange) and 0.2 (yellow).

It can be seen that we obtain similar LBWs when using either terminal voltage (blue) or optical signal (orange) as a basis, which can be seen in Fig. 3.18b. The slight deviation from theory ($\Omega_{\mathrm{LBW}} \propto \sqrt{\kappa^2}$ - green) especially for small coupling strengths may occur due to a non-perfect calibration of the coupling strength provided by the two polarizers. For a good visual comparision, we therefore shifted the theory by $0.26\,\mathrm{GHz}$ to see the agreement. It is assumed

that the polarizers do not provide $100\,\%$ absorption, when both are crossed by $90°$. Nevertheless, the measurement verifies Eq. (3.47), because the LBW is proportional to the coupling strength κ. Thus, a measure was found, which is linearly related to the amount of illuminated radiation. **This finding verifies the feasibility of the LAD approach for unidirectional injection and is of high importance for this thesis.** It enables the spectroscopy application, where we utilize the LBW as a metric for the amount light injected in the slave ICL. The idea is that a gas within the injecting path absorbs the amount of injected light and therefore reduces the LBW, which can be detected utilizing only the terminal voltage of the slave, which will be discussed in Section 4.7.

Another finding in Fig. 3.18a is the symmetrical proportionality of upper and lower edge of the LBW in respect to κ. Remembering Eq. (3.47), we conclude that this is a direct consequence of the low LEF of the ICLs. Indeed we can verify the LEF using the technique described in [173] and [247]. From the ratio of the two slopes for the edges of the LBW, both obtained by a separate linear fit, the LEF of ICL 2183/10-12 is found to be 0.199. The result not only verifies the symmetry of the LBW, it is also in agreement with previously determined LEF for ICL 2183/22-25 in Section 2.9.4.

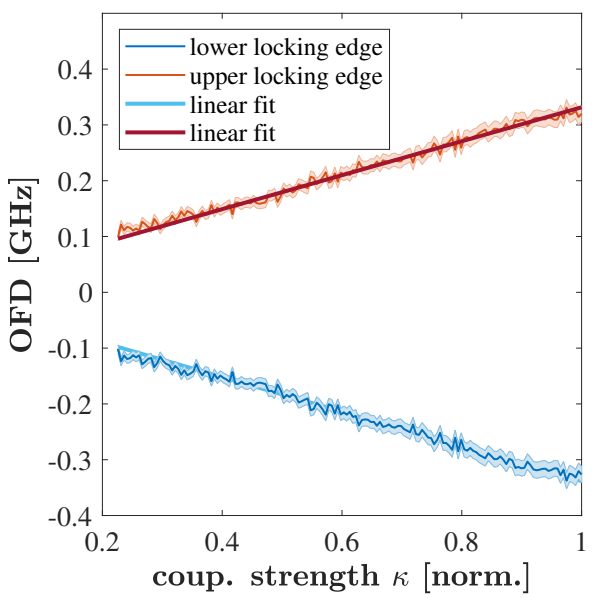

(a) Boundaries of the LBW as a function of normalized coupling strength κ (amplitude domain) taken from the terminal voltage traces. The linear fits are used for evaluation of the LEF.

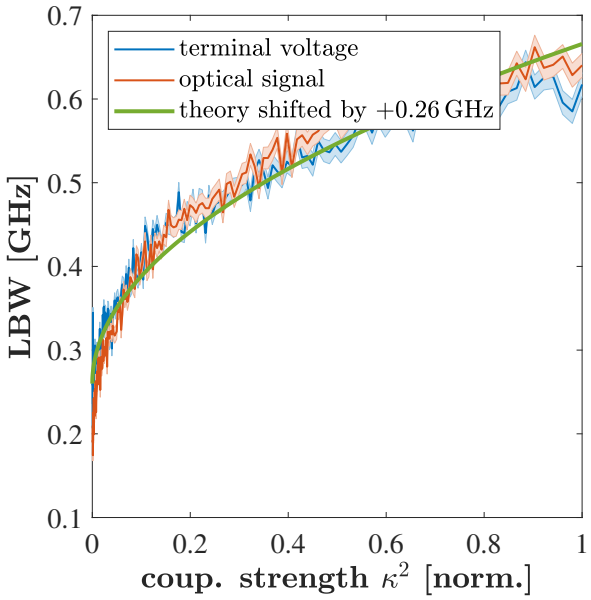

(b) Locking bandwidth (LBW) as a function of the normalized coupling strength κ^2 (power domain).

Figure 3.18: (a) Boundaries of the locking bandwidth (LBW) and (b) LBW as a function of the coupling strength compared with theory.

3.6.4 Influence of the modulation frequency - The electrical detection bandwidth

So far we verified that a forward biased slave ICL can act as a detector in the case of unidirectional injection. It is commonly known that every optical detector possesses an electrical detection bandwidth. Therefore, we experimentally examine relationship between modulation frequency of the master and amplitude of the electrical response of the slave revealing the detection bandwidth of the LAD approach. In order to do so we modulate the master ICL with a fixed electrical amplitude of $-15\,\mathrm{dBm}$ using a bias-tee. We check the power of the electrical response, which is the amplitude of the terminal voltage, of slave laser at this frequency with an electrical spectrum analyzer as a function of the OFD. The setup is schematically visualized in Fig. 3.19.

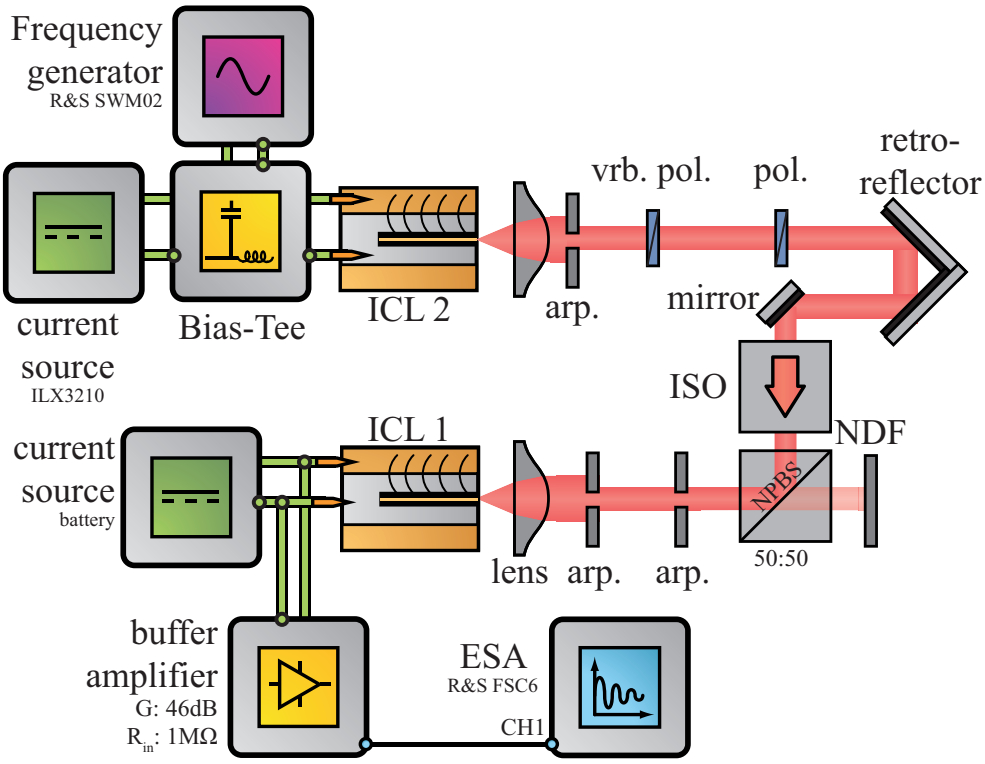

Figure 3.19: Setup to investigate the detection bandwidth of the laser as detector approach for unidirectional OIL. The coupling strength is maximized by aligning both polarizers parallel.

Figure 3.20 shows the RF response power in the plane of OFD and the master lasers modulation frequency. It can be seen that for OFDs outside the LBW (left and right from the green marked locking edges), the electrical response is weaker than within the boundaries. That verifies that to use the LAD approach OIL of the slave to the master ICL is required. Outside the LBW we can see that the LAD approach can be applied for only few OFDs and modulation frequencies. For the major part outside the LBW no significant signal can be detected. We conclude that slave ICL serves as a wavelength-selective detector with an optical bandwidth

corresponding to the width of the LBW. This is a very advantageous feature, because the acceptance wavelengths, i.e. the position of the LBW, can be tuned with the current of the slave ICL. It can be wrongly assumed that the LBW increases with increasing modulation frequency. This misunderstanding is caused by the fact that for increasing modulation frequencies the master laser tunes over a smaller optical frequency range, because the optical modulation bandwidth shrinks. Therefore for higher modulation frequencies the calibration of the OFD axis is no longer valid. The white lines in Fig. 3.20 therefore indicate the real OFD with increasing modulation frequency of the master. A sample response for the case of a OFD amounting to $-1\,\mathrm{GHz}$ is shown in Fig. 3.21.

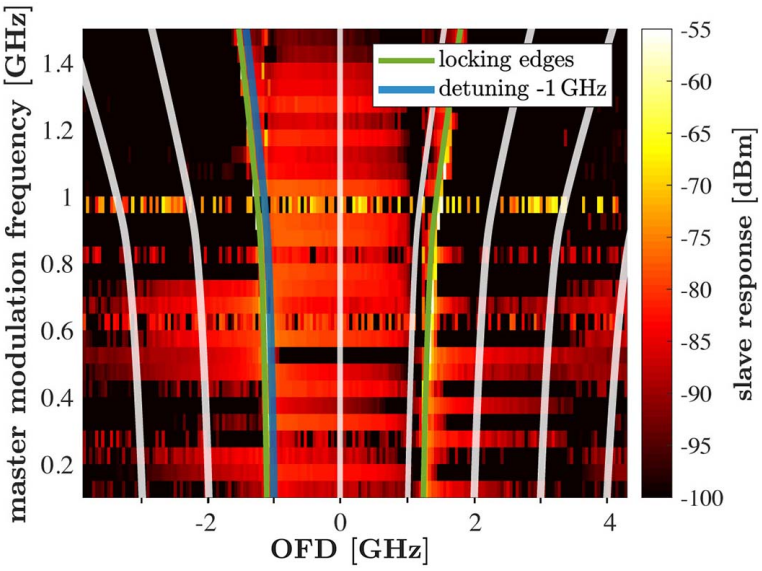

Figure 3.20: Slave lasers amplitude response in the plane of OFD and the master lasers modulation frequency. The edges of the LBW are marked with green. The blue line marks the cross-section in the map, which we exemplary depict in Fig. 3.21. The white lines indicate the OFD with increasing modulation frequency of the master, because for increasing modulation frequency the optical modulation bandwidth of the master laser shrinks and therefore the original OFD calibration is no longer valid.

Figure 3.21 shows that the LAD works for modulation frequencies up to $1.4\,\mathrm{GHz}$, above which no response can be detected. Although the modulation of the master laser's electric signal is $-15\,\mathrm{dBm}$ the electrical signal response is $-80\,\mathrm{dBm}$. As in conventional optical detectors, which usually use a transimpedance amplifier to amplify the small electric currents due to optical illumination, we suggest that the electrical signal of the LAD approach must also finally be amplified if it is to be used in a real application. Nevertheless, we first determine the electrical $-3\,\mathrm{dB}$ bandwidth without amplification. We find that the $-3\,\mathrm{dB}$ electrical bandwidth of our ICL based LAD sensor amounts up to $1.05\,\mathrm{GHz}$. This is a very favorable property, because in the MIR wavelength domain detectors are usually slow - their bandwidth is usually below $200\,\mathrm{MHz}$. Only modern MCT detectors reach bandwidths up to $2.12\,\mathrm{GHz}$[51]. Still they require elaborate

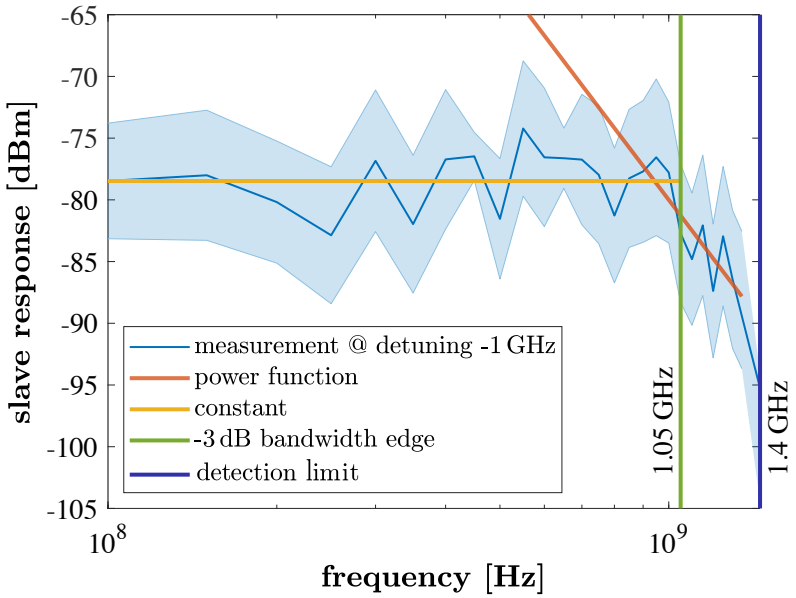

Figure 3.21: Slave lasers electrical amplitude response as a function of the master lasers modulation frequency for a optical frequency detuning (OFD) of $-1\,\mathrm{GHz}$. The master laser is modulated with an electrical amplitude of $-15\,\mathrm{dBm}$.

cooling and additionally need highly specialized electronics. The LAD approach presented here does not require all this and also works at room temperature. It is assumed that with better electrical shielding the electrical bandwidth achieved in this demonstration experiment can be increased significantly.

3.6.5 Summary of the section

We have demonstrated that our LAD approach with ICLS is very well suited for the detection of external coherent radiation. The slave laser serves as a wavelength-selective detector with an optical bandwidth corresponding to the LBW. The width of the LBW, so the optical bandwidth, is proportional to the root of the injected optical power by the master and reaches up to $1.4\,\mathrm{GHz}$ with the ICLs used. The electrical bandwidth ranges from DC to $1.05\,\mathrm{GHz}$, especially when a OFD close to the edge of the LBW is chosen. In this respect the LAD approach is much more performant than most commonly deployed MCT-detectors. It could therefore be used in applications where a high electrical frequency bandwidth is required. This is especially interesting not only in the MIR, but also in the THz spectral range range, where few or no performant detectors exist and it is suitable for applications where a conventional optical detector is not available or needs to be omitted. Also from the cost-perspective the LAD approach offers additional benefits. A second laser that serves as the detector could be easily grown on the same chip as the master laser and thus be produced cost-effectively, which could reduce costs of the whole optical setup.

In general, a big advantage is that the concept is basically independent of the type of SCL. Consequently, the LAD approach could offer a cost advantage in many wavelength ranges - not only the MIR and THz - where the production of fast detectors is cost-intensive or has not been possible yet. The findings will be used to introduce a spectroscopy experiment using the LAD approach in combination with unidirectional injection in Section 4.7. Before that, the LAD approach will be extended in the following section to include bidirectional operation. This will enable further applications that require detection at two spatially separated locations such as bidirectional communication, which we will discuss in Chapter 5.

3.7 Evaluation of the laser-as-detector approach for bidirectional coupling of two ICLs

All physical coupled oscillators and thus also a coupled ICL system are influenced by time delay τ, which is determined by the propagation velocity of the coupling signal and the spatial distance between the oscillators. In many mechanically coupled oscillator the resulting delay is significant smaller than all other typical time scales of the oscillators and therefore can be neglected. Since the ICLs couple via their emitted photons, the speed of light c represents the coupling speed. Together with the spatial optical distance L it specifies the delay time via the term $\tau = \frac{L}{c}$. Figure 3.22 schematically depicts the coupling mechanism of two ICLs. The retarded electrical field amplitude $E^1(t-\tau)$ and the phase $\phi^1(t-\tau)$ of ICL 1 influence their corresponding values in ICL 2, namely $E^2(t)$ and $\phi^2(t)$. Its retarded output again influences E^1, ϕ^1 and so on. Already in this simple thought experiment it becomes obvious that time delay τ is a key parameter significantly influencing the output and the dynamics of the coupled system. In experimental setups the delay is usually lager than the internal time scales, which for our ICLs is in the order of a few nanoseconds (compare Section 2.9.5). It has been found that even for a finite parameter space, delay introduces infinite degrees of freedom, which can lead to - depending on ones perspective - desired or undesired high-dimensional dynamics[248] such as spontaneous symmetry breaking [249] or even chaos [232].

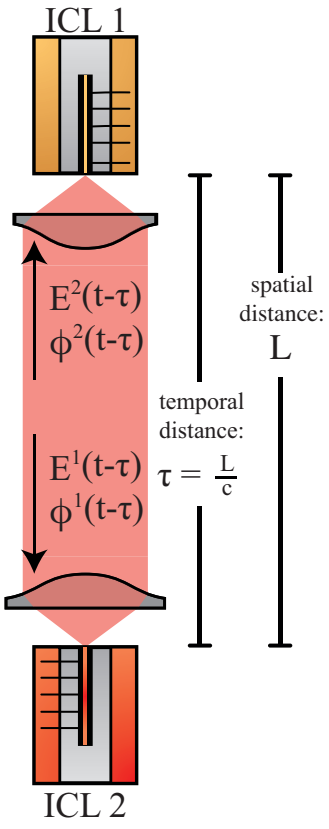

Figure 3.22: Schematic principle of two mutually coupled ICLs. The superscripts 1 and 2 help to distinguish between the electrical field E and phase ϕ of both lasers.

In this thesis we look for deterministic behavior and therefore we avoid high injection strengths or long delay, which both are known to cause undesirable non-deterministic emission[249]. In the regime, where we intend the coupled ICLs to operate, they begin to operate on stable so-called compound laser-states (CLS), which are also often referred to as compound-laser-modes in other literature [250].

Goals of the section

The purpose of this section is to create a basis for our detector-free free-space-optical communication application utilizing the voltage change across two mutually coupled ICLs. Therefore our goals for this section are

1. introduce a theoretical model, which is capable to describe the phenomena, which appear when two ICLs with similar optical frequencies become mutually coupled (Subsection 3.7.1)
2. experimentally detect the effect of the injection strength on the locking signal (Subsection 3.7.2),
3. compare the optical locking signal with the locking signal of the terminal voltage (also discussed Subsection 3.7.2),
4. with that verify the applicability of the theoretical model (Subsections 3.7.2 and 3.7.3),
5. and finally verify the later described reflection symmetry (Subsection 3.7.4).

We close the section with a summary in Subsection 3.7.5.

3.7.1 Rate-equation model for mutually delay-coupled ICLs

A very good foundation for the description of mutually coupled ICLs is provided by an extension of the rate-equation model, which has already been introduced in Eqs. (3.16) to (3.18). The model including the optical perturbation term can easily be extended to describe bidirectional injection, i.e. mutual coupling, of two ICLs. For this purpose two sets of these rate-equations are needed - one for each ICL, both including an external perturbation term. For each ICL the latter is represented by the retarded electric field $\tilde{E}^{k,j}(t-\tau)$ of the other ICL retarded by the delay time τ. Using the SVEA we obtain the rate-equation system for mutually coupled ICLs:

$$\frac{\mathrm{d}\Delta N^1(t)}{\mathrm{d}t} = \frac{\zeta J}{q} - \frac{\Delta N^1(t)}{\tau_{\text{eff}}} - g\cdot\Delta N^1(t)\cdot E^{1*}(t)\,E^1(t)\,, \tag{3.48}$$

$$\begin{aligned}\frac{\mathrm{d}E^1(t)}{\mathrm{d}t} &= \left(Zg\cdot\Delta N^1 - \frac{1}{\tau_{\text{ph}}}\right)E^1(t)\\ &\quad + |\kappa_{\text{inj}}|\,E^2(t-\tau)\,E^1(t)\cos\left(\theta_{\text{inj}} + \left(\phi^2(t-\tau) - \phi^1(t)\right) + 2\pi\Delta\nu t - 2\pi\nu^1\tau\right),\end{aligned} \tag{3.49}$$

$$\begin{aligned}\frac{\mathrm{d}\phi^1(t)}{\mathrm{d}t} &= \frac{\alpha}{2}\left(Zg\cdot\Delta N^1 - \frac{1}{\tau_{\text{ph}}}\right)\\ &\quad + |\kappa_{\text{inj}}|\,\frac{E^2(t-\tau)}{E^1(t)}\sin\left(\theta_{\text{inj}} + \left(\phi^2(t-\tau) - \phi^1(t)\right) + 2\pi\Delta\nu t - 2\pi\nu^1\tau\right)\end{aligned} \tag{3.50}$$

$$\frac{d\Delta N^2(t)}{\mathrm{d}t} = \frac{\zeta J}{q} - \frac{\Delta N^2(t)}{\tau_{\text{eff}}} - g \cdot \Delta N^2(t) \cdot E^{2*}(t) E^2(t), \tag{3.51}$$

$$\begin{aligned}\frac{\mathrm{d}E^2(t)}{\mathrm{d}t} &= \left(Zg \cdot \Delta N^2 - \frac{1}{\tau_{\text{ph}}}\right) E^2(t) \\ &\quad + |\kappa_{\text{inj}}| E^1(t-\tau) E^2(t) \cos\left(\theta_{\text{inj}} + \left(\phi^1(t-\tau) - \phi^2(t)\right) - 2\pi\Delta\nu t - 2\pi\nu^2\tau\right)\end{aligned} \tag{3.52}$$

$$\begin{aligned}\frac{\mathrm{d}\phi^2(t)}{\mathrm{d}t} &= \frac{\alpha}{2}\left(Zg \cdot \Delta N^2 - \frac{1}{\tau_{\text{ph}}}\right) \\ &\quad + |\kappa_{\text{inj}}| \frac{E^1(t-\tau)}{E^2(t)} \sin\left(\theta_{\text{inj}} + \left(\phi^1(t-\tau) - \phi^2(t)\right) - 2\pi\Delta\nu t - 2\pi\nu^2\tau\right)\end{aligned} \tag{3.53}$$

where the superscripts 1 and 2 distinguish between both ICLs. So the first three rate-equations describe ICL 1 and the last three rate-equations describe ICL 2. We highlighted the terms describing mutual coupling in **orange**. It is reminded that the coupling coefficients of the above described equations are given by

$$|\kappa_{\text{inj}}| = \frac{\kappa}{\tau_{\text{round}}}, \tag{3.54}$$

$$\theta_{\text{inj}} = 2\pi\Delta\nu\tau_{\text{round}} + \theta_C, \tag{3.55}$$

where κ denotes the coupling strength in the amplitude domain. These rate-equations represent a set of delay-differential equations (DDEs) quite similar to that of common coupled SCLs[226], but include a parameter for the number of active stages Z. DDEs of common SCLs have been intensively investigated in the past and comprehensive reviews can be found in [251] as well as in [57, 127, 250].

There are two favored options to obtain solutions of the DDEs: Numerical integration or the steady-state approach. The steady state solutions of these DDEs are the so-called compound-laser-states (CLSs).

3.7.1.1 Compound-laser-states

By performing a steady-state analysis of the DDEs (Eqs. (3.48) to (3.53)), one finds that the solutions are described by the compound-laser-states (CLSs) [250], which are of the form

$$\begin{aligned} N^1(t) &= N^1_{\text{CLS}}, \\ E^1(t) &= E^1_{\text{CLS}}, \\ \phi^1(t) &= 2\pi\nu_{\text{op}}t, \\ N^2(t) &= N^2_{\text{CLS}}, \\ E^2(t) &= E^2_{\text{CLS}}, \\ \phi^2(t) &= 2\pi\nu_{\text{CLS}}t + \sigma, \end{aligned} \tag{3.56}$$

Here, $N^j_{\text{CLS}}, E^j_{\text{CLS}}, \phi^j_{\text{CLS}}, \nu_{\text{CLS}}$ and σ are real valued and $E^j_{\text{CLS}} > 0$ with the superscript $j \in [1,2]$ that differentiates between the two ICLs. The term ν_{CLS} describes the frequency of the coupled laser system and will be derived later. It is noted that due to the later described S^1-symmetry only solutions are allowed, where both lasers operate on the same optical frequency, thus CLS represent frequency locked states. There may be a time-independent phase shift σ between the lasers. If the solutions in Eq. (3.56) are inserted in Eqs. (3.48) to (3.53) one obtains a set of 6 coupled nonlinear transcendental equations with no obvious analytical solution. These equations are usually solved by finding the roots using a root-finding algorithm, which finally reveal the $N^j_{\text{CLS}}, E^j_{\text{CLS}}, \phi^j_{\text{CLS}}, \nu_{\text{CLS}}$.

We are not only interested in the CLS, but also the LBW. Therefore, we can find a seventh transcendental equation for calculating the operation frequency, which then gives us the possibility to obtain a term for the estimation of the LBW. In order to find that, we begin again with Eqs. (3.48) to (3.53) and define

$$\mathcal{A}^j \equiv \phi^k(t-T) - \phi^j(t) + 2\pi\left(\nu^k - \nu^j\right)t - 2\pi\nu^k\tau, \tag{3.57}$$

with $k, j \in [1,2]$ for ICL1 and ICL 2 respectively. In case of frequency locking of the two lasers, the system has reached a steady state, for which it can easily be shown that

$$\mathcal{A}^j = -\mathcal{A}^k - 4\pi\nu_{\text{CLS}}\tau, \tag{3.58}$$

where ν_{CLS} is the operation frequency in the locked state. We now introduce the variable

$$\chi(t) \equiv \mathcal{A}^1(t) + 2\pi\nu_{\text{CLS}}\tau \tag{3.59}$$

and replace $\mathcal{A}^2(t)$ by

$$\mathcal{A}^2(t) = -\chi(t) - 2\pi\nu_{\text{CLS}}\tau, \tag{3.60}$$

which is exact in the steady state, but is also assumed to be a good approximation near steady state. In summary we can now express $\mathcal{A}^j$ in Eqs. (3.59) and (3.60) as

$$\mathcal{A}^j = (-1)^{j+1}\chi(t) - 2\pi\nu_{\text{CLS}}\tau. \tag{3.61}$$

With Eq. (3.61) substituted in Eqs. (3.52) and (3.53) and approximating

$$E^k(t-\tau) \approx E^k(t) \tag{3.62}$$

the Eqs. (3.52) and (3.53) are identical in form to the equations for two coupled common semiconductor lasers *without* delay, for which an iterative approach has been developed extensively in [226]. However, in contrast to that it is seen that the role of the delay is to introduce an additional coupling phase $2\pi\nu_{\text{CLS}}\tau$ to the injection phase, which is marked in **orange** in the Eq. (3.63). The operation frequency follows from combining Eq. (3.49) and Eq. (3.50) resulting in the transcendental equation

$$\nu_{\text{CLS}} = \nu^j + \frac{\left|\kappa^j_{\text{inj}}\right|}{2\pi}\sqrt{1+(\alpha^j)^2}\frac{E^k}{E^j}\sin\left(\theta^j_{\text{inj}} - 2\pi\nu_{\text{CLS}}\tau - \arctan\left(\alpha^j\right) + (-1)^k\chi(t)\right). \tag{3.63}$$

Now we can apply the same solution method as in Ref. [226]. It is emphasized that the system in Eqs. (3.48) to (3.50), will lead to exact fixed point solutions corresponding to steady state operation satisfying

$$\frac{E^1}{E^2} = -\frac{2\left|\kappa_{\text{inj}}\right| + (\phi^1 - \phi^2)}{Z^1 g^1 \Delta N^1} \tag{3.64}$$

and

$$\frac{E^2}{E^1} = -\frac{2\left|\kappa_{\text{inj}}\right| + (\phi^2 - \phi^1)}{Z^2 g^2 \Delta N^2} \tag{3.65}$$

However, the dynamics towards these solutions are approximate, such that stable solutions need not necessarily be stable solutions of the exact problem. In contrast, stable solutions of the exact problem will form a subset of the stable solutions of the approximated problem.

Assuming that both lasers are equal in their parameters, which is a good approximation for our twin-ICLs originating from the same waver, we find the LBW according to

$$\Omega_{\text{LBW}} = \pi^{-1} \left|\kappa_{\text{inj}}\right| \sqrt{1+\alpha^2} \left|\cos\left(\theta_C + 2\pi\nu_{\text{CLS}}\tau + \arctan\left(\alpha\right)\right)\right|. \tag{3.66}$$

We see that the delay introduces an effective coupling phase equal to the product of operation frequency ν_{CLS} and delay time τ. The LBW periodically changes when the delay time changes over an interval equal to half of the operation oscillation period. This periodicity is linked to the π and 2π symmetries of this DDE system, which we introduce in the following paragraph.

3.7.1.2 Symmetries of the model

It is known that the model of coupled semiconductor lasers, thus also our model for ICLs, exhibits several symmetries [250]. For a better overview we define the total coupling phase Θ by

$$\Theta \equiv \theta_C + 2\pi\nu_{\text{CLS}}\tau + \arctan\left(\alpha\right). \tag{3.67}$$

S^1-symmetry

Any solution of the equations Eqs. (3.48) to (3.53) is invariant under an arbitrary phase shift b of both electrical fields, representing a S^1-symmetry. This symmetry is important for the later described compound laser state ansatz as a solution for the rate-equations of mutually coupled ICLs.

$$\begin{pmatrix} E^1, \phi^1, \Delta N^1 \\ E^2, \phi^2, \Delta N^2 \\ \Delta\nu \\ \Theta \end{pmatrix} \rightarrow \begin{pmatrix} E^1, \phi^1 + b, \Delta N^1 \\ E^2, \phi^2 + b, \Delta N^2 \\ \Delta\nu \\ \Theta \end{pmatrix} \tag{3.68}$$

Reflection symmetry

Any solution of the equations Eqs. (3.48) to (3.53) is invariant under interchanging both lasers. This invariance can also be interpreted as a point-symmetry with respect to the detuning. If we change the sign of the detuning both lasers exchange all of its physical variables $E, \phi, \Delta N$.

This symmetry is of great importance for our private communication application based on the compound-laser-states.

$$\begin{pmatrix} E^1, \phi^1, \Delta N^1 \\ E^2, \phi^2, \Delta N^2 \\ \Delta\nu \\ \Theta \end{pmatrix} \rightarrow \begin{pmatrix} E^2, \phi^2, \Delta N^2 \\ E^1, \phi^1, \Delta N^1 \\ -\Delta\nu \\ \Theta \end{pmatrix} \tag{3.69}$$

2π translation symmetry

Thirdly, there is a 2π translation symmetry in the feedback phase θ_C.

$$\begin{pmatrix} E^1, \phi^1, \Delta N^1 \\ E^2, \phi^2, \Delta N^2 \\ \Delta\nu \\ \Theta \end{pmatrix} \rightarrow \begin{pmatrix} E^1, \phi^1, \Delta N^1 \\ E^2, \phi^2, \Delta N^2 \\ \Delta\nu \\ \Theta + 2\pi \end{pmatrix} \tag{3.70}$$

1π-translation symmetry

Lastly, there is also a 1π-translation symmetry in the feedback phase θ_C.

$$\begin{pmatrix} E^1, \phi^1, \Delta N^1 \\ E^2, \phi^2, \Delta N^2 \\ \Delta\nu \\ \Theta \end{pmatrix} \rightarrow \begin{pmatrix} E^1, \phi^1, \Delta N^1 \\ -E^2, \phi^2, \Delta N^2 \\ \Delta\nu \\ \Theta + \pi \end{pmatrix} \tag{3.71}$$

The 1π- and 2π-translation symmetries with respect to the total coupling phase Θ is supported by the fact that the LBW is periodic in the delay τ (compare Eq. (3.66)).

After discussing the model theoretically, we experimentally verify its predictions in the following sections. We first evaluate the relation of Eq. (3.66), which describes that the LBW is proportional to the coupling strength κ (in the amplitude domain). Then we check the 1π- and 2π-translation symmetries (Eq. (3.70) and Eq. (3.71)), which together with Eq. (3.66) state that the LBW should change periodically with the delay τ. Finally, we verify the reflection symmetry (Eq. (3.69)).

3.7.2 Influence of coupling strength - Experiment and comparison with model

We experimentally evaluate the relationship described by Eq. (3.66) with respect to the coupling strength. Therefore we utilize the setup, which is schematically depicted in Fig. 3.23. We utilize ICL 2183-22/25 as ICL1 and ICL 2183-10/12 as ICL 2. The operation parameters can be found in Table 3.2.

Laser	parameter	value
ICL 1: ICL 2183-22/25	temperature	$29\,^{\circ}\mathrm{C}$
	mean current	$53.7\,\mathrm{mA}$
	current modulation	$5\,\mathrm{mA}$
	wavelength modulation	$3427.5\,\mathrm{nm}$ to $3428.5\,\mathrm{nm}$
	modulation frequency	$584\,\mathrm{Hz}$
ICL 2: ICL 2183-10/12	temperature	$20\,^{\circ}\mathrm{C}$
	current (constant)	$28.1\,\mathrm{mA}$
	wavelength	$3428\,\mathrm{nm}$
	coupling strength	variable
	macroscopic distance	$1.5\,\mathrm{m}$
	optical frequency detuning	$-10\,\mathrm{GHz}$ to $10\,\mathrm{GHz}$

Table 3.2: Operation parameters for mutual coupling experiment determining the influence of the injection strength on the locking bandwidth

ICL1 is constantly operated at a specified current and thus at a fixed wavelength. ICL 2 scans its wavelength across the wavelength of ICL1. We convert the time-axis to an OFD via the reference measurements described in Section 2.9.2.

The traces are shown in Fig. 3.24a (top) for the AC-coupled optical signal in terms of detector voltage and in Fig. 3.24b (top) for the by $46\,\mathrm{dB}$ amplified AC-coupled terminal-voltage in the map of frequency detuning and coupling strength. In both figures three example traces are visualized (bottom), whose cross-sections are marked with a specific color in the map. Since the terminal voltage traces contain noise with high-frequencies components, we added the lowpass filtered signals in purple for better visualization in Fig. 3.24b.

Both signals show plateaus with respect to the detuning. This is in contrast to the traces in the case of unidirectional OIL, where we obtain continuous traces. We conclude that every step within the locking region corresponds to a stable mode of the delay-coupled ICL system, each resembling a specific CLS. Unfortunately, we are not able to perform an experimental analysis of the optical spectra within the LBW, because no spectrometer with required resolution is available. It is believed that the mode-separation of two consecutive CLS is in the range of the external cavity frequency amounting in our case to $\nu_{\mathrm{ext}} = \frac{c}{2L} = 96\,\mathrm{MHz}$. To obtain a comprehensive insight into the spectrum within the LBW a spectrometer with a resolution

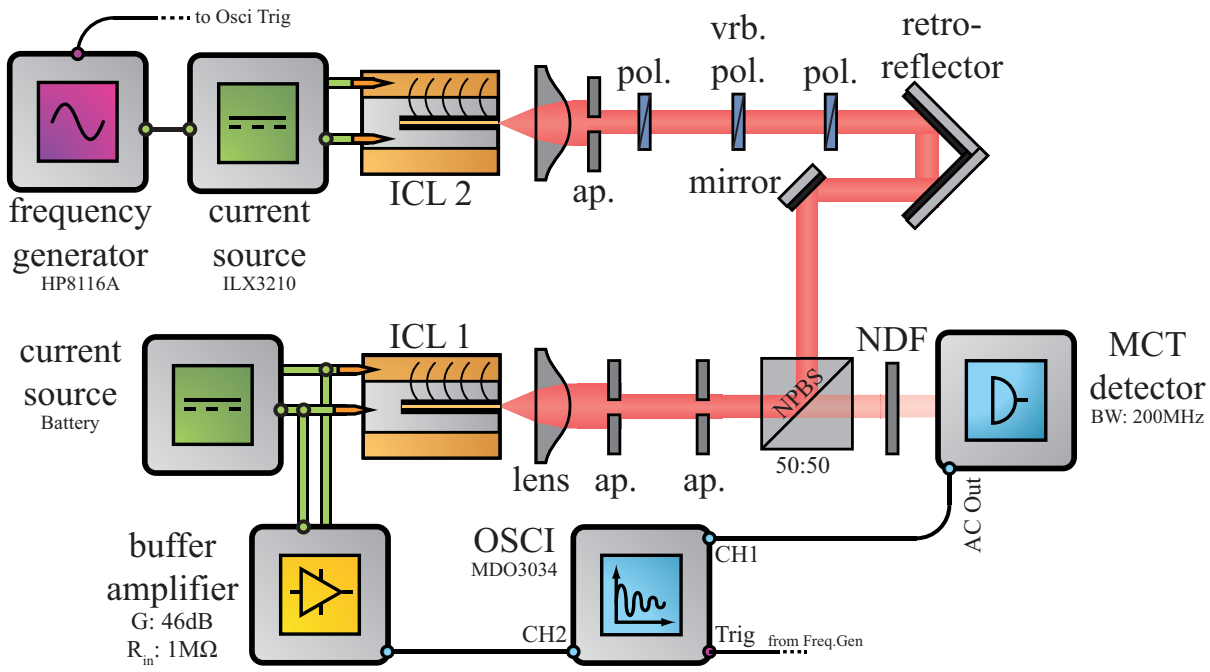

Figure 3.23: Setup for investigating the influence of coupling strength on terminal voltage and optical output of ICL1 in the bidirectional coupling scenario. The optical setup consists of three apertures (ap.) and two lenses, one mirror and a non-polarizing beam splitter for beam alignment. The variable rotatable polarizer (vrb. pol.) and the two fixed polarizers (pol.) allow continuous attenuation of the coupling strength via the law of Malus. The polarizers in front of each ICL also ensure that the incident polarization matches the original polarization of the laser. The non-polarizing beam splitter ensures that the beam of ICL1 is injected into ICL 2, but also allows to investigate the optical power of ICL 2. A neutral density filter (NDF) attenuates the beam of the ICL 2 illuminating the MCT-detector. We record the AC-coupled time traces of the optical power and the by $46\,\mathrm{dB}$ amplified terminal voltage with an oscilloscope. It is noted that in contrast to Fig. 3.16 this setup does not include an optical isolator.

greater than the external cavity frequency would be required. The used Bruker Vertex 80V offers a spectral resolution of $0.075\,\mathrm{cm}^{-1}$ or $2.4\,\mathrm{GHz}$ and is therefore not suitable. A measurement could be performed with a scanning Fabry-Perot spectrometer, but all commercially available products do not offer high enough finesse to achieve this resolution.

In Fig. 3.25a and Fig. 3.25b we compare the experimental traces at a normalized coupling strenght of 0.8 Fig. 3.24a and Fig. 3.24b with numerical integrations of the DDEs Eqs. (3.48) to (3.53) using the solving algorithm described in Eqs. (3.19) to (3.21).[7] The parameters used for the numerical integration are summarized in Table 3.3.

[7]The full MATLAB®-Code of the simulation can be reviewed in the appendix of this thesis

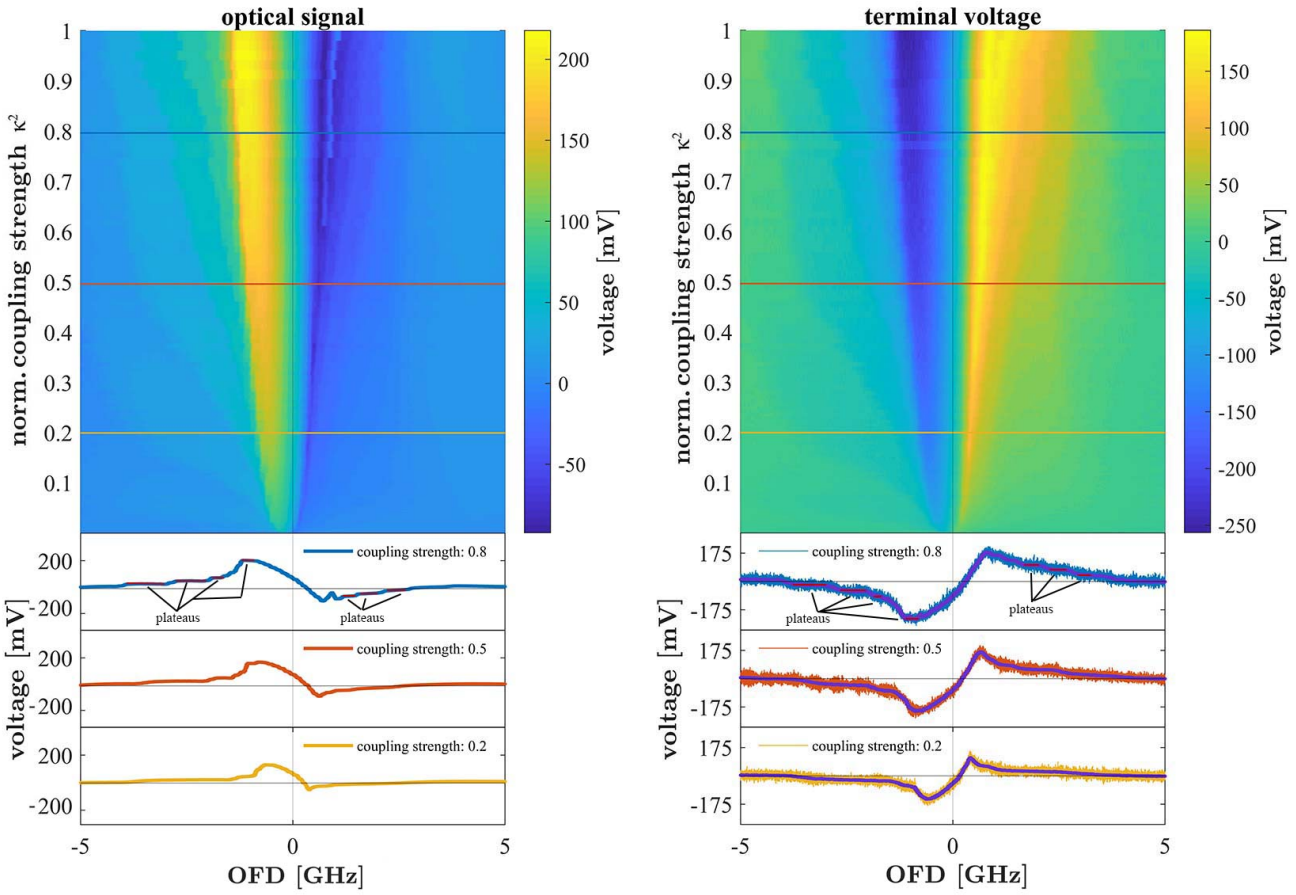

(a) AC-coupled voltage of the optical detector illuminated by ICL 2 (proportional to the optical power of ICL 2) in the plane of detuning and coupling strength, with three example traces with different coupling strenghts marked by different colors.

(b) AC-coupled terminal voltage of ICL 2 in the plane of detuning and coupling strength, with three example traces with different coupling strenghts marked by different colors.

Figure 3.24: (a) Optical and (b) terminal voltage signal in the plane of detuning and coupling strength (top), when the optical frequency scanning master ICL is bidirectionally coupled to ICL 2 operated with constant optical frequency. The cross-sections (top) corresponding to a normalized coupling strength 0.8 (blue), 0.5 (red) and 0.2 (yellow) are separately depicted at the bottom of the figures. The red "plateaus" in the traces for a coupling strength of 0.8 (blue traces) shall exemplary indicate that the signals show a step like shape.

The qualitative agreement of numerical integration and experiment in Figs. 3.25a and 3.25b is good and reveals a coupling phase of $\theta_c = \frac{3}{8}$ as well as a coupling strength κ_{model} of 0.16. It must be noted that the experimental coupling strength of 0.8 is normalized to the experimental maximum and that relative value is not comparable with the absolute theoretical coupling strength. The step-like shape has not been reproduced by the simulation, because the delay was chosen to be $0\,\text{s}$ to obtain the results a reasonable computation time. Nevertheless, with the

set of parameters for numerical integration

parameter	symbol	value
number of cascades	Z	3
photon lifetime	τ_{ph}	$7.02\,\text{ps}$
effective carrier lifetime	τ_{eff}	$3\,\text{ns}$
gain parameter	g	$1.4 \times 10^4\,\text{s}^{-1}$
laser cavity roundtrip time	τ_{round}	$24.01\,\text{ps}$
current injection efficiency	ζ	1
injection current	J	$24\,\text{mA}$
delay	τ	0
linewidth enhancement factor (LEF)	α	0.2
transmission coefficient	t_{abs}	0.16
phase shift	$\arg(\theta_{\text{c}})$	$\frac{3}{8}$
solitary optical frequency of QCLs	ν^1 ν^2	variable $92.815\,\text{THz}$
frequency detuning	$\Delta\nu = \nu^1 - \nu^2$	$-9\,\text{GHz}$ to $9\,\text{GHz}$

Table 3.3: ICL parameters and their values for time integration. Symbols with superscripts label the value for one particular ICL. Symbols without superscript hold for both ICLs.

good reproduction of the experimental results, we verified that our model is qualitatively able to describe carrier density and optical output power in mutual coupled operation. [8]

Because of that good agreement we verify the steady-state theory prediction in Eq. (3.66), i.e. $\Omega_{\text{LBW}} \propto \kappa$. Remember that κ describes the coupling strength in the amplitude domain. From the viewpoint of the coupling strength described in the power domain κ^2, it predicts that the LBW is proportional to $\sqrt{\kappa^2}$. The verification process is done as followed: We verify the models predictions by determining the lower and upper edges of the LBW using the lowpass filtered terminal voltage time traces of Fig. 3.24b for each coupling strength κ^2 (power domain). They are displayed as a function of coupling strength (amplitude domain) in Fig. 3.26a in blue and orange, respectively. The LBW is then derived by calculating the distance between the edges,

[8] Simulations are accelerated by taking advantage of the Lichtenberg Cluster at the TU Darmstadt. To produce a single time trace one core of an Intel® Xeon® Processor E5-2670 CPU needs approx. $1\,\text{s}$ using a self-written Matlab® script. The mean of the last 10000 values of each time trace are finally interpreted as the value of convergence and are plotted in Figs. 3.25a and 3.25b for several different detunings ultimately resulting in the orange line. The overall time to compute a single numerical integration including all detunings takes approx. $201\,\text{s}$.

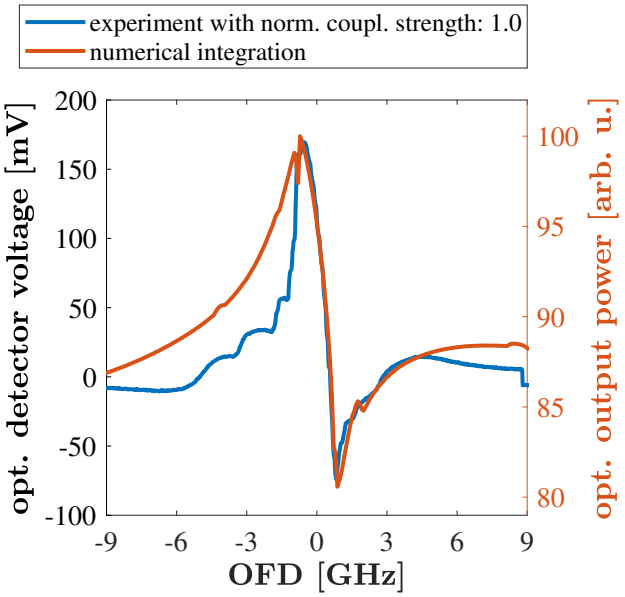

(a) Experimental signal from the optical detector (blue - left scale) for maximum coupling strength vs. OFD output power vs OFD obtained by the numerical integration (orange - right scale).

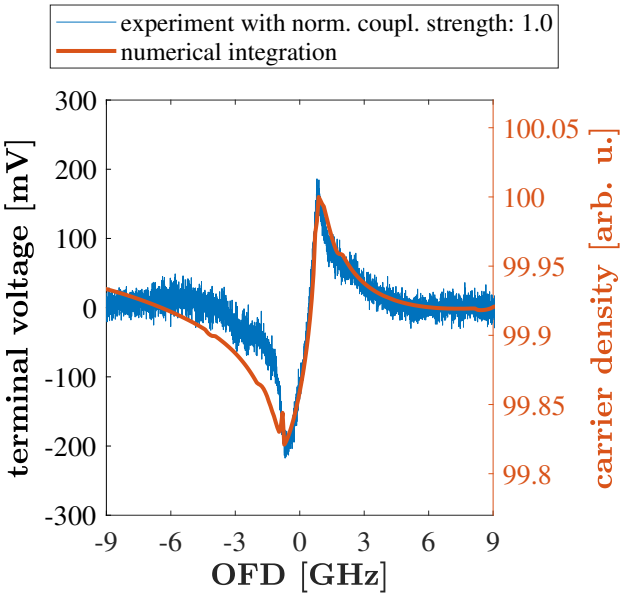

(b) Experimental signal from the terminal voltage for maximum coupling strength vs. OFD (blue - left scale) and carrier density vs. OFD obtained by the numerical integration (orange - right scale). The comparison of terminal voltage and carrier density is reasonable, because according to Section 3.1 they are linearly connected.

Figure 3.25: Comparison of experimental coupling signals (blue) as a function for optical frequency detuning (OFD) with numerical integration simulations (orange).

which is then shown in Fig. 3.26b as a function of coupling strength κ^2 (power domain). It can be seen that we obtain similar LBWs when using either terminal voltage (blue) or optical signal (orange) as basis. The deviation from theory especially for small coupling strengths may occur due to a non-perfect calibration of the coupling strength provided by the two wire grid polarizers. Therefore we shift the theoretical LBW in Fig. 3.26b by $0.35\,\mathrm{GHz}$ to properly see the qualitative influence of the coupling strength. It is reasonable that the polarizers do not provide $100\,\%$ absorption, when both are crossed by $90°$.

Considering the influence of the coupling strength, the good agreement of theory and experimental results Fig. 3.26b shows that the model is well-suited to reproduce experimental results. In the next paragraph we tackle the question whether the model also correctly predicts the influence of the delay.

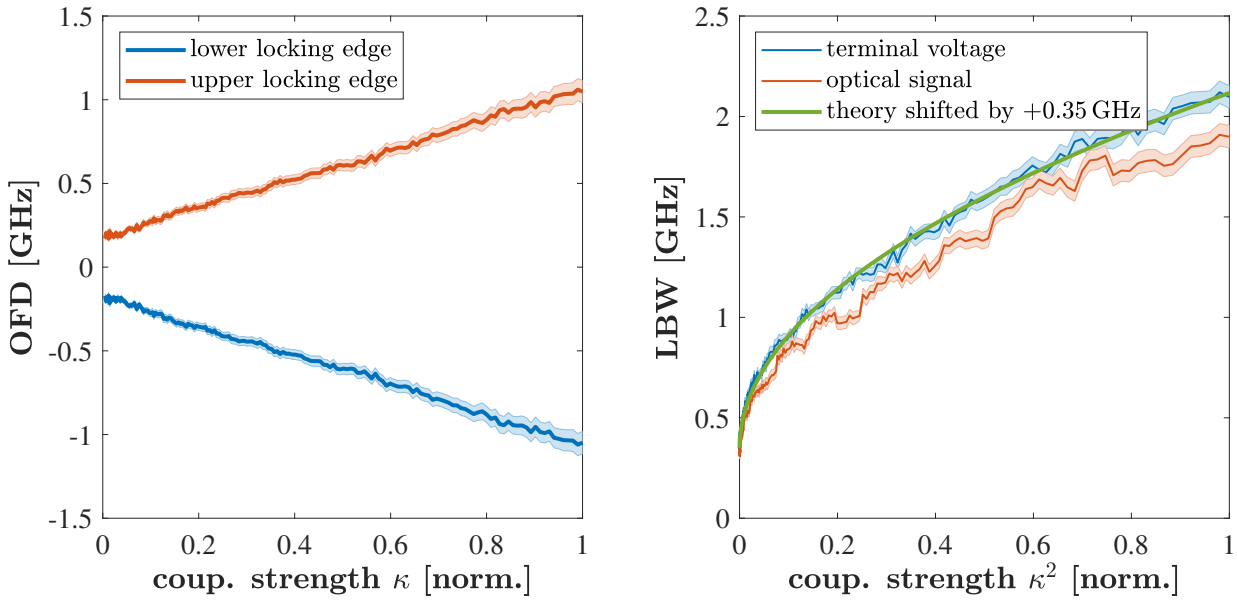

(a) Boundaries of the LBW as a function of normalized coupling strength κ (amplitude domain) taken from the terminal voltage traces.

(b) Locking bandwidth (LBW) as a function of the normalized coupling strength κ^2 (power domain). Theory (green) is simulated according to Eq. (3.66).

Figure 3.26: Locking bandwidth (LBW) and boundaries as a function of the coupling strength a) coupling strength in the amplitude domain b) coupling strength in the optical power domain.

3.7.3 Influence of microscopic delay - Experiment and comparison with model

We experimentally evaluate now the relationship described by Eq. (3.66) considering the influence of delay τ. The model predicts that the LBW periodically changes with the delay with a periodicity of $\nu_{\mathrm{CLS}}\tau$. Therefore we utilize the setup, which is schematically depicted in Fig. 3.27. We utilize ICL 2183-22/25 as ICL 1 and ICL 2183-10/12 as ICL 2. The operation parameters can be found in Table 3.4.

ICL 2 is constantly operated at a specified wavelength. ICL 1 scans its wavelength across the wavelength of ICL 2. ICL 1 laser is therefore injected by an amplitude modulated current source using a triangular signal. The optical setup contains of three apertures for beam alignment. The retroreflector can be moved with a piezo electrical stage to introduce additional microscopic delay. The non-polarizing beam splitter ensures that the beam of ICL 1 is injected into ICL 2, but also allows to investigate the optical power of ICL 2. An neutral density filter (NDF) attenuates the beam of the slave laser illuminating the MCT-detector to avoid saturation. We record the AC-coupled timetraces of the optical power and the by $46\,\mathrm{dB}$ amplified terminal voltage with an oscilloscope. The time is converted to an OFD via the reference measurements of the wavelength

Laser	parameter	value
ICL 1: ICL 2183-22/25	temperature	$29\,°C$
	mean current	$53.7\,mA$
	current modulation	$5\,mA$
	wavelength modulation	$3427.5\,nm$ to $3428.5\,nm$
	modulation frequency	$584\,Hz$
ICL 2: ICL 2183-10/12	temperature	$20\,°C$
	current (constant)	$28.1\,mA$
	wavelength	$3428\,nm$
	coupling strength	fixed (maximum, which can be achieved)
	macroscopic distance	$1.5\,m$
	microscopic distance	$0\,\mu m$ to $2.5\,\mu m$
	optical frequency detuning	$-10\,GHz$ to $10\,GHz$

Table 3.4: Operation parameters for mutual coupling experiment determining the influence of the delay on the locking bandwidth

in Section 2.9.2. Without loss of generality we set the microscopic delay in Fig. 3.28 to be $0\,ps$ delay. The macroscopic delay length still amounts to $1.5\,m$ converting to a temporal delay of $5\,ns$.

The experimentally obtained traces are shown in Fig. 3.28a (top) for the AC-coupled optical signal in terms of detector voltage and in Fig. 3.28b (top) for the by $46\,dB$ amplified AC-coupled terminal-voltage in the map of frequency detuning and delay length. In both figures three example traces are visualized (bottom) corresponding to a microscopic delay length of $2032\,nm$, $1244\,nm$ and $380\,nm$, whose cross-sections are marked with a specific color in the map. Since the terminal voltage traces contain noise with high-frequencies components, we added the lowpass filtered signals in purple for better visualization in the three lower parts of Fig. 3.28b.

Surprisingly, it is revealed that the delay shows *no* influence on our experiment, because all three traces are identical. This experimental finding contradicts with the derivation in Eq. (3.66). Hence, one could presume that the theory is not valid. We check this apparent contradiction with the simulation. Therefore, we numerically integrate the DDEs described in Eqs. (3.48) to (3.53) for two macroscopic delay regimes, short ($3\,ps$) and long ($5\,ns$) delay, as a function of an additional microscopic delay τ_{mic}, with the parameters found in Table 3.5.

In Fig. 3.29a we visualize the results of the numerical integration short macroscopic delay $3.34\,ps$ as a function of the dimensionless additional phase, which is introduced by the microscopic delay via $2\pi\nu\tau_{\text{mic.}}$. The subfigure 3.29a shows the difference of the optical frequencies of ICL 1 and ICL 2, i.e. $|\nu_1 - \nu_2|$ in the plane of OFD and additional phase, which is introduced by the microscopic delay. From that we calculate the LBW which is shown in Fig. 3.29b. We reasonably consider both simulated ICLs to operate within the LBW, when $|\nu_1 - \nu_2| < 100\,kHz$. The steady-state solution Eq. (3.66) predicts that the LBW is proportional to $|\cos(2\pi\nu\tau + c.)|$ with delay independent, thus constant values $c.$. Figure 3.29b verifies this

set of parameters for numerical integration

parameter	**symbol**	**value**
number of cascades	Z	3
photon lifetime	τ_{ph}	$7.02\,\text{ps}$
effective carrier lifetime	τ_{eff}	$3\,\text{ns}$
gain parameter	g	$1.4 \times 10^4\,\text{s}^{-1}$
laser cavity roundtrip time	τ_{round}	$24.01\,\text{ps}$
current injection efficiency	ζ	1
injection current	J	$24\,\text{mA}$
macroscopic delay	τ	short $3.34\,\text{ps}$ and long $5\,\text{ns}$
microscopic delay	τ_{mic}	variable
linewidth enhancement factor (LEF)	α	0.2
transmission coefficient	t_{abs}	0.16
phase shift	$\arg(\theta_{\text{c}})$	0
solitary optical frequency of QCLs	ν^1 ν^2	variable $92.815\,\text{THz}$
frequency detuning	$\Delta\nu = \nu^1 - \nu^2$	$-12.5\,\text{GHz}$ to $12.5\,\text{GHz}$

Table 3.5: ICL parameters and their values for time integration to observe the influence of delay. Symbols with superscripts label the value for one particular ICL. Symbols without superscript hold for both ICLs.

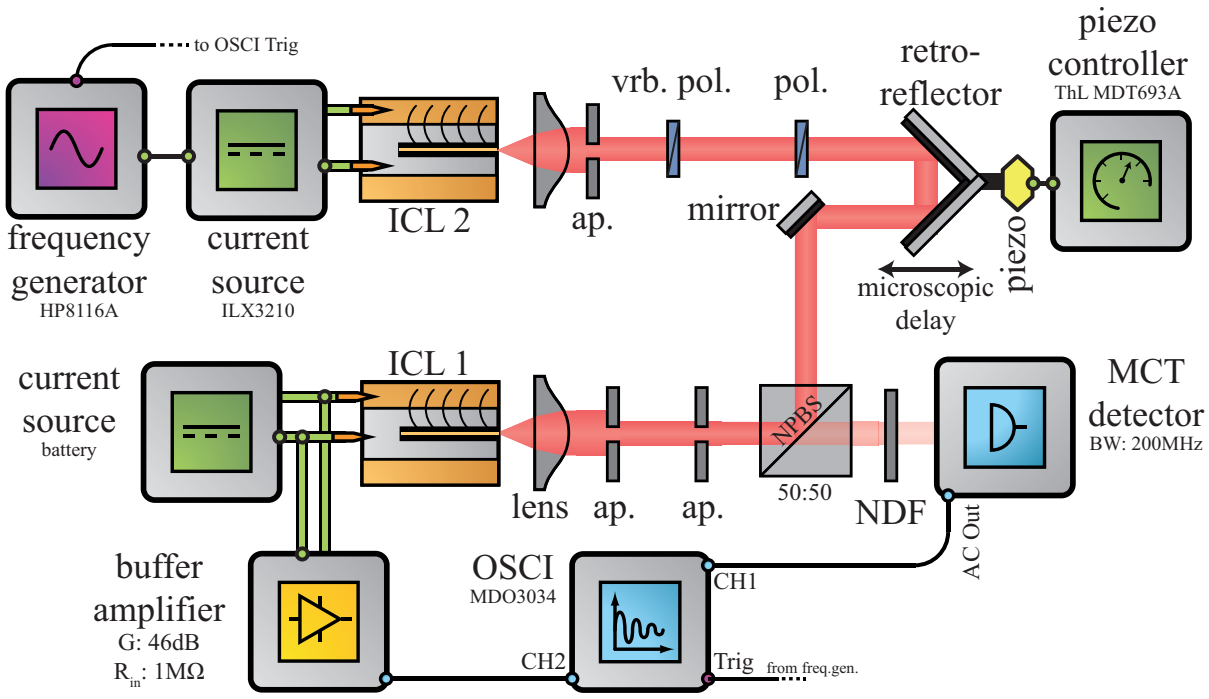

Figure 3.27: Setup for investigating the influence delay on terminal voltage and optical output of ICL 1 in the bidirectional coupling scenario. The optical setup consists of three apertures (ap.) and 2 lenses, 1 mirror and 1 non-polarizing beam splitter for beam alignment. The retro reflector can be moved microscopically to change the microscopic delay length. The macroscopic delay length amounts to $1.5\,\mathrm{m}$. The variable rotatable polarizer (vrb. pol.) and the polarizer allow continuous attenuation of the coupling strength, but remain at the same position for the whole measurement. The polarizers in front of each ICL also ensure that the incident polarization matches the original polarization of the laser. The non-polarizing beam splitter ensures that the beam of ICL 1 is injected into ICL 2, but also allows to investigate the optical power of ICL 2. An neutral density filter (NDF) attenuates the beam of the ICL 2 irritating the MCT-detector. We record the AC-coupled time traces of the optical power and the by $46\,\mathrm{dB}$ amplified terminal voltage with an oscilloscope.

prediction. Therefore steady-state theory holds for short macroscopic delays. The Fig. 3.29d also show the optical power of ICL 1 and Fig. 3.29c depict the carrier density (proportional to the terminal voltage) also of ICL 1. It is confirmed that the aforementioned periodicity is also evident in these physical variables, which confirms the 2π- and 1π-translation symmetry introduced Eqs. (3.70) and (3.71). This is in contrast to our measurements, where we found that neither optical power nor terminal voltage change with additional introduced delay (compare Fig. 3.28).

Therefore, we redo the simulation, but implement large macroscopic delays, where we exemplified this large delay with a macroscopic delay length of $5\,\mathrm{ns}$ resembling a macroscopic

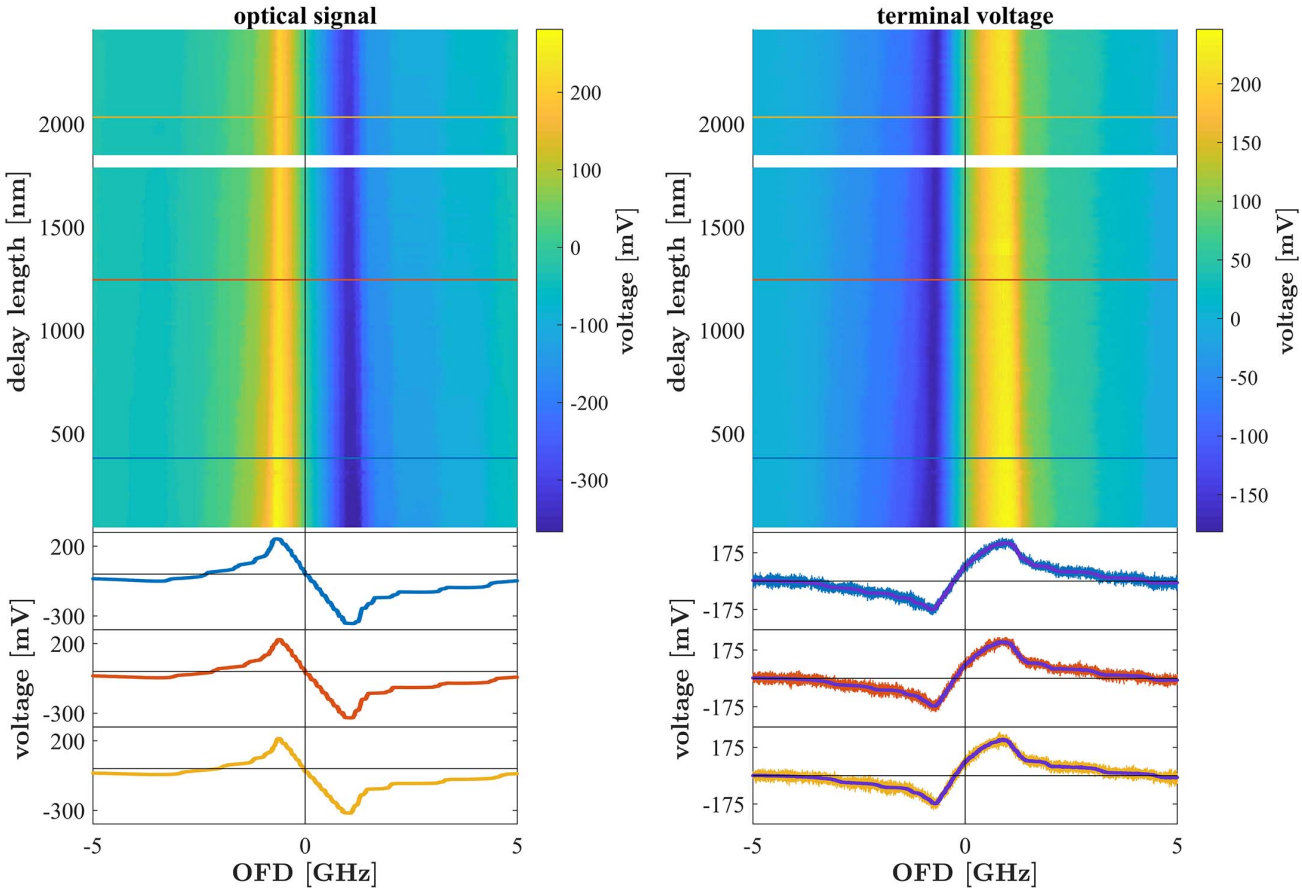

(a) AC-coupled voltage at the optical detector illuminated by ICL 2 (proportional to the optical power of ICL 2) in the plane of detuning and coupling strength, with three example traces with different coupling strenghts marked by different colors.

(b) AC-coupled terminal voltage of ICL 2 in the plane of detuning and coupling strength, with three example traces with different coupling strenghts marked by different colors.

Figure 3.28: (a) Optical and (b) terminal voltage signal measurements in the plane of detuning and microscopic delay length, when the wavelength scanning ICL 1 is bidirectionally injected into the ICL 2 operated with constant bias. The whole microscopic delay length range corresponds to an additional coupling phase range from 0 to 1.5π. The shown cross-sections correspond to a microscopic delay $2032\,\mathrm{nm}$ (blue), $1244\,\mathrm{nm}$ (red) and $380\,\mathrm{nm}$ (yellow) corresponding to an additional coupling phase of 1.22π, 0.75π and 0.23π respectively. The white areas in both plots mark areas, where no data has been collected due to a software error.

distance of $150\,\mathrm{cm}$. The results in Fig. 3.30 are shown as a function of the dimensionless additional phase, which is introduced by the microscopic delay via $2\pi\nu\tau_{\text{mic.}}$. The subfigure 3.30a shows the difference of the optical frequencies of ICL 1 and ICL 2, i.e. $|\nu_1 - \nu_2|$ in the plane of OFD and additional phase. The corresponding LBW is then shown in Fig. 3.29b. In contrast to short delay, the, by the steady-state theory predicted proportionality to $|\cos(2\pi\nu\tau + c.)|$ is no longer valid for large delays. This contradiction to steady-state theory can be explained by the assumption we introduced in Eq. (3.62), where we assumed that the electrical field amplitude between both lasers is transferred without retardation. This assumption is no longer valid for long delays and therefore the 2π- and 1π-translation symmetries with respect to the coupling phase are broken. The results of the numerical integration for carrier density and optical power in Figs. 3.30c and 3.30d strongly support the experimental findings in Fig. 3.28, that in the long macroscopic delay regime, microscopic delay has no major influence on the OIL characteristics.

From a theorist's perspective it can be concluded that for the case of large delay it is beneficial to perform numerical integration rather than utilizing the steady-state approach. From an experimental point of view, this finding is of great importance for every experimental setup based on mutual coupling. It demonstrates the insensitivity of these application to small variations of the distance, which could be e.g. caused by vibrations. In fact the proposed communcation scheme described in the last chapter of this thesis strongly profits from this insensitivity.

Since we found, that the 2π and 1π-translation symmetry are no longer valid for long macroscopic delays, we lastly want to experimentally test the validity of the reflection symmetry in the long delay scenario. This reflection symmetry will be the basis for the bidirectional communication scheme discussed in Chapter 5.

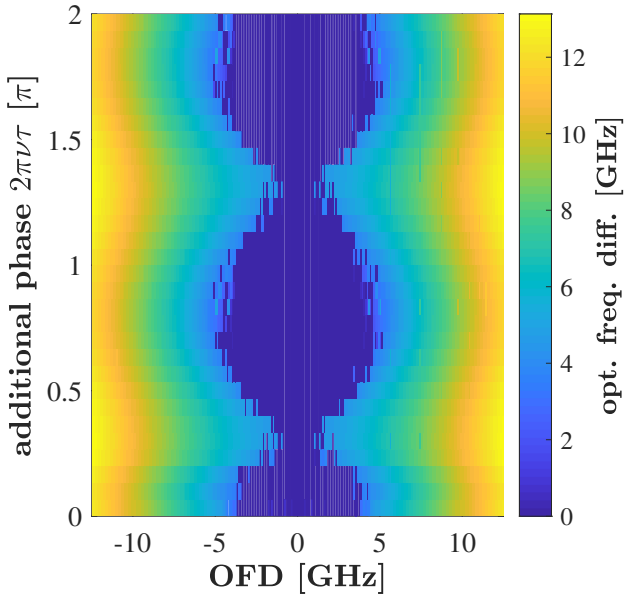

(a) Optical frequency difference of both ICLs in the plane of OFD and delay phase

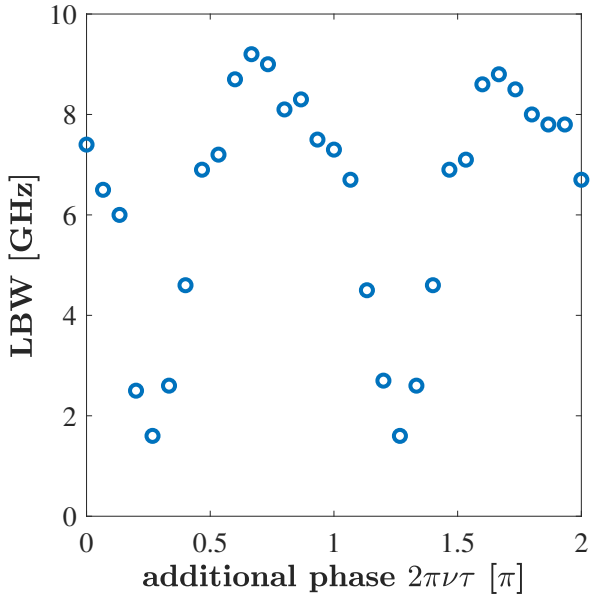

(b) LBW as a function of delay phase obtained using the results shown in Fig. 3.29a. We reasonably consider both simulated ICLs to operate within the LBW, when $|\nu_1 - \nu_2| < 100\,\mathrm{kHz}$.

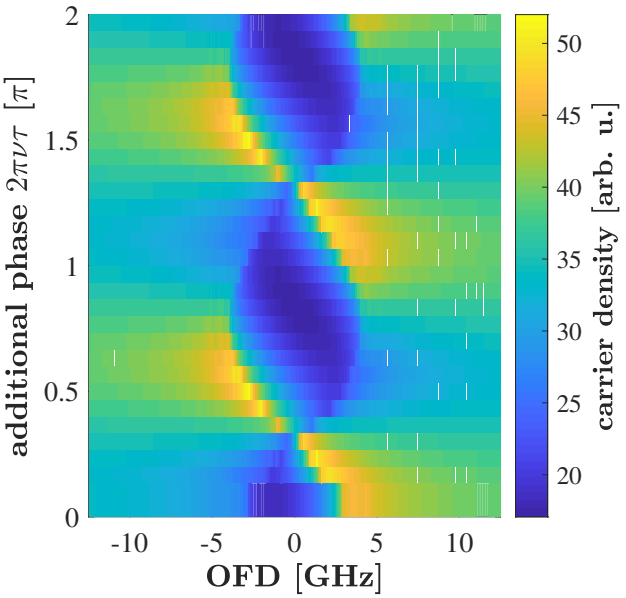

(c) Carrier density in the plane of OFD and delay phase

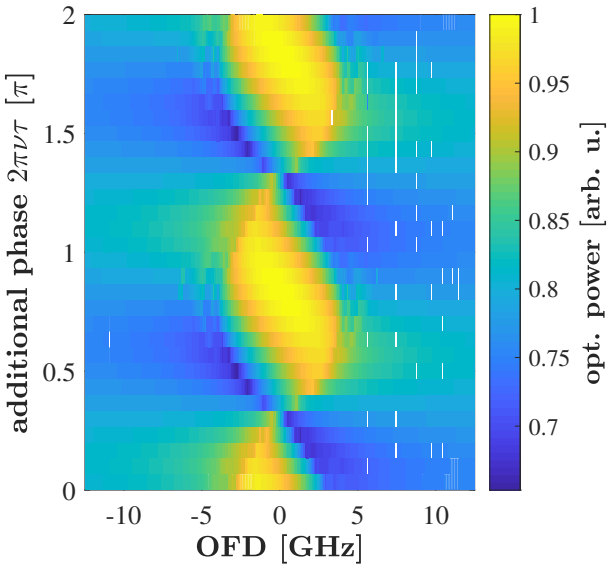

(d) Optical power in the plane of OFD and delay phase

Figure 3.29: Simulation results of optical frequency **(a)**, LBW **(b)**, carrier density (linearly connected to terminal voltage), **(c)** and optical power **(d)** of a time integration simulation using the parameters summarized in Table 3.5, with a short macroscopic delay of τ of $3.34\,\mathrm{ps}$ as a function of the additional phase $2\pi\nu\tau_{\mathrm{mic.}}$ introduced by the additional microscopic delay. The values taken for the numerical rate-equation model can be reviewed in Table 3.5.

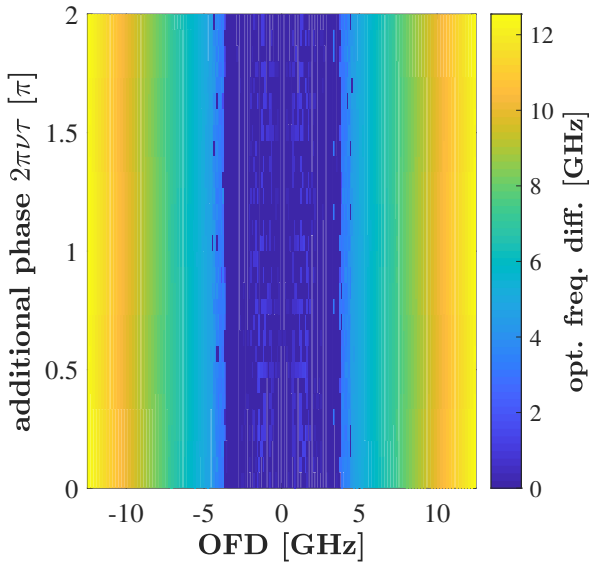

(a) optical frequency difference of both ICLs in the plane of OFD and delay phase

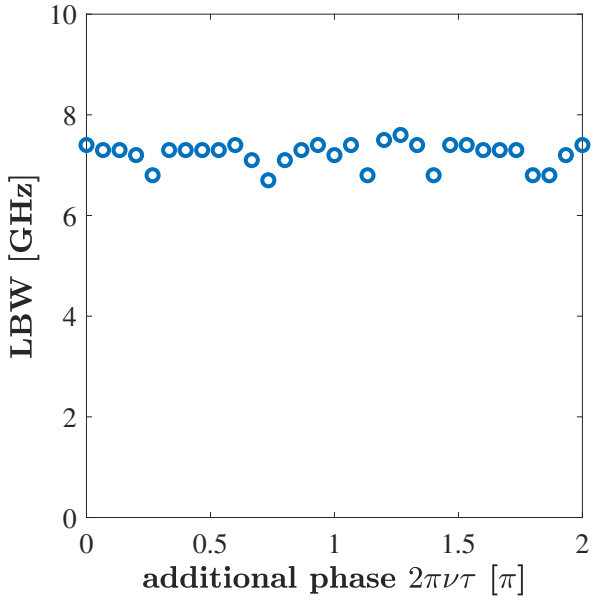

(b) LBW as a function of delay phase obtained using the results shown in Fig. 3.30a

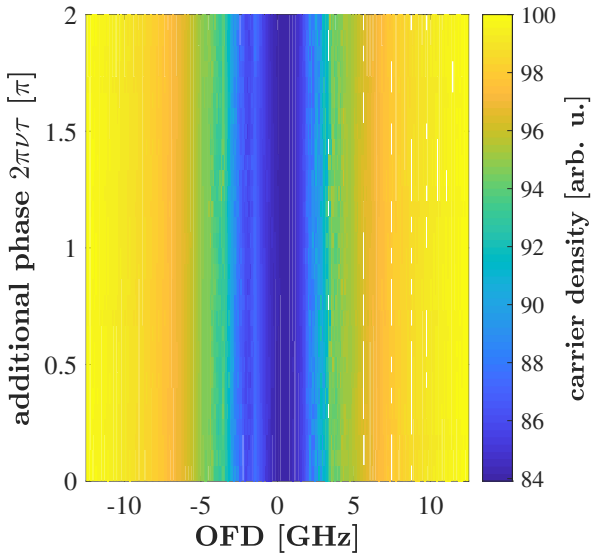

(c) Carrier density in the plane of OFD and delay phase

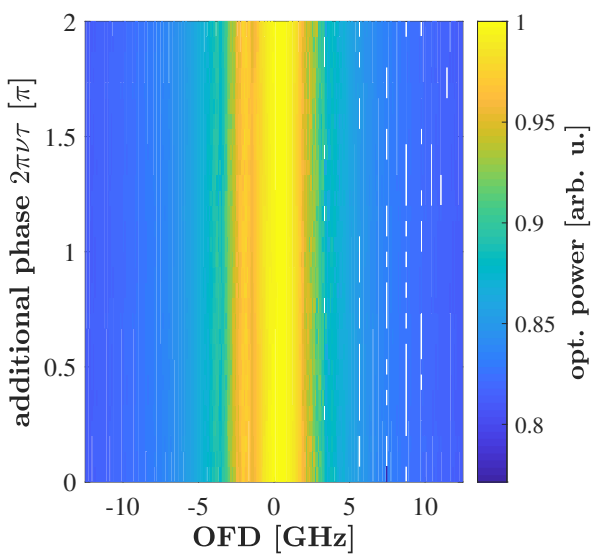

(d) Optical power in the plane of OFD and delay phase

Figure 3.30: Simulation results of optical frequency **(a)**, LBW **(b)**, carrier density (linearly connected to terminal voltage) **(c)** and optical power **(d)** of a time integration simulation using the parameters summarized in Table 3.5, with a large macroscopic delay of τ of $5\,\mathrm{ns}$ as a function of the additional phase $2\pi\nu\tau_{\mathrm{mic.}}$ introduced by the additional microscopic delay. The values taken for the numerical rate-equation model can be reviewed in Table 3.5.

3.7.4 Experimental verification of the reflection symmetry

The reflection symmetry was introduced in Eq. (3.69) and essentially states that the reflection of the OFD value resembles an exchange of lasers. For an experimental verification, we utilize the setup shown in Fig. 3.31. In contrast to previous measurements we use two ICLs of batch 3150 (see Table 2.1), ICL3150/19-06 is denoted with ICL 1 and ICL3150/13-06 is denoted with ICL 2. With the lock-in detection setup, we are able to detect the voltage changes with respect to the solitary case directly without the need of a reference measurement. We used two different amplifiers to amplify the terminal voltage for two reasons. Firstly we did not have access to a second buffer amplifier providing an input impedance of $1\,\mathrm{M\Omega}$. This high input impedance is necessary because otherwise the current would partly flow through the amplifier and not only through the ICL. The second reason is the possibility to observe the real voltage change without amplification. If detection of the voltage change were possible without an amplifier, the costs of a possible application would be greatly reduced.

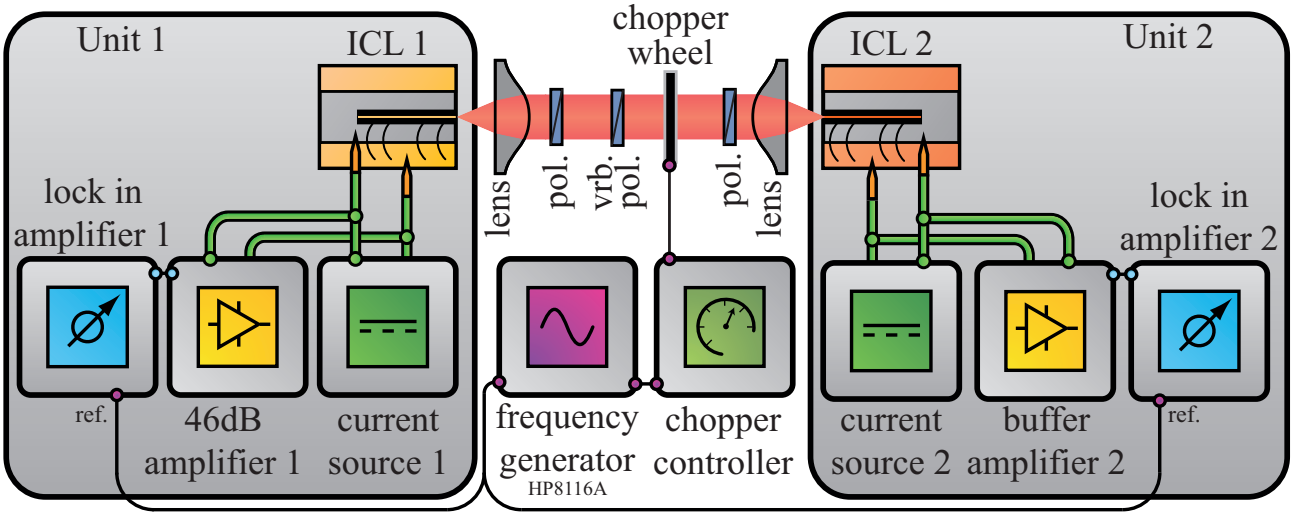

Figure 3.31: Setup for the simultaneous investigations of changes in the terminal voltage of both ICLs. The coupling beam is collimated by two lenses and passes three polarizers (pol.). The polarizers in front of each ICL ensure that the incident polarization matches the original polarization of the laser. With the variable polarizer (vrb. pol.) it is possible to set the coupling strength so that we obtain stable emission on a CLS. With the chopper wheel included in the coupling path, we are able to investigate the voltage change due to mutual coupling directly with two lock-in amplifiers. Note that the terminal voltage change of ICL 1 is amplified by $46\,\mathrm{dB}$ and that of ICL 2 is not amplified. The buffer amplifier attached to ICL 2 provides an electrical impedance transformation from the laser circuit to the lock-in amplifier circuit. The input impedance of this self-built device amounts to $1\,\mathrm{M\Omega}$ and the output impedance is $50\,\Omega$.

The results of the voltage-change measurement are depicted in Fig. 3.32 as a function of

the OFD. We find that voltage of ICL1 strongly increases at the lower edge of the LBW and then decreases until the upper edge of the LBW with a zero crossing at a OFD of approx $0\,\mathrm{GHz}$. It is also observed that voltage changes of both ICLs are diametrically opposed[9] within a detuning range from $-1\,\mathrm{GHz}$ to $1\,\mathrm{GHz}$. That domain is the LBW, which is marked with a transparent green area.

With these findings we confirm that the reflection symmetry described in Eq. (3.69) is fulfilled. This diametrical voltage change with respect to the OFD offers a high potential for applications, where information can be transferred and acquired at both ends of the setup at the same time, just by choosing different OFDs and observing the terminal voltage. In fact, we use this incredibly powerful feature as the basis to create a free-space-optical communication platform, which does not require any additional optical detection, which will be described in Chapter 5.

It can also be seen that the voltage change at ICL 2 without amplifier is three orders of magnitude lower than the amplified voltage change of ICL 1. However, it can also be seen that both show a similar relative noise level. Thus, we conclude that an amplification of the terminal voltage is not always mandatory for possible applications. This would eliminate not only the detector but also the electrical amplifier, which is another cost-intensive component in every optical detection setup.

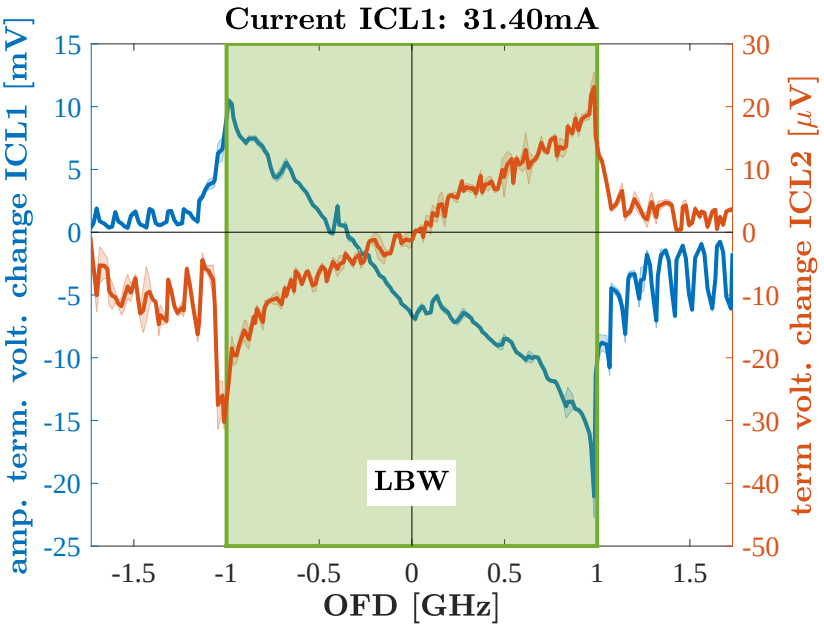

Figure 3.32: Terminal voltage change of ICL 1 (blue - left scale and amplified) and ICL 2 (orange - right scale) with respect its voltage in solitary operation as a function of the OFD. The LBW is marked with a transparent green area. Note that the units of the primary ordinate are displayed in mV and those of the secondary ordinate in μV.

[9]Note that the terminal voltage change of ICL 1 is amplified by $46\,\mathrm{dB}$ and that of ICL 2 is not amplified.

3.7.5 Summary of the section

In this section we have for the first time theoretically described two mutually coupled ICLs using a set of six nonlinear DDEs. We outlined the CLSs that represent stable solutions of this system and described the relationship of LBW, coupling strength and coupling phase. We verified the model via experimental measurements of the LBW utilizing the ICLs terminal voltage as a function of coupling strength and delay. We found that the steady-state solutions correctly predicted the influence of coupling strength but failed for long macroscopic delay breaking the 2π- and π-translation symmetries. By utilizing numerical integration of the DDEs, the reason was found to be that the steady-state approach approximates the injected optical field amplitude $E(t-\tau)$ by $E(t)$. From an experimentalists perspective this finding is quite valuable. It demonstrates the insensitivity of applications based on mutual coupling to small variations of the distance, which could be e.g. caused by vibrations. Finally we were able to experimentally verify the introduced reflection symmetry, which manifested itself in opposed terminal voltage changes observed at both ICLs.

Based on these results we design a communication system that uses CLS of different detunings as information carriers and uses the changes of the terminal voltage to retrieve the information and demonstrate it in Chapter 5. Since the optical signal then no longer needs to be detected by an optical detection unit, the amount of optical components, which is required for ordinary data transmission, is reduced.

3.8 Conclusion of the chapter

In this chapter we have both experimentally and theoretically characterized the effects on the ICLs terminal voltage in three different configurations of an external optical perturbation:

1. self-mixing (discussed in Sections 3.4 and 3.5),
2. unidirectional coupling (discussed in Section 3.6)
3. and bidirectional coupling (discussed in Section 3.7).

It was experimentally found that the changes of the ICL's terminal voltage can be used to detect the strength of each the optical perturbation utilizing the modulation index in self-mixing experiments and the width of the LBW in uni- and bidirectional coupling setups. With that we verified that an interband cascade laser can be used as a detector, i.e. the laser-as-detector approach is feasible. We accompanied our experimental findings by introducing a semi-classical rate-equation model for ICLs subjected to an external optical perturbation. We found a model, which is quite similar to that of conventional diode lasers and extended it to include bidirectional coupling of two ICLs separated by a delay τ. The experimental findings showed extraordinarily good agreement with the model and create the basis for applications relying on the laser-as-detector approach exploiting different configurations of optical perturbation. It is noteworthy that we found that the width of the LBW in the unidirectional injection scenario differs from the

LBW in the bidirectionally coupled scenario. In latter case the delay τ introduces an additional coupling phase, which can periodically alter the locking bandwidth. It was experimentally found and theoretically verified that this periodicity is valid for short macroscopic delays, but does not hold for long macroscopic delays. This is beneficial, because the LBW is therefore not affected by changes in the ICL's distance, which can be caused by e.g. vibrations or thermal elongations. That means the LBW as metric for injection strength is insensitive to these kind of mechanical perturbations.

With the knowledge acquired in this chapter, we design three applications where we use each type of optical perturbation separately in combination with the laser-as-detector approach:

1. a spectroscopy setup utilizing a ICL subjected to optical feedback to detect the amount of a sample gas (see Section 4.6)
2. a spectroscopy setup spectroscopy utilizing a ICL subjected to optical injection of a secondary ICL to detect the amount of a sample gas (see Section 4.7)
3. a communication scheme exploiting two bidirectionally coupled ICLs (see Chapter 5)

All these applications do not require an additional optical detection unit and as a result, they are in this respect advantageous to setups that are conventionally used for these applications. We will experimentally demonstrate the feasibility of all three applications in the next two chapters and evaluate further advantages and disadvantages.

„Eine Flugmaschine zu erfinden bedeutet wenig; sie zu bauen schon mehr; aber sie zu fliegen, das ist das Entscheidende.“

Otto Lilienthal

4 Absorption spectroscopy with interband cascade lasers exploiting the laser-as-detector approach

The term spectroscopy refers to a variety of experiments to decompose the optical radiation according to wavelength[252]. From the intensity distribution with respect to the wavelength it is usually possible to deduce the source of the radiation or which absorptive substances the radiation has passed through. The determination of an unknown substance is also referred to as absorption spectroscopy, which we will discuss in detail. Usually a material absorbs only specific wavelengths with a specific strength. This is also often referred to as the spectroscopic fingerprint of the substance. Each material can thus be identified by its specific absorption spectrum $S(\lambda)$, which is normalized to 1. The absorption spectrum also allows to draw conclusions about the amount of the unknown substance. The foundation for this is Lambert-Beer's law of absorption. It describes the transmitted percentage of radiation T_{LB} as a function of the wavelength λ passing through the substance of interest with absorption length L via

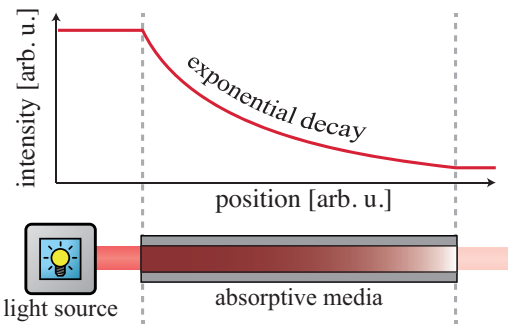

Figure 4.1: Visualization of Lambert Beer Absorption law.

$$T_{LB}(\lambda) = \exp(-\alpha(\lambda) \cdot L). \tag{4.1}$$

The absorption coefficient $\alpha(\lambda)$ of a transition is given by the density N_a of the absorbing substance and the absorption cross section $\sigma(\lambda)$, which is specific for each substance[253] following

$$\alpha(\lambda) = N_a \sigma(\lambda). \tag{4.2}$$

With the relation $T_{LB}(\lambda) = \frac{I_{abs.}(\lambda)}{I_0(\lambda)} = 1 - S(\lambda)$, where $I_0(\lambda)$ is the original optical power before absorption and $I_{abs.}(\lambda)$ the optical power after absorption and the information of the absorption length L and the atomic cross section $\sigma(\lambda)$ it is possible to calculate the density of absorbing molecules N_a. Figure 4.1 shows a schematically depicted course of the intensity of monochromatic light after passing an absorption medium exhibiting an absorption line at the wavelength of the monochromatic light source.

Basically, absorption spectroscopic experiments can be divided into two classes[254]. On the one hand there are experiments where a spectrally broadband light source is used, the absorptive medium is then placed in the beam path and absorbs spectral components of broadband light. The detection unit then splits the radiation into its spectral components revealing the absorbed spectral components. Grating spectrometers and Fourier transform infrared interferometers (FTIRs) work according to this principle. FTIR for example the Bruker Vertex 80V use a Michelson-interferometer to record an interferogram, which can be transformed into a spectrum by a Fourier-transformation. The advantage of this principle is that due to the broadband source, a wide range of wavelengths can be covered so that numerous different types of substances can be examined with a single instrument.

The second possibility is to shift the wavelength resolution from the detection unit to the radiation source. A wavelength-adjustable monochromatic radiation source and a suitable detector can be used for this. The absorption spectrum is obtained by placing the absorptive medium in the beam path and tuning the wavelength of the monochromatic light source over the wavelengths absorbed by the material and recording the transmitted intensity. The advantage of this method is the high intensity, monochromatic wavelength and stability of the light source usually a laser. This not only yields a high spectral resolution, but also allows the strength of the absorption to be determined accurately. Consequently, a very precise determination of the amount of the absorbing medium is possible. The disadvantage is that this approach usually only covers a small bandwidth of wavelengths, so each spectrometer can detect only one or very few media. This is not a problem if only the concentration of a certain medium has to be determined, but a high degree of accuracy is required. This is the case, for example, when only a small amount of a single substance is to be detected in a composition of different substances. Due to their high intensity and spectral monochromasy lasers have enabled this type of spectroscopic technique and made it possible to investigate the amount of a medium with a precision like it never had been done before[255]. Semiconductor lasers have revolutionized this technique a second time. Due to their easily accessible wavelength adjustment and potential for miniaturization, they became the most appropriate choice for laser absorption spectroscopy (LAS) applications. Not only miniaturization, but also low-cost production paved the way for diverse application fields of LAS, therefore called tunable diode laser spectroscopy (TDLAS). They range from the monitoring of industrial processes, in which environmentally harmful trace gases are emitted during e.g. combustion processes[61, 256, 257], to the monitoring of the environment [41], to the early detection of diseases [65, 258, 259] through respiratory gas analysis.

Since many gas-molecules have their specific fingerprint region in the MIR wavelength domain due to their strong fundamental rovibrational energy transitions, the MIR absorption

spectroscopy is an outstanding precise technique with the tremendous advantage of simple applicability [44]. The most prominent gas absorption lines are visualized in Fig. 4.2 for a variety of different molecules including our test gas methane.

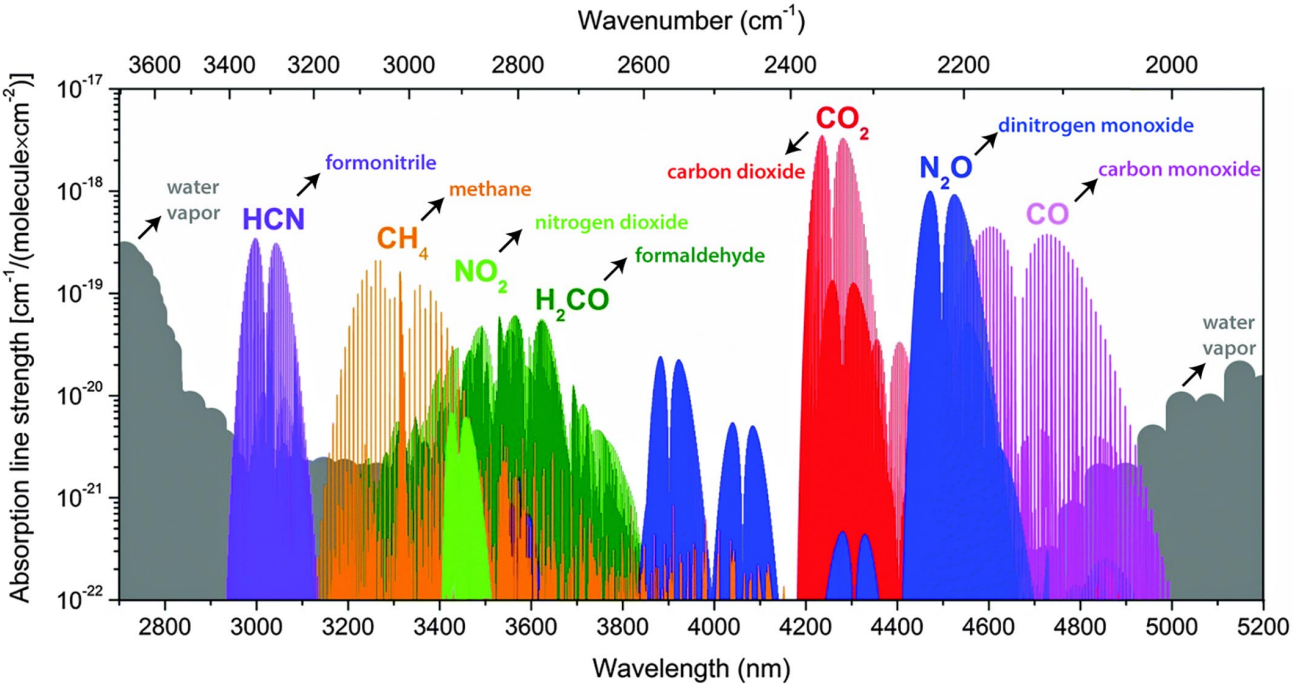

Figure 4.2: Absorption spectra of some important trace gases in the wavelength region from $2.7\,\mu m$ to $5.2\,\mu m$. The molecular line data are taken from the HITRAN 2012 database [60]. HCN: formonitrile CH_4: methane, NO_2: nitrogen dioxide, H_2CO: formaldehyde, N_2O: dinitrogen monoxide (laughing gas), CO_2 carbon dioxide, CO: carbon monoxide, The grey absorption lines belong to water (H_2O).

Tunable QCLs have been the laser-of-choice for LAS in the MIR wavelength domain for the last 20 years [41, 42]. They are not only compact and offer a high quantum efficiency, but they also offer a customizable output wavelength by varying the material thickness, not changing the semiconductor material itself. However, in the recent years the ICL is challenging the QCLs with respect to spectroscopy applications. Compared to QCLs, ICLs offer production at lower cost and operation at significantly lower voltages enabling the use of simpler electronics. Thus, they reduce the price of each spectroscopic setup, but still offer the same quality regarding the detection limit. ICLs therefore are becoming the most appropriate choice for this emission range [33].

We deploy a setup based on ICLs to perform spectroscopic measurements with the test gas methane. Methane is very well suited as a test gas because it is non-toxic and absorbs radiation in the desired wavelength range from $3.2\,\mu m$ to $3.5\,\mu m$. Gas sensors based on the principle presented in the next sections do not necessarily have to detect methane, but can investigate other trace gases depending on the wavelength range covered. In the range of $3.4\,\mu m$

to $3.5\,\mu m$ there are for example also absorption bands of dangerous nitrogen oxides. These occur especially during high pressure combustion processes in modern car engines and were the main subject of the diesel scandal [260]. Nitric oxide and especially NO_2 detection, is in fact one of the aim of the ILLIAS project. However, for the safe laboratory evaluation of the sensors performance, we use methane because of the aforementioned reasons. Before we present the absorption spectrum of our test gas methane, we describe why simple gas molecules have their strongest absorption lines in the MIR wavelength domain and discuss broadening mechanisms of absorption lines in a generalized way.

4.1 Molecular absorption spectra

In solitary atoms, it is considered that electrons orbit only on quantized levels E_i around the positively charged atomic nucleus[261]. Transitions can only occur between those levels following quantum mechanical transition rules. In this process an electron captures or sets free the energy difference $\Delta E = E_i - E_j$ of two orbits. This takes place either by absorbing or emitting a photon with the energy $h \cdot \nu_{ij} = \Delta E$, respectively, where ν_{ij} is the frequency of the corresponding photon and h the Planck-constant. In the case of photon capture, i.e. absorption, the absorbed optical frequency can be detected with an spectroscopic instrument using spectroscopy techniques.

Usually spectroscopists use the wavenumber $\bar{\lambda} = \lambda^{-1}$ as a unit to describe the position of absorption lines instead of optical frequency or wavelength. However, in this thesis we will refrain from using this unit, because wavelength and optical frequency have already been used frequently and especially the latter is better suited to describe frequency detuning. Consequently, the reader would be confused by the frequent change of units. Thus, we agree on using wavelength as the unit for the spectral position of absorption lines and optical frequency as a unit to specify the detuning.

A molecule, a chemical bonding of two or more atoms, has additional vibrational and rotational states, which are quantized just like the electronic states. It is remarkable, that transitions between those states, which are induced by external optical radiation can only occur, when the molecule exhibits a dipole momentum. Therefore, for example O_2 and N_2 do not show absorption in the MIR since they have no dipole momentum due to their symmetry. Compared to diatomic molecules like, molecules with at least three atoms have an increased number of degrees of freedom F. In general (e.g. for methane) this can be determined for a molecule of N atoms to $F = 3N - 6$ [262]. Multi-atomic molecules therefore have more complicated rotational and vibrational spectra with a considerably larger number of transitions. Additionaly, to the fundamental absorption lines, overtones/harmonics can be observed, but also combinations of the single or multiple frequency amount of two or more vibration modes can occur.

In the case of fundamental vibrational modes of many gases, the corresponding energy transitions of many molecules occur at wavelengths in the MIR range from $2\,\mu m$ to $25\,\mu m$, which is why the MIR wavelength regime is so useful for spectroscopy applications [44]. They are

particularly strong because the change in dipole moment is large compared to other types of transitions, which we will discuss in the next section. The most dominant of them are visualized in Fig. 4.2 for a variety of different molecules including our test gas methane. For the excitation of rotational transitions a significantly smaller amount of energy is required. Therefore, pure rotational spectra arise in the far infrared (FIR) or in the microwave range. Nevertheless, many rotational levels are associated with both the ground and excited vibrational state and the superposition creates an absorption spectrum around the fundamental vibrational state with many lines.

4.1.1 Lineshape of an molecular absorption line

The spectral absorption lineshape $S(\nu - \nu_0, T)$ of a molecule's absorption transition can be divided into a line-strength $\sigma_{\nu_0}(T)$ and lineshape function $\Gamma(\nu - \nu_0)$ with the central frequency of the absorption line ν_0 [263].

$$S(\nu - \nu_0, T) = \sigma_{\nu_0}(T) \cdot \Gamma(\nu - \nu_0) \tag{4.3}$$

with

$$\int_{-\infty}^{\infty} \Gamma(\nu - \nu_0)\, \mathrm{d}\nu = 1 \tag{4.4}$$

The line strength

The line strength $\sigma_{\nu_0}(T)$ can be calculated using the oscillator strength from the classical electrodynamics theory following [40]. With the dipole-matrix element for the individual transition R_{ν_0} from excited energy level E_i to ground state E_j the following expression for σ_{ν_0} can be deduced

$$\sigma_{\nu_0}(T) = \frac{8\pi^3}{4\pi\epsilon_0 \cdot 3hc} \frac{\nu_0}{g_i} \exp\left(-\frac{E_j}{k_\mathrm{B}T}\right) \cdot \left(1 - \exp\left(-\frac{h\nu_0}{k_\mathrm{B}T}\right)\right) \cdot |R_{\nu 0}|^2, \tag{4.5}$$

where $\epsilon_0(T)$ is the electrical field constant, h denotes Planck's constant, c is the speed of light, k_B is the Boltzmann constant, T is the temperature and g_i the degeneracy of the excited state E_i.

The reason why MIR absorption spectroscopy is so advantageous, is because the MIR the dipole-matrix element R_{ν_0} is quite large compared to other types of transitions. The change of the dipole-moment during a molecular vibrational transition is significantly larger than the change other types of transitions. This is because a molecular vibration provides large oscillation amplitudes of its charge carriers, namely its atomic core resulting in strong dipole oscillation.

The line shape function

The line shape function results from a combination of several broadening mechanisms. The quantum mechanical limit of a linewidth is given by the so-called natural linewidth due to the finite lifetime τ_{trans} of the excited state. It originates from Heisenberg's uncertainty principle [264], which is given by

$$\Delta E \Delta \tau_{trans} \leq \frac{\hbar}{2}. \tag{4.6}$$

With that the natural linewidth $\Delta\nu_N$ can be derived

$$\Delta\nu_N = \frac{\Delta E}{\hbar} = \frac{1}{2\pi\tau_{trans}}. \tag{4.7}$$

The broadening creates a Lorentzian profile, which is derived from the model of the damped harmonic oscillator. Typically, the natural line width lies in a range of a few MHz and is therefore negligible compared to the other broadening mechanisms like the Doppler or pressure broadening.

Doppler broadening

Due to thermal motion, particles move relative to the radiation source of an absorption spectroscopy setup, all at different speeds. Due to the Doppler effect, the particle sees higher frequencies when it moves towards the radiation source and lower frequencies when it moves away from it[44]. This widens the spectral absorption line significantly. The process can be described considering the Maxwell-Boltzmann distribution. With it it is possible to deduce the mean velocity v_{mean} at given temperature T.

$$v_{\text{mean}} = \sqrt{\frac{2k_{\text{B}}T}{m}} \tag{4.8}$$

with the Boltzmann-constant k_{B} and m the mass of the particle. We find a mean velocity of methane is in the range of approx. $550\,\text{m}\,\text{s}^{-1}$ at room temperature. With the Boltzmann-distribution the full-width-half-maximum of the Doppler broadening $\Delta\nu_{\text{Doppler}}$ follows to be

$$\Delta\nu_{\text{Doppler}} = \frac{2\nu_0}{c}\sqrt{\frac{2k_{\text{B}}T\ln 2}{m}}. \tag{4.9}$$

For a hypothetical absorption line of methane in the MIR the Doppler-broadening will give rise to a linewidth in the magnitude of $100\,\mathrm{MHz}$ with a Gaussian shape. Doppler broadening is not the only broadening mechanism. When particles move, they might collide giving rise to the third broadening mechanism: Pressure broadening.

Pressure broadening

Since molecules in the gas-phase move relatively fast, they might interact with each other. Depending on the structure of the molecules electron shell and the distance between two adjacent molecules, a shift of the individual energy levels occurs, because the molecules potentials slightly overlap for a short period of time. This leads to altered lifetimes and thus affects the width of a transition. We call the approximation of two molecules to a distance at which they noticeably influence each other collision or impacts. Such collisions between molecules occur more frequently when the pressure increases, so that this broadening mechanism is also known as pressure broadening or impact broadening [44]. This type of broadening results in a Lorentzian lineshape with the linewidth $\Delta\nu_{\text{Pressure}}$ given by

$$\Delta\nu_{\text{Pressure}} = \gamma_P \frac{P}{P_0} \left(\frac{T_0}{T}\right)^n, \tag{4.10}$$

where γ_P is the linewidth in the case of P_0 and T_0 representing standard conditions. The terms P and T denote the actual pressure and temperature. With kinetic gas theory it is possible to obtain the temperature coefficient n, which can be in the range between 0.5 and 1 depending on the type of molecule [44].

The final line shape function

The convolution of the lineshapes given by Doppler broadening (Gaussian) and pressure broadening (Lorentzian) is given by a so-called Voigt-Profile

$$S(\nu) = \int S_{\text{Doppler}}(\nu - \nu') \cdot S_{\text{Pressure}}(\nu - \nu')\,\mathrm{d}\nu'. \tag{4.11}$$

Therefore, it is a generally accepted way to accompany absorption spectra with a fit to a Voigt-profile. These Voigt-profiles can also be simulated using the description above and inserting known coefficients of an absorption line. In fact the coefficients for many molecules are tabulated in the so-called HITRAN database.

4.1.2 HITRAN Database

The high-resolution transmission molecular absorption (HITRAN) database is a collection of a variety of theoretically and experimentally determined spectroscopic parameters (line position, line strength and line broadening) for a very large number of gases (including methane). A variety of researchers use the HITRAN database to model the transmission in order to qualitatively evaluate their experimental results[129]. The database is updated regularly since the expansion of the line-transition format in 1987 [265] and has firstly been introduced 1973 [266]. We use a self-written Matlab code, which is inspired by [267] to access and calculate the absorption line positions, strengths and linewidth directly from the HITRAN database files for our test gas methane. We include the broadening of the natural linewidth, the Doppler-broadening as well as pressure broadening, but do not take into account the temperature dependence of the line strength. This is a reasonable simplification, because the HITRAN coefficients are tabulated for a standard temperature of $296\,\mathrm{K}$ (room temperature), which is also the temperature we perform our experiments.

4.1.3 The methane molecule

The molecule methane is composed of one carbon atom surrounded by four hydrogen atoms and thus is represented by the molecular formula CH_4. It is schematically visualized in Fig. 4.3. This colorless, odorless, combustible gas occurs naturally and is the main component of natural gas. Its molecular weight amounts to $16.04\,\mathrm{g\,mol^{-1}}$ and a has a density of $0.72\,\mathrm{kg\,m^{-3}}$. The atmosphere also contains a small amount of methane, with the largest quantities being produced by biological processes such as livestock farming. These and leaks from gas piplines as well as melting of the permafrost, which contains methane also contribute to the significant increase in methane concentrations in the late Holocene [268]. At present, the atmospheric concentration of 1876.3 ppbv continues to rise steadily[269].

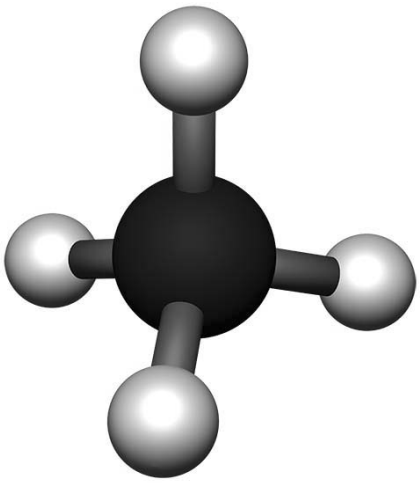

Figure 4.3: Visualization of a methane molecule with carbon atom (black) and four hydrogen atoms (white) linked via chemical bonds (grey).

We utilize methane as a test gas because it is non-toxic, commercially available and absorbs radiation in the desired wavelength range from $3.2\,\mu\mathrm{m}$ to $3.5\,\mu\mathrm{m}$. Its transmission spectrum $T_{\mathrm{CH4}}(\lambda) = 1 - S_{\mathrm{CH4}}(\lambda)$ is demonstrated in Fig. 4.4 and has been simulated using the HITRAN 2016 database [129]. The absorption lines of methane in the HITRAN 2016 database are based on the findings described in [270]. The ILLIAS project

however aims at the detection of nitric oxides like NO or NO_2, which have their fingerprint region also in the wavelength domain from $3.4\,\mu m$ to $3.5\,\mu m$. The spectrum of NO_2 is therefore also included in Fig. 4.4. Subsequently, the later described sensor, can be either used for methane detection or nitric oxides depending on the deployment of the ICL batch.

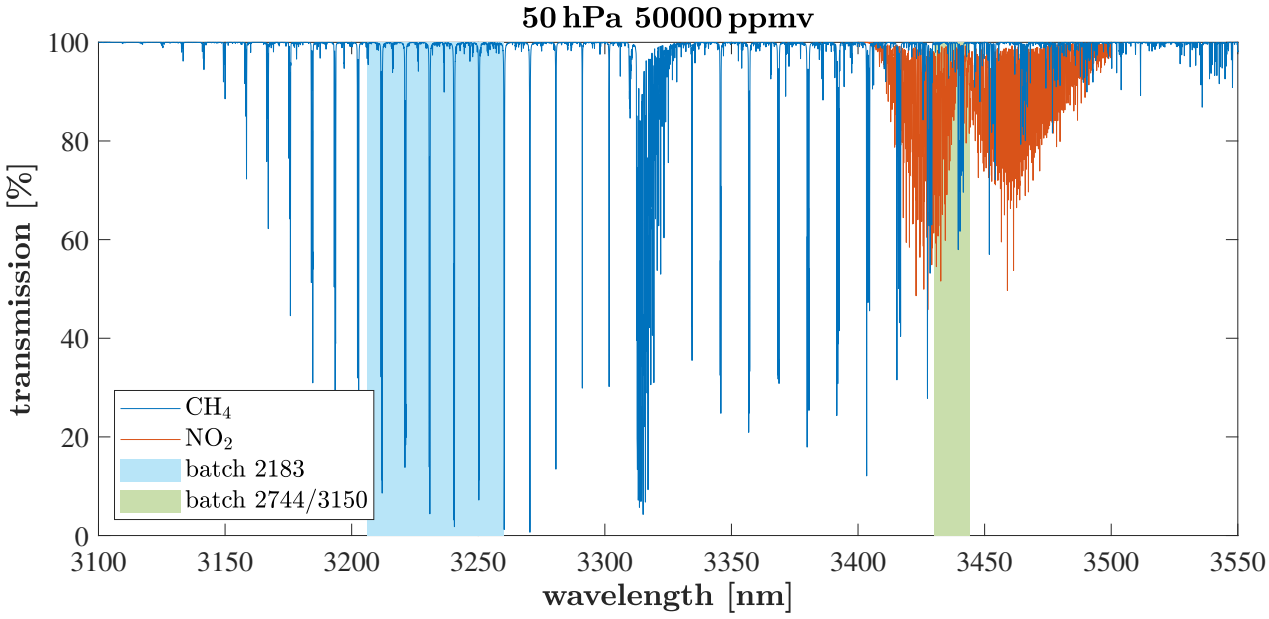

Figure 4.4: Simulated example of transmission spectra of CH_4 (blue) and NO_2 (orange) in the MIR wavelength regime from $3.1\,\mu m$ to $3.55\,\mu m$ at an pressure of $50\,hPa$ and concentration of 50000 ppmv using [129], which is based on [270]. We highlighted the emission spectra of the ICL batches 2183 (transparent blue), 2744 (transparent red) and 3150 (transparent green) to show which wavelength ranges we are able to address.

The absorption spectrum of the molecule methane arises from energy transitions inbetween so-called rovibrational energy-states of the molecule, which emerge in analogy to the energy-states of single atoms.

4.1.3.1 Rovibrational states of methane

As previously described methane is a molecule composed of five atoms, four hydrogen and one carbon atom. Its structure deploys vibrational and rotational states. The former have been schematically visualized in Fig. 4.5. Not all displayed oscillations exhibit a dipole momentum and thus only ν_3- and ν_4-transitions contribute to the MIR absorption spectrum[271]. Following quantum mechanical selection rules, it was found that only transitions between vibrational states and the ground state (GS) are possible at room temperature [272]. Therefore, methane deploys only two vibrational MIR absorption lines. The vibrational state is then substructured by several rotational states, which finally give rise to many more absorption lines around the

central vibrational lines. The final spectrum from the rovibrational ν_3-state to GS transition has already been depicted in Fig. 4.4.

The specific absorption lines of methane can not be easily deduced theoretically and therefore experimental data are the basis for the spectral methane coefficients tabulated in the HITRAN 2016 database [270]. The reason is that methane has more than two atoms and thus it is not possible to theoretically describe it with the help of a single harmonic oscillator and easily evaluate its energy states. A full description of a theoretical model to calculate the energies of rovibrational states of methane is not in the scope of this thesis. Usual models are based on a general tensor approach of the energies and intensities of spherical-top molecules and can be reviewed in [273]. A very good description of vibrational states in methane is obtained using a so-called polyad-structure well described in [271]. In this calculation the Pentad (5-body) system gives rise to the absorption lines from $3\,\mu\mathrm{m}$ to $5\,\mu\mathrm{m}$.

4.1.4 Absorption lines in Laser spectroscopy

It has already been discussed how absorption lines are formed in molecules and what happens when monochromatic light is absorbed by them (see Lambert-Beer absorption law). Every laser, as we have already learned in Section 2.9.3, has a finite line width. That ultimately means that, the linewidth measured with laser spectroscopy depends both on the broadened linewidth of the transition of methane and on the linewidth of the laser itself. The final measured lineshape therefore can be found by the convolution

$$S_{\text{final}}(\nu) = \int S_{\text{Laser}}(\nu) \cdot S_{\text{Methane}}(\nu - \nu')\,\mathrm{d}\nu'. \tag{4.12}$$

In the following comparisons, we always modify our HITRAN spectrum with this formula to obtain a proper reference. For that purpose we use the laser linewidth we measured in Section 2.9.3 assuming a Lorentzian lineshape for $S_{\text{Laser}}(\nu)$.

4.1.5 Summary of the section

All following spectroscopic measurements of methane are accompanied by a comparison to a model spectra generated with coefficients from the HITRAN 2016 database. For a proper comparison we include a measurement of the gas cell's pressure using a digital probe. We always feed this value to the HITRAN reference calculation as we also do with the assumed temperature of $23\,^{\circ}\mathrm{C}$. Additionally, we modify the HITRAN spectrum with the laser linewidth obtained in Section 2.9.3 according to Eq. (4.12). With that we are able to calculate the volume-mixing-ratio (VMR) methane in the gas-cell, which we finally linearly convert to a concentration assuming methane to be an ideal gas. The VMR is defined as the number of molecules of the sample substance per number of molecules of air. Thus, a VMR of 1 converts to 1.000.000 ppm

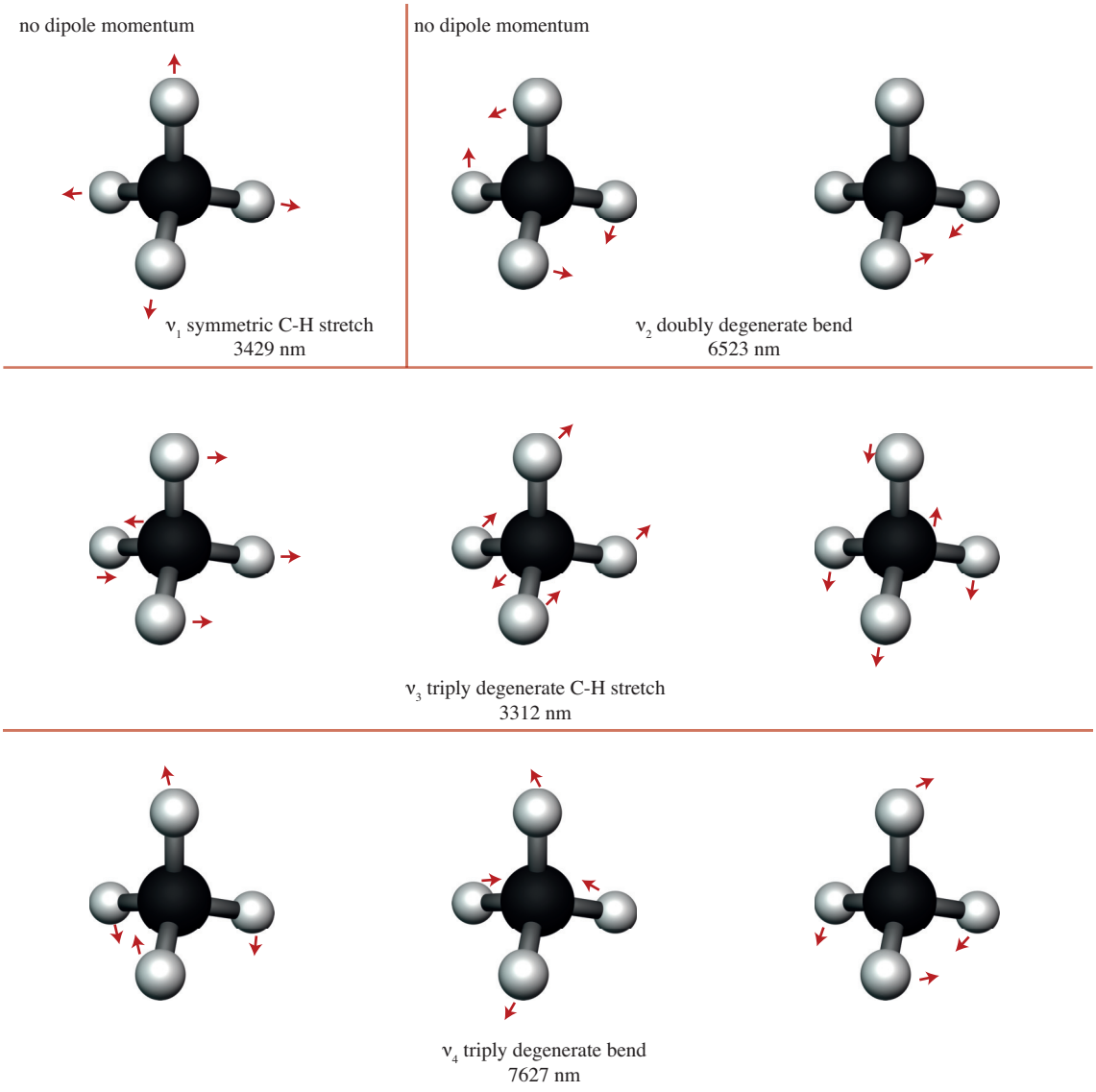

Figure 4.5: Vibrational normal modes of methane. Carbon atom: black, Hydrogen atoms: white, bonds: grey. Adapted from [274].

(parts per million) and a VMR of 0.1 converts to 100.000 ppm. Furthermore, in a real world experiment, the detection of a concentration using any spectroscopic technique always comes with a detection limit, which we discuss in the next section.

4.2 Detection limit and the Allan variance

The detection limit of all LAS based spectroscopic sensors is determined by the noise and drifts of the parameters in the spectroscopic setup. Noise sources are of quantum mechanical origin or can result from electrical noise of the laser-driver as well as electrical noise of the detection unit. Mechanical elongations and vibration can also cause the signal to fluctuate or drift. Other noise sources can occur due to back-reflection of the laser light from any surfaces, which results in optical feedback, erratically modulating the output of the laser.

A widely recognized concept to define the detection limit of a spectroscopic sensor is the so-called *Allan-variance*[275]. The Allan-variance is, generally spoken, a metric for the frequency stability of a system [276]. In other words a measurement with a high accuracy will produce the same results in a repetitive measurement series, but it will still show some fluctuations/noise around the true concentration value. In that case the resolution can usually be increased by averaging many individual measurements. But the accuracy will not improve for any number of averages. The limiting factor is the long term stability of the sensor. In the case of LAS based sensors, the wavelength drift and intensity drift represent the most dominant sources of long term instablities. To determine the best estimation, how many averages are needed in order to receive the best resolution, the Allan-variation can be utilized. Suggesting a series of measurements with N results $x_1, x_2, ..., x_N$ the arithmetic mean $\bar{x}$ and the variance σ^2 are defined as

$$\bar{x} = \frac{1}{N} \sum_{i=0}^{N} x_i \tag{4.13}$$

$$\sigma^2 = \frac{1}{N-1} \sum_{i=0}^{N} \left(x_i - \bar{x}\right)^2 . \tag{4.14}$$

The number of elements N can be divided into groups of k elements. For every group $j \in 1, 2, ..., \frac{N}{k}$ an arithmetic mean and a variance can be derived

$$\bar{x}_j\,(k) = \frac{1}{k} \sum_{l=1}^{k} x_{(j-1)k+l} \tag{4.15}$$

$$\sigma_j^2\,(k) = \frac{1}{k-1} \sum_{l=1}^{k} \left(x_{(j-1)k+l} - \bar{x}_j\right)^2 . \tag{4.16}$$

By choosing $\frac{N}{k} = 2$ the variance of $\bar{x}(k)$ results in

$$\text{Var}\left(\bar{x}(k)\right) = \frac{1}{2m}\sum_{j=1}^{m}\left(\bar{x}_{j+1}(k) - \bar{x}_j(k)\right)^2 \equiv \sigma_A^2(k) \tag{4.17}$$

In order to find the averaging limit, the Allan-variance is calculated for increasing averages of number k. The minimal Allan-variance and the associated number of averages then represent the minimal measurement variance and the optimum averaging number. Finally, the Allan-deviation $\sigma_A(k)$ represents the detection limit of a measurement system at that specific number of averages k. In the case of LAS based sensors, the detection limit represents the least amount of gas concentration, which can be detected with the system. If the measurements were conducted with a constant sampling rate of Δt, the number of averages k can be transformed to a integration- or averaging time τ using $\tau \equiv k \cdot \Delta t$, which is the case for all following measurements.

To communicate a feeling for the Allan variance, we generate an example data-set of normal distributed values, which is shown in Fig. 4.6a. It includes a linear drift mimicking a 'long term' instability. The calculated Allan deviation of this data-set is depicted in Fig. 4.6b. At short integration times, the Allan deviation is high due to the non-averaged white noise. It decreases because the noise averages out step-by-step. The decreasing Allan-deviation in that region is proportional to $\sqrt{\tau_{\text{int}}}$, where τ_{int} denotes the integration time, which is an indication for white noise. By further increasing the integration time, the Allan deviation starts rising again, which is due to the artificially introduced drift in the sample data-set. The point of the least Allan-deviation defines the detection limit (y-dimension) and its optimal integration time (x dimension). It is therefore generally recognized, that in order to provide a proper quality rating of a spectroscopic technique a detection limit has always to be accompanied with an indicated integration time.

4.3 Laser spectroscopy techniques - A brief overview

Utilizing Tunable Diode Laser Absorption Spectroscopy (TDLAS) is the modern way to approach the characterization of the medium of interest in the MIR wavelength regime [4, 254, 277, 278]. In order to scan an absorption line, the wavelength is being tuned by current-ramping a single mode DFB-Laser. The passage through the absorption cell affects the optical power of the laser beam as it has already been depicted in Fig. 4.1. With TDLAS it is possible to achieve detection limits in the order of 0.1ppbv (parts per billion by volume) for many small molecules by averaging over a few minutes. This is sufficient for the most application requirements[279]. Several improvements, such as improvements of the low-frequency jitter of the laser current[280] or balanced photodetection [281] can be used to increase the sensitivity. Other techniques such as cavity ring down spectroscopy (CRDS)[282], wavelength modulation spectroscopy (WMS)[283], quartz enhanced photoacustic spectroscopy (QEPAS) [69, 284, 285] or intracavity absorption spectroscopy (ICLAS) [286] and cavity enhanced absorption spectroscopy with

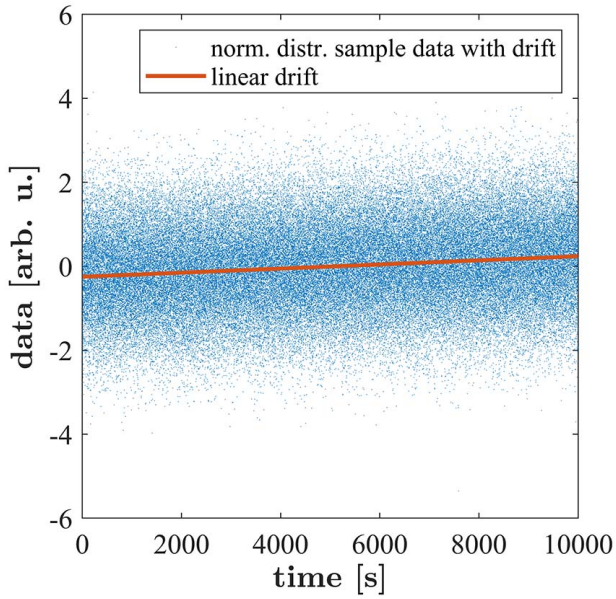

(a) Normal distributed sample data (blue) with a linear drift (red). The data has been generated by the nrmrnd()-MATLAB-function.

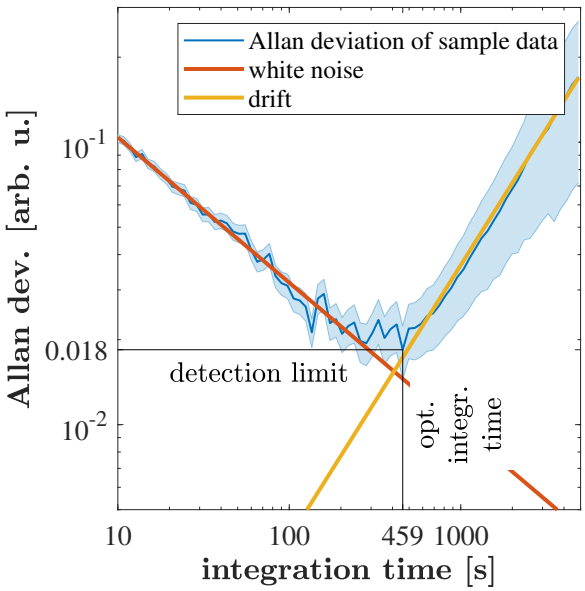

(b) Allan deviation for the normal distributed sample data (blue) exhibiting a linear drift. The black lines indicate the detection limit and the corresponding optimal integration time (opt. integr. time).

Figure 4.6: Example plot of the Allan variation (right) of artificially generated normal distributed sample data with a drift (left).

optical feedback (OFCEAS) [287] are different laser based measurement techniques and can furthermore increase the sensitivity sustainably. Today also optical frequency comb techniques challenge these known spectroscopic techniques providing a large optical bandwidth and high precision[288–290]. Sub-parts-per-trillion detection limits have fore example been achieved with QEPAS using the sample gas hydrogen fluoride [291].

However, all of the described techniques require a sophisticated, mostly cost-intensive detection unit to precisely evaluate the strength of absorption. Therefore, the objective of this chapter is to use the power of the LAD approach to conduct a laser absorption spectroscopy experiment by finally removing the detection unit of the spectroscopic setup. Our requirement is that the detection limit remains in the same order of magnitude as TDLAS. For this purpose we define our goals in the next section.

4.4 Goals of this chapter

In this chapter, we perform the analysis of three different spectroscopy techniques. Their conceptual setups are schematically visualized in Figs. 4.7a to 4.7c.

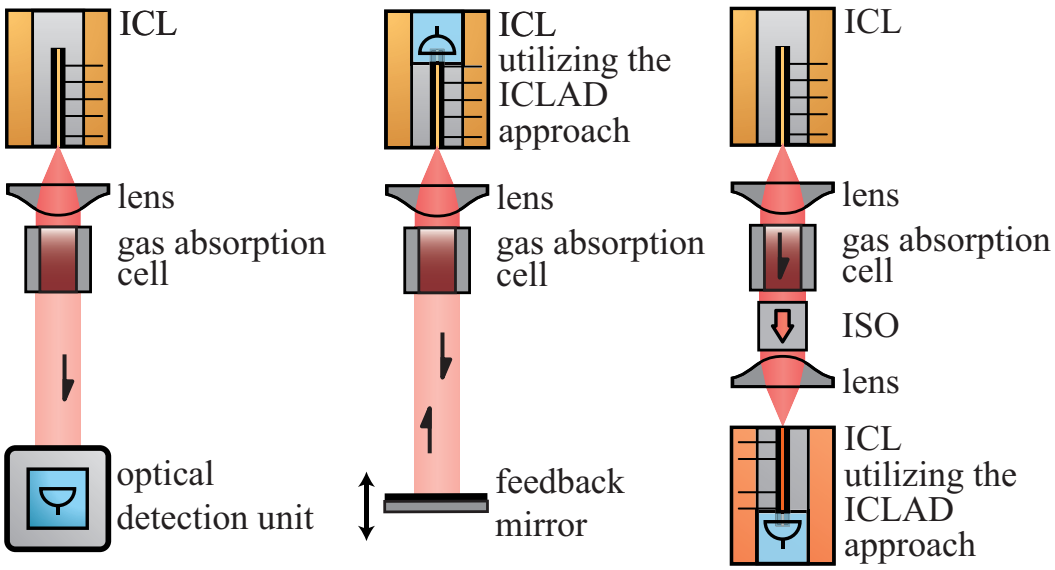

(a) Well known concept of TDLAS, which serves as a reference.

(b) Spectroscopy setup without additional detection unit utilizing the self-mixing signal as detector.

(c) Spectroscopy setup without additional detection unit utilizing the LAD approach of two uni-directionally coupled ICL with the 2nd ICL as the laser-detector.

Figure 4.7: Schematically visualized concept setups of three different spectroscopy techniques.

The analysis is presented as follows

1. In Section 4.5 a conventional TDLAS experiment is demonstrated, whose findings will serve as a reference in the further course. Therefore, we use the same ICLs as in the following experiments.
2. Then, we present a self-mixing spectroscopy experiment in Section 4.6, where a single ICL is used as a radiation source and simultaneously as a detection unit following the conceptual setup in Fig. 4.7b. We use knowledge already gained from Sections 3.1 and 3.4 and follow the experimental procedure described in [223]. We quantify the potential of this detector-free approach with an analysis of the detection limit.
3. In Section 4.7 we then perform a spectroscopy experiment based on the unidirectionally coupled ICL setup conceptually depicted in Fig. 4.7c. By using a frequency selective radiation source (master ICL) and a frequency selective detector (slave ICL) we hope to achieve an improved detection limit. The idea here follows the work described in [56],

but we stick on an unidirectional coupled rather than mutually coupled system. The idea in [56] was that nonlinear properties of a bidirectionally coupled laser system should amplify the absorption signal, whereas the noise remains at the same level. Eventually, this will result in an improved SNR. We suggest that also a unidirectionally injected and wavelength selective detector (slave ICL) can be advantageous compared to a conventional detection unit. Not only does it provide wavelength selection it could also save production costs, because it can be manufactured simultaneously with the master-ICL, i.e. can be grown on the same waver. This could lead to a cost reduction of the overall detection setup compared to TDLAS.

Via these approaches and by the best knowledge of the author, we demonstrate a spectroscopy application of self-mixing and unidirectional coupled ICLs for the very first time.

4.5 Tunable diode laser absorption spectroscopy

Tunable diode laser absorption spectroscopy (TDLAS) is the most common optical technique to evaluate the concentration and components of an unknown substance. This is due to the fact that sensors based on TDLAS not only achieve very good detection limits, but the technique is also simple and therefore robust and compact. There are already TDLAS sensors utilizing interband cascade lasers[292], which are also deployed in a mobile applications[293]. In this thesis we use the TDLAS technique as a reference to compare it with other measurement techniques. In this section, we introduce this technique to the readers and discuss the detection limit of this concept.

Technique

In order to scan an absorption line, the wavelength is being tuned by current-ramping a single mode DFB-ICL. The passage through the absorption cell affects the optical power of the laser beam as depicted in Fig. 4.8a. The resulting intensity is given by

$$P\left(I\right) = P_0\left(I\right) \cdot T_{LB}\left(\lambda\left(I\right)\right), \tag{4.18}$$

which is the product of $P_0\left(\lambda\right)$ the intensity of the laser depending on its output wavelength λ and the transmitted intensity $P_{LB}\left(\lambda\right)$ described by the Lambert-Beer absorption law described in Eq. (4.1).

The transmission can be calculated by dividing the obtained signal $P\left(I\right)$ by a reference trace of $P_0\left(I\right)$.

$$T_{LB}\left(\lambda\left(I\right)\right) = \frac{P\left(I\right)}{P_0\left(I\right)}, \tag{4.19}$$

A typical signal $P\left(I\right)$ and the reference $P_0\left(I\right)$ is is exemplary visualized in Fig. 4.8b (top). The bottom graph then shows $T_{LB}\left(\lambda\left(I\right)\right)$.

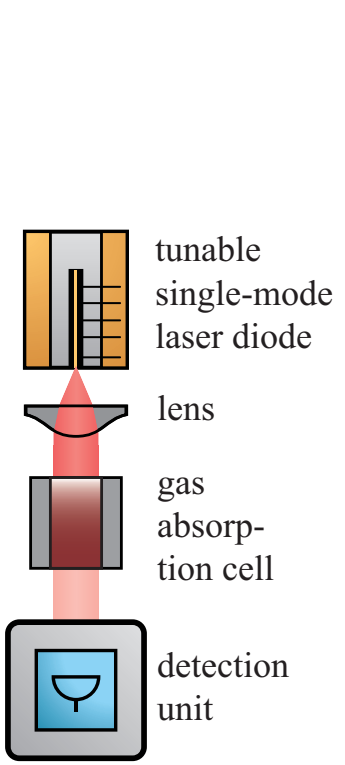

(a) Schematic setup of the TDLAS concept. The wavelength tunable laser beam is collimated by a lens, passes the absorption cell including an absorptive gas and is detected by the detection unit.

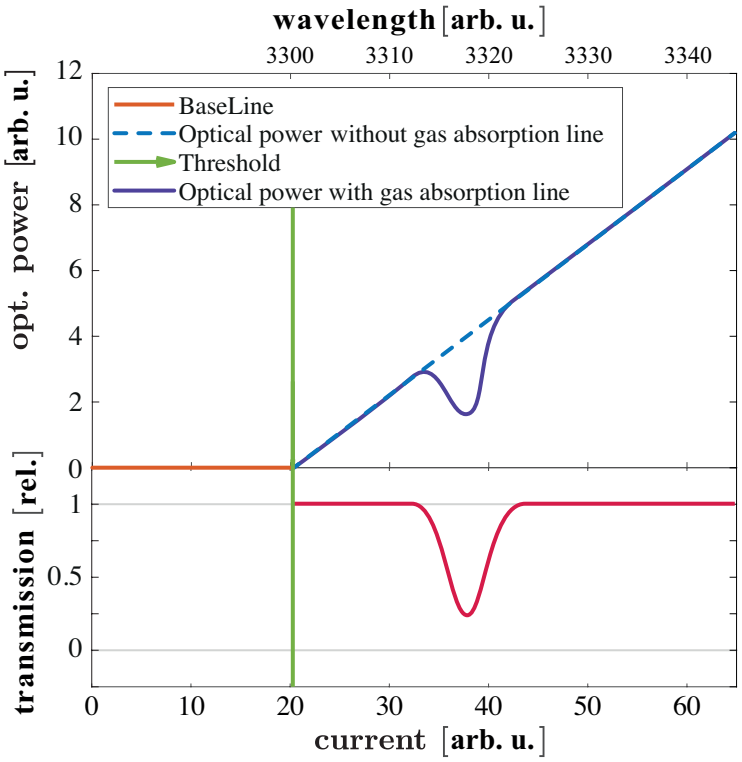

(b) Simulated signal observed at the detection unit of a TDLAS experiment with and without gas cell within the path (top). Calculated transmission, which is a division of the signal with absorption line by the signal without the absorption line.

Figure 4.8: (a) Schematic concept and **(b)** signal of a common TDLAS experiment.

The reference trace $P_0\left(I\right)$ can be obtained by a simple reference measurement removing the gas from the absorption cell. Another possibility is to perform a spline fitting of $P\left(I\right)$ taking only points into account which do not contribute to the absorption line. Thisf process is visualized in Fig. 4.9.

While the first option provides a more accurate result in theory, it is technically more complex. By simply removing the entire gas cell, one would also remove optical elements such as

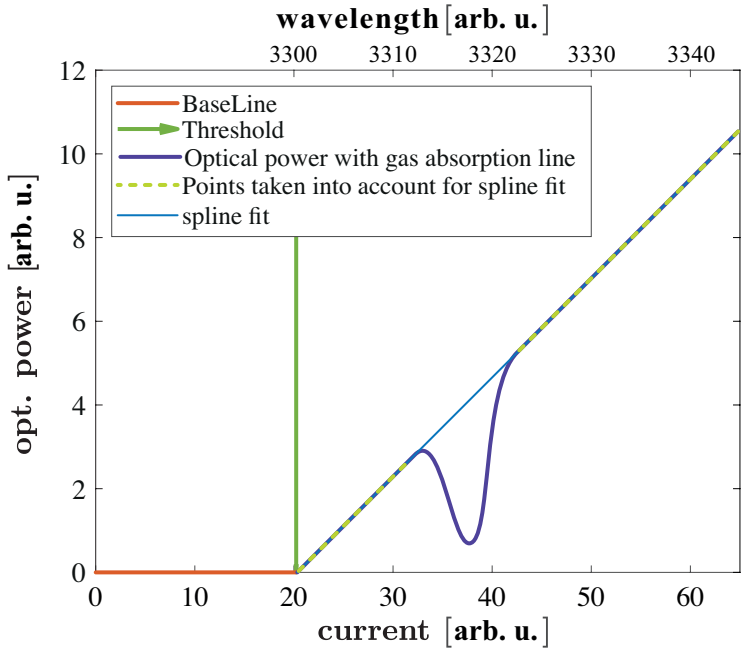

Figure 4.9: Process to obtain the reference signal of a common TDLAS experiment without actually taking a reference measurement.

the windows of the gas cells from the structure. Because the windows are usually not AR-coated, they significantly influence the intensity of the laser beam. Therefore, such a procedure is not acceptable. A reference measurement would therefore have to be made with an empty gas cell exactly of the same orientation and at the same position. This is hardly practicable even in the laboratory, since the gas cell usually has to be removed from the beam path for filling and purging. However, in order to carry out high-precision measurements, this effort is required.

For a portable gas sensor without a built-in gas cell, a reference measurement could be made before the first use. However, environmental changes such as thermal expansion of optical components can manipulate the beam path in such a way that the original reference measurement is no longer valid.

Therefore, in common TDLAS experiments the method with spline-fit is used. Such a setup is thus practically calibration- and maintenance-free.

Experiment

The actual TDLAS setup is shown in Fig. 4.10. Compared to the previous concept (Fig. 4.8a) it includes an additional optical isolator (ISO) to avoid back reflections from any surfaces into the ICL. It has already been shown that feedback can cause undesired changes in the optical power and therefore introduce noise. The neutral density filter (NDF) avoids saturation of the MCT detector. The HP8116A frequency generator is connected to the power source that drives an ICL

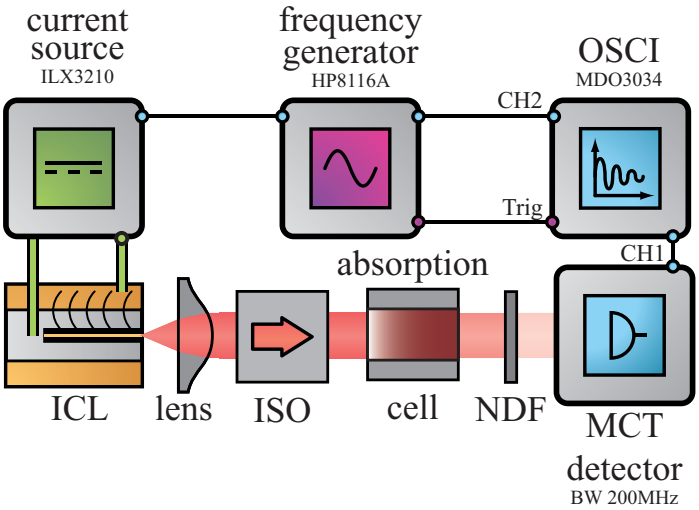

Figure 4.10: Actual tunable diode laser absorption spectroscopy setup.

and provides a sawtooth signal that is converted into a sawtooth modulation of the current. Since for the desired operation regime of currents the wavelength of the laser is linearly connected to the current, finally the wavelength is scanned. We record the time-trace of the optical signal with an oscilloscope (Textronix MDO 3034). To correctly track the actual wavelength, we also record the signal of the frequency generator with the oscilloscope. To obtain a reference we use the spline-fit method described earlier. Therefore, our TDLAS setup is practically calibration-free.

The gas cell is filled using the following procedure, which ensures a high gas concentration within the cell.

1. The gas cell contains only air with ambient pressure.
2. We add methane with high pressure.
3. We reduce the pressure in the cell with a vacuum pump with the gas concentration well established in the cell.

The parameters of a demonstration measurement are tabulated in Table 4.1.

parameter	value
gas cell length	10 cm
gas cell pressure	49 hPa
temperature of laboratory	25 °C
ICL device	3150/19-06
ICL temperature	32 °C
scanned wavelengths	3437.58 nm to 3438.65 nm
scanning frequency	5 kHz

Table 4.1: Operation parameters for the TDLAS experiment including information about the gas cell.

The result of the transmission spectrum is shown in Fig. 4.11 together with a Fit to a spectrum generated with the HITRAN database.

The measurement shows two gas absorption lines, a weak one at 3437.86 nm and a strong one at 3438.4 nm. The fit to the HITRAN database shows a great agreement concerning the

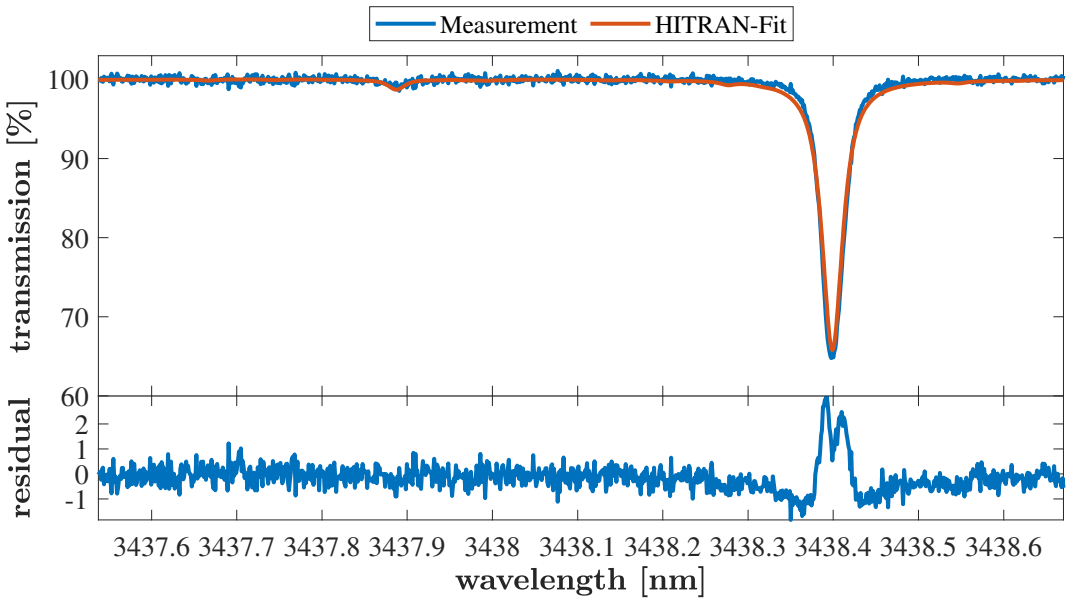

Figure 4.11: Transmission spectrum of methane from $3437.58\,\mathrm{nm}$ to $3438.65\,\mathrm{nm}$ obtained by the TDLAS setup shown in Fig. 4.10. The parameters for this measurements are found in Table 4.1. The fit to HITRAN presented here results in a methane concentration of 326747 ppmv.

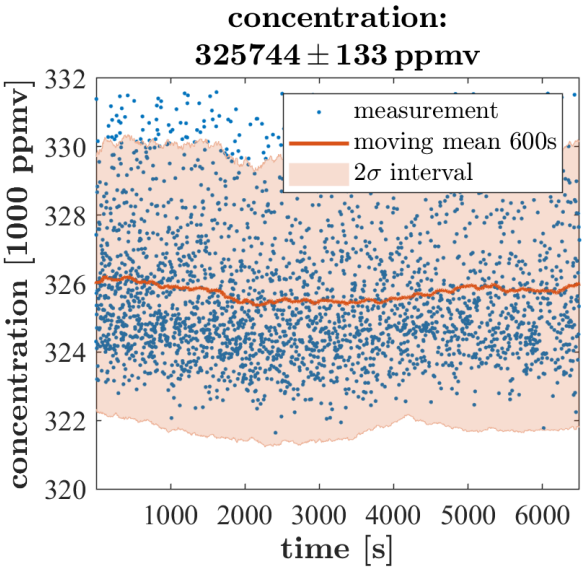

(a) Observed concentrations (blue points) using a fitted version of the HITRAN spectrum. We also plot a calculated moving mean average including $600\,\mathrm{s}$ of data and the 2σ-interval (orange) in order to show the slow drift. The overall mean amounts to 325744 ppmv.

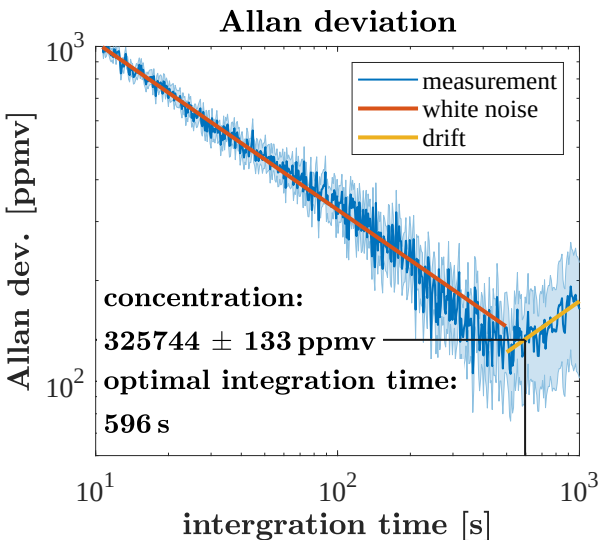

(b) Allan-Plot utilizing the data of Fig. 4.12a indicating the trend of the Allan-deviation. Until $596\,\mathrm{s}$ the Allan-deviation decreases because of the averaging of white noise (red). For longer integration times the drift of the measurement dominates the evaluation (yellow) and thus averaging is not useful for times longer than $596\,\mathrm{s}$. The trend of the Allan deviation follows the ideal trend, which we have visualized in our artificially simulated example in Fig. 4.6b.

Figure 4.12: Evaluation to determine the concentration and the detection limit of the TDLAS setup using the setup parameters found in Table 4.1

spectral position as well as to the absorption strength, which can be seen in the plot of the residual (difference between fit and measurement) in Fig. 4.11 (bottom). The good position agreement of both absorption lines can be interpreted that the spectral calibration of our system has been accurately performed. Evaluating the HITRAN fit of that particular measurement results in a gas concentration of (reasonable) 326747 ppmv, which has to be confronted to reveal the detection limit. Therefore, we repeat this measurement and the evaluation of the concentration 3000 times and calculate the Allan-deviation. The obtained concentrations are visualized in Fig. 4.12a as a function of the time and the corresponding Allan-plot is shown in Fig. 4.12b.

It is revealed that the mean concentration amounts to 325744 ppmv. By averaging all obtained results, we achieve a detection-limit of 131 ppmv at an optimal averaging time of $596\,\mathrm{s}$ using the Allan-deviation method. For this demonstration experiment we did not scan a strong absorption line of methane. In fact the absorption line is very weak compared to other absorption lines, which can be verified by observing the inset in the full methane absorption spectrum in Fig. 4.13.

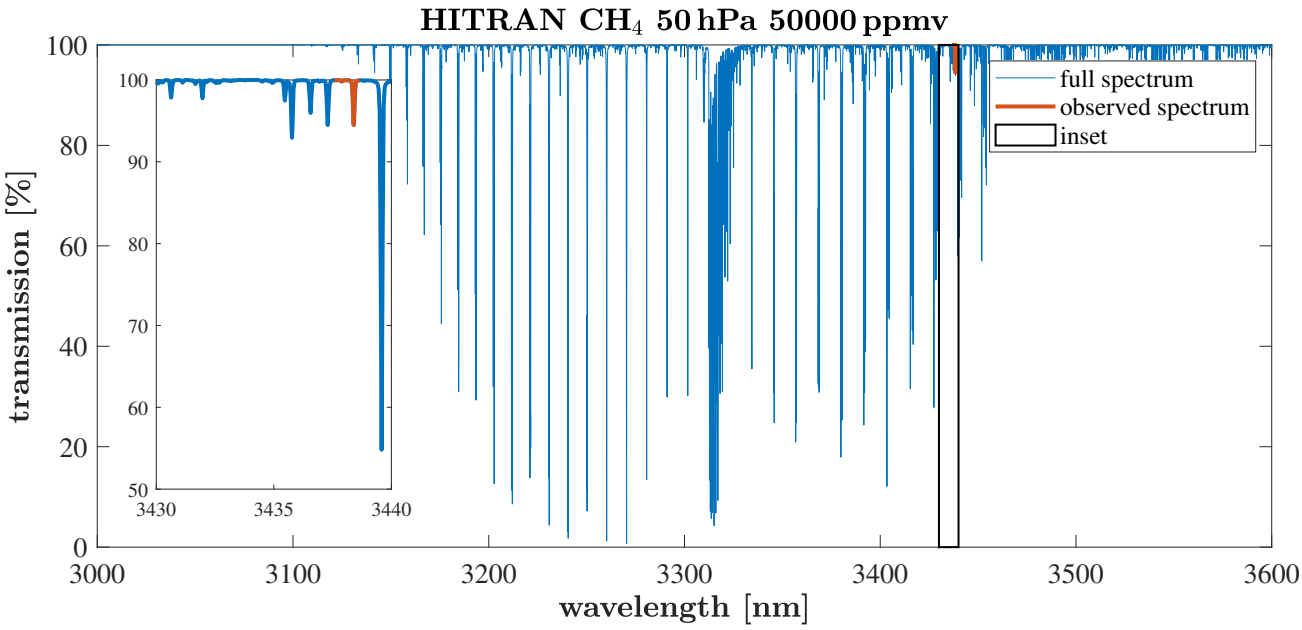

Figure 4.13: Rovibrational spectrum of methane around $3300\,\mathrm{nm}$ (blue) with an inset showing the accessed absorption line (red). Here we only show a spectrum using a concentration of 50000 ppmv, because for a concentration of 325000 ppmv, most of the lines would show saturation (which would manifest itself in absorption lines with 0% transmission) and thus the reader would get a wrong feeling with respect to the relative strengths of different absorption lines.

We utilize this particular absorption line just for comparison with the unidirectional injection spectroscopy technique in a later experiment. In the latter setup we have to require that both ICLs operate on close-by and overlapping wavelengths. The wavelength overlap of the batch 3150 ICLs does not allow to address a stronger absorption line. The idea is that even though we are addressing a weak absorption line, we can get a feeling for the detection limit using both spectroscopy setups, because we are utilizing the SAME absorption line. We conclude that addressing a stronger absorption line would result in a significantly increased performance with both setups in the same way.

4.5.1 Summary of the section

We conclude that this demonstration of TDLAS leads to a detection-limit of 133 ppm addressing a weak absorption line of methane at $3438.4\,\mathrm{nm}$ with an optimal averaging time of $596\,\mathrm{s}$, when the pressure amounts to $49\,\mathrm{hPa}$.

4.6 Self-mixing laser absorption spectroscopy

When it comes to mobile applications the required cooling of the used MCT-detector is not practicable for a simple, low maintenance setup. Therefore, a more applicable and simpler solution would be desirable reducing the cost and complexity of the optical setup. We use a solution that exploits the LAD approach in the case of self-mixing, in which a single ICL acts both as a light source and as a detector. The concept of this ansatz is schematically visualized in Fig. 4.14 and we refer to it as self-mixing laser absorption spectroscopy (SMLAS). Its feasibility has been proved with QCLs and is especially interesting the Terahertz region [236], where detectors need even more maintenance than MIR detectors. For the development of our first-approach detector-free gas sensor we utilize our finding in Section 3.4.

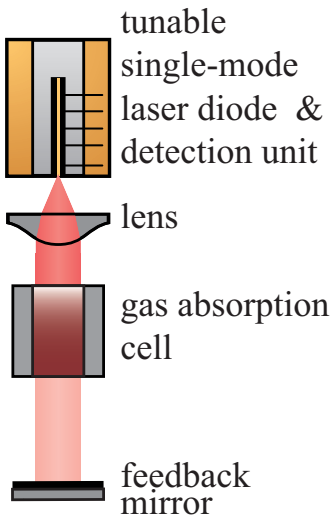

Figure 4.14: Concept of self-mixing laser absorption spectroscopy

Technique

The technique uses the relationship between the amount of feedback and the change in terminal voltage at the laser. Therefore, we recall the linear connection of the change of the voltage ΔU and the change of the carrier density ΔN, which has already been described in Eqs. (3.7) and (3.8).

$$e\Delta U = B\left(N\right)\Delta N. \tag{4.20}$$

(4.21)

We also take advantage of the steady-states of the rate-equations for lasers exposed to feedback, which have already been described in Eq. (3.24):

$$\Delta N_0 = -2\frac{|\kappa_{\text{inj}}|}{Zg}\frac{E_{\text{ext}}}{E}\cos\left(\phi_{\text{FB}}\right) \text{ with}$$

$$\phi_{\text{FB}} \equiv \frac{4\pi\nu}{c}\cdot L \tag{4.22}$$

and

$$\Delta N = N_{\text{th}} + \Delta N_0 \tag{4.23}$$

It shall be also recalled that ν_{FB} was the optical frequency in case of feedback, which had to full-fill the following condition for a steady-state:

$$\nu_{\text{FB}}\left(\phi_{\text{FB}}\right) = \nu_0 - \left|\kappa_{\text{inj}}\right| \sqrt{1+\alpha^2} \cdot \sin\left(2\pi\nu_{\text{FB}}\left(\phi_{\text{FB}}\right) \cdot \frac{2L}{c} + \arctan\left(\alpha\right)\right), \tag{4.24}$$

In the case of $|\kappa_{\text{inj}}| < 1$, the approximation $|\kappa_{\text{inj}}| \sqrt{1+\alpha^2} \cdot \sin\left(2\pi\nu_{\text{FB}}\left(\phi_{\text{FB}}\right) \cdot \frac{2L}{c} + \arctan\left(\alpha\right)\right) \simeq 0$ is valid and therefore, Eq. (4.22) becomes

$$Zg\Delta N = -2\left|\kappa_{\text{inj}}\right| \sqrt{1+\alpha^2} \cos\left(2\pi\nu \cdot \tfrac{2L_{\text{ext}}}{c}\right) + \frac{1}{\tau_{\text{ph}}}. \tag{4.25}$$

Together with Eq. (4.20) we conclude that

$$\Delta U \propto \Delta N \propto \Delta\left|\kappa_{\text{inj}}\right| \cos\left(2\pi\nu \cdot \tfrac{2L_{\text{ext}}}{c}\right), \tag{4.26}$$

where $|\kappa_{\text{inj}}|$ is a measure of back reflected light from the external feedback mirror in the amplitude domain. This finding represents the foundation of this spectroscopy concept and is in agreement with the literature described in [223].

To obtain a transmission spectrum, we also require spectral resolution. The idea is that we scan the wavelength of the ICL step-wise across an absorption line, while the laser is exposed to feedback, when the feedback phase ϕ_{FB} is modulated constantly. If the wavelength of the ICL approaches the position of the absorption line, the amplitude of the self-mixing signal decreases according to Eq. (4.26). The reason for that is absorption affects the feedback strength $|\kappa_{\text{inj}}|$ according to the Lambert-Beer-Absorption law. We can finally obtain a transmission spectrum by comparing the self-mixing amplitude to a reference, where we observed the self-mixing amplitude without absorption.

Experiment

The actual setup for demonstration of the applicability of this concept is schematically depicted in Fig. 4.15. The MIR laser beam passes the gas absorption cell, which is placed within the feedback arm twice (forward and backwards) and reenters the laser after passing several optical components, which are required to ensure operation in the weak feedback regime. Both, the non-polarizing beam splitter and optical detection unit are not necessary for the overall spectrocopic concept, but have been deployed for alignment and evaluation purposes. The feedback is deployed by a moving feedback mirror. The movement follows a triangular signal provided by a frequency generator and thus modulates the external cavity length L_{ext} continuously. Finally,

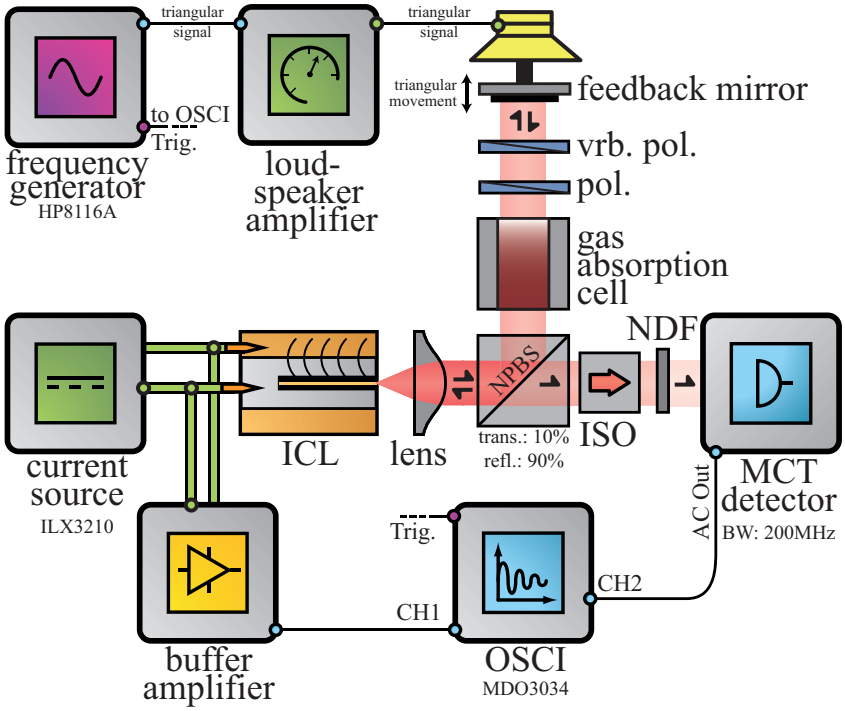

Figure 4.15: SMLAS setup. The rotatable variable polarizer (vrb. pol.) together with the fixed polarizer (pol.) act as a continuous attenuator to ensure operation in the weak feedback regime. The polarizers also ensure that the polarization of the feedback matches the original polarization. The isolator (ISO) is placed behind the non-polarizing beamsplitter (NPBS) to avoid back reflections from an additional detection unit, which was used to align the feedback path. The buffer amplifier ensures a high input impedance so that all current from the current source flows through the ICL.

we record the timetraces of the terminal voltage modulation using an oscilloscope (Textronix MDO3034).

To evaluate the quality of this concept we use ICL 2744/13-25 and utilize two absorption lines of methane in the range from $3415.88\,\mathrm{nm}$ to $3416.09\,\mathrm{nm}$, which are visualized in the inset of Fig. 4.16. All other parameters of this demonstration-experiment are tabulated in Table 4.2.

Measurement process

In order to provide a reference, we gradually scan the lasers wavelength step by step increasing the driver current and each time take self-mixing time-traces of the AC-coupled terminal voltage, when the gas cell is **not** filled with methane. After filling the gas cell without moving the gas cell during the filling process with a specific amount of gas, we repeat that procedure.

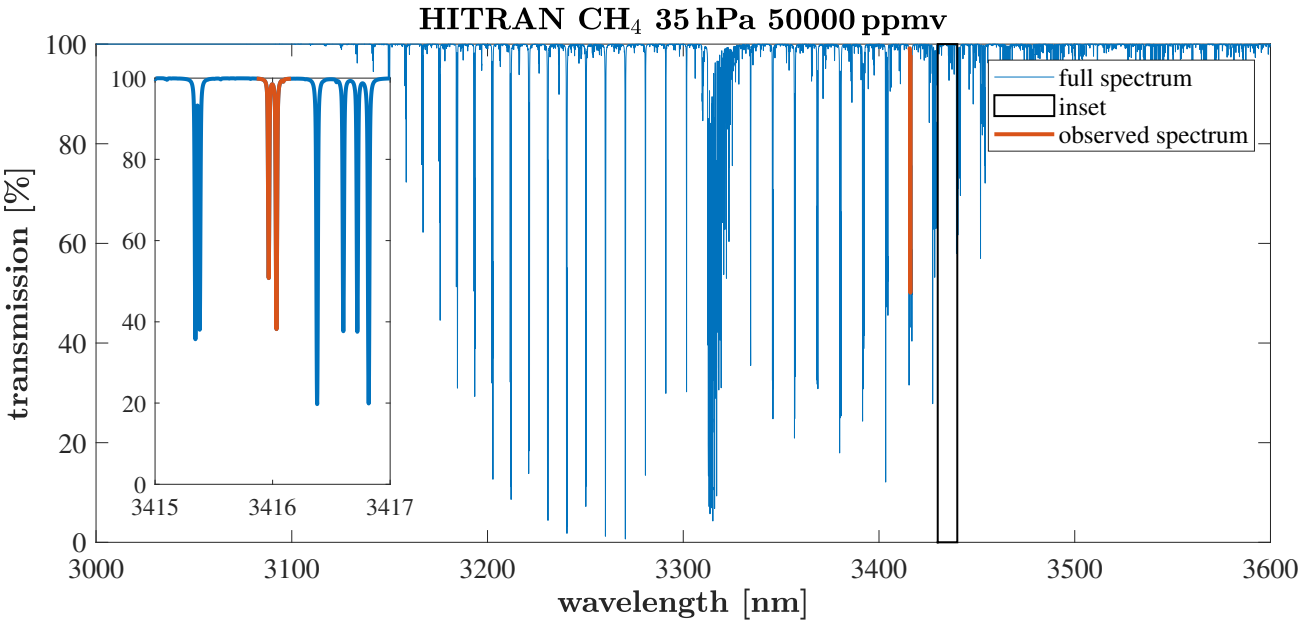

Figure 4.16: Simulated rovibrational spectrum of methane around $3300\,\mathrm{nm}$ (blue) with an inset showing the accessed absorption line (red). Here we show a spectrum using a sample concentration of 50000 ppmv to visualize the relative strength of the absorption lines. The inset shows the observed absorption lines in greater detail.

parameter	value
gas cell length	$10\,\mathrm{cm}$
gas cell pressure	$35\,\mathrm{hPa}$ (SMLAS)
gas cell pressure	$34\,\mathrm{hPa}$ (TDLAS)
temperature of laboratory	$25\,^{\circ}\mathrm{C}$
ICL device	2744/13-25
ICL temperature	$24\,^{\circ}\mathrm{C}$
scanned wavelengths	$3415.88\,\mathrm{nm}$ to $3416.09\,\mathrm{nm}$
scanning frequency	$574\,\mathrm{Hz}$

Table 4.2: Operation parameters for the SMLAS experiment including information about the gas cell.

Both the reference trace and self-mixing trace in the case of absorption are shown in Fig. 4.17a when the ICL operated at $3415.93\,\mathrm{nm}$. From the ratio of the amplitudes it is possible to calculate the transmission for each wavelength considering the double pass of the gas cell. The obtained transmission spectrum is visualized in Fig. 4.17b, where we also included a HITRAN-simulation fitted to the measurement as well as a TDLAS-transmission spectrum. The latter has been performed $18\,\mathrm{h}$ before the SMLAS experiment in order to provide a proper comparison of both techniques. Therefore, we used the same parameters found in Table 4.2, but used the standard TDLAS technique described in the previous section.

In order to find the detection limit we repeat the concentration evaluation for 50 times and calculate the Allan-deviation. The observed concentrations and the Allan-deviation derived from these are shown in Figs. 4.18a and 4.18b, respectively. Each determination of the amplitudes takes approximately $95\,\mathrm{s}$ to $105\,\mathrm{s}$ and the overall duration for the detection-limit determination

amounts to $1\,\mathrm{h}$ and $25\,\mathrm{min}$. Most of the time is needed to transfer the time series from the oscilloscope to computer. With integrated electronics it would be possible to significantly increase the speed. As a result of the long measuring times, the Allan-plot in Fig. 4.18b provides less accurate information about the detection limit, since noise or drifts with characteristic times smaller than $95\,\mathrm{s}$ to $105\,\mathrm{s}$ cannot be represented correctly. This and the non-usual trend of the Allan-deviation[1] implies that the found detection limit has to be interpreted controversially.

[1] An ideal trend of the Allan-Deviation is shown in our artificially generated example in Fig. 4.6b.

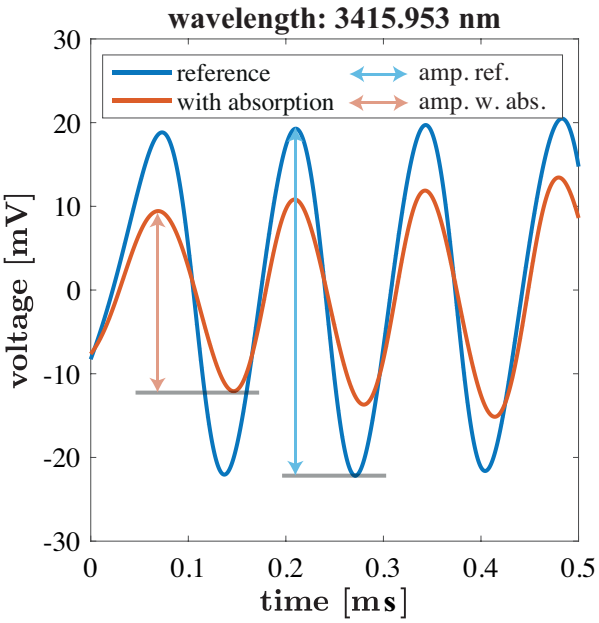

(a) Exemplary time traces of the terminal voltage self-mixing signal at $3415.93\,\mathrm{nm}$ in the case of no sample gas in the gas cell (blue) and with gas in the gas cell (orange). The amplitudes of the traces are marked with light blue and light red, respectively. The ratio between of the blue amplitude and the orange amplitude amounts to 0.45. The value $0.45 = 45\,\%$ represents the value of transmission, achieved at $3415.93\,\mathrm{nm}$, which is highlighted with the green line in Fig. 4.17b.

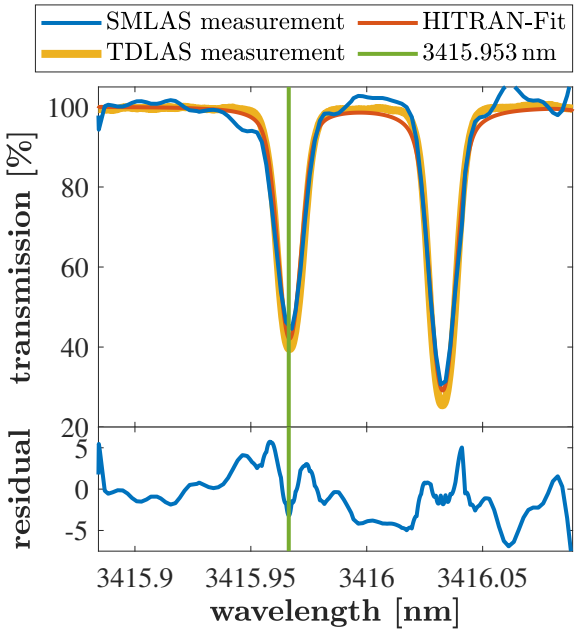

(b) Obtained transmission spectrum using the SMLAS approach including a HITRAN-simulation fitted to the measurement. The fit in this case results in a concentration of 68101 ppmv. A measurement of the transmission spectrum obtained by TDLAS is also shown in yellow. For the latter we have used the same setup as in the previous section. The SMLAS spectrum is obtained by calculating the ratios between the self-mixing signal amplitude with no sample gas in the cell and the self-mixing signal amplitude with gas in the cell for each wavelength. The green line marks the wavelength, for which we exemplified the self-mixing signals in Fig. 4.17a.

Figure 4.17: Exemplary time traces and obtained transmission spectrum using the SMLAS approach including a comparison with a HITRAN simulation and a TDLAS measurement of the same gas cell.

Therefore, we assume that the calculated detection limit of SMLAS, which amounts to 64 ppmv, is not ultimately precise, but we still suspect that the "true" detection limit of the technique remains in the same order of magnitude of that value.

A method to increase the measurement speed would therefore be ideal to study the trend of the Allan-deviation. In fact a technique with the same setup as the previously described SMLAS exists. The only two differences are to be keep feedback mirror fixed and to scan only the wavelength of the laser. This approach is also described in [236]. In this measurement process, the challenge is to precisely separate the voltage signals caused by the wavelength scanning from the amplitude resulting from self-mixing. This would require a very selective and performant electronic setup with equipment that was not available and would have exceeded the scope of this work.

We compare the gas concentration to a TDLAS scan we performed $18\,\mathrm{h}$ before with the same ICL using the same setup as in the previous section. The obtained gas concentrations are shown in Fig. 4.19a and the corresponding Allan-Plot is shown in Fig. 4.19b. We finally determine a mean concentration of 68478 ppmv and find that it is slightly higher than in the case of SMLAS, where we determined 65019 ppmv. It is possible that small amounts of air entered the gas cell, which caused a small pressure change and also lowered the concentration of methane. With the help of Fig. 4.19b we find that TDLAS scan accessing the same absorption line results in a detection limit of 2 ppm after $578\,\mathrm{s}$ integration. It is noted that each measurement with the TDLAS technique takes $0.5\,\mathrm{s}$ to $3\,\mathrm{s}$.

It is obvious that the ordinary TDLAS experiment performs about 32 times better in terms of detection-limit than SMLAS. The reason for this is that the self-mixing signal is relatively small, actually in the order of $10\,\mathrm{mV}$. A better signal to noise ratio and thus a better detection limit could only be achieved by a lower noise. This is because the maximum amplitude of the self-mixing signal at low feedback levels is intrinsically determined by the ICL. Increasing the feedback level, for example, would increase the amplitude of the signal, but the linearity of the sensor would be lost, which is only given at low feedback levels according to Eq. (4.26).

Still in the future will be space for improvements of the SNR by reducing the noise of the signal. On the one hand, the power supply of the laser can be replaced by a less noisy one (e.g. by a battery power source), on the other hand, the experimental setup can be better isolated against mechanical vibrations. Especially the latter has already been taken into account, e.g. the oscillating feedback mirror has been completely mechanically decoupled from the optical table. Still, mechanical frequencies were transmitted via sound to other optical components. Therefore, the loudspeaker frequency of $574\,\mathrm{Hz}$ was empirically chosen in a way that no obvious resonances of the components were visible in self-mixing amplitude.

Nevertheless, we emphasize that the detection unit [2], was one of the lowest noise detectors for the desired wavelength range at the time of purchase. Hence, the detection unit provided the state-of-the-art device for spectroscopy purposes. Considering that, SMLAS does not perform better than TDLAS, but requires less optical components, we want to underline that we consider that the cost of the detection unit accounts for approximately 20% of the total cost of the

[2] VIGO PVI-4TE-4-1x1-TO8-wAl2O3AR-35 with PIP-DC-200M-F-M4 preamplifier

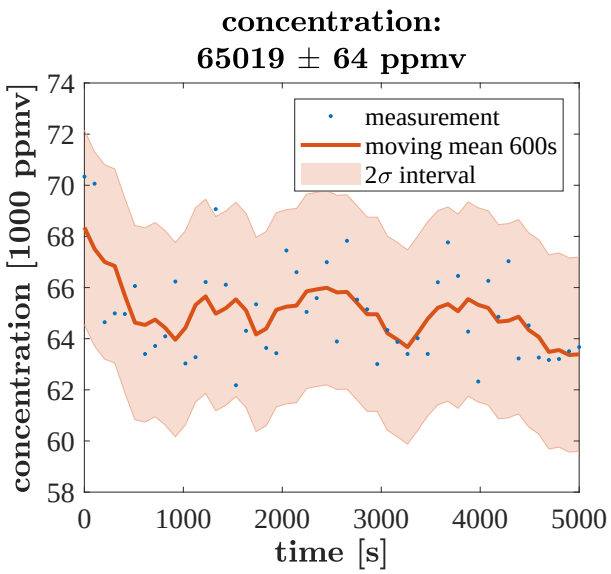

(a) Obtained concentrations (blue) using fitted version of the HITRAN spectrum. We also plot a calculated moving mean average including 600 s of data and the 2σ-interval (orange). The overall mean amounts to 65019 ppmv.

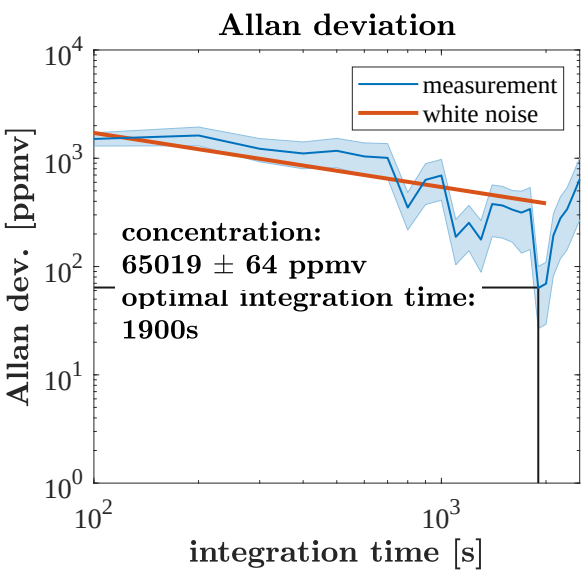

(b) Allan-Plot utilizing the data Fig. 4.18a indicating the trend of the Allan-deviation. The optimal integration time is found to be 1900 s and the averaging limit is 64 ppmv.

Figure 4.18: (a) Obtained concentrations of 50 measurements of the concentration using the SMLAS approach and **(b)** corresponding Allan-Plot.

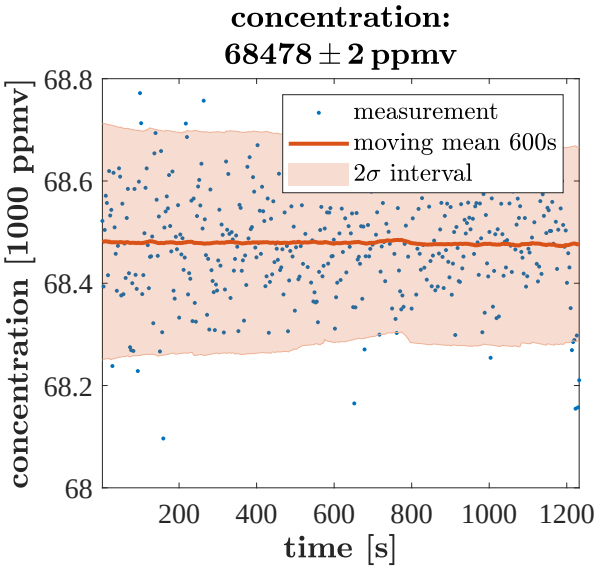

(a) Obtained concentrations (blue) using fitted version of the HITRAN spectrum. We also plot a calculated moving mean average including 600 s of data and the 2σ-interval (orange). The overall mean amounts to 64536 ppmv.

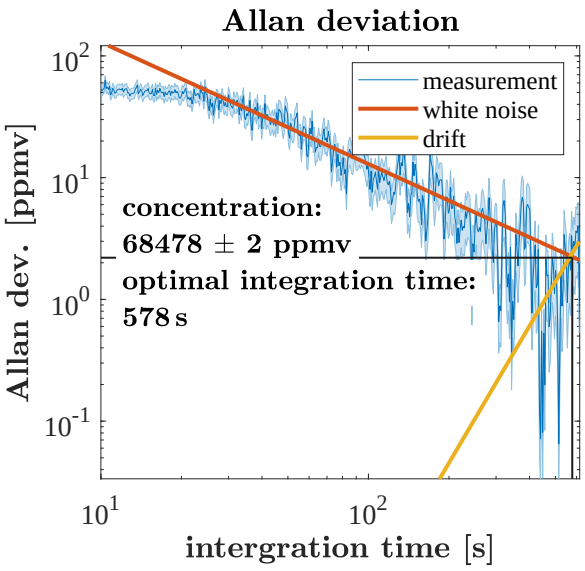

(b) Allan-Plot utilizing the data Fig. 4.18a indicating the trend of the Allan-deviation. The optimal integration time is found to be more than 578 s and the averaging limit is 2 ppmv.

Figure 4.19: (a) Obtained concentrations of 400 measurements of the concentration using the TDLAS approach and **(b)** corresponding Allan-Plot.

measurement system. This makes SMLAS desirable for applications where cost is more important than precision.

4.6.1 Summary of the section

For the first time we demonstrated the feasibility of high-resolution molecular spectroscopy based on the SMLAS technique utilizing an ICL operating at $3416\,\mathrm{nm}$ by accessing an absorption line of methane. The determined concentration is in the same range as a comparative measurement with TDLAS. However, the detection limit is worse, because the self-mixing signal is very low due to intrisical properties of the ICL. The SMLAS technique is therefore suitable if a very low detection limit is not requested ultimately, but the costs of the whole measuring system have to be reduced. It was found that the quantity, which determines the detection limit is, besides the noise, especially the small amplitude of the self-mixing signal. To achieve a better SNR, while still avoiding the additional MCT detection unit, a spectroscopy application based on unidirectional injection locked ICLs will be discussed in the following section.

4.7 Injection Locking Laser Absorption Spectroscopy

In the last section the self-mixing laser absorption spectroscopy (SMLAS) concept has been discussed. In a demonstration experiment, a certain concentration of the sample gas methane was determined, which was located within a gas cell. The advantage of this method was that no additional detection unit was required. A disadvantage was the low signal, which led to a low signal-to-noise ratio (SNR) and thus to a relatively bad detection limit.

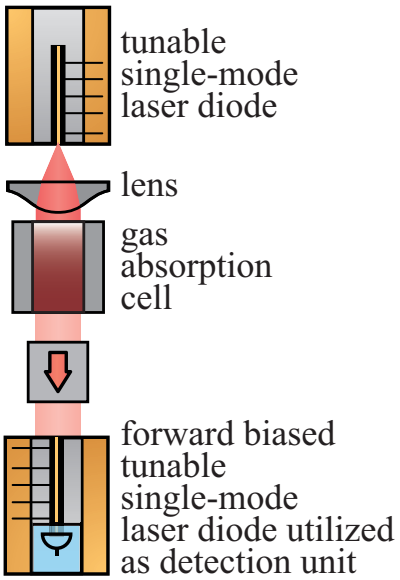

Figure 4.20: Concept of self-mixing laser absorption spectroscopy

To overcome the disadvantage of the previous concept, we introduce an additional detection unit again. Following the findings in Chapter 3, where it has been shown that optical injection locking (OIL) can produce a relative high terminal voltage signal, which can enhance the SNR. We also found that a sensor based on the laser-as-detector (LAD) approach has a very selective optical detection bandwidth, i.e. it can only detect wavelengths within the so-called locking bandwidth (LBW). This fact can also be interpreted that no wavelengths outside the LBW can disturb the sensor and thus decrease the noise, which further improves the SNR. Thus, we still use the LAD approach by using a secondary also operating ICL as a detector. The principle of this concept, which we refer to as injection locking laser absorption spectroscopy (ILLAS), is schematically depicted in Fig. 4.20. The ICL of the detection unit is in operation, i.e. it is forward-biased. Since the detection principle is based on the already described injection-locking, the concept offers the advantage that signal is much larger than the self-mixing signal which has been exploited in the previous concept. Therefore, an improved SNR is suggested.

The principle of optical injection locking (OIL) makes the sensor very selective with regard to the wavelength. This can be seen initially as a disadvantage, but the central acceptance wavelength and even the acceptance bandwidth of the detector is freely selectable within the operating range of the laser and can both be very finely controlled.

Technique

To find a suitable metric that is directly linked to the amount of light injected we recall Eq. (3.46).

$$\Omega_{\mathrm{LBW}} = |\kappa_{\mathrm{inj}}| \cdot \left(1 + \sqrt{1+\alpha^2}\right) \tag{4.27}$$

We found that the LBW is proportional to the injection strength $|\kappa_{\text{inj}}|$ (amplitude domain), which in the case of an absorptive medium in the path is affected by the absorption line via the Lambert-Beer-aborption law (compare Eqs. (4.1) and (4.2)):

$$P_{\text{ICL1}} \cdot \sqrt{|\kappa_{\text{inj}}|^2} = P_{\text{ICL1}} \cdot T(\lambda) = P_{\text{ICL1}} \cdot \exp\left(-N_a \sigma(\lambda) \cdot L_a\right), \tag{4.28}$$

where P_{ICL1} is the original output intensity of the injected ICL1. We wrote $\sqrt{|\kappa_{\text{inj}}|^2}$ by intention, because $|\kappa_{\text{inj}}|^2$ describes the coupling strength in the power domain. Thus, we find

$$T(\lambda) \propto \sqrt{LBW(\lambda)}. \tag{4.29}$$

In order to determine the LBW when scanning an absorption line, it must be noted that the absorption line also has a finite spectral width. Therefore, we first perform a thought experiment. The LBW is being determined for each wavelength of ICL1, which scans stepwise over the absorption line. The artificial visualization in Figs. 4.21a and 4.21b shows two scenarios:

1. Visualized in Fig. 4.21a. The wavelength of ICL1, namely λ_{ICL1} is far away from the absorption line. In blue we see a function, which is proportional to the coupling strength κ (amplitude domain). The points of intersection with the absorption line (red) finally determine the edges of the LBW, which is visualized in green. In this scenario the LBW has its maximal width, because the transmission is 100% for the left and the right edge of the LBW.
2. Visualizated in Fig. 4.21b. The wavelength of ICL1, namely λ_{ICL1} is very close to the absorption line. The points of intersection of the blue LBW function and the absorption line (red) again determine the edges of the LBW, which is visualized in green. In this scenario the LBW (green) is smaller, because the right edge of the LBW experiences a lower transmission and thus is shifted to smaller frequencies.

A peculiarity appears when the LBW is in the same order of magnitude or larger than the linewidth of the absorption line. In Fig. 4.22 we therefore compare the influence of the different ratios $\frac{\text{linewidth}}{\text{LBW}}$ on a transmission spectrum considering an artificial absorption line. At a ratio of 1:1 (violet) we see that the calculated transmission spectrum does not match the original transmission spectrum (red). As the ratio increases, the agreement improves. At a ratio of 10:1 they agree to such an extent that differences can be neglected. Thus, a 10:1 ratio or a larger ratio of these both bandwidths is required for an accurate determination of the transmission spectrum and this is the reason why we choose a rather broad absorption line compared to the LBW in the following experiment realized by pressure broadening. In contrast to previous experiments we do not investigate methane absorption with pressures below ambient pressure, but we now fill the gas cell with methane at ambient pressure. This is enough to create the required 10:1 ratio.

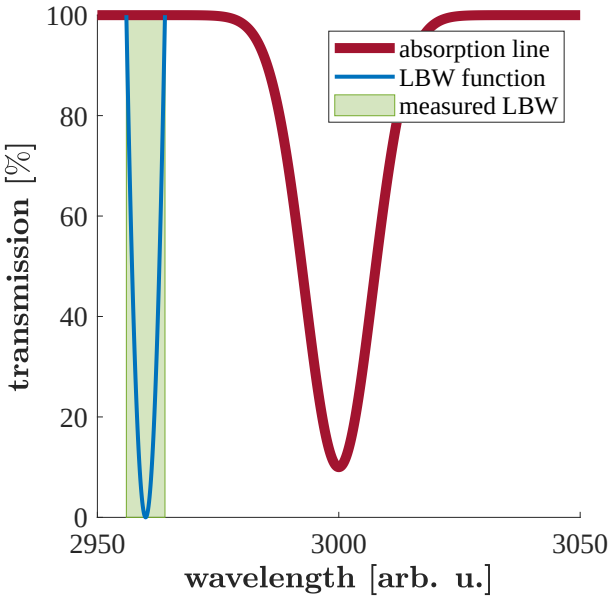

(a) Scenario 1: The wavelength of ICL1, namely λ_{ICL1} is far away from the position of the absorption line λ_{abs}. This results in a large LBW, if λ_{ICL1} matches λ_{ICL2} within the LBW.

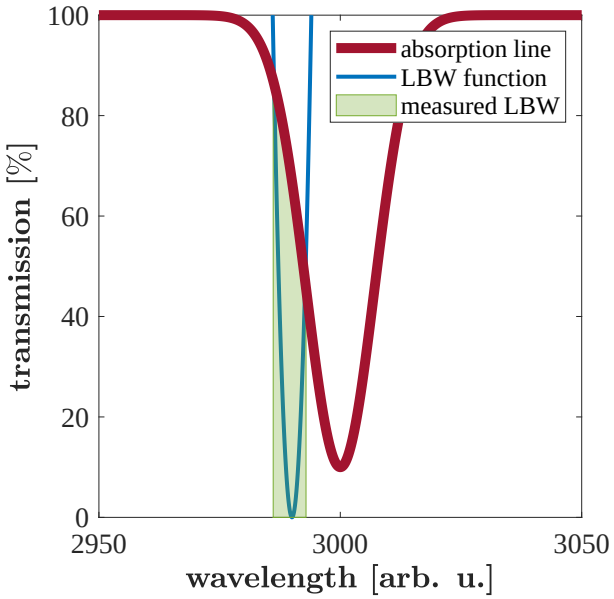

(b) Scenario 2: The wavelength of ICL1, namely λ_{ICL1} is very close to the position of the absorption line λ_{abs}. This results in a smaller LBW.

Figure 4.21: Visualization of the measurement principle. LBW as a function of transmission (blue), absorption line (red) and resulting LBW (green area), which is determined by the intersection of blue and red.

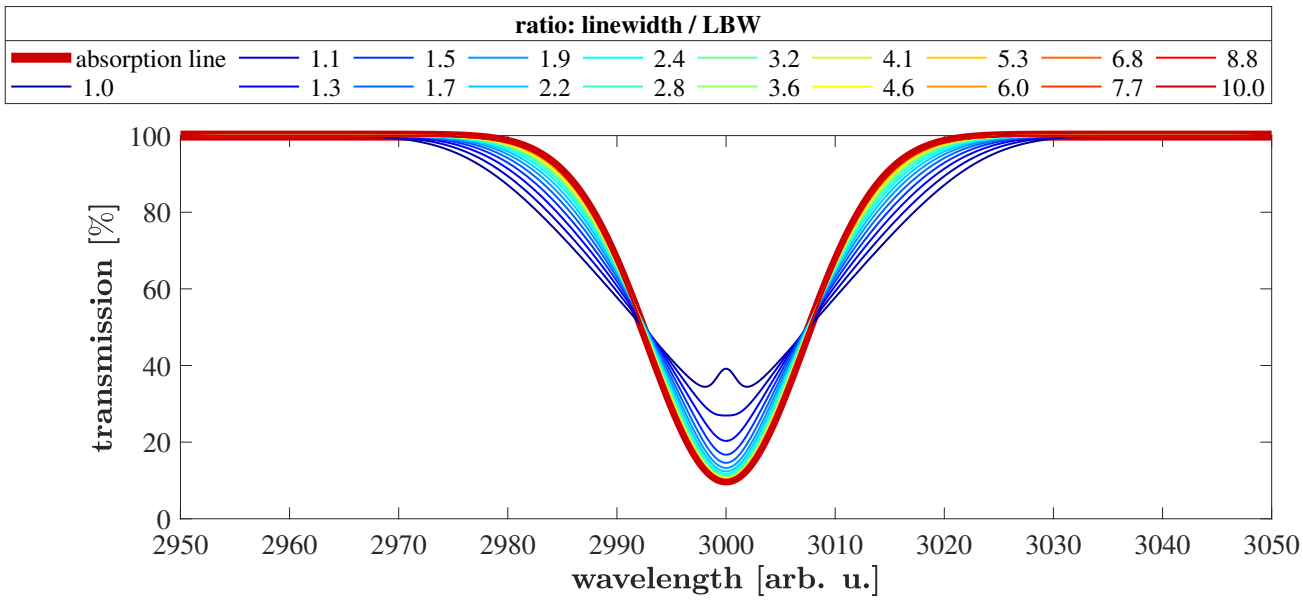

Figure 4.22: Visualization of the influence of the ratio between linewidth and LBW on the observed transmission spectrum.

Experiment

In previous experiments with unidirectionally coupled ICLs we observed LBWs up to $0.6\,\mathrm{GHz}$ (compare Section 3.6). At atmospheric pressure, the lines of methane are broadened such that the absorption lines are rather in the order of a few gigahertz. In this respect, the condition that the ratio between the line width of the absorption line and the LBW should be about 10 is guaranteed.

The actual setup for the demonstration of the feasibility of this concept is schematically depicted in Fig. 4.23. The MIR laser beam of ICL2 passes the gas absorption cell, which is placed within the injection arm and enters ICL1 after passing several optical components, which are required for alignment and polarization matching. Both, the non-polarizing beam splitter and optical detection unit are not necessary for the overall spectroscopic concept, but have been deployed for alignment and evaluation purposes.

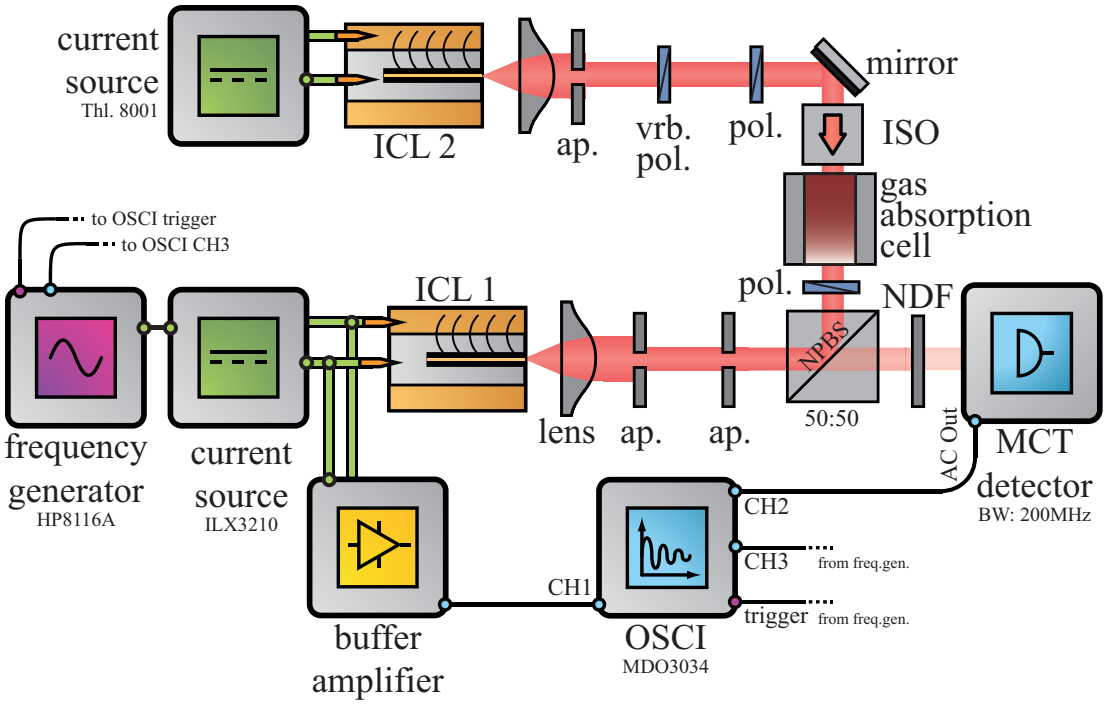

Figure 4.23: ILLAS setup. The variable polarizer (vrb. pol.) together with the fixed polarizer (pol.) act as a continuous attenuator to create avoid higher dimensional dynamics. The polarizers also ensure that the polarization of the in ICL1 injected light matches the original polarization of ICL1. The isolator (ISO) is placed in the coupling path to avoid mutual coupling. An additional detection unit is used to align the injection path and is placed behind a neutral density filter (NDF) to avoid damage to the detector. The apertures provide filtering. The buffer amplifier ensures a high input impedance so that all current from the current source flows through the ICL.

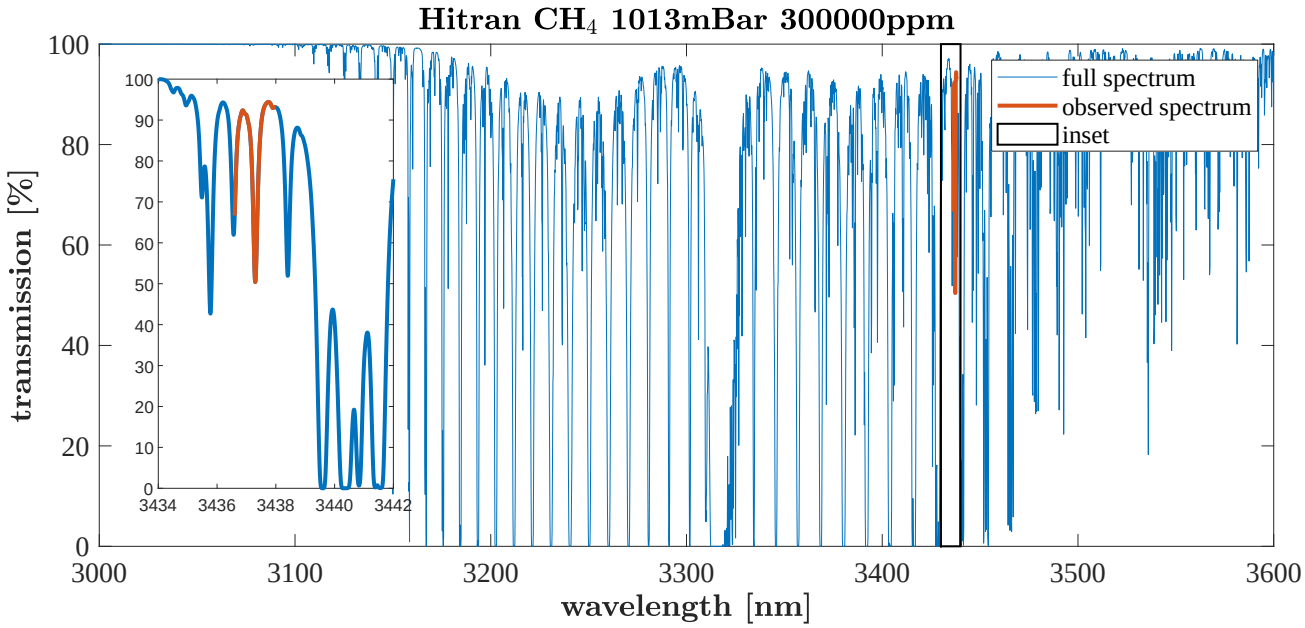

Figure 4.24: Simulated rovibrational spectrum of methane at atmospheric pressure around $3300\,\mathrm{nm}$ (blue) with an inset showing the accessed absorption line (red). Here we show a spectrum using a concentration of 300000 ppmv to provide feeling for the relative strengths of different absorption lines.

To evaluate the quality of this concept we deploy ICL 3150/19-06 as ICL2 and ICL 3150/07-21 as ICL1. We utilize an absorption line of methane in the range from $3437.2\,\mathrm{nm}$ to $3437.4\,\mathrm{nm}$, which is visualized in the inset of Fig. 4.24 at atmospheric pressure.

All other parameters of this demonstration-experiment are tabulated in Table 4.3.

parameter	value
gas cell length	$10\,\mathrm{cm}$
gas cell pressure	$1008\,\mathrm{hPa}$
temperature of laboratory	$25\,^{\circ}\mathrm{C}$
ICL1 device	3150/19-06
ICL1 temperature	$32\,^{\circ}\mathrm{C}$
ICL2 device	3150/13-06
ICL2 temperature	$30\,^{\circ}\mathrm{C}$
scanned wavelength ICL1	$3435.0\,\mathrm{nm}$ to $3439.0\,\mathrm{nm}$
scanning frequency ICL1	$5\,\mathrm{kHz}$
scanned wavelength ICL2	$3436.8\,\mathrm{nm}$ to $3438.0\,\mathrm{nm}$

Table 4.3: Operation parameters for the IL-LAS experiment including information about the gas cell.

Measurement process

We increase the current, i.e. the wavelength of ICL1, step-by-step. Each step we scan the wavelength of ICL2 across the gas absorption line. We record the terminal voltage time-trace of ICL1 with an oscilloscope (Textronix MDO 3034) and from it we deduce the LBW. First, we record the LBW as a function of the wavelength of ICL1 with a non-filled gas cell using it as a reference. Then, we fill the

gas cell and repeat the process. The results of both, reference and LBW with absorption line is shown in Fig. 4.25. It is visible that a strong decrease of the LBW manifests itself at $3437.3\,\mathrm{nm}$.

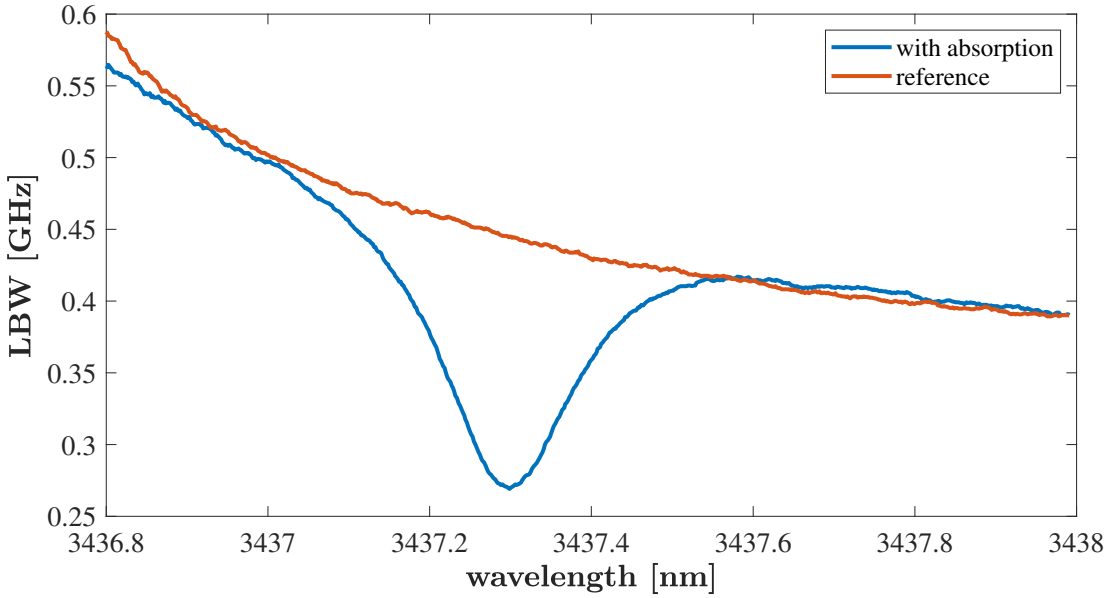

Figure 4.25: LBW as a function of the wavelength. The orange line shows a reference measurement, while the blue line shows the LBW scan with methane in the gas cell.

From that we calculate the transmission profile exploiting Eq. (4.29) and find the transmission spectrum depicted in Fig. 4.26. The fit of a HITRAN simulation shows extraordinary agreement. We also perform a comparative TDLAS-scan indicating also good agreement. The latter has been performed chronologically before the ILLAS experiment in order to provide a proper comparison of both techniques. Therefore, we used the same parameters shown in Table 4.3, but used the TDLAS technique described in section (Section 4.5).

The fit of this particular measurement results in a gas concentration of 303456 ppmv. Since each measurement with the ILLAS principle takes $7.5\,\mathrm{min}$ and produces approximately $500\,\mathrm{MB}$ data, we omit a large number of repetitive measurements. In order to still enable a comparison, we carry out 20 gas concentration determinations with TDLAS on the one hand, and on the other hand we perform 20 measurements according to the ILLAS-concept, which we also use to calculate the Allan-deviation. The results are depicted in Fig. 4.27a together with an indication of the standard deviation and the mean value.

We find that the determination of the gas concentration yields a good agreement with both measuring methods. However, Fig. 4.27a shows that the mean concentration determined with both methods differs by 2091 ppmv. A possible cause could be that the TDLAS experiment was performed chronologically before the ILLAS determination and therefore smaller amounts of methane could have leaked out in the standby time of $5\,\mathrm{h}$. Most importantly and very promising is that we find very similar ranges of measurement uncertainty for the two comparative methods. This is verified by an analysis of the Allan-Deviation. In Fig. 4.27b it is shown that

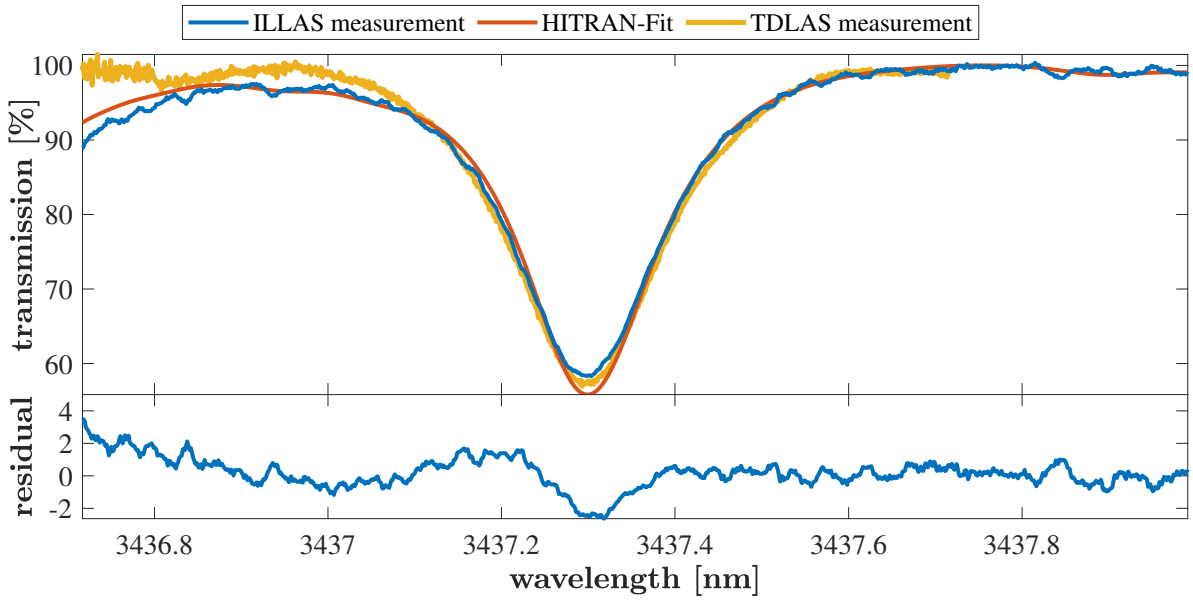

Figure 4.26: Transmission spectrum of methane from $3436.8\,\mathrm{nm}$ to $3438.0\,\mathrm{nm}$ obtained by the ILLAS setup shown in Fig. 4.23 (top). The residual between Hitran-Fit and ILLAS measurement is also visualized (bottom). The parameters for this measurements are found in Table 4.3.

optimal integration time for ILLAS is found to be more than $4050\,\mathrm{s}$ and the averaging limit of 20 ILLAS measurements amounts to 61.4 ppmv. The optimal integration time for TDLAS is found to be more than $13.5\,\mathrm{s}$ and the averaging limit of only 3000 TDLAS measurements is 88.7 ppmv. The latter is a little bit better than the detection limit achieved in our first TDLAS measurementSection 4.5, but the result remains in the same magnitude. This slight detection limit improvement can be explained by an mechanically optimized setup.

The fact, that we observe a similar, even improved detection-limit using the ILLIAS technique, compared to TDLAS technique, shows the feasibility of this approach and meets the goal we set us in the beginning. In fact the detection-limit is $30.8\,\%$ improved. To prove the improvement, we also calculate the signal to noise ratio of the first 20 shown in gas concentration determinations using

$$\mathrm{SNR} = \frac{\mathrm{mean}\,(conc.)}{\sigma}, \tag{4.30}$$

where mean $(conc.)$ is the mean concentration obtained by both concepts and σ is the standard deviation of each measurement set (one for ILLAS and one for TDLAS). For TDLAS we find a SNR of 294 and for ILLAS we obtain a slightly better SNR of 349. This improvement is pretty surprising, because we compare our proposed technique here with TDLAS, which uses

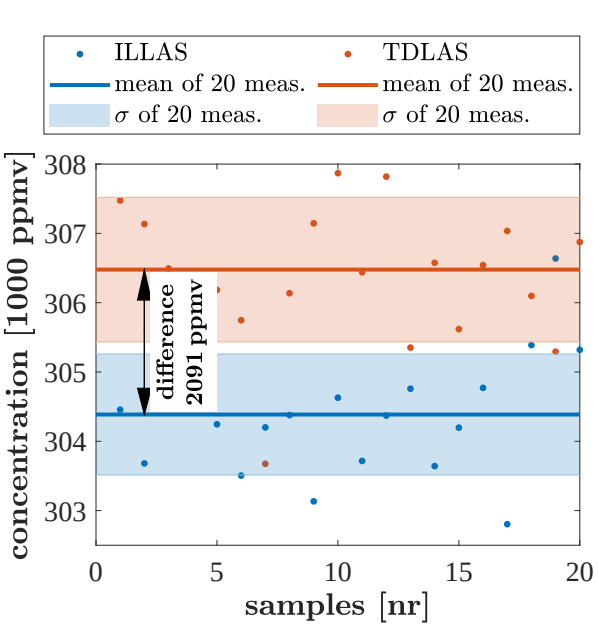

(a) First 20 obtained gas concentrations of methane using the spectral range from $3436.8\,\mathrm{nm}$ to $3438.0\,\mathrm{nm}$ obtained by the ILLAS setup and a comparision with the TDLAS results shown in Fig. 4.23. The parameters for this measurements are found in Table 4.1.

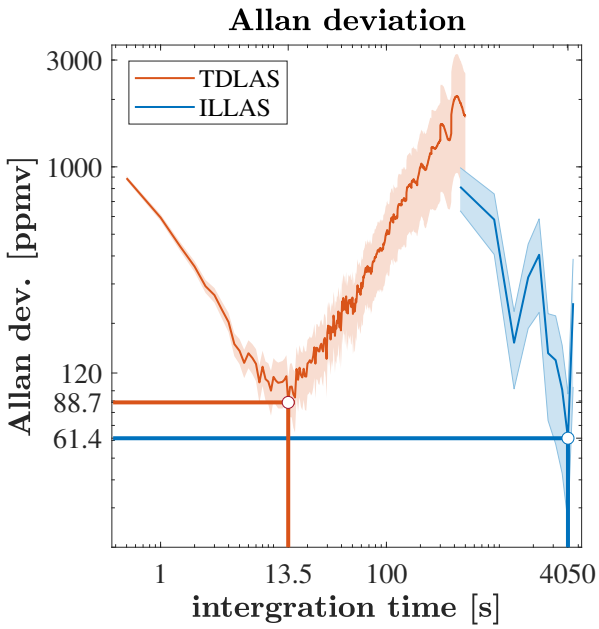

(b) Allan-Plot utilizing the data depicted in Fig. 4.27a indicating the trend of the Allan-deviation for TDLAS and ILLAS. The optimal integration time for ILLAS is found to be more than $4050\,\mathrm{s}$ and the averaging limit of only 20 ILLAS measurements is 61.4 ppmv. The optimal integration time for TDLAS is found to be more than $13.5\,\mathrm{s}$ and the averaging limit of only 3000 TDLAS measurements is 88.7 ppmv.

Figure 4.27: (a) Obtained concentrations of 20 measurements of the concentration using the ILLAS approach and **(b)** corresponding Allan-Plots compared to a set of 3000 reference scans with TDLAS.

a noise-optimized optical detection unit. This could be explained by the fact that the laser-as-detector approach is very selective regarding the detectable optical frequencies, i.e. it only detects optical frequencies within the locking bandwidth. Noise on other optical frequencies, i.e. wavelengths can therefore not negatively affect the approach. However, it must be emphasized that conventional TDLAS achieved its detection-limit within $13.5\,\mathrm{s}$ integration, whereas the ILLAS method took about $67.5\,\mathrm{min}$ to achieve this detection limit, which is exactly 300 times longer. This time is mainly needed for the large amount of data, which is transferred from the oscilloscope to the computer.

It must also be noted here that TDLAS and ILLAS were made at different times of the day. The TDLAS measurement took place around noon, the ILLAS measurement in the evening and the night. In Fig. 4.27b a strong drift of the TDLAS Allan-Deviation can be observed. It can be interpreted that during the measurement the environmental influences drifted relatively strong. A drift of the room temperature, for example, could have had an effect on the temperature of

the ICL, causing the optical output power and wavelength to drift over time. Since the ILLAS measurement was started in the evening and continued into the night, it cannot entirely be ruled out that minor environmental fluctuations could have had a positive influence on the detection limit. This and the non-usual trend of the Allan-deviation[3] means that the found detection limit of the ILLAS technique has to be interpreted controversially. Therefore, we assume that the calculated detection limit of 61.4 ppmv is ultimately not precise, but we still suspect that the "true" detection limit of the technique remains in the same order of magnitude. Therefore, this result is not bad at all, because we compare the very first demonstration experiment using the newly developed ILLAS technique with a TDLAS measurement using a commercially available and highly optimized optical MCT-detection unit.

4.7.1 Summary of the section

In summary, we conclude that the LAD approach is suited for the detection of MIR light and thus for spectroscopic applications, for example by using our here presented ILLAS scheme. We assume that the technique at least allows a detection limit, which is comparable to that of TDLAS or even better. However, we emphasize that the ILLAS technique has to prove its performance and reliability in more extensive studies. A very effective way to do this would be to test the sensor in different environments. The schedule of the German-Greek ILLIAS project already contains a corresponding plan to be carried out by partners of the Kapodistrian University of Athens. It is planned to complete this task by early 2021.

4.8 Conclusion of the chapter

In this chapter we have presented three different techniques to determine a methane gas concentration in the MIR wavelength range.

The method of tunable diode laser spectroscopy discussed in Section 4.5 was used as a reference.

With the self-mixing-laser-spectroscopy approach presented in Section 4.6 it was possible to determine methane concentrations without an additional optical detection unit. To achieve this, the laser-as-detector approach based on an interband cascade laser was exploited in combination with the self-mixing technique. It turned out that the technique could achieve slightly worse detection limits than aforementioned tunable diode laser spectroscopy, but still proved to be feasible. It must also be noted here that the concept can generally be extended to all wavelengths, where semiconductor lasers are available and thus spectral domains such as THz can be addressed with this technique, where optical detection units are expensive or impractical. Therefore, we suggest to use the SMLAS technique when the cost of the optical detection

[3] An ideal trend of the Allan-Deviation is shown in our artificially generated example in Fig. 4.6b.

unit is large compared to other optical components or the unit only exists with non-sufficient performance.

In the last section of the chapter (Section 4.7) we discussed a new spectroscopic method based on unidirectional injection of one interband cascade laser into a second interband cascade laser, which we referred to as injection locking laser absorption spectroscopy. The technique also exploited the laser-as-detector approach and it was shown that the signal of a methane absorption line manifested itself in a quantitative reduction of LBW yielding in a determination of the gas concentration. The detection limit achieved was slightly better than that of ordinary TDLAS. It is assumed that this $30.8\,\%$ improvement is attributed to the wavelength selectivity of the laser-as-detector based sensor. Nevertheless, the here presented improvement has to prove its reliability in future experiments, which are already scheduled within the scope of the Greek-German ILLIAS-project, which is funded by the German Federal Ministry of Education and Research and the Greek General Secretariat for Research and Technology.

In summary, it can be concluded that the laser-as-detector concept is - as a whole - very well suited to perform spectroscopic experiments and we have proven its feasibility.

"Wer höher fliegt, bleibt länger oben..."

Segelflieger Weisheit

5 Communication using mutually coupled Interband Cascade Lasers

With the digital revolution the humanity began to exchange a huge amount of information utilizing digital telecommunication systems. Today, this data exchange occurs mainly via the internet, which was developed from the military ARPANET in 1982 [295]. Since then data-traffic grew exponentially. In the beginning of 2020 it is estimated that around 212 EB (ExaByte) of information are transferred via the internet per month and the amount is still growing significantly every year [294, 296]. The structure of the internet can be described as a huge web-like network, where computers are connected to other computers via big data-nodes. The fastest and energy efficient connections are realized by optical-interconnects and can transfer 283 Terabit per second via a single transmission line [296, 297]. A transmission line usually consists of optical emitters at the transmitters position, optical detector at the receiver position, while an optical fiber is used as the connecting message transport medium[298, 299]. To extend this type of common transmission line for bidirectional communication, an additional second set of emitters and detectors has to be deployed, where former transmitter and receiver change roles. In order to reduce size, both transmitter and receiver are often placed on the same chip in a photonic integrated circuit. However, this type of bidirectional communication requires only a single bidirectional transport medium - namely the fiber - whereas at least two optical transmitters and two receivers are needed.

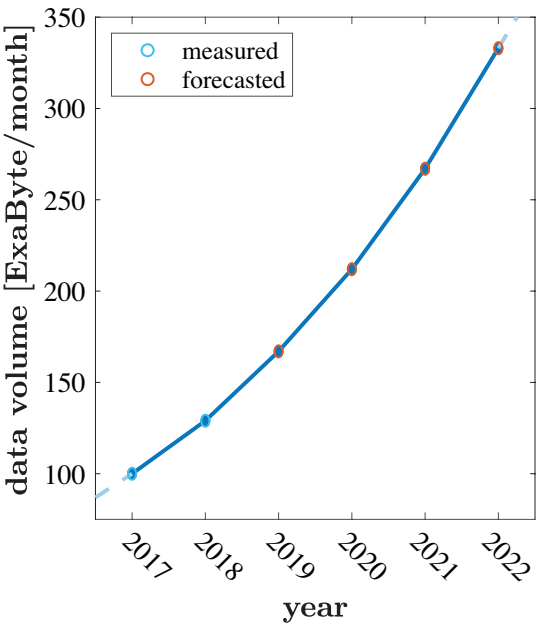

Figure 5.1: Forecast for the data volume of worldwide consumer IP traffic until 2022. Consumer traffic includes fixed IP traffic generated by households, university populations, and internet cafés[294].

There are application areas where the deployment of a fiber as a transport medium is not useful. Connections from the last data node to the consumer are often of that kind. Considering a low density of consumers within the line to the last data node, the connection with a fiber

is probably not economical and might be significantly oversized in capacity. This economical problem is often referred to as the "last mile problem"[300]. In other areas the deployment of fibers is not possible, such as connection to from ground to moving objects as well as from ground to satellites or other objects in space.

The conventional way to overcome these kind of challenges, is to connect the data-nodes using radio-transmitters. Since the technique has been well established since decades, radio-transmission is very economical and also proofed its robustness in countless real-world applications[301]. Since data-traffic grew significantly in the past years, however, those radio-transceivers begin to reach their capacity limit.

Therefore, free-space optical (FSO) communication schemes, where the atmosphere is the transport medium of an optical wave, have experienced a renewed interest in the last years[302, 303]. The atmosphere offers only few spectral domains where it has transparency high enough to provide data-transmission, which lie mainly in the MIR, VIS [304] and some in the UV [305]. Experiments in the ultraviolet have for example recently achieved a transmission at $1\,\mathrm{Gbit\,s^{-1}}$ with III-nitride micro-LEDs[306]. Nevertheless, the MIR offers an even higher potential for FSO communication, because the mid-infrared is not as affected from Rayleigh scattering as light with lower wavelength is. Several strategies have therefore emerged in order to produce high-bandwidth sources emitting in the transparency window around $4\,\mu\mathrm{m}$. Communications up to $70\,\mathrm{Mbit\,s^{-1}}$ have been demonstrated with ICLs [307] while QCLs also showed great performance achieving similar transmissions speeds both at room[48] and cryogenic temperatures[49].

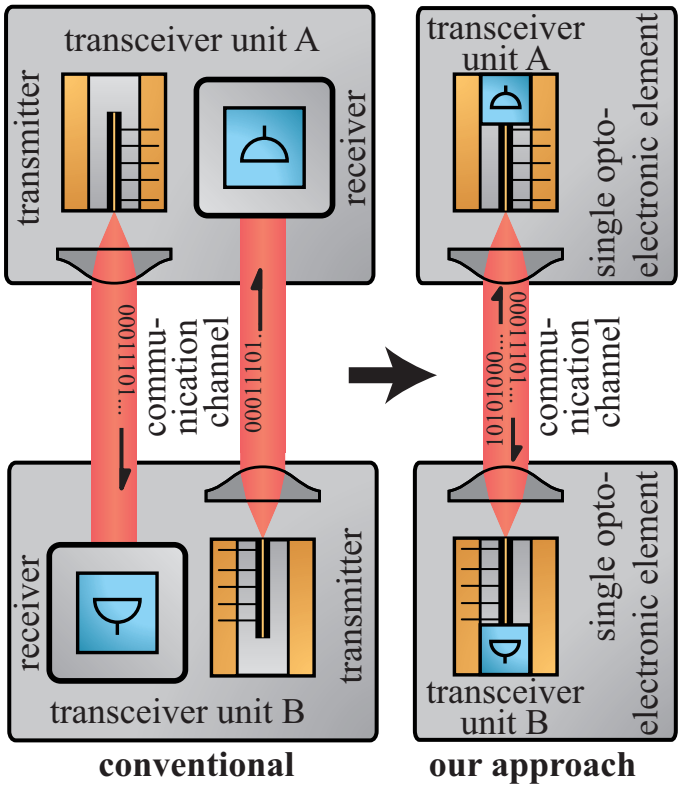

Figure 5.2: Conventional bidirectional communication setups (left) compared to the bidirectional approach (right).

Still these FSO communication systems have in common with fiber based systems that two transmitters and two receivers are required for a bidirectional communication line. Especially in the MIR wavelength range, detectors are expensive or require complex cooling and high effort maintenance.

In this chapter we present a communication system that overcomes all these disadvantages utilizing two mutually coupled ICLs. The data transmission scheme exploits the in Chapter 2 evaluated LAD approach to avoid an additional detection unit. The idea is schematically depicted in Fig. 5.2, where we visualized the proposed concept (right) and a conventional bidirectional transmission scheme on the left. We proceed as follows to quantify the performance and robustness of the approach and verify its applicability.

5.1 Goals of the chapter

1. Initially, we recall the physical basis of the compound laser states (CLSs) already considering the bidirectional communication scheme (Section 5.2).
2. Secondly, we describe the encoding (Section 5.4) and decoding (Section 5.5) of information onto the CLSs.
3. Then, we show a demonstration experiment, where we bidirectionally transfer a string of letters (Section 5.6) and
4. Lastly, we theoretically discuss further potentials of the scheme with respect to privacy, transmission speed and robustness (Section 5.7).

   We close the chapter with a summary of the findings.

5.2 Bidirectional symmetric communication using mutually coupled twin ICLs

The principle of the bidirectional symmetric communication scheme based on mutually coupled twin ICLs is surprisingly simple. The idea is that if a single operation value - for example the wavelength - of one of both ICLs changes, the operation values at the second ICL also change, which can easily be detected. This can be interpreted as a data-transfer from the first ICL to the second ICL. Since the ICLs are coupled mutually, the data transmission direction can also be reversed. Later, it will be presented that with a proper encoding scheme, bidirectional communication can also be performed simultaneously. For the detection of the transferred data we finally utilize the LAD approach. This concept simplifies the experimental setup compared to conventional bidirectional transmission techniques, because transmitter and receiver are united in a single opto-electronic component, namely the ICL itself. To achieve this, the scheme exploits CLSs for the first time ever as data-carriers for a communication setup.

5.2.1 Compound laser states

We recall that if two ICLs become mutually injected, they begin operation on a CLS, when the injection strength is not too strong. In that case two ICL twins ICL-A and ICL-B emitting on two close-by wavelengths λ^A and λ^B they lock on a joint operation wavelength λ_{op}. In particular, the difference in wavelengths $\Delta\lambda \equiv \lambda^A - \lambda^B$ must stay in a specific region - the locking bandwidth (LBW). The difference in wavelengths is usually converted to a difference in the optical frequencies, which we recall is defined as the optical frequency detuning $\Delta\nu$ with

$$\Delta\nu \equiv \nu_A - \nu_B \equiv c \cdot \left(\frac{1}{\lambda^A} - \frac{1}{\lambda^B} \right), \tag{5.1}$$

with c denoting the speed of light and ν^A, ν^B representing the optical frequencies of ICL-A and ICL-B, respectively. The maximal detuning, where frequency locking still occurs, defines the edges of the LBW Ω_{LBW}. The width of Ω_{LBW} is affected by the coupling coefficient $|\kappa_{\text{inj}}|$, delay τ and the linewidth enhancement factor α of the ICLs and can be retrieved by evaluating the DDEs of the coupled ICL system, which we already described in Section 3.7.1. For weakly coupled symmetrically pumped and identical ICLs well above threshold the LBW is given by the equation

$$\Omega_{\text{LBW}} = \pi^{-1} \left|\kappa_{\text{inj}}\right| \sqrt{1+\alpha^2} \left|\cos\left(\theta_C + 2\pi\nu_{\text{CLS}}\tau + \arctan\left(\alpha\right)\right)\right| \tag{5.2}$$

and the solutions of the delay differential equations of the coupled ICL system are the compound laser states, which are represented by

$$\begin{aligned} N^A(t) &= N^A_{\text{CLS}}, \\ E^A(t) &= E^A_{\text{CLS}}, \\ \Phi^A(t) &= 2\pi\nu_{\text{CLS}}t, \\ N^B(t) &= N^B_{\text{CLS}}, \\ E^B(t) &= E^B_{\text{CLS}}, \\ \Phi^B(t) &= 2\pi\nu_{\text{CLS}}t + \sigma, \end{aligned} \tag{5.3}$$

Inside the LBW the electrical field amplitude E^j, the optical frequency ν_{CLS} and most importantly the population inversion N^i are different to their solitary state. Recalling Section 3.7.1, the quantities are fully specified by the detuning $\Delta\nu$, the coupling coefficients κ_{inj} and the delay τ. For a more intuitive description, we write the CLS in the following representation

$$\begin{pmatrix} E^A, \Phi^A, \Delta N^A \\ E^B, \Phi^B, \Delta N^B \\ \Delta\nu \end{pmatrix}, \tag{5.4}$$

where we assumed a constant coupling strength, constant delay and the same LEF for both ICLs. These are valid assumptions for a stable communication line. Because the output power S of an ICL is more intuitive than the electrical field amplitude E, we substitute $E = \sqrt{S}$. In Section 3.1 we also already introduced that changes of the population inversion $\Delta\,(\Delta N)$ are

linearly linked to the terminal voltage change of the ICL ΔU due to changes of the quasi-fermi-level separation. Finally and because we can not experimentally access the electrical field phase of the CLS, we rewrite Eq. (5.4) to

$$\begin{pmatrix} S^A, U^A, \nu_{\text{CLS}} \\ S^B, U^B, \nu_{\text{CLS}} \\ \Delta\nu \end{pmatrix}. \tag{5.5}$$

In that description the first row describes the operation values of ICL-A and second row that of ICL-B.

5.3 Experimental setup to create compound laser states with ICLs

In the experimental setup visualized in Fig. 5.3 we utilize ICL 3150/19-06 as ICL-A temperature stabilized at $30\,^{\circ}\mathrm{C}$ and ICL 3150/07-21 temperature stabilized at $32\,^{\circ}\mathrm{C}$. In order to experimentally create a CLS, the proposed scheme takes advantage of the easy wavelength control of the utilized ICLs. We already verified in Section 2.9.2 that the wavelength in our DFB-ICLs, is controlled linearly by the applied current. The relation between current I and optical frequency ν_i for our communication setup amounts to

$$\nu_A^{\text{solitary}}(I) = -1.8\,\frac{\text{GHz}}{\text{mA}} \cdot I + 87.418\,\text{THz} \tag{5.6}$$

$$\nu_B^{\text{solitary}}(I) = -1.8\,\frac{\text{GHz}}{\text{mA}} \cdot I + 87.416\,\text{THz}, \tag{5.7}$$

for ICL-A and ICL-B, respectively. By mutually coupling these two ICLs a CLS with any desired detuning can be created using the tunable current sources. The setup for mutual coupling that is schematically depicted in Fig. 5.3 shows the coupling path visualized in red, passing through several optical components.

The setup also contains the electrical devices for the identification of a CLS. For that purpose two Lock-In amplifiers measure the terminal voltage changes at each ICL. With this setup no additional reference measurement is needed. Exemplary traces of the terminal voltage change as a function of OFD are visualized for both ICLs in Fig. 5.4 (red and blue) together with the LBW (green). To obtain this picture, we measure the terminal voltages of both ICLs when ν_B is being scanned across the fixed optical frequency of ICL-B via current tuning. We record these voltage changes with respect to their free-running voltage with both Lock-In amplifiers. The optical frequency of ICL-A is set to $\nu_A = \nu_0 \equiv 87\,361.48\,\text{GHz}$[1] for measurement shown in

[1]The optical frequency of $\nu_A = 87\,361.48\,\text{GHz}$ converts to a wavelength of $\lambda_A = 3431.63\,\text{nm}$.

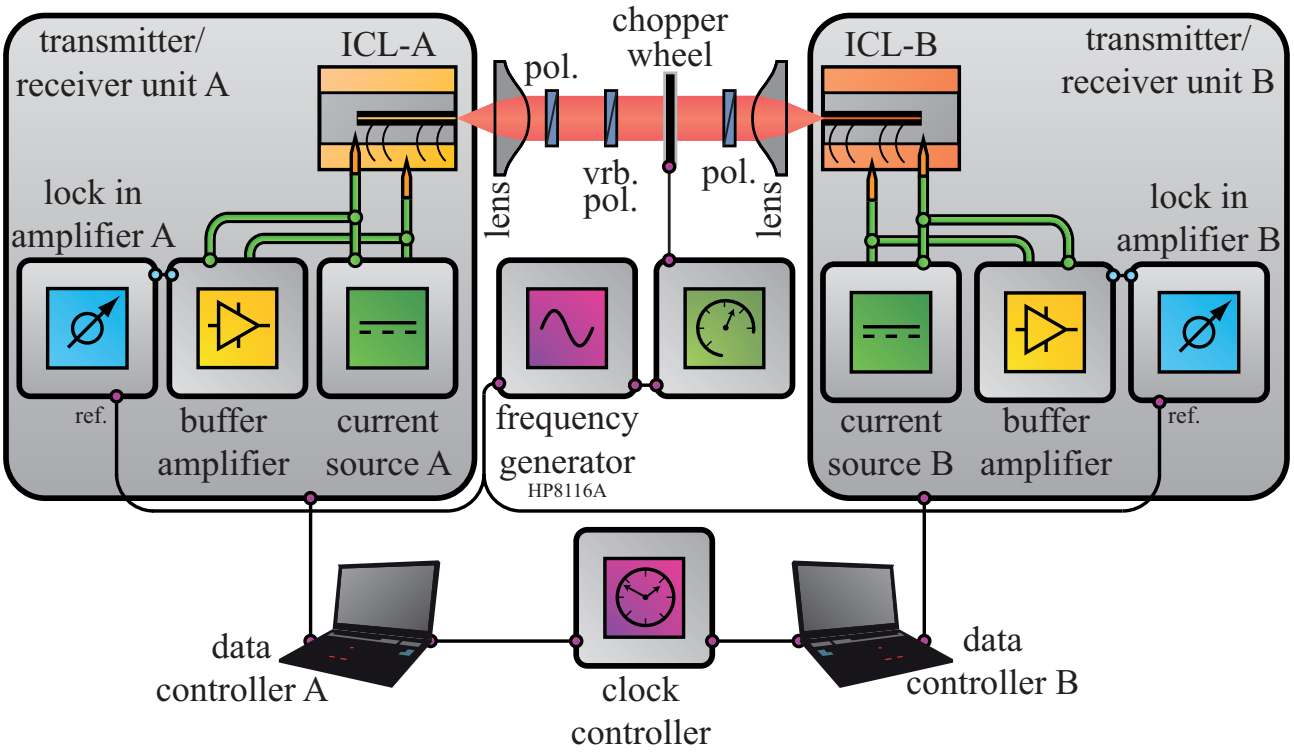

Figure 5.3: Bidirectional detector-free free-space communication setup with ICLs. It must be noted that the buffer-amplifier connected ICL-A does not amplify the signal and only provides a high input impedance. The buffer-amplifier of ICL-B has a built-in $46\,\mathrm{dB}$ specified DC-amplifier.

Fig. 5.4a, by providing a constant current. We keep the delay constant by keeping the distance fixed and also provide a constant coupling strength κ. We repeat the measurement for a optical frequency of ICL-A of $\nu_A = \nu_1 \equiv 87\,360.60\,\mathrm{GHz}$, which is depicted in Fig. 5.4b. The here chosen frequencies ν_0 and ν_1, will later be used for data communication.

The OFD axis is obtained by the frequency difference

$$\Delta\nu = \nu_A\,(I)^{\text{solitary}} - \nu_B^{\text{solitary}}. \tag{5.8}$$

The LBW amounts to approximately $2\,\mathrm{GHz}$ in both shown cases. It is observed that the change of the terminal voltages within the LBW of ICL-A is opposed to that of ICL-B with a zero crossing at $\Delta\nu = 0\,\mathrm{GHz}$. That calibration enables to detect the signum of $\Delta\nu$, ensuring $\Delta\nu \in \Omega_{\text{LBW}}$ only by the terminal voltage of each ICL. If - for example - the terminal voltage in ICL-B U_B decreases with respect to its solitary value, then the injected optical frequency by ICL-A must be smaller: $\Delta U_B < 0 \rightarrow \nu_{\text{A}}^{\text{solitary}} < \nu_B^{\text{solitary}}$. When no voltage change is observed,

both ICLs must operate on the same frequency: $\Delta U_B = 0 \rightarrow \nu_{\mathrm{A}}^{\mathrm{solitary}} = \nu_B^{\mathrm{solitary}}$. If the voltage of ICL-B is increased with respect to its solitary value, the injected optical frequency must be higher: $\Delta U_B > 0 \rightarrow \nu_{\mathrm{A}}^{\mathrm{solitary}} > \nu_B^{\mathrm{solitary}}$. This dependency holds also when interchanging ICL-A with ICL-B, i.e. interchanged subscripts A and B in the previous equations.

In conclusion we find that the voltage change is perfectly suited to determine the original detuning of both ICLs and thus identify different CLSs. This remarkable feature enables using the CLS to carry information. The process to encode data onto CLSs and decoding CLSs back to Bits will be discussed in the following section.

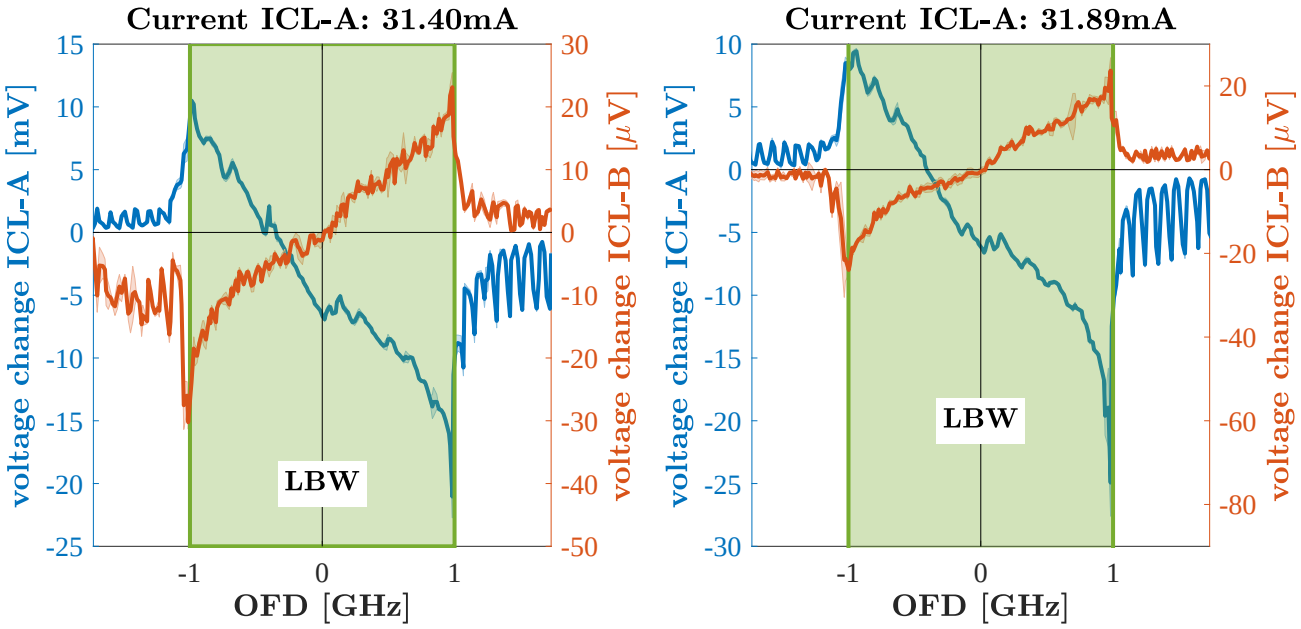

(a) Case where ICL-A is operated at $31.40\,\mathrm{mA}$, i.e. at an optical frequency of $\nu_{\mathrm{A}} = \nu_0 = 87\,361.48\,\mathrm{THz}$.

(b) Case where ICL-A is operated at $31.89\,\mathrm{mA}$, i.e. at an optical frequency of $\nu_{\mathrm{A}} = \nu_1 = 87\,360.60\,\mathrm{THz}$.

Figure 5.4: Voltage changes, when ICL-B scans its optical frequency ν_B across a fixed optical frequency of ICL-A. The black line marks a OFD of $0\,\mathrm{GHz}$. In **(a)** ICL-A operates at $31.40\,\mathrm{mA}$, which results in a (solitary) operation wavelength of $\nu_A = \nu_0 = 87\,361.48\,\mathrm{GHz}$. In **(b)** ICL-A operates at $31.89\,\mathrm{mA}$, which results in a (solitary) operation wavelength of $\nu_A = 87\,360.60\,\mathrm{GHz}$. The lower abscissa showing the OFD are obtained by reference measurements of the optical spectrum of each ICL operating solitary (see Section 2.9.2. The green areas visualize the locking bandwidths Ω_{LBW}.

5.4 Data encoding onto compound laser states

For a complete bidirectional communication it is required to make sure that transferring all possible Bit combinations (00), (01), (10) and (11) is possible. These Bit combinations are now referred to as compound Bits. The first digit of a compound Bit represents the Bit transferred by ICL-A and the second digit the Bit transferred by ICL-B, respectively. The compound Bits are encoded onto four different CLSs $\Gamma_{(00)}, \Gamma_{(01)}, \Gamma_{(10)}$ and $\Gamma_{(11)}$, which serve as the data-carriers. In order to create these four states we utilize two different frequencies ν_0 and $\nu_1 > \nu_0$ ensuring that $\nu_1 - \nu_0 \in \Omega_{\text{LBW}}$:

$$\Gamma_{(00)} = \begin{pmatrix} S^A_{(00)}, U^A_{(00)} \\ S^B_{(00)}, U^B_{(00)} \\ \Delta\nu = 0 \end{pmatrix} \text{ with } \nu_A = \nu_B = \nu_0 \tag{5.9}$$

$$\Gamma_{(01)} = \begin{pmatrix} S^A_{(01)}, U^A_{(01)} \\ S^B_{(01)}, U^B_{(01)} \\ \Delta\nu = \nu_0 - \nu_1 \end{pmatrix} \text{ with } (\nu_A = \nu_0,\ \nu_B = \nu_1) \tag{5.10}$$

$$\Gamma_{(10)} = \begin{pmatrix} S^A_{(10)}, U^A_{(10)} \\ S^B_{(10)}, U^B_{(10)} \\ \Delta\nu = \nu_1 - \nu_0 \end{pmatrix} \text{ with } (\nu_A = \nu_1,\ \nu_B = \nu_0) \tag{5.11}$$

$$\Gamma_{(11)} = \begin{pmatrix} S^A_{(11)}, U^A_{(11)} \\ S^B_{(11)}, U^B_{(11)} \\ \Delta\nu = 0 \end{pmatrix} \text{ with } \nu_A = \nu_B = \nu_1 \tag{5.12}$$

It can be seen that both Γ_{00} and Γ_{11} yield a detuning of $\Delta\nu = 0$. Recalling the findings of Figs. 5.4a and 5.4b, this results in an observed change of the terminal voltage close to zero. The compound Bits (01) and (10) represent a non-zero detuning $\Delta\nu \neq 0$ and the corresponding voltage change in both ICLs is non-zero. For a better overview the compound Bits, the optical frequencies ν_i and the resulting voltage changes (Vc) are summarized in Table 5.1. It will become clear later, that the identification of the CLSs does not require a measurement of the sign of the voltage change in order to decode the compound Bit.

compound Bit	opt. freq. ν_A	ν_B	Vc ICL-A	ICL-B
(00)	ν_0	ν_0	~ 0	~ 0
(01)	ν_0	ν_1	$\neq 0$	$\neq 0$
(10)	ν_1	ν_0	$\neq 0$	$\neq 0$
(11)	ν_1	ν_1	~ 0	~ 0

Table 5.1: Compound Bits and the corresponding optical frequencies ν_A and ν_B, which result in the voltage changes. Vc ICL-A: terminal voltage change at ICL-A compared to solitary reference; Vc ICL-B: terminal voltage change at ICL-B compared to solitary reference.

5.5 Data decoding from compound laser states

According to Table 5.1 it is known how the previously defined compound Bits affect the voltages of both ICLs, a tool to decode the compound Bit at each transceiver unit is needed. Only with this, it becomes possible to decode the message sent by the secondary unit. This decoding scheme holds for both transceiver units and takes advantage of the terminal voltage changes, but also the knowledge of the own transferred Bit value is required. The decoding table follows a logical exclusive-or-gate (XOR-gate) with its own transferred Bit value as an argument and its individual recognized terminal voltage change (Vc) as the second argument and is presented in Table 5.2, which holds for both transceiver units.

Tx	Vc	Rx
0	0	0
0	1	1
1	0	1
1	1	0

Table 5.2: Decoding table resembling a XOR-gate, which holds for both transceiver units. Tx: Own transferred Bit "0" $\rightarrow$ Tx = 0, Own transferred Bit "1" $\rightarrow$ Tx= 1; Vc: Voltage change recognized, Yes $\rightarrow$ Vc = 1, No $\rightarrow$ Vc = 0; Result: Rx: Received Bit

Now we have the tools for experimental en- and decoding data onto CLSs. Together with the decoding scheme we are now ready to describe a demonstration experiment in order to verify the applicability.

5.6 Demonstration of a data transfer

Figure 5.3 schematically depicts the experimental setup with the mutually coupled at $3230\,\mathrm{nm}$ emitting ICLs. They are independently driven by a constant current source (ILX LDX 3210 and Rök-Master-1000 battery source). The terminal voltages are individually measured by two

Lock-In Amplifiers (Stanford Research SR530). The combination of one current source, a Lock-In Amplifier and one ICL represent one transceiver unit. The $1.5\,\mathrm{m}$ long coupling path contains three wire-grid polarizers to fine tune the coupling strength such that the optical injection locked ICLs operate in a stable regime. The Lock-In detection enables access to the terminal voltage change with respect to the uncoupled reference inherently, thus no reference measurement is needed. With the polarizers we also guarantee that each incident light polarization matches the original polarization of both ICLs radiation.

The data transmission is established by the following process: The data controller encodes the text into a series of Bits using the UTF-8 format and transfers the Bit series to the transceiver units. A Bit representing a 0 value is transferred by setting the optical frequency to $\nu_0 = 87\,361.48\,\mathrm{GHz}$, a Bit representing a 1 value with $\nu_1 = 87\,360.60\,\mathrm{GHz}$ [2]. Thus, the frequency difference $|\nu_0 - \nu_1| = 0.88\,\mathrm{GHz}$ is smaller than the half of the LBW $\Omega_{\mathrm{LBW}}/2 = 1\,\mathrm{GHz}$. Each transceiver unit sends its message utilizing the previously described encoding scheme and simultaneously receives the Bit series of the other transceiver unit by measuring the voltage changes. The clock is given by the clock controller. By utilizing the decoding Table 5.2 the voltage changes can then be converted into text. In this demonstration experiment, the data controllers both have to agree in advance on how many Bits they have to transfer.

For a demonstration we transfer the following Bit series from ICL-A to ICL-B and that from ICL-B to ICL-A:

$$\text{ICL-A} \rightarrow \text{ICL-B} : ”01000001”,$$

$$\text{ICL-B} \rightarrow \text{ICL-A} : ”01010100”.$$

In UTF-8 code $”01000001”$ resembles the capital letter "A" and $”01010100”$, resembles "T". The Bit series sent by both ICLs is visualized in the two top rows of Fig. 5.5. In the rows below the measured voltage changes (Vc) are shown for both ICLs. The horizontal green lines in the third and fourth row represent the threshold, where a voltage change is considered to be non-zero, which is needed to recover the received Bit using Table 5.2.

Transfer of the bidirectional Bit (00) - first Bit in Fig. 5.5

Consider the first transferred bidirectional Bit in Fig. 5.5. Transceiver unit A sends a "0" Bit and Transceiver unit B also sends a "0" Bit. The optical frequencies of ICL-A and ICL-B are therefore set to ν_0 via current tuning, which ensures that $\Delta\nu = 0$ is set. According to Table 5.1 this theoretically leads to a voltage change close to 0 at both transceiver units. The observed voltage changes of the first bidirectional Bit in Fig. 5.5 verify this assumption. For decoding tranceiver unit A insert its own sent Bit "0" and the recognized voltage change "0" into the

[2] The optical frequency ν_0 converts to a wavelength of $3431.63\,\mathrm{nm}$ and the optical frequency ν_1 to $3431.67\,\mathrm{nm}$.

XOR-Gate (Table 5.2) and decodes the received Bit to be "0". The same decoding algorithm takes places at tranceiver unit B, resulting also in a received "0" Bit.

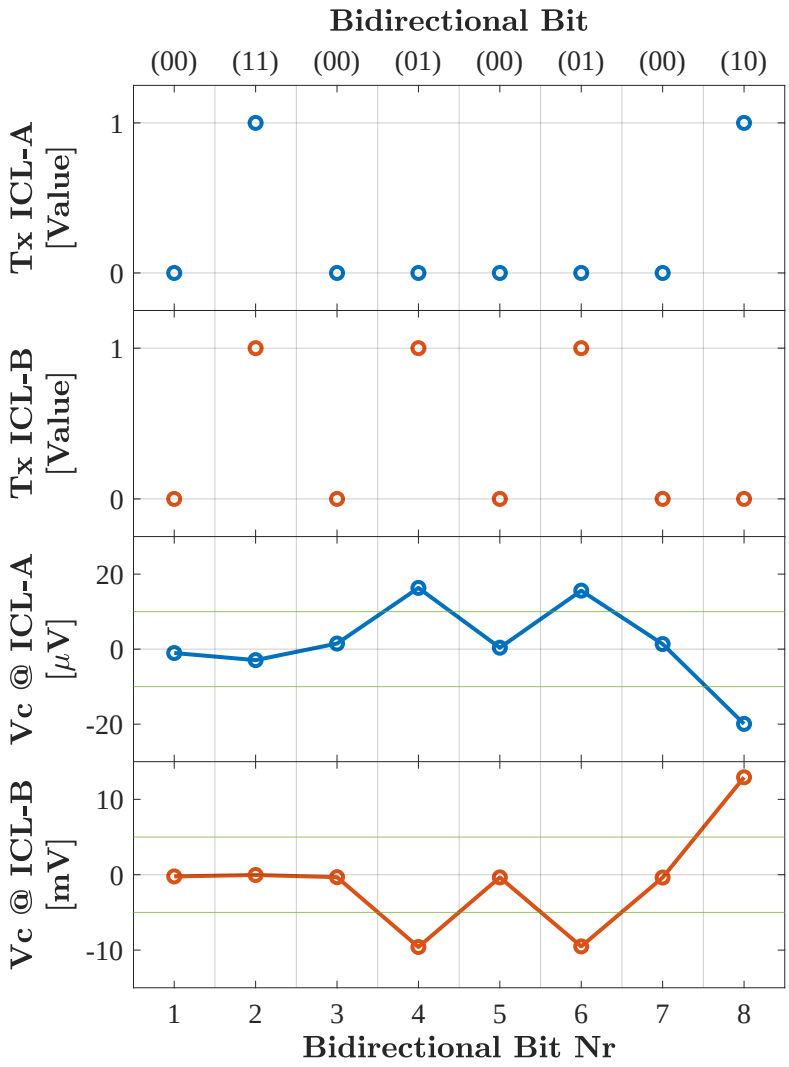

Figure 5.5: Transfer of the 8-Bit long bidirectional series. First row: transferred (Tx) Bit Value of from ICL-A to ICL-B. Second row: transferred Bit Value of from ICL-B to ICL-A. Third row: Observed terminal voltage change (Vc) at ICL-A. Fourth row: Observed terminal voltage change (Vc) at ICL-B. The horizontal green lines in the third and fourth row represent the threshold, where a voltage change is considered to be non-zero. The color blue indicates values of ICL-A and the color orange ICL-B. It must be noted that the voltage change registered at ICL-A is three magnitudes lower than that of ICL-B, because the buffer-amplifier connected ICL-A did not amplify the signal and only provided a high input impedance. The buffer-amplifier of ICL-B has a built-in $46\,\mathrm{dB}$ specified amplifier.

Transfer of the bidirectional Bit (11) - second Bit in Fig. 5.5

Consider the second transferred bidirectional Bit in Fig. 5.5. Transceiver unit A sends a "1" Bit and Transceiver unit B also sends a "1" Bit. The optical frequencies of ICL-A and ICL-B are therefore set to ν_1 via current tuning, which ensures that $\Delta\nu = 0$ is set. According to Table 5.1 this theoretically leads to a voltage change close to 0 at both transceiver units. The observed voltage changes of the second bidirectional Bit in Fig. 5.5 verify this assumption. For decoding tranceiver unit A insert its own sent Bit "1" and the recognized voltage change "0" into the XOR-Gate (Table 5.2) and decodes the received Bit to be "1". The same decoding algorithm takes places at tranceiver unit B, resulting also in a received "1" Bit.

Transfer of the bidirectional Bit (01) - fourth Bit in Fig. 5.5

Another bidirectional Bit transfer can be understood looking at the fourth bidirectional Bit. Transceiver unit A sends a "0" value and Transceiver unit B sends a "1" value. The optical frequencies of ICL-A is therefore set to ν_0 via current tuning and that of ICL-B to ν_1, which means that $\Delta\nu = \nu_0 - \nu_1 \neq 0$. According to Table 5.1 this theoretically leads to a non-zero change of the terminal voltage at each ICL. This is experimentally verified observing at the voltage changes of the fourth bidirectional Bit in Fig. 5.5. The terminal voltage of ICL-A increases by $20\,\mu\mathrm{V}$ and that of ICL-B decreases by $10\,\mathrm{mV}$ and is therefore considered non-zero. For decoding tranceiver unit A insert its own sent Bit "0" and the recognized voltage change "1" into the XOR-Gate (Table 5.2) and decodes the received Bit to be "1". For decoding tranceiver unit B insert its own sent Bit "1" and the recognized voltage change "1" into the same XOR-Gate and decodes the received Bit to be "0".

Transfer of the bidirectional Bit (10) - eighth Bit in Fig. 5.5

The eighth Bit represents the last remaining bidirectional Bit-configuration, where the same algorithm to decode the bidirectional Bit can be used.

5.6.1 Transfer of the first full letter strings

In that manner we transfer the first full letter strings "Technische Universitat Darmstadt" from tranceiver unit A to B and "Arbeitsgruppe – Halbleiteroptik" in opposite direction, including blank spaces and dashes. The total length of the Bit string is 256, where we converted the letters into Bits using the UTF-8 format. In Fig. 5.6 we compare the sent Bits (circles) with the received Bits (dots). The upper row refers to the string "Arbeitsgruppe – Halbleiteroptik". It can be seen that all dots overlap with circles, which means that data-transmission from tranceiver unit B to A has been performed without an error. The same holds for the transmission from transceiver unit A to B. The received message has only been reconstructed from the detected voltage changes

with the knowledge of the originally transferred Bits using the decoding Table 5.2 as in the previous example.

Figure 5.6: Data transfer at both transceiver units units showing the sent (circle) and received (dot) Bits. The received text-message, recovered from the Bit-series is then shown inside both graphs. Top: transceiver unit A. Bottom: transceiver unit B.

Figure 5.6 verifies that the transfer scheme performs remarkably well. However, at the moment the system is only capable to transfer messages of equal length and in fact "Arbeitsgruppe – Halbleiteroptik" and "Technische Universitat Darmstadt" have equal length. In this demonstration experiment we do not transfer data with unequal length. Nevertheless, in order to extend the concept presented here for asymmetric communication, only the partner sending less data would have to transmit a previously agreed string, which the receiver then ignores.

5.6.2 Transmission speed and Bit-error-rate

The transmission speed of our proof-of-concept setup performs with an average Bit rate of $4.2\,\mathrm{B/s}$. The transmission speed in our case is only limited by the control unit and not by physical processes. Thus, it can be significantly increased until its physical limitation is reached, which is given the time it takes to establish a CLS. That time depends on the used ICLs and their internal parameters as well as on the distance and is in our case in the order of $10\,\mathrm{ns}$. Beside that low transmission speed, we proofed the reliability of that system to be very good. It was possible to demonstrate a transmission of more than $48\,000\,\mathrm{bit}$ within a continuous transmission of random compound Bits during $3.1\,\mathrm{h}$. In total we obtained $27\,\mathrm{bit}$ mistransferred compound

Bits resulting in a Bit-error-rate of $\frac{27\,\mathrm{bit}}{48\,000\,\mathrm{bit}} = 5.6 \cdot 10^{-4}$. We omit a visualization of this data, because the errors could not be seen in the graph of so many transferred Bits. Errors occur when the terminal voltage does not correctly change above/below the agreed upon threshold (compare green lines in Fig. 5.5), which can for example be caused by electrical perturbation from the current source. As a result the wrong Bit is decoded using Table 5.1, thus an error is generated. To tackle this issue, one could implement software-based error-correction, such as Hamming-codes [308] or modern alternatives[309]. The approach also provides detection of a disconnection by statistics. In the case of a disconnection event each transceiver would recognize a zero voltage change for every Bit it is transmitting. Since for very large data-transfers the probability of the compound Bits (10) and (01) is statistically the same as the probability for (11) and (00), the disconnection can then be recognized when the equilibrium shifts significantly.

With that we have shown the first demonstration of a data transmission without additional optical detectors utilizing two mutually coupled ICLs operating on CLSs. The approach offers further potentials with respect to data-rate improvement and privacy, which we theoretically discuss in the next paragraph.

5.7 Outlook and potentials of the scheme

After the scheme has been improved in terms of transmission speed by increasing the modulation frequency until the physical limit has been reached, there are further methods to enhance the transmission rate. A popular technique is the so-called wavelength division multiplexing (WDM) [310]. With that technique the number of information channels is increased by using many different wavelengths as data-carriers. Each channel contains its own stream of information and is being multiplexed onto a single transmission line, in conventional telecommunication systems a fiber, here a free-space optical path. At the end of the transmission line, the signal gets demultiplexed (divided) and each individual stream of information is observed at a separate detection unit.

Multi- and demultiplexing units for the MIR wavelength domain such as [311] are not yet commercially available, costly and show insertion losses up to $4\,\mathrm{dB}$. Therefore WDM in MIR FSO communication systems is not yet commercially successful. Here, we see potential for our presented scheme. In Section 3.1 we have already described that at large optical frequency detunings, which are far away from the LBW, two mutually coupled ICLs do not interact with each other. Hence, the LAD based detection of a CLS is selective with respect to the wavelength, i.e. it can only detect wavelengths within the LBW. Subsequently, the here presented scheme offers an intrinsic potential for wavelength demultiplexing with no sophisticated additional wavelength multi- and demultiplexing units. The wavelengths of two separate communication setups (using the new scheme) must only be separated by (at least a few) LBWs. The coupling-beams of those two setups can be joined at the primary transceiver location by a simple non-wavelength-selective beam-splitter and divided again by a non-wavelength-selective beam-splitter at the secondary transceiver location. The wavelength selection is then done at the ICL itself. The

potential here is great to dramatically increase the data rate and the feasibility remains an exciting open challenge for future investigations.

As the data rate of FSO transmission techniques increases, the development of secure transmission on the phyical layer also becomes an urgent goal[312]. State-of the art secure transmission techniques are currently represented by quantum key distribution (QKD) [313] or ghost polarization communications (GPC)[314]. In particular, the first has been a candidate of choice with free-space sources emitting in the visible spectrum[315]. Yet, many efforts have tried to use these systems to communicate with satellites[316] but the background noise from the scattered sunlight, which is typically five orders of magnitude larger than the background noise during the night, complicates the process during daytime[317], therefore, many trials have been performed during night[318]. However, they are not suitable for global applications where secure communications have to be required anytime. This is the reason why recent attempts have considered using near-infrared light to get rid of the perturbations without restraining to nighttime communications[70]. Nevertheless, development of long range secure communication QKD systems utilizing photon entanglement is still facing a wide number of important challenges such as data transmission rate, distance, size, cost and ratio between the number of photons generated and the number of intricated photons finally available[319]. Last but not least, QKD technology is currently limited by the single photon flux environment [320] and not easy to implement in the mid-infrared since no single photon detectors exist yet at these wavelengths. The deployment of GPC systems can solve the problem of low intensity. GPC is based on polarization rotations of classical unpolarized light[321], such that the message can be camouflaged and subsequently retrieved by recovering the hidden polarization change exploiting correlations. GPC is very promising but involves many optical components and sophisticated detection unit and the transmission speed is even slower than our proposed setup with only $13\,\mathrm{bit\,h^{-1}}$. Another promising and recently investigated approach for FSO communication in the MIR wavelength domain is the chaos-communication concept using QCLs[322]. The latter has already proofed its feasibility at common fiber-telecommunication wavelengths [135] and offers transmission speeds up to $2.5\,\mathrm{Gbit\,s^{-1}}$ [323]. In chaos-communication schemes, the message is hidden within a chaotic signal and chaos-pass-filtering [212, 324] is used for message recovering. A disadvantage of this technique is that for an unidirectional transmission at least two lasers and two optical detectors are required. A bidirectional scheme would therefore require four lasers and four optical detectors.

Our demonstrated scheme also provides provides a special form privacy, but is minimal with the requirement for optical components. The privacy is given by the fact that decoding always requires the knowledge of the sent Bit. A hypothetical eavesdropper, which do not have access to the sent messages could therefore not easily decode the message in a trivial way. We assume that a hypothetical eavesdropper only has access to the optical signals S_A and S_B in coupling path as well as to the optical frequency ν_{CLS}, where both ICLs emit on simultaneously. The fundamental reflection-symmetry of the mutually coupled laser rate-equation system described in Eq. (3.69) together with Eq. (5.1) yields for our scheme that the compound Bits (01) and (10) are not distinguishable using the optical frequency ν_{CLS}. However one has to ensure that $S^A_{(01)} = S^A_{(10)}$, which is not the case for the CLS we selected for data-carriers. In theory the state with $S^A_{(01)} = S^A_{(10)}$ can easily be created, when the coupling phase θ_{c} is zero and thus the

locking peak becomes symmetrical. This has not yet been achieved in our setup and we leave the verification of the security open for future investigations including security analysis of other potential attack vectors, for example transient analysis or man in the middle attacks, which can be reviewed in [312]. Nevertheless, the advantage of our approach compared to conventional QKD, is that it is not limited by single photon environments and thus, the data-rate can be significantly higher and no special detection units have to be deployed. Compared to both QKD and chaos-communication our approach also provides bidirectional communication via a single channel with only two optoelectronic elements, namely the ICLs and is therefore cost-effective and simple to deploy.

Nevertheless, it must be noted that the here proposed free-space optical communication setup has to compete with well-known optical data transmission techniques and radio frequency transmission, which both are already highly optimized for their purpose. Only future investigations can reveal how well our setup does compare with those established techniques.

5.8 Conclusion of the chapter

We have demonstrated a novel bidirectional symmetric free space optics communication scheme based on two mutually coupled $3250\,\mathrm{nm}$ single mode ICLs without an additional optical detection unit. This proof-of-concept shows a remarkable reliability demonstrated with an transmission of more than $48\,000\,\mathrm{bit}$ with an Bit-error rate of $5.6 \cdot 10^{-4}$. Since the scheme does not require many optical components and additional optical detection units, the system may be competitive in costs with regard to conventional transmission systems. At a first view our transmission approach compares poorly with conventional techniques offering transmission speeds 15 magnitudes higher [296, 297]. However beside the reduction of optical components, the concept offers exceptional potential with regard to an improvement in transmission speed, enhancement in privacy, which all have to be evaluated in further investigations. Lastly, but certainly not less interesting is the fact that the scheme is not limited to the utilized twin MIR operating ICLS. By using other types of semiconductor laser pairs, like quantum cascade lasers this proof of-principle experiment can be transferred to other wavelengths, where detectors are even more expensive, slow or even not available, such as the THz region. It can also deployed with common telecommunication diode lasers operating in the $1550\,\mathrm{nm}$ band, where fibers can be used as a transport medium. Indeed the latter has been also investigated by researchers of our group and is about to be published.

"Pour ce qui est de l'avenir, il ne s'agit pas de le prévoir, mais de le rendre possible."

Antoine de Saint-Exupéry

6 Conclusion and Summary

Interband cascade lasers are exceptionally versatile, high-technology semiconductor lasers. They represent the latest generation of semiconductor lasers that generate radiation in the mid-infrared wavelength domain and are therefore preferred as coherent light sources in gas spectroscopy and free-space-optical communication setups. In this thesis they were used to analyze the laser-as-detector approach, which was then exploited to evaluate a novel gas spectroscopy technique with improved detection-limit and was also utilized in a bidirectional free-space-optical scheme without additional optical detectors and thus a reduced number of optical components.

The laser-as-detector approach is a well-known but little used technique that allows to avoid external optical detection units. The approach is functional, realizing that a detector is a single-mode laser working in forward operation. Its basis is the fact that an injected external optical perturbations change the charge carrier density in the laser's active region, which manifest themselves in changes of the terminal-voltage. These changes in the terminal-voltage are more pronounced when the externally optical injected light has the same or a similar wavelength as the original laser, which refers to optical injection locking a dramatically nonlinear response. This approach is particularly interesting if few, expensive or only low performing detectors are available for the considered wavelength range. This "detector gap" exists especially in the THz range, but is also present in the mid-infrared wavelength range.

In order to describe the charge carrier transport through the Interband-cascade-lasers, a model of this laser type was therefore introduced in Chapter 2. Based on this model, the ICLs, which were made available through the German-Greek ILLIAS project were extensively characterized experimentally. Using the self-mixing technique, a remarkably low linewidth enhancement factor in the range of 0.2 and a comparatively small optical linewidth of $582\,\mathrm{kHz}$ could be determined. Since the literature also frequently mentions low linewidth enhancement factors for quantum-cascade-lasers based on similar material structures, it can be assumed that the materials and the quantum well structure are responsible for the low linewidth enhancement factor. Such a low LEF can be an advantage, because the interband cascade laser is less susceptible to external optical interference and can therefore be used well in regular operation without optical isolators. However, a high linewidth enhancement factor can also be advantageous for generating higher-dimensional dynamics, for example for chaos generation.

In Chapter 3 we discussed the laser-as-a-dectector approach using optical feedback, unidirectional injection and bidirectional coupling, both theoretically and experimentally. First, the theoretical interband cascade laser model was extended to include optical perturbation. In

all three configurations we found experimentally that the process of quasi-Fermi level changes dominates the changes in carrier density. This is in contrast to other semiconductor lasers where other processes such as photo-conduction effects or decreasing the current leaking from the p-type active region to the p-type cladding layer also play a role [52]. With these first findings we could verify the theoretical model of the interband cascade laser by successfully comparing the steady-state solutions of the model with experimental findings. The laser-as-detector approach was investigated by analyzing the terminal-voltage of the interband cascade lasers depending on the optical frequency detuning. As predicted by the model, the change was diametrically opposed to the optical power. The accurate description by the model was also revealed by the excellent prediction of the influence of the coupling or injection strength in all three configurations. Especially the locking bandwidth, the detuning range where one interband cascade laser locks on the optical frequency of a secondary interband cascade laser, showed a linear relationship with respect to the optical injection strength (in the amplitude domain). The locking bandwidth thus represents a metric, that is proportional to the injected radiation, which finally verifies the feasibility of the laser-as-detector approach. In order to evaluate the high-frequency performance laser-as-detector approach, we carried out investigations to detect the maximum electrical bandwidth of the laser-as-detector. It was shown that the $-3\,\mathrm{dB}$ limit of the laser-as-detector approach in our case was $1.2\,\mathrm{GHz}$, which is significantly higher than that of most commonly used mercury-cadmium-telluride detectors, which are usually used for optical detection in this wavelength domain.

With the rich knowledge from Chapter 2 and Chapter 3 we have then established two novel spectroscopic schemes in Chapter 4 and evaluated their quality utilizing methane absorption lines as example. The realized schemes were compared with the conventional tunable diode laser spectroscopy technique as reference. It was shown that a combination of self-mixing and the laser-as-detector approach can be used to build a gas sensor without an additional optical detector. However, the detection limit was 32 times worse in direct comparison to tunable diode laser spectroscopy. This is satisfactory if the optical detector has to be omitted due to cost reasons or lack of detectors. To increase the detection limit, a second novel spectroscopy scheme based on unidirectionally injected interband cascade laser was realized. It was found that the detection limit was even $30.8\,\%$ better compared to using a conventional noise-optimized optical sensor with the TDLAS technique. This was surprising and could be explained by the fact that the laser-as-detector approach is very selective regarding the detectable optical frequencies, i.e. it only detects optical frequencies within the locking bandwidth. Due to that background noise of other nearby wavelengths is not detected, thus resulting in a lower noise level. Nevertheless, the improvement presented here has to prove its reliability in future experiments which are already scheduled within the framework of the Greek-German ILLIAS project funded by the German Federal Ministry of Education and Research and the Greek General Secretariat for Research and Technology.

Besides the applicability of the mid-infrared domain for spectroscopy of fundamental gases, the mid-infrared domain also offers two atmospheric optical windows, so that free-space-optical communication applications become possible. In the last chapter we realized such an application based on two bidirectionally coupled interband cascade lasers and the associated reflection symmetry with respect to the optical frequency detuning, which was extensively

investigated in the Chapter 3. In the presented communication scheme, the data was encoded onto so-called compound-laser-states. Using the laser-as-detector approach, they can also be decoded again. Both generation/transmission and reception are accomplished simultaneously. The scheme is not only very simple, but also robust against vibrations due to the fact that the 2π and π coupling phase translation symmetry were no longer valid, which had already been shown in Chapter 3. As a result a total of $48\,000\,\mathrm{bit}$ were transferred with a low error rate of $5.6 \cdot 10^{-4}$. The first transmitted words were " Arbeitsgruppe – Halbleiteroptik" and " Technische Universitat Darmstadt". The concept presented here also offers numerous starting points for further research. On the one hand it would be possible to increase the data rate with the help of e.g. wavelength division multiplexing. Furthermore, the concept provides basic features to ensure a more secure data communication. The measure of this security is open to further research in the future.

Beside the applications presented here, the laser-as-detector approach offers a huge potential, because the results presented in this thesis can be transferred to a variety of other semiconductor lasers such as near-infrared lasers. In that manner the approach could be also deployed on photonic integrated circuits. We assume that the laser-as-detector approach could additionally also convince from a economical perspective. Since a second matching semiconductor laser can be grown on the same chip as the first one, cost advantages will be achieved, especially considering the promising photonic integrated circuit technology. The laser-as-detector approach can then show its full advantages in wavelength ranges, where no optical detectors or such with poor performance and detectivity are available. Especially in the THz domain, wheresome quantum cascade laser are able to generate coherent light, many novel applications could become possible, because the THz range offers only low performance or high-maintenance detection units.

The results presented in this thesis thus provide an excellent starting point for further research into the laser-as-detector approach, a concept, which definitely deserves more attention in the future. In consideration of all previous observations, we conclude that the laser is not only an extraordinary powerful light source, but can also be an exceptional detector.

Zusammenfassung

In dieser Arbeit wurde das Laser-als-Detektor-Konzept anhand im mittel-infraroten Wellenlängenbereich emittierenden Interband-Kaskaden-Lasern untersucht. Der Laser-als-Detektor-Ansatz ist eine bekannte, aber selten eingesetzte Technik, die es erlaubt, auf externe optische Detektionseinheiten zu verzichten. Er basiert auf der Tatsache, dass externe optische Störungen die Ladungsträgerdichte im aktiven Bereich des Lasers verändern, was sich in Änderungen der Laserspannung manifestiert. Diese Spannungsänderungen sind dann besonders ausgeprägt, wenn die externe optische Störung die gleiche oder eine ähnliche Wellenlänge wie der ursprüngliche Laser hat. Dieser Ansatz kann dann besonders nützlich sein, wenn für den Wellenlängenbereich wenige, teure oder nur wenig leistungsfähige Detektoren zur Verfügung stehen. Diese "Detektorlücke" besteht vor allem im THz-Bereich, ist aber auch im Mittelinfraroten-Wellenlängenbereich vorhanden.

Um den Ladungstransport durch den Interbandkaskadenlaser und damit den Einfluss optischer Störungen zu beschreiben, wurde deshalb in Kapitel 2 ein Ratengleichungsmodell des Interbandkaskadenlaser eingeführt. Auf der Grundlage dieses Modells wurden die im Rahmen des ILLIAS-Projekts zur Verfügung gestellten Interbandkaskadenlasern umfassend experimentell charakterisiert. Mit Hilfe eines Rückkopplungsexperiments konnte ein bemerkenswert niedrige Linienverbreiterungsfaktor im Bereich von 0.2 und eine vergleichsweise schmale optische Linienbreite von $582\,\mathrm{kHz}$ bestimmt werden. Ein solch niedriger Linienverbreiterungsfaktor kann bei vielen Anwendungen von Vorteil sein, da dadurch Interbandkaskadenlasern weniger anfällig für externe optische Interferenzen sind. Daher können sie zum Beispiel im regulären Betrieb ohne aufwendige doppelstufige optische Isolatoren gut eingesetzt werden. Ein hoher Linienverbreiterungsfaktor kann aber auch vorteilhaft sein, wenn es es erwünscht ist höherdimensionale Dynamik zu erzeugen, zum Beispiel Chaos. Es wurde außerdem gezeigt, dass alle verwendeten Interbandkaskadenlasern im Mittelinfrarot zwischen $3206\,\mathrm{nm}$ und $3439\,\mathrm{nm}$ emittieren und sich damit sowohl für Freistrahl-Kommunikation, als auch zur Spektroskopie von Methan eignen.

Anschließend wurde der Laser-als-Detektor-Ansatz mit optischer Rückkopplung, unidirektionaler Injektion und bidirektionaler Kopplung sowohl theoretisch als auch experimentell in Kapitel 3 detailliert diskutiert. Zunächst wurde dafür das theoretische Interbandkaskadenlaser-Modell um einen Term zur Beschreibung der optische Störungen erweitert. In allen drei Störungskonfigurationen stellten wir experimentell fest, dass hauptsächlich Änderungen des Quasi-Fermi-Niveaus die Änderungen der Ladungsträgerdichte und damit der Laserspannung dominierten. Dies steht im Kontrast zu anderen Halbleiterlasern, bei denen auch andere Prozesse

wie Photoleitungseffekte oder die Verringerung des aus der aktiven p-Typ-Region in die p-Typ-Mantelschicht austretenden Stroms eine Rolle spielen [52]. Mit diesen Erkenntnissen konnten wir das theoretische Modell des Interbandkaskadenlaser verifizieren, indem wir die stationären Lösungen des Modells erfolgreich mit experimentellen Ergebnissen verglichen. Der Laser-als-Detektor-Ansatz konnte anschließend erfolgreich evaluiert werden, indem gezeigt wurde, dass sich die Spannung der Interbandkaskadenlasern in Abhängigkeit der optischen Frequenzverstimmung änderte. Wie vom Modell vorhergesagt änderte sich die Spannung diametral zur optischen Leistung. Diese Abhängigkeit konnte durch eine Analyse der elektrischen Antwort bis zu einer elektrischen Frequenz von $1.2\,\mathrm{GHz}$ nachgewiesen, wobei letztere die $-3\,\mathrm{dB}$ Grenze darstellt. Die präzise Beschreibung durch das Modell zeigte sich auch durch die ausgezeichnete Vorhersage des Einflusses der Kopplungs- oder Injektionsstärke in allen drei Konfigurationen. Insbesondere die sogenannte Kopplungsbandbreite, der Verstimmungsbereich, in dem ein Interbandkaskadenlaser auf der optischen Frequenz eines sekundären Interbandkaskadenlaser emittiert, zeigte eine lineare Beziehung in Bezug auf die optische Injektionsstärke in der Amplitudendomäne. Im Speziellen dieses Ergebnis verifiziert, dass der Laser-als-Detektor Ansatz praktisch einsetzbar ist. Darauf aufbauend wurden spektroskopische Experimente mit dem Laser-as-Detektor-Ansatz in Kapitel 4 durchgeführt. Für bidirektional gekoppelte Interbandkaskadenlasern wurden die Modellsymmetrien theoretisch eingeführt und experimentell evaluiert. Es stellte sich heraus, dass die 2π- und π-Translationssymmetrien für große Kopplungsdistanzen nicht mehr gültig sind, da im Modell Annahmen getroffen werden, die für diesen Fall nicht mehr gültig sind. Auf der anderen Seite konnte gezeigt werden, dass eine dritte Symmetrie, die Reflexionssymmetrie, auch bei mitteleren Interbandkaskadenlaser-Distanzen seine Gültigkeit behält. Letzteres bildet die Grundlage für ein von uns entwickeltes Kommunikationsschema, welches wir in Chapter 5 diskutiertierten.

Mit den Erkenntnissen aus Kapuitel 3 konnten wir dann zwei neuartige experimentelle spektroskopie Aufbauten untersuchen und ihre Detektivität anhand von Absorptionslinien des Testgases Methan bewerten. Die Aufbauten wurden dabei jeweils mit der konventionellen durchstimmbaren Diodenlaser-Spektroskopietechnik (TDLAS) verglichen. Es wurde zunächst ein Gassensor-Aufbau ohne einen zusätzlichen optischen Detektor untersucht, der auf einer Kombination von Rückkopplung und dem Laser-als-Detektor-Ansatz beruhte. Es zeigte sich jedoch dass die bestimmte Nachweisgrenze im direkten Vergleich mit der TDLAS-Technik 32-mal schlechter war. Trotz dieses Ergebnisses kann dieser Gassensor praktiabel sein, genau dann wenn aus Kostengründen oder gar wegen nicht vorhandener Detektoren auf den optischen Detektor verzichtet werden muss. Anschließend wurde ein zweiter neuartiger Spektroskopie Aufbau realisiert um die Nachweisgrenze zu erhöhen, der auf unidirektional injizierten Interbandkaskadenlasern basiert. Es zeigte sich, dass die Nachweisgrenze sogar $30.8\ \mathrm{Prozent}$ gegenüber der konventionellen TDLAS-Technik verbessert werden konnte, wobei bei letzterer sogar eine rauschoptimierte optische Detektionseinheit eingesetzt wurde. Dieses überaschendes Ergebnis könnte damit erklärt werden, dass der Laser-as-Detektor-Ansatz hinsichtlich der detektierbaren optischen Frequenzen bzw. Wellenlängen sehr selektiv ist. Die optische Detektionsbandbreite entspricht dabei der Breite der Kopplungsbandbreite. Dadurch wird Hintergrundrauschen auf anderen benachbarten Wellenlängen nicht wahrgenommen, was zu einem niedrigeren Rauschpegel beitragen könnte, welches wiederum ein besseres Signal-zu-Rausch Verhältnis

(SNR) ermögliche könnte. Mit einem niedrigeren SNR lassen sich schließlich auch geringere Nachweisgrenze erreichen. Nicht nur im Hinblick auf die Nachweisgrenze kann sich der Einsatz des Laser-as-Detektor-Ansatz lohnen. Ein zweiter passender Interbandkaskadenlaser, der später als Detetkor dient, könnte bspw. auf dem gleichen Chip wie der erste gezüchtet werden. Dabei entstehen Kostenvorteile, die den gesamten Gas-Sensor entscheidend vergünstigen könnte. Es kann außerdem angenommen werden, dass der Laser-as-Detektor-Ansatz insbesondere auch dann Potential bietet, wenn er bei integrierten photonischen Schaltungstechnik etabliert wird, um so einfach einen Detektor zu integrieren.

Neben des spektroskopischen Anwendungsgebietes, stellt der mittelinfrarote Wellenlängenbereich auch zwei atmosphärische optische Fenster bereit, sodass die Atmosphäre als Kanal für Kommunikationsanwendungen genutzt werden kann. In Kapitel 5 stellten wir daher eine Freistrahlkommunikationsanwendung auf Basis zweier bidirektional gekoppelter Interbandkaskadenlaser vor, die auf der Reflexionssymmetrie des Systems beruht, wobei letztere im dritten Kapitel ausführlich untersucht wurde. Im vorgestellten Kommunikationsschema wurden die Daten in sogenannte Compound-Laser-Zustände kodiert. Mit dem Laser-als-Detektor-Ansatz konnten diese dann schließlich wieder dekodiert werden. Übertragung und Empfang erfolgen dabei immer gleichzeitig und symmetrisch. Der verwendete Aufbau war nicht nur sehr simpel gehalten, sondern auch robust gegenüber Vibrationen, da die 2π und π Symmetrie des gekoppelten Systems nicht mehr gültig war. Im Zuge dessen wurden insgesamt $48\,000\,\mathrm{bit}$ mit einer erstaunlich niedrigen Fehlerrate von $5,6 \cdot 10^{-4}$ übertragen. Die ersten übertragenen Worte waren dabei "Arbeitsgruppe – Halbleiteroptik" und "Technische Universitat Darmstadt". Das hier vorgestellte Konzept bietet zahlreiche Ansatzpunkte für die weitere Forschungen und Verbesserungen. Zum einen wäre es möglich, die Datenrate zunächst klassisch und dann z.B. mit Hilfe von Wellenlängenmultiplexing zu erhöhen. Zum anderen bietet das Konzept grundlegende Möglichkeiten, um eine sicherere Datenkommunikation zu gewährleisten. Das Sicherheitsmaß bleibt hier offen für zukünftige Forschung.

Neben den hier vorgestellten Anwendungen konnte gezeigt werden, dass das Laser-als-Detektor-Konzept im Allgemeinen ein großes sehr Potential bietet. Die in dieser Arbeit vorgestellten Ergebnisse können nicht nur bei Interbandkaskadenlaser angewendet werden, sondern auf eine Vielzahl anderer Halbleiterlaser wie z.B. im nahen Infrarot emittierende Dioden, übertragen werden. In dieser Hinsicht könnte sich der Einsatz auch in integrierten photonische Schaltkreisen lohnen. Der Laser-als-Detektor-Ansatz kann allerdings dann seine Vorteile voll ausspielen, wenn nur schlechte optische Detektoren im Wellenlängenbereich zur Verfügung stehen. Besonders im THz-Bereich, wo nur einige Quantenkaskadenlaser Strahlung emittieren können, könnten viele neuartige Anwendungen möglich werden, denn im THz-Bereich stehen keine leistungsfähige und sehr wartungsintensive Detektoreinheiten zur Verfügung. Die in dieser Arbeit vorgestellten Ergebnisse bieten somit eine hervorragende Ausgangsbasis für die weitere Erforschung des Laser-als-Detektor-Ansatzes, ein Konzept, das in Zukunft definitiv mehr Aufmerksamkeit verdient.

Im Rückblick auf alle in dieser Arbeit erzielten Ergebnisse, kommen wir zu dem Schluss, dass ein Laser und insbesondere der Interbandkaskadenlaser nicht nur eine außergewöhnlich einzigartige Lichtquelle ist, sondern auch ein exzellenter Detektor sein kann.

Bibliography

[1] T. H. Maiman. “Stimulated Optical Radiation in Ruby”. *Nature* 187.4736 (1960), pp. 493–494. DOI: 10.1038/187493a0.

[2] “Sixty years of lasers”. *Nature Reviews Physics* 2.5 (2020), pp. 221–221. DOI: 10.1038/s42254-020-0181-9.

[3] Qixiang Cheng et al. “Recent advances in optical technologies for data centers: a review”. *Optica* 5.11 (2018), p. 1354. DOI: 10.1364/OPTICA.5.001354.

[4] Peter Werle. “A review of recent advances in semiconductor laser based gas monitors”. *Spectrochimica Acta - Part A: Molecular and Biomolecular Spectroscopy* 54.2 (1998), pp. 197–236. DOI: 10.1016/S1386-1425(97)00227-8.

[5] Paul. S. Wu and Jagdish C. Tandon. “Omnidirectional Laser Scanner For Supermarkets”. *Optical Engineering* 20.1 (1981). DOI: 10.1117/12.7972675.

[6] Heng Wang et al. “Pedestrian recognition and tracking using 3D LiDAR for autonomous vehicle”. *Robotics and Autonomous Systems* 88 (2017), pp. 71–78. DOI: 10.1016/j.robot.2016.11.014.

[7] Marshall I. Nathan et al. “Stimulated emission of radiation from GaAs p-n junctions”. *Applied Physics Letters* 1.3 (1962), pp. 62–64. DOI: 10.1063/1.1777371.

[8] Nick Holonyak and S. F. Bevacqua. “COHERENT (VISIBLE) LIGHT EMISSION FROM Ga(As 1-x P x) JUNCTIONS”. *Semiconductor Devices: Pioneering Papers*. Vol. 82. October. WORLD SCIENTIFIC, (1962), pp. 898–899. DOI: 10.1142/9789814503464_0122.

[9] R. N. Hall et al. “Coherent Light Emission From GaAs Junctions”. *Physical Review Letters* 9.9 (1962), pp. 366–368. DOI: 10.1103/PhysRevLett.9.366.

[10] T. M. Quist et al. “Semiconductor maser of GaAs”. *Applied Physics Letters* 1.4 (1962), pp. 91–92. DOI: 10.1063/1.1753710.

[11] Manijeh Razeghi. “Semiconductor Lasers”. *Technology of Quantum Devices*. Boston, MA: Springer US, (2010), pp. 209–270. DOI: 10.1007/978-1-4419-1056-1_6.

[12] C Pollock and Michal Lipson. *Integrated photonics*. 20. Springer, (2003).

[13] Vilson R. Almeida et al. “All-optical control of light on a silicon chip”. *Nature* 431.7012 (2004), pp. 1081–1084. DOI: 10.1038/nature02921.

[14] Benjamin S. Williams et al. “3.4-THz quantum cascade laser based on longitudinal-optical-phonon scattering for depopulation”. *Applied Physics Letters* 82.7 (2003), pp. 1015–1017. DOI: 10.1063/1.1554479.

[15] Michael Kneissl et al. “Ultraviolet AlGaN multiple-quantum-well laser diodes”. *Applied Physics Letters* 82.25 (2003), pp. 4441–4443. DOI: 10.1063/1.1585135.

[16] J Faist et al. “Quantum Cascade Laser”. *Science* 264.5158 (1994), pp. 553–556. DOI: 10.1126/science.264.5158.553.

[17] R. F. Kazarinov and R. A. Suris. “Possibility of the amplification of electromagnetic waves in a semiconductor with a superlattice”. *Soviet Physics - Semiconductors* 5.4 (1971), pp. 707–709.

[18] A. Y. Cho and J. R. Arthur. “Molecular beam epitaxy”. *Progress in Solid State Chemistry* (1975). DOI: 10.1016/0079-6786(75)90005-9.

[19] Jérôme Faist et al. “Quantum cascade laser: Temperature dependence of the performance characteristics and high T0 operation”. *Applied Physics Letters* 65.23 (1994), pp. 2901–2903. DOI: 10.1063/1.112524.

[20] J. Devenson et al. “InAsAlSb quantum cascade lasers emitting at 2.75-2.97 μm”. *Applied Physics Letters* 91.25 (2007), pp. 1–4. DOI: 10.1063/1.2825284.

[21] K. Pierściński et al. “Room temperature, single mode emission from two-section coupled cavity InGaAs/AlGaAs/GaAs quantum cascade laser”. *Journal of Applied Physics* 118.13 (2015), p. 133103. DOI: 10.1063/1.4932141.

[22] R. Köhler et al. “Terahertz quantum cascade lasers”. *THz 2002 - 2002 IEEE 10th International Conference on Terahertz Electronics, Proceedings*. (2002). DOI: 10.1109/THZ.2002.1037573.

[23] Sudeep Khanal et al. “High-temperature operation of broadband bidirectional terahertz quantum-cascade lasers”. *Scientific Reports* 6.August (2016), p. 32978. DOI: 10.1038/srep32978.

[24] O. Cathabard et al. “Quantum cascade lasers emitting near 2.6 μm”. *Applied Physics Letters* 96.14 (2010), p. 141110. DOI: 10.1063/1.3385778.

[25] Christoph Walther et al. “Quantum cascade lasers operating from 1.2to1.6THz”. *Applied Physics Letters* 91.13 (2007), p. 131122. DOI: 10.1063/1.2793177.

[26] Miriam Serena Vitiello et al. “Quantum cascade lasers: 20 years of challenges”. *Optics Express* 23.4 (2015), p. 5167. DOI: 10.1364/OE.23.005167.

[27] Rui Q. Yang. “Infrared laser based on intersubband transitions in quantum wells”. *Superlattices and Microstructures* 17.1 (1995), pp. 77–83. DOI: 10.1006/spmi.1995.1017.

[28] Chih-Hsiang Lin et al. “Type-II interband quantum cascade laser at 3.8 [micro sign]m”. *Electronics Letters* 33.7 (1997), p. 598. DOI: 10.1049/el:19970421.

[29] M. Kim et al. “Interband cascade laser emitting at λ=3.75 μm in continuous wave above room temperature”. *Applied Physics Letters* 92.19 (2008), pp. 10–13. DOI: 10.1063/1.2930685.

[30] M. von Edlinger et al. “DFB interband cascade lasers for tunable laser absorption spectroscopy from 3 to 6 μm”. *Proc. SPIE*. Ed. by Manijeh Razeghi, Eric Tournié, and Gail J. Brown. (2013), p. 899318. DOI: 10.1117/12.2039734.

[31] R.Q. Yang. “Interband cascade (IC) lasers”. *Semiconductor Lasers*. Elsevier, (2013), pp. 487–513. DOI: 10.1533/9780857096401.3.487.

[32] I. Vurgaftman et al. “Rebalancing of internally generated carriers for mid-infrared interband cascade lasers with very low power consumption”. *Nature Communications* 2.1 (2011), p. 585. DOI: 10.1038/ncomms1595.

[33] I. Vurgaftman et al. “Interband cascade lasers”. *Journal of Physics D: Applied Physics* 48.12 (2015), p. 123001. DOI: 10.1088/0022-3727/48/12/123001.

[34] Christopher R. Webster et al. “Mars methane detection and variability at Gale crater”. *Science* 347.6220 (2015), pp. 415–417. DOI: 10.1126/science.1261713.

[35] Joseph Fraunhofer. “Bestimmung des Brechungs- und des Farbenzerstreungs-Vermögens verschiedener Glasarten, in Bezug auf die Vervollkommnung achromatischer Fernröhre”. *Annalen der Physik* 56.7 (1817), pp. 264–313. DOI: 10.1002/andp.18170560706.

[36] G. Kirchhoff. “Ueber die Fraunhofer’schen Linien”. *Annalen der Physik und Chemie* 185.1 (1860), pp. 148–150. DOI: 10.1002/andp.18601850115.

[37] Wolfgang Petrich. “MID-INFRARED AND RAMAN SPECTROSCOPY FOR MEDICAL DIAGNOSTICS”. *Applied Spectroscopy Reviews* 36.2-3 (2001), pp. 181–237. DOI: 10.1081/ASR-100106156.

[38] Ronald W. Waynant, Ilko K. Ilev, and Israel Gannot. “Mid–infrared laser applications in medicine and biology”. *Philosophical Transactions of the Royal Society of London. Series A: Mathematical, Physical and Engineering Sciences* 359.1780 (2001). Ed. by A. R. Adams et al., pp. 635–644. DOI: 10.1098/rsta.2000.0747.

[39] Michael von Edlinger et al. “Monomode Interband Cascade Lasers at 5.2 µm for Nitric Oxide Sensing”. *IEEE Photonics Technology Letters* 26.5 (2014), pp. 480–482. DOI: 10.1109/LPT.2013.2297447.

[40] Florian Michel. “Ein Quantenkaskadenlaser-Spektrometer zur in-situ Bestimmung von CO, NO, N_2O und CO_2 Konzentrationen in Hochtemperatur-Umgebungen”. *Thesis* (2016).

[41] Anatoliy A. Kosterev and Frank K Tittel. “Chemical sensors based on quantum cascade lasers”. *IEEE Journal of Quantum Electronics* 38.6 (2002), pp. 582–591. DOI: 10.1109/JQE.2002.1005408.

[42] Robert F. Curl et al. “Quantum cascade lasers in chemical physics”. *Chemical Physics Letters* 487.1-3 (2010), pp. 1–18. DOI: 10.1016/j.cplett.2009.12.073.

[43] C. Bauer et al. “Potentials and limits of mid-infrared laser spectroscopy for the detection of explosives”. *Applied Physics B* 92.3 (2008), pp. 327–333. DOI: 10.1007/s00340-008-3134-z.

[44] F Tittel, Dirk Richter, and Alan Fried. “Mid-infrared laser applications in spectroscopy”. *Solid-State Mid-Infrared Laser Sources* 516.7 (2003), pp. 445–516. DOI: 10.1007/3-540-36491-9_11.

[45] Yajun Yu et al. “CW EC-QCL-based sensor for simultaneous detection of H2O, HDO, N2O and CH4 using multi-pass absorption spectroscopy”. *Optics Express* 24.10 (2016), p. 10391. DOI: 10.1364/OE.24.010391.

[46] P. I. Abramov, E. V. Kuznetsov, and L. A. Skvortsov. “Prospects of using quantum-cascade lasers in optoelectronic countermeasure systems: review”. *Journal of Optical Technology* 84.5 (2017), p. 331. DOI: 10.1364/JOT.84.000331.

[47] Alexander Soibel et al. “Midinfrared interband cascade laser for free space optical communication”. *IEEE Photonics Technology Letters* 22.2 (2010), pp. 121–123. DOI: 10.1109/LPT.2009.2036449.

[48] Xiaodan Pang et al. “4 Gbps PAM-4 and DMT Free Space Transmission using a 4.65-pm Quantum Cascaded Laser at Room Temperature”. *2017 European Conference on Optical Communication (ECOC)*. IEEE, (2017), pp. 1–3. DOI: 10.1109/ECOC.2017.8345985.

[49] R. Martini et al. “High-speed modulation and free-space optical audio/video transmission using quantum cascade lasers”. *Electronics Letters* 37.3 (2001), p. 191. DOI: 10.1049/el:20010102.

[50] H.C. Liu. “Quantum Well Infrared Photodetector Physics and Novel Devices”. *Semiconductors and Semimetals*. (1999). Chap. 3, pp. 129–196. DOI: 10.1016/S0080-8784(08)60306-3.

[51] Adam Piotrowski et al. “HgCdTe and Sb-based infrared detection modules for gas sensing manufactured at VIGO System S.A. (Conference Presentation)”. *Electro-Optical and Infrared Systems: Technology and Applications XIV*. Ed. by David A. Huckridge, Reinhard Ebert, and Helge Bürsing. SPIE, (2017), p. 12. DOI: 10.1117/12.2279783.

[52] Shuichi Mitsutsuka and Junichi Shimada. “Voltage Change Across the Self-Coupled Semiconductor Laser”. *IEEE Journal of Quantum Electronics* 17.7 (1981), pp. 1216–1225. DOI: 10.1109/JQE.1981.1071267.

[53] S. Shinohara et al. “Laser Doppler velocimeter using the self-mixing effect of a semiconductor laser diode”. *Applied Optics* 25.9 (1986), p. 1417. DOI: 10.1364/AO.25.001417.

[54] Roy Lang and Kohroh Kobayashi. “External Optical Feedback Effects on Semiconductor Injection Laser Properties”. *IEEE Journal of Quantum Electronics* 16.3 (1980), pp. 347–355. DOI: 10.1109/JQE.1980.1070479.

[55] M. L. Skolnick and Robert J. Freiberg. “Laser Injection Locking”. *Proceedings of the IEEE* 61.10 (1973), pp. 1411–1431. DOI: 10.1109/PROC.1973.9294.

[56] Adonis Bogris et al. “Mid-Infrared Gas Sensor Based on Mutually Injection Locked Quantum Cascade Lasers”. *IEEE Journal of Selected Topics in Quantum Electronics* 23.2 (2017), pp. 8–14. DOI: 10.1109/JSTQE.2016.2603341.

[57] H. Erzgräber et al. “Mutually delay-coupled semiconductor lasers: Mode bifurcation scenarios”. *Optics Communications* 255.4-6 (2005), pp. 286–296. DOI: 10.1016/j.optcom.2005.06.016.

[58] Max Karl Ernst Ludwig Planck. “Zur Theorie des Gesetzes der Energieverteilung im Normalspektrum”. *Verhandlungen der Deutschen Physikalischen Gesselschaft* 2 (1900), p. 237.

[59] M. Vainio and L. Halonen. “Mid-infrared optical parametric oscillators and frequency combs for molecular spectroscopy”. *Physical Chemistry Chemical Physics* 18.6 (2016), pp. 4266–4294. DOI: 10.1039/C5CP07052J.

[60] L. S. Rothman et al. “The HITRAN2012 molecular spectroscopic database”. *Journal of Quantitative Spectroscopy and Radiative Transfer* (2013). DOI: 10.1016/j.jqsrt.2013.07.002.

[61] O. Diemel et al. “An interband cascade laser-based in situ absorption sensor for nitric oxide in combustion exhaust gases”. *Applied Physics B* 123.5 (2017), p. 167. DOI: 10.1007/s00340-017-6741-8.

[62] Nazanin Mansouri. “A Case Study of Volkswagen Unethical Practice in Diesel Emission Test”. *International Journal of Science and Engineering Applications* 5.4 (2016), pp. 211–216. DOI: 10.7753/IJSEA0504.1004.

[63] Ulrike Willer et al. “Near- and mid-infrared laser monitoring of industrial processes, environment and security applications”. *Optics and Lasers in Engineering* 44.7 (2006), pp. 699–710. DOI: 10.1016/j.optlaseng.2005.04.015.

[64] Eric B. Takeuchi et al. “Standoff detection of explosives and chemical agents using broadly tuned external-cavity quantum cascade lasers (EC-QCLs)”. *Optics and Photonics for Counterterrorism and Crime Fighting III*. Ed. by Colin Lewis. (2007), p. 674104. DOI: 10.1117/12.768932.

[65] Ramin Ghorbani and Florian M. Schmidt. “ICL-based TDLAS sensor for real-time breath gas analysis of carbon monoxide isotopes”. *Optics Express* 25.11 (2017), p. 12743. DOI: 10.1364/oe.25.012743.

[66] Frank K. Tittel. “Current status of midinfrared quantum and interband cascade lasers for clinical breath analysis”. *Optical Engineering* 49.11 (2010), p. 111123. DOI: 10.1117/1.3498768.

[67] Matthew R McCurdy et al. “Recent advances of laser-spectroscopy-based techniques for applications in breath analysis”. *Journal of Breath Research* 1.1 (2007), p. 014001. DOI: 10.1088/1752-7155/1/1/014001.

[68] Caryn Hughes and Matthew J. Baker. “Can mid-infrared biomedical spectroscopy of cells, fluids and tissue aid improvements in cancer survival? A patient paradigm”. *The Analyst* 141.2 (2016), pp. 467–475. DOI: 10.1039/C5AN01858G.

[69] A.A. Kosterev et al. “QEPAS methane sensor performance for humidified gases”. *Applied Physics B* 92.1 (2008), pp. 103–109. DOI: 10.1007/s00340-008-3056-9.

[70] Sheng Kai Liao et al. “Long-distance free-space quantum key distribution in daylight towards inter-satellite communication”. *Nature Photonics* (2017). DOI: 10.1038/nphoton.2017.116.

[71] Tyler D. Robinson. “A Theory of Exoplanet Transits with Light Scattering”. *The Astrophysical Journal* 836.2 (2017), p. 236. DOI: 10.3847/1538-4357/aa5ea8.

[72] Victoria S. Meadows et al. “The Habitability of Proxima Centauri b: Environmental States and Observational Discriminants”. *Astrobiology* 18.2 (2018), pp. 133–189. DOI: 10.1089/ast.2016.1589.

[73] Andrew Sijan. “Development of military lasers for optical countermeasures in the mid-IR”. Ed. by David H. Titterton and Mark A. Richardson. (2009), p. 748304. DOI: 10.1117/12.835439.

[74] Robert J. Grasso. “Defence and security applications of quantum cascade lasers”. *Optical Sensing, Imaging, and Photon Counting: Nanostructured Devices and Applications 2016*. (2016). DOI: 10.1117/12.2238963.

[75] John Powell. *CO2 Laser Cutting*. London: Springer London, (1998). DOI: 10.1007/978-1-4471-1279-2.

[76] M. Bhaumik, W. Lacina, and M. Mann. “Characteristics of a CO laser”. *IEEE Journal of Quantum Electronics* 8.2 (1972), pp. 150–160. DOI: 10.1109/JQE.1972.1076906.

[77] Maurus Tacke. “Lead–salt lasers”. *Philosophical Transactions of the Royal Society of London. Series A: Mathematical, Physical and Engineering Sciences* 359.1780 (2001). Ed. by A. R. Adams et al., pp. 547–566. DOI: 10.1098/rsta.2000.0742.

[78] Damien Weidmann et al. “Application of a widely electrically tunable diode laser to chemical gas sensing with quartz-enhanced photoacoustic spectroscopy”. *Optics Letters* 29.16 (2004), p. 1837. DOI: 10.1364/OL.29.001837.

[79] Hiroshi Ishikawa et al. “Distributed feedback laser emitting at 1.3 μm for gigabit communication systems”. *Journal of Lightwave Technology* 5.6 (1987), pp. 848–855. DOI: 10.1109/JLT.1987.1075570.

[80] S.-J. Park et al. “Fiber-to-the-Home Services Based on Wavelength-Division-Multiplexing Passive Optical Network”. *Journal of Lightwave Technology* 22.11 (2004), pp. 2582–2591. DOI: 10.1109/JLT.2004.834504.

[81] Marcus Nebeling. *Coarse Wavelength Division Multiplexing*. Ed. by Marcus Nebeling and Hans Joerg Thiele. CRC Press, (2018). DOI: 10.1201/9781420018691.

[82] S. L. McCall et al. “Whispering-gallery mode microdisk lasers”. *Applied Physics Letters* 60.3 (1992), pp. 289–291. DOI: 10.1063/1.106688.

[83] Jerôme Faist et al. “Quantum cascade disk lasers”. *Applied Physics Letters* 69.17 (1996), pp. 2456–2458. DOI: 10.1063/1.117496.

[84] J. P. Hohimer, G. A. Vawter, and D. C. Craft. “Unidirectional operation in a semiconductor ring diode laser”. *Applied Physics Letters* 62.11 (1993), pp. 1185–1187. DOI: 10.1063/1.108728.

[85] D. H. Wu and M. Razeghi. “High power, low divergent, substrate emitting quantum cascade ring laser in continuous wave operation”. *APL Materials* 5.3 (2017), p. 035505. DOI: 10.1063/1.4978810.

[86] Martin Holzbauer et al. “Substrate-emitting ring interband cascade lasers”. *Applied Physics Letters* 111.17 (2017). DOI: 10.1063/1.4989514.

[87] Richard M De La Rue, Siyuan Yu, and Jean-michel Lourtioz. *Compact Semiconductor Lasers*. Ed. by Richard M. De La Rue, Yu Siyuan, and Jean-Michel Lourtioz. Weinheim, Germany: Wiley-VCH Verlag GmbH & Co. KGaA, (2014). DOI: 10.1002/9783527655342.

[88] Hui Cao et al. “Complex lasers with controllable coherence”. *Nature Reviews Physics* 1.2 (2019), pp. 156–168. DOI: 10.1038/s42254-018-0010-6.

[89] Govind P. Agrawal and Niloy K. Dutta. *Semiconductor Lasers*. Boston, MA: Springer US, (1995). DOI: 10.1007/978-1-4613-0481-4.

[90] Herbert Kroemer. “A Proposed Class of Hetero-junction Injection Lasers”. *Proceedings of the IEEE* (1963). DOI: 10.1109/PROC.1963.2706.

[91] H. Kroemer. “Heterostructure bipolar transistors and integrated circuits”. *Proceedings of the IEEE* 70.1 (1982), pp. 13–25. DOI: 10.1109/PROC.1982.12226.

[92] L. Esaki and R. Tsu. “Superlattice and Negative Differential Conductivity in Semiconductors”. *IBM Journal of Research and Development* 14.1 (1970), pp. 61–65. DOI: 10.1147/rd.141.0061.

[93] Andreas Wacker. “Gain in quantum cascade lasers and superlattices: A quantum transport theory”. *Physical Review B* 66.8 (2002), p. 085326. DOI: 10.1103/PhysRevB.66.085326.

[94] Jürgen Eichler and Hans Joachim Eichler. *Laser*. Berlin, Heidelberg: Springer Berlin Heidelberg, (2003). DOI: 10.1007/978-3-662-08243-0.

[95] Jérôme Faist. *Quantum Cascade Lasers*. Oxford University Press, (2013). DOI: 10.1093/acprof:oso/9780198528241.001.0001.

[96] Patrick Janassek et al. “Investigations of the polarization behavior of quantum cascade lasers by Stokes parameters”. *Optics Letters* 41.2 (2016), p. 305. DOI: 10.1364/OL.41.000305.

[97] Federico Capasso et al. “Quantum cascade lasers: Ultrahigh-speed operation, optical wireless communication, narrow linewidth, and far-infrared emission”. *IEEE Journal of Quantum Electronics* 38.6 (2002), pp. 511–532. DOI: 10.1109/JQE.2002.1005403.

[98] L. J. Olafsen et al. “Near-room-temperature mid-infrared interband cascade laser”. *Applied Physics Letters* 72.19 (1998), pp. 2370–2372. DOI: 10.1063/1.121359.

[99] Cory J. Hill, Baohua Yang, and Rui Q. Yang. “Low-threshold interband cascade lasers operating above room temperature”. *Physica E: Low-dimensional Systems and Nanostructures* 20.3-4 (2004), pp. 486–490. DOI: 10.1016/j.physe.2003.08.064.

[100] Rui Q. Yang, Cory J. Hill, and B. H. Yang. “High-temperature and low-threshold midinfrared interband cascade lasers”. *Applied Physics Letters* 87.15 (2005), p. 151109. DOI: 10.1063/1.2103387.

[101] W. W. Bewley et al. “Interband cascade laser operating cw to 257K at λ=3.7μm”. *Applied Physics Letters* 89.16 (2006), p. 161106. DOI: 10.1063/1.2363169.

[102] K. Mansour et al. “Mid-infrared interband cascade lasers at thermoelectric cooler temperatures”. *Electronics Letters* 42.18 (2006), p. 1034. DOI: 10.1049/el:20062442.

[103] Krishnan R. Parameswaran et al. “Off-axis integrated cavity output spectroscopy with a mid-infrared interband cascade laser for real-time breath ethane measurements”. *Applied Optics* 48.4 (2009), B73. DOI: 10.1364/AO.48.000B73.

[104] Zehua Wang et al. “Ultrahigh resolution spectroscopy for dimethyl sulfide at the ν1- and ν8-bands by a distributed feedback interband cascade laser”. *Journal of Quantitative Spectroscopy and Radiative Transfer* 246 (2020), p. 106930. DOI: 10.1016/j.jqsrt.2020.106930.

[105] Mahmood Bagheri et al. “Passively mode-locked interband cascade optical frequency combs”. *Scientific Reports* 8.1 (2018), pp. 1–7. DOI: 10.1038/s41598-018-21504-9.

[106] Benedikt Schwarz et al. “Interband cascade laser frequency combs for monolithic and battery driven spectrometers”. *Conference on Lasers and Electro-Optics*. Washington, D.C.: OSA, (2019), STu4O.6. DOI: 10.1364/CLEO_SI.2019.STu4O.6.

[107] Benedikt Schwarz et al. “Monolithic frequency comb platform based on interband cascade lasers and detectors”. *Optica* 6.7 (2019), p. 890. DOI: 10.1364/OPTICA.6.000890.

[108] Dominik Auth et al. “Frequency comb interband cascade laser stabilization by time-delayed optical self-injection”. *Novel In-Plane Semiconductor Lasers XIX*. Ed. by Alexey A. Belyanin and Peter M. Smowton. SPIE, (2020), p. 45. DOI: 10.1117/12.2547154.

[109] M. Horstjann et al. “Formaldehyde sensor using interband cascade laser based quartz-enhanced photoacoustic spectroscopy”. *Applied Physics B* 79.7 (2004), pp. 799–803. DOI: 10.1007/s00340-004-1659-3.

[110] Angelo Sampaolo et al. “Methane, ethane and propane detection using a compact quartz enhanced photoacoustic sensor and a single interband cascade laser”. *Sensors and Actuators B: Chemical* 282 (2019), pp. 952–960. DOI: 10.1016/j.snb.2018.11.132.

[111] Lukasz A. Sterczewski et al. “Mid-infrared dual-comb spectroscopy with interband cascade lasers”. *Optics Letters* 44.8 (2019), p. 2113. DOI: 10.1364/ol.44.002113.

[112] Z. Tian et al. “InAs-based interband cascade lasers with emission wavelength at 10.4 [micro sign]m”. *Electronics Letters* 48.2 (2012), p. 113. DOI: 10.1049/el.2011.3555.

[113] Leon Shterengas et al. “Cascade type-I quantum well diode lasers emitting 960 mW near 3 μ m”. *Applied Physics Letters* 105.16 (2014), p. 161112. DOI: 10.1063/1.4900506.

[114] Igor Vurgaftman et al. “Mid-IR Type-II Interband Cascade Lasers”. *IEEE Journal of Selected Topics in Quantum Electronics* 17.5 (2011), pp. 1435–1444. DOI: 10.1109/JSTQE.2011.2114331.

[115] R.Q. Yang et al. “Mid-infrared type-II interband cascade lasers”. *IEEE Journal of Quantum Electronics* 38.6 (2002), pp. 559–568. DOI: 10.1109/JQE.2002.1005406.

[116] L. L. Chang et al. “Semimetallic InAs-GaSb superlattices to the heterojunction limit”. *Applied Physics Letters* 38.1 (1981), pp. 30–32. DOI: 10.1063/1.92115.

[117] Leo Esaki. “New Phenomenon in Narrow Germanium p-n Junctions”. *Physical Review* 109.2 (1958), pp. 603–604. DOI: 10.1103/PhysRev.109.603.

[118] Junji Ohtsubo. “Semiconductor lasers stability, instability and chaos: Third edition”. *Springer Series in Optical Sciences*. (2013), pp. 12–15. DOI: 10.1007/978-3-642-30147-6.

[119] Carl O Weiss and Ramon Vilaseca. “5.1 Laser Equations”. *Dynamics of lasers*. Vol. 1. Wiley-VCH Verlag GmbH & Co. KGaA, (1991), pp. 81–87.

[120] Tilmann Heil. “Delay dynamics in semiconductor lasers : feedback and coupling induced instabilities, stabilization, and synchronization”. PhD Thesis. Technische Universität Darmstadt, 2001, p. 9.

[121] Kenju Otsuka. *Nonlinear Dynamics in Optical Complex Systems*. 1st ed. Springer Netherlands, (2000).

[122] T.L. Paoli and J.E. Ripper. “Direct modulation of semiconductor lasers”. *Proceedings of the IEEE* 58.10 (1970), pp. 1457–1465. DOI: 10.1109/PROC.1970.7971.

[123] Junji Ohtsubo. *Semiconductor lasers stability, instability and chaos: Third edition*. (2013). DOI: 10.1007/978-3-642-30147-6.

[124] Farhan Rana and Rajeev J. Ram. “Current noise and photon noise in quantum cascade lasers”. *Physical Review B* 65.12 (2002), p. 125313. DOI: 10.1103/PhysRevB.65.125313.

[125] F. Mogensen, H. Olesen, and G. Jacobsen. “Locking conditions and stability properties for a semiconductor laser with external light injection”. *IEEE Journal of Quantum Electronics* 21.7 (1985), pp. 784–793. DOI: 10.1109/JQE.1985.1072760.

[126] Roy Lang. “Injection Locking Properties of a Semiconductor Laser”. *IEEE Journal of Quantum Electronics* 18.6 (1982), pp. 976–983. DOI: 10.1109/JQE.1982.1071632.

[127] Thomas Erneux and Pierre Glorieux. *Laser Dynamics*. Cambridge: Cambridge University Press, (2010). DOI: 10.1017/CBO9780511776908.

[128] Yu Deng and Cheng Wang. “Rate Equation Modeling of Interband Cascade Lasers”. *2019 Conference on Lasers and Electro-Optics Europe & European Quantum Electronics Conference (CLEO/Europe-EQEC)*. Vol. Part F140-. 2. IEEE, (2019), pp. 1–1. DOI: 10.1109/CLEOE-EQEC.2019.8871482.

[129] I.E. Gordon et al. “The HITRAN2016 molecular spectroscopic database”. *Journal of Quantitative Spectroscopy and Radiative Transfer* 203 (2017), pp. 3–69. DOI: 10.1016/J.JQSRT.2017.06.038.

[130] Gianni Di Domenico, Stéphane Schilt, and Pierre Thomann. “Simple approach to the relation between laser frequency noise and laser line shape”. *Applied Optics* 49.25 (2010), pp. 4801–4807. DOI: 10.1364/AO.49.004801.

[131] J. Mørk, J. Mark, and B. Tromborg. “Route to chaos and competition between relaxation oscillations for a semiconductor laser with optical feedback”. *Physical Review Letters* 65.16 (1990), pp. 1999–2002. DOI: 10.1103/PhysRevLett.65.1999.

[132] Raúl Vicente et al. “Dynamics of semiconductor lasers with bidirectional optoelectronic coupling: Stability, route to chaos, and entrainment”. *Physical Review E* 70.4 (2004), p. 046216. DOI: 10.1103/PhysRevE.70.046216.

[133] Ingo Fischer, Yun Liu, and Peter Davis. “Synchronization of chaotic semiconductor laser dynamics on subnanosecond time scales and its potential for chaos communication”. *Physical Review A* 62.1 (2000), p. 011801. DOI: 10.1103/PhysRevA.62.011801.

[134] Yanli Li, Yuncai Wang, and Anbang Wang. “Message filtering characteristics of semiconductor laser as receiver in optical chaos communication”. *Optics Communications* 281.9 (2008), pp. 2656–2662. DOI: 10.1016/j.optcom.2008.01.001.

[135] Apostolos Argyris et al. “Chaos-based communications at high bit rates using commercial fibre-optic links”. *Nature* 438.7066 (2005), pp. 343–346. DOI: 10.1038/nature04275.

[136] G. E. Shtengel et al. “Impedance-corrected carrier lifetime measurements in semiconductor lasers”. *Applied Physics Letters* 67.1995 (1995), p. 1506. DOI: 10.1063/1.114474.

[137] L. Jumpertz et al. “Measurements of the linewidth enhancement factor of mid-infrared quantum cascade lasers by different optical feedback techniques”. *AIP Advances* 6.1 (2016), p. 015212. DOI: 10.1063/1.4940767.

[138] Christoph Harder, Kerry Vahala, and Amnon Yariv. “Measurement of the linewidth enhancement factor α of semiconductor lasers”. *Applied Physics Letters* (1983). DOI: 10.1063/1.93921.

[139] A. L. Schawlow and C. H. Townes. “Infrared and optical masers”. *Physical Review* 112.6 (1958), pp. 1940–1949. DOI: 10.1103/PhysRev.112.1940.

[140] Charles H. Henry. “Theory of the Linewidth of Semiconductor Lasers”. *IEEE Journal of Quantum Electronics* (1982). DOI: 10.1109/JQE.1982.1071522.

[141] C. Z. Ning. “What is Laser Threshold?” *IEEE Journal of Selected Topics in Quantum Electronics* 19.4 (2013), pp. 1503604–1503604. DOI: 10.1109/JSTQE.2013.2259222.

[142] E. Bartholdi and R. R. Ernst. “Fourier spectroscopy and the causality principle”. *Journal of Magnetic Resonance (1969)* (1973). DOI: 10.1016/0022-2364(73)90076-0.

[143] Andreas Ebel, Wolfgang Dreher, and Dieter Leibfritz. “Effects of zero-filling and apodization on spectral integrals in discrete Fourier-transform spectroscopy of noisy data”. *Journal of Magnetic Resonance* (2006). DOI: 10.1016/j.jmr.2006.06.026.

[144] Matteo Frigo and Steven G. Johnson. “FFTW: An adaptive software architecture for the FFT”. *ICASSP, IEEE International Conference on Acoustics, Speech and Signal Processing - Proceedings*. (1998). DOI: 10.1109/ICASSP.1998.681704.

[145] F.J. Harris. “On the use of windows for harmonic analysis with the discrete Fourier transform”. *Proceedings of the IEEE* 66.1 (1978), pp. 51–83. DOI: 10.1109/PROC.1978.10837.

[146] B. P. Abbott et al. “LIGO: The laser interferometer gravitational-wave observatory”. *Reports on Progress in Physics* (2009). DOI: 10.1088/0034-4885/72/7/076901.

[147] Yu Deng et al. “Narrow linewidth characteristics of interband cascade lasers”. *Applied Physics Letters* 116.20 (2020), p. 201101. DOI: 10.1063/5.0006823.

[148] Simone Borri et al. “Unveiling quantum-limited operation of interband cascade lasers”. *APL Photonics* 5.3 (2020), p. 036101. DOI: 10.1063/1.5139483.

[149] Y. Arakawa and A. Yariv. “Theory of gain, modulation response, and spectral linewidth in AlGaAs quantum well lasers”. *IEEE Journal of Quantum Electronics* 21.10 (1985), pp. 1666–1674. DOI: 10.1109/JQE.1985.1072555.

[150] L. Tombez et al. “Linewidth of a quantum-cascade laser assessed from its frequency noise spectrum and impact of the current driver”. *Applied Physics B* 109.3 (2012), pp. 407–414. DOI: 10.1007/s00340-012-5005-x.

[151] Klaus Petermann. “External optical feedback phenomena in semiconductor lasers”. *IEEE Journal of Selected Topics in Quantum Electronics* 1.2 (1995), pp. 480–489. DOI: 10.1109/2944.401232.

[152] T. Okoshi, K. Kikuchi, and A. Nakayama. “Novel method for high resolution measurement of laser output spectrum”. *Electronics Letters* 16.16 (1980), p. 630. DOI: 10.1049/el:19800437.

[153] Hanne Ludvigsen, Mika Tossavainen, and Matti Kaivola. “Laser linewidth measurements using self-homodyne detection with short delay”. *Optics Communications* 155.1-3 (1998), pp. 180–186. DOI: 10.1016/S0030-4018(98)00355-1.

[154] G. Giuliani and M. Norgia. “Laser diode linewidth measurement by means of self-mixing interferometry”. *IEEE Photonics Technology Letters* 12.8 (2000), pp. 1028–1030. DOI: 10.1109/68.867997.

[155] J. Reid, D. T. Cassidy, and R. T. Menzies. “Linewidth measurements of tunable diode lasers using heterodyne and etalon techniques”. *Applied Optics* 21.21 (1982), p. 3961. DOI: 10.1364/AO.21.003961.

[156] M.O. van Deventer, P. Spano, and S.K. Nielsen. “Comparison of DFB laser linewidth measurement techniques: results from COST 215 round robin”. *Electronics Letters* 26.24 (1990), p. 2018. DOI: 10.1049/el:19901304.

[157] Max Born, Emil Wolf, and Eugene Hecht. “ Principles of Optics: Electromagnetic Theory of Propagation, Interference and Diffraction of Light ”. *Physics Today* (2000). DOI: 10.1063/1.1325200.

[158] A. Barkan et al. “Linewidth and tuning characteristics of terahertz quantum cascade lasers”. *Optics Letters* 29.6 (2004), p. 575. DOI: 10.1364/OL.29.000575.

[159] P.H. Siegel. “Terahertz technology”. *IEEE Transactions on Microwave Theory and Techniques* 50.3 (2002), pp. 910–928. DOI: 10.1109/22.989974.

[160] K. Petermann. *Laser Diode Modulation and Noise*. Dordrecht: Springer Netherlands, (1988). DOI: 10.1007/978-94-009-2907-4.

[161] T. K. Boehme and Ron Bracewell. "The Fourier Transform and its Applications." *The American Mathematical Monthly* 73.6 (1966), p. 685. DOI: 10.2307/2314845.

[162] S. Bartalini et al. "Observing the intrinsic linewidth of a quantum-cascade laser: Beyond the schawlow-townes limit". *Physical Review Letters* 104.8 (2010), pp. 1–4. DOI: 10.1103/PhysRevLett.104.083904.

[163] Melvin Lax. "Quantum Noise. X. Density-Matrix Treatment of Field and Population-Difference Fluctuations". *Physical Review* 157.2 (1967), pp. 213–231. DOI: 10.1103/PhysRev.157.213.

[164] H. Haug and H. Haken. "Theory of noise in semiconductor laser emission". *Zeitschrift für Physik* (1967). DOI: 10.1007/BF01326200.

[165] Weng W. Chow, Stephan W. Koch, and Murray Sargent. *Semiconductor-Laser Physics*. Berlin, Heidelberg: Springer Berlin Heidelberg, (1994). DOI: 10.1007/978-3-642-61225-1.

[166] Marek Osinski and Jens Buus. "Linewidth Broadening Factor in Semiconductor Lasers - An Overview". *IEEE Journal of Quantum Electronics* 23.1 (1987), pp. 9–29. DOI: 10.1109/JQE.1987.1073204.

[167] Guido Giuliani. "The linewidth enhancement factor of semiconductor lasers: usefulness, limitations, and measurements". *2010 IEEE Photinic Society's 23rd Annual Meeting*. IEEE, (2010), pp. 423–424. DOI: 10.1109/PHOTONICS.2010.5698940.

[168] Asier Villafranca et al. "Linewidth enhancement factor of semiconductor lasers: Results from round-robin measurements in COST 288". *Conference on Lasers and Electro-Optics/Quantum Electronics and Laser Science Conference and Photonic Applications Systems Technologie*. (2007).

[169] Sergey Melnik, Guillaume Huyet, and Alexander Uskov. "The linewidth enhancement factor α of quantum dot semiconductor lasers". *Optics Express* 14.7 (2006), p. 2950. DOI: 10.1364/OE.14.002950.

[170] I.D. Henning and J.V. Collins. "Measurements of the semiconductor laser linewidth broadening factor". *Electronics Letters* 19.22 (1983), p. 927. DOI: 10.1049/el:19830633.

[171] Christoph Harder, Kerry Vahala, and Amnon Yariv. "Measurement of the linewidth enhancement factor α of semiconductor lasers". *Applied Physics Letters* 42.4 (1983), pp. 328–330. DOI: 10.1063/1.93921.

[172] F. Devaux, Y. Sorel, and J.F. Kerdiles. "Simple measurement of fiber dispersion and of chirp parameter of intensity modulated light emitter". *Journal of Lightwave Technology* 11.12 (1993), pp. 1937–1940. DOI: 10.1109/50.257953.

[173] R. Hui et al. "Novel measurement technique of α factor in DFB semiconductor lasers by injection locking". *Electronics Letters* 26.14 (1990), p. 997. DOI: 10.1049/el:19900647.

[174] Jens Von Staden et al. “Measurements of the α factor of a distributed-feedback quantum cascade laser by an optical feedback self-mixing technique”. *Optics Letters* 31.17 (2006), pp. 2574–2576. DOI: 10.1364/OL.31.002574.

[175] M. Lerttamrab et al. “Linewidth enhancement factor of a type-I quantum-cascade laser”. *Journal of Applied Physics* 94.8 (2003), pp. 5426–5428. DOI: 10.1063/1.1611285.

[176] Richard P. Green et al. “Linewidth enhancement factor of terahertz quantum cascade lasers”. *Applied Physics Letters* 92.7 (2008), p. 071106. DOI: 10.1063/1.2883950.

[177] Yanguang Yu, Guido Giuliani, and Silvano Donati. “Measurement of the linewidth enhancement factor of semiconductor lasers based on the optical feedback self-mixing effect”. *IEEE Photonics Technology Letters* 16.4 (2004), pp. 990–992. DOI: 10.1109/LPT.2004.824631.

[178] Henning Olesen, J. Osmundsen, and Bjarne Tromborg. “Nonlinear dynamics and spectral behavior for an external cavity laser”. *IEEE Journal of Quantum Electronics* 22.6 (1986), pp. 762–773. DOI: 10.1109/JQE.1986.1073061.

[179] Yu Deng, Bin-Bin Zhao, and Cheng Wang. “Linewidth broadening factor of an interband cascade laser”. *Applied Physics Letters* 115.18 (2019), p. 181101. DOI: 10.1063/1.5123005.

[180] M. Lerttamrab et al. “Linewidth enhancement factor of a type-II Interband-cascade laser”. *Journal of Applied Physics* 96.6 (2004), pp. 3568–3570. DOI: 10.1063/1.1782269.

[181] Nagaatsu Ogasawara, Ryoichi Ito, and Ryuji Morita. “Linewidth Enhancement Factor in GaAs/AlGaAs Multi-Quantum-Well Lasers”. *Japanese Journal of Applied Physics* 24.Part 2, No. 7 (1985), pp. L519–L521. DOI: 10.1143/JJAP.24.L519.

[182] Olivier Spitz et al. “Extensive study of the linewidth enhancement factor of a distributed feedback quantum cascade laser at ultra-low temperature”. *Quantum Sensing and Nano Electronics and Photonics XVI*. Ed. by Manijeh Razeghi et al. SPIE, (2019), p. 42. DOI: 10.1117/12.2510502.

[183] M. Willatzen et al. “Nonlinear gain suppression in semiconductor lasers due to carrier heating”. *IEEE Photonics Technology Letters* 3.7 (1991), pp. 606–609. DOI: 10.1109/68.87928.

[184] Frédéric Grillot et al. “Gain Compression and Above-Threshold Linewidth Enhancement Factor in 1.3-μm InAs–GaAs Quantum-Dot Lasers”. *IEEE Journal of Quantum Electronics* 44.10 (2008), pp. 946–951. DOI: 10.1109/JQE.2008.2003106.

[185] Peter P Vasil’ev, Ian H White, and John Gowar. “Fast phenomena in semiconductor lasers”. *Reports on Progress in Physics* 63.12 (2000), pp. 1997–2042. DOI: 10.1088/0034-4885/63/12/203.

[186] Robert Pawlus et al. “Control of dual-wavelength laser using monolithically integrated phase-controlled optical feedback”. *Semiconductor Lasers and Laser Dynamics IX*. Ed. by Krassimir Panajotov et al. SPIE, (2020), p. 6. DOI: 10.1117/12.2557305.

[187] R.K. Ahrenkiel. “Measurement of minority-carrier lifetime by time-resolved photoluminescence”. *Solid-State Electronics* 35.3 (1992), pp. 239–250. DOI: 10.1016/0038-1101(92)90228-5.

[188] N. Dutta, R. Hartman, and W. Tsang. “Gain and carrier lifetime measurements in AlGaAs single quantum well lasers”. *IEEE Journal of Quantum Electronics* 19.8 (1983), pp. 1243–1246. DOI: 10.1109/JQE.1983.1072033.

[189] C. Becker et al. “GaAs quantum box cascade lasers”. *Applied Physics Letters* 81.16 (2002), pp. 2941–2943. DOI: 10.1063/1.1515135.

[190] J. M. Pikal et al. “Impedance independent optical carrier lifetime measurements in semiconductor lasers”. *Review of Scientific Instruments* 69.12 (1998), pp. 4247–4248. DOI: 10.1063/1.1149239.

[191] Andrew P. Ongstad et al. “Determination of carrier lifetimes using Hakki-Paoli gain data”. *Applied Physics Letters* 72.7 (1998), pp. 836–838. DOI: 10.1063/1.120909.

[192] G.E Shtengel, D.A. Ackerman, and P.A Morton. “True carrier lifetime measurements of semiconductor lasers”. *Electronics Letters* 31.20 (1995), pp. 1747–1748.

[193] G.H.B. Thompson. “Analysis of radiative and nonradiative recombination law in lightly doped InGaAsP lasers”. *Electronics Letters* 19.5 (1983), p. 154. DOI: 10.1049/el:19830108.

[194] Robert Olshansky et al. “Measurement of radiative and nonradiative recombination rates in InGaAsP and AlGaAs light sources”. *IEEE Journal of Quantum Electronics* 20.8 (1984), pp. 838–854. DOI: 10.1109/JQE.1984.1072500.

[195] W. W. Bewley et al. “Lifetimes and Auger coefficients in type-II W interband cascade lasers”. *Applied Physics Letters* 93.4 (2008), pp. 1–4. DOI: 10.1063/1.2967730.

[196] Christiaan Huygens. *Oeuvres complètes de Christiaan Huygens. Publiées par la Société hollandaise des sciences.* La Haye: M. Nijhoff, (1888). DOI: 10.5962/bhl.title.21031.

[197] Jonatan Peña Ramirez et al. “The sympathy of two pendulum clocks: beyond Huygens’ observations”. *Scientific Reports* 6.1 (2016), p. 23580. DOI: 10.1038/srep23580.

[198] Hermann Haken. *Laser light dynamics*. 1st ed. North-Holland Amsterdam, (1985).

[199] Edward N. Lorenz. “SECTION OF PLANETARY SCIENCES: THE PREDICTABILITY OF HYDRODYNAMIC FLOW*,†”. *Transactions of the New York Academy of Sciences* 25.4 Series II (1963), pp. 409–432. DOI: 10.1111/j.2164-0947.1963.tb01464.x.

[200] Steven H. Strogatz and Ian Stewart. “Coupled Oscillators and Biological Synchronization”. *Scientific American* 269.6 (1993), pp. 102–109. DOI: 10.1038/scientificamerican1293-102.

[201] Moshe Gitterman. *The Chaotic Pendulum*. World Scientific, (2010).

[202] G. J. Sussman and J. Wisdom. “Numerical Evidence That the Motion of Pluto Is Chaotic”. *Science* 241.4864 (1988), pp. 433–437. DOI: 10.1126/science.241.4864.433.

[203] Barbara Drossel, Alan J McKane, and Christopher Quince. “The impact of nonlinear functional responses on the long-term evolution of food web structure”. *Journal of Theoretical Biology* 229.4 (2004), pp. 539–548. DOI: 10.1016/j.jtbi.2004.04.033.

[204] H. A. Braun et al. “Computer Simulations of Neuronal Signal Transduction: The Role of Nonlinear Dynamics and Noise”. *International Journal of Bifurcation and Chaos* 08.05 (1998), pp. 881–889. DOI: 10.1142/S0218127498000681.

[205] Jean-Michel Grandmont. *Nonlinear economic dynamics*. Academic Press Orlando, Fla., (1987).

[206] Yingjie Fan et al. “Nonlinear dynamics and chaos in a simplified memristor-based fractional-order neural network with discontinuous memductance function”. *Nonlinear Dynamics* 93.2 (2018), pp. 611–627. DOI: 10.1007/s11071-018-4213-2.

[207] Salim Lahmiri and Stelios Bekiros. “Cryptocurrency forecasting with deep learning chaotic neural networks”. *Chaos, Solitons & Fractals* 118 (2019), pp. 35–40. DOI: 10.1016/j.chaos.2018.11.014.

[208] Svetlana Khasminskaya et al. “Fully integrated quantum photonic circuit with an electrically driven light source”. *Nature Photonics* 10.11 (2016), pp. 727–732. DOI: 10.1038/nphoton.2016.178.

[209] Andrzej Tabaka et al. “Dynamics of vertical-cavity surface-emitting lasers in the short external cavity regime: Pulse packages and polarization mode competition”. *Physical Review A - Atomic, Molecular, and Optical Physics* 73.1 (2006), pp. 1–14. DOI: 10.1103/PhysRevA.73.013810.

[210] Tilmann Heil et al. “Statistical properties of low-frequency fluctuations during single-mode operation in distributed-feedback lasers:?experiments and modeling”. *Optics Letters* 24.18 (1999), p. 1275. DOI: 10.1364/OL.24.001275.

[211] Claudio R. Mirasso et al. “Optoelectronic devices for optical chaos communications”. *Semiconductor Optoelectronic Devices for Lightwave Communication*. Ed. by Joachim Piprek. SPIE, (2003), p. 24. DOI: 10.1117/12.512210.

[212] Atsushi Murakami and K. Alan Shore. “Chaos-pass filtering in injection-locked semiconductor lasers”. *Physical Review A* 72.5 (2005), p. 053810. DOI: 10.1103/PhysRevA.72.053810.

[213] Olivier Spitz et al. “Investigation of Chaotic and Spiking Dynamics in Mid-Infrared Quantum Cascade Lasers Operating Continuous-Waves and Under Current Modulation”. *IEEE Journal of Selected Topics in Quantum Electronics* 25.6 (2019), pp. 1–11. DOI: 10.1109/JSTQE.2019.2937445.

[214] Olivier Spitz et al. “Peculiarities and predictions of rogue waves in mid-infrared quantum cascade lasers under conventional optical feedback”. *Quantum Sensing and Nano Electronics and Photonics XVII*. Ed. by Manijeh Razeghi et al. SPIE, (2020), p. 10. DOI: 10.1117/12.2545217.

[215] O. Spitz et al. “Square Wave Emission in a Mid-infrared Quantum Cascade Oscillator Under Rotated Polarization”. *Conference on Lasers and Electro-Optics*. Washington, D.C.: OSA, (2019), SW3N.2. DOI: 10.1364/CLEO_SI.2019.SW3N.2.

[216] Miguel C. Soriano et al. “Complex photonics: Dynamics and applications of delay-coupled semiconductors lasers”. *Reviews of Modern Physics* 85.1 (2013), pp. 421–470. DOI: 10.1103/RevModPhys.85.421.

[217] Fan Yi Lin and Jia Ming Liu. “Chaotic radar using nonlinear laser dynamics”. *IEEE Journal of Quantum Electronics* 40.6 (2004), pp. 815–820. DOI: 10.1109/JQE.2004.828237.

[218] Kunihito Hirano et al. “Fast random bit generation with bandwidth-enhanced chaos in semiconductor lasers”. *Optics Express* 18.6 (2010), p. 5512. DOI: 10.1364/OE.18.005512.

[219] Timothy Day et al. “Quantum cascade lasers for defense and security”. *Technologies for Optical Countermeasures X; and High-Power Lasers 2013: Technology and Systems*. Ed. by David H. Titterton et al. SPIE, (2013), p. 889802. DOI: 10.1117/12.2031536.

[220] Andreas Herdt. “Novel Mid-infrared Gas Sensor Based on Mutually Coupled Quantum Cascade Lasers”. Masterth. 2016.

[221] Jia-Ming Liu. “Photodetection”. *Principles of Photonics*. Cambridge: Cambridge University Press, (2016), pp. 362–395. DOI: 10.1017/CBO9781316687109.012.

[222] Wen Lei, Jarek Antoszewski, and Lorenzo Faraone. “Progress, challenges, and opportunities for HgCdTe infrared materials and detectors”. *Applied Physics Reviews* 2.4 (2015), p. 041303. DOI: 10.1063/1.4936577.

[223] James Thomas Keeley. “Self-Mixing in Terahertz Quantum Cascade Lasers”. PhD Thesis. University of Leeds, 2016, p. 250.

[224] Andreas Herdt et al. “Theory of delay-coupled nonidentical quantum cascade lasers”. *Semiconductor Lasers and Laser Dynamics VIII*. Ed. by Krassimir Panajotov, Marc Sciamanna, and Rainer Michalzik. SPIE, (2018), p. 16. DOI: 10.1117/12.2305907.

[225] S. Wieczorek et al. “The dynamical complexity of optically injected semiconductor lasers”. *Physics Reports* 416.1-2 (2005), pp. 1–128. DOI: 10.1016/j.physrep.2005.06.003.

[226] Daan Lenstra. “Self-consistent rate-equation theory of coupling in mutually injected semiconductor lasers”. *Proc. SPIE*. Ed. by Bernd Witzigmann, Marek Osiński, and Yasuhiko Arakawa. Vol. 10098. (2017), 100980K. DOI: 10.1117/12.2247687.

[227] Rüdiger Seydel. *Practical Bifurcation and Stability Analysis*. (2009). DOI: 10.1007/978-0-387-75847-3.

[228] Hartmut Erzgräber. “Dynamics of delay-coupled semiconductor laser systems”. PhD thesis. Vrije Universiteit Amsterdam, 2006.

[229] Gulnaz Baimenshina. “Simulation and Qualitative Analysis of a Single Mode Semiconductor Laser Model”. *Proceedings of the International Conference on Computer, Networks and Communication Engineering (ICCNCE 2013)*. Paris, France: Atlantis Press, (2013). DOI: 10.2991/iccnce.2013.95.

[230] J. C. Butcher. *Numerical Methods for Ordinary Differential Equations, Second Edition*. (2008). DOI: 10.1002/9780470753767.

[231] Marlis Hochbruck and Alexander Ostermann. "Exponential integrators". *Acta Numerica* (2010), pp. 209–286. DOI: 10.1017/S0962492910000048.

[232] David W. Sukow, Jeff R. Gardner, and Daniel J. Gauthier. "Statistics of power-dropout events in semiconductor lasers with time-delayed optical feedback". *Physical Review A - Atomic, Molecular, and Optical Physics* 56.5 (1997), R3370–R3373. DOI: 10.1103/PhysRevA.56.R3370.

[233] Nikolaus Schunk and Klaus Petermann. "Noise Analysis of Injection-Locked Semiconductor Injection Lasers". *IEEE Journal of Quantum Electronics* 22.5 (1986), pp. 642–650. DOI: 10.1109/JQE.1986.1073018.

[234] Tobias Gensty, Wolfgang Elsäßer, and Christian Mann. "Intensity noise properties of quantum cascade lasers". *Optics Express* 13.6 (2005), p. 2032. DOI: 10.1364/OPEX.13.002032.

[235] Paul Dean et al. "Terahertz imaging through self-mixing in a quantum cascade laser". *Optics Letters* 36.13 (2011), p. 2587. DOI: 10.1364/OL.36.002587.

[236] T. Hagelschuer et al. "Terahertz gas spectroscopy through self-mixing in a quantum-cascade laser". *Applied Physics Letters* 109.19 (2016), p. 191101. DOI: 10.1063/1.4967435.

[237] Thierry Bosch. "An overview of self-mixing sensing applications". *Conference on Optoelectronic and Microelectronic Materials and Devices, Proceedings, COMMAD* (2005), pp. 385–392. DOI: 10.1109/COMMAD.2004.1577571.

[238] Gerard A. Acket et al. "The Influence of Feedback Intensity on Longitudinal Mode Properties and Optical Noise in Index-Guided Semiconductor Lasers". *IEEE Journal of Quantum Electronics* 20.10 (1984), pp. 1163–1169. DOI: 10.1109/JQE.1984.1072281.

[239] Guido Giuliani et al. "Laser diode self-mixing technique for sensing applications". *Journal of Optics A: Pure and Applied Optics* 4.6 (2002), pp. 283–294. DOI: 10.1088/1464-4258/4/6/371.

[240] M. Wienold et al. "Real-time terahertz imaging through self-mixing in a quantum-cascade laser". *Applied Physics Letters* 109.1 (2016), p. 011102. DOI: 10.1063/1.4955405.

[241] Takuya Sano. "Antimode dynamics and chaotic itinerancy in the coherence collapse of semiconductor lasers with optical feedback". *Physical Review A* 50.3 (1994), pp. 2719–2726. DOI: 10.1103/PhysRevA.50.2719.

[242] G H M van Tartwijk and D Lenstra. "Semiconductor lasers with optical injection and feedback". *Quantum and Semiclassical Optics: Journal of the European Optical Society Part B* 7.2 (1995), pp. 87–143. DOI: 10.1088/1355-5111/7/2/003.

[243] Joseph Lee Rodgers and W. Alan Nicewander. "Thirteen Ways to Look at the Correlation Coefficient". *The American Statistician* 42.1 (1988), pp. 59–66. DOI: 10.1080/00031305.1988.10475524.

[244] T. Heil et al. “Dynamics of semiconductor lasers subject to delayed optical feedback: The short cavity regime”. *Physical Review Letters* 87.24 (2001), pp. 243901–1–243901–4. DOI: 10.1103/PhysRevLett.87.243901.

[245] Ch Risch and C. Voumard. “Self-pulsation in the output intensity and spectrum of GaAs-AlGaAs cw diode lasers coupled to a frequency-selective external optical cavity”. *Journal of Applied Physics* 48.5 (1977), pp. 2083–2085. DOI: 10.1063/1.323922.

[246] Isabelle Petitbon et al. “Locking Bandwidth and Relaxation Oscillations of an Injection-Locked Semiconductor Laser.” *IEEE Journal of Quantum Electronics* 24.2 (1988), pp. 148–154. DOI: 10.1109/3.108.

[247] G. Liu, X. Jin, and S.L. Chuang. “Measurement of linewidth enhancement factor of semiconductor lasers using an injection-locking technique”. *IEEE Photonics Technology Letters* 13.5 (2001), pp. 430–432. DOI: 10.1109/68.920741.

[248] Sjoerd M. Verduyn Lunel and Bernd Krauskopf. “The mathematics of delay equations with an application to the Lang-Kobayashi equations”. *AIP Conference Proceedings* 548 (2000), pp. 66–86. DOI: 10.1063/1.1337759.

[249] Tilmann Heil et al. “Chaos Synchronization and Spontaneous Symmetry-Breaking in Symmetrically Delay-Coupled Semiconductor Lasers”. *Physical Review Letters* 86.5 (2001), pp. 795–798. DOI: 10.1103/PhysRevLett.86.795.

[250] Hartmut Erzgräber, Bernd Krauskopf, and Daan Lenstra. “Compound Laser Modes of Mutually Delay-Coupled Lasers”. *SIAM Journal on Applied Dynamical Systems* 5.1 (2006), pp. 30–65. DOI: 10.1137/040619958.

[251] Thomas Erneux. *Applied Delay Differential Equations*. Vol. 3. New York, NY: Springer New York, (2009). DOI: 10.1007/978-0-387-74372-1.

[252] Wolfgang Demtröder. *Laser spectroscopy 1: Basic principles*. (2014). DOI: 10.1007/978-3-642-53859-9.

[253] D. F. Swinehart. “The Beer-Lambert Law”. *Journal of Chemical Education* 39.7 (1962), p. 333. DOI: 10.1021/ed039p333.

[254] Wolfgang Demtröder. *Laser spectroscopy: Vol. 2 experimental techniques*. (2008). DOI: 10.1007/978-3-540-74954-7.

[255] Frank K. Tittel et al. “Semiconductor Laser Based Trace Gas Sensor”. *Ebrahim-Zadeh M., Sorokina I.T. (eds) Mid-Infrared Coherent Sources and Applications. NATO Science for Peace and Security Series B: Physics and Biophysics. Springer, Dordrecht* 134 (2008), pp. 467–493. DOI: 10.7326/0003-4819-134-8-200104170-00012.

[256] Andreas Dreizler, Volker Sick, and Jürgen Wolfrum. “Applied laser spectroscopy in technical combustion systems”. *Berichte der Bunsengesellschaft für physikalische Chemie* 101.5 (1997), pp. 771–782. DOI: 10.1002/bbpc.19971010502.

[257] Felix Stritzke et al. “Ammonia concentration distribution measurements in the exhaust of a heavy duty diesel engine based on limited data absorption tomography”. *Optics Express* 25.7 (2017), p. 8180. DOI: 10.1364/oe.25.008180.

[258] Uri Lachish et al. “Tunable diode laser based spectroscopic system for ammonia detection in human respiration”. *Review of Scientific Instruments* 58.6 (1987), pp. 923–927. DOI: 10.1063/1.1139577.

[259] Erhan Tütüncü and Boris Mizaikoff. “Cascade laser sensing concepts for advanced breath diagnostics”. *Analytical and Bioanalytical Chemistry* 411.9 (2019), pp. 1679–1686. DOI: 10.1007/s00216-018-1509-5.

[260] Christian Brand. “Beyond ‘Dieselgate’: Implications of unaccounted and future air pollutant emissions and energy use for cars in the United Kingdom”. *Energy Policy* 97 (2016), pp. 1–12. DOI: 10.1016/j.enpol.2016.06.036.

[261] Helge Kragh. *Niels Bohr and the Quantum Atom: The Bohr Model of Atomic Structure 1913-1925*. (2012). DOI: 10.1093/acprof:oso/9780199654987.001.0001.

[262] Wolfgang Demtröder. *Atoms, Molecules and Photons*. Berlin/Heidelberg: Springer-Verlag, (2006), p. 388. DOI: 10.1007/3-540-32346-5.

[263] F.K. Tittel and R. Lewicki. “Tunable mid-infrared laser absorption spectroscopy”. *Semiconductor Lasers*. Elsevier, (2013), pp. 579–629. DOI: 10.1533/9780857096401.3.579.

[264] David J. Griffiths and Darrell F. Schroeter. *Introduction to Quantum Mechanics*. Cambridge University Press, (2018). DOI: 10.1017/9781316995433.

[265] L. S. Rothman et al. “The HITRAN database: 1986 edition”. *Applied Optics* (1987). DOI: 10.1364/ao.26.004058.

[266] Robert A McClatchey et al. *AFCRL atmospheric absorption line parameters compilation*. Tech. rep. Air Force Cambridge Research Labs HANSCOM AFB MA, 1973.

[267] Peter T.S. DeVore. *Load HITRAN 2004+ Data*. (2014).

[268] T. Blunier et al. “Variations in atmospheric methane concentration during the Holocene epoch”. *Nature* 374.6517 (1995), pp. 46–49. DOI: 10.1038/374046a0.

[269] Ed Dlugokencky. *Trends in Atmospheric Methane*. (2020).

[270] L.R. Brown et al. “Methane line parameters in HITRAN”. *Journal of Quantitative Spectroscopy and Radiative Transfer* 82.1-4 (2003), pp. 219–238. DOI: 10.1016/S0022-4073(03)00155-9.

[271] J.C. Hilico et al. “New Analysis of the Pentad System of Methane and Prediction of the (Pentad-Pentad) Spectrum”. *Journal of Molecular Spectroscopy* 168.2 (1994), pp. 455–476. DOI: 10.1006/jmsp.1994.1293.

[272] L. Féjard et al. “The Intensities of Methane in the 3–5 μm Region Revisited”. *Journal of Molecular Spectroscopy* 201.1 (2000), pp. 83–94. DOI: 10.1006/jmsp.2000.8065.

[273] Alfons Weber and K. Narahari Rao. *Spectroscopy of the Earth’s Atmosphere and Interstellar Medium*. (1992), pp. 339–422. DOI: 10.1016/0003-2670(93)80030-o.

[274] L.B.F. Juurlink, D.R. Killelea, and A.L. Utz. “State-resolved probes of methane dissociation dynamics”. *Progress in Surface Science* 84.3-4 (2009), pp. 69–134. DOI: 10.1016/j.progsurf.2009.01.001.

[275] Marilena Giglio et al. “Allan Deviation Plot as a Tool for Quartz-Enhanced Photoacoustic Sensors Noise Analysis”. *IEEE Transactions on Ultrasonics, Ferroelectrics, and Frequency Control* 63.4 (2016), pp. 555–560. DOI: 10.1109/TUFFC.2015.2495013.

[276] D.W. Allan. “Time and Frequency (Time-Domain) Characterization, Estimation, and Prediction of Precision Clocks and Oscillators”. *IEEE Transactions on Ultrasonics, Ferroelectrics and Frequency Control* 34.6 (1987), pp. 647–654. DOI: 10.1109/T-UFFC.1987.26997.

[277] Andreas Dreizler. *Verbrennung im Laserlicht. Methoden zur Validierung numerischer Simulationen*. wbg Academic in Wissenschaftliche Buchgesellschaft, (2006), pp. 1–208.

[278] Yufei Ma, Vicet Aurore, and Karol Krzempek. *State-of-the-art Laser Gas Sensing Technologies*. MDPI, (2020). DOI: 10.3390/books978-3-03928-399-6.

[279] P. Werle, R. Mücke, and F. Slemr. “The limits of signal averaging in atmospheric trace-gas monitoring by tunable diode-laser absorption spectroscopy (TDLAS)”. *Applied Physics B Photophysics and Laser Chemistry* 57.2 (1993), pp. 131–139. DOI: 10.1007/BF00425997.

[280] J. Reid et al. “Sensitivity limits of a tunable diode laser spectrometer, with application to the detection of NO_2 at the 100-ppt level”. *Applied Optics* 19.19 (1980), p. 3349. DOI: 10.1364/AO.19.003349.

[281] Clinton B. Carlisle and David E. Cooper. “Tunable-diode-laser frequency-modulation spectroscopy using balanced homodyne detection”. *Optics Letters* 14.23 (1989), p. 1306. DOI: 10.1364/OL.14.001306.

[282] Giel Berden, Rudy Peeters, and Gerard Meijer. “Cavity ring-down spectroscopy: Experimental schemes and applications”. *International Reviews in Physical Chemistry* 19.4 (2000), pp. 565–607. DOI: 10.1080/014423500750040627.

[283] James M. Supplee, Edward A. Whittaker, and Wilfried Lenth. “Theoretical description of frequency modulation and wavelength modulation spectroscopy”. *Applied Optics* 33.27 (1994), p. 6294. DOI: 10.1364/AO.33.006294.

[284] Pietro Patimisco et al. “Quartz-Enhanced Photoacoustic Spectroscopy: A Review”. *Sensors* 14.4 (2014), pp. 6165–6206. DOI: 10.3390/s140406165.

[285] Pietro Patimisco et al. “Recent advances in quartz enhanced photoacoustic sensing”. *Applied Physics Reviews* 5.1 (2018), p. 011106. DOI: 10.1063/1.5013612.

[286] V.M. Baev, T. Latz, and P.E. Toschek. “Laser intracavity absorption spectroscopy”. *Applied Physics B: Lasers and Optics* 69.3 (1999), pp. 171–202. DOI: 10.1007/s003400050793.

[287] Jérôme Morville, Daniele Romanini, and Erik Kerstel. “Cavity Enhanced Absorption Spectroscopy with Optical Feedback”. *Cavity-Enhanced Spectroscopy and Sensing*. Ed. by Gianluca Gagliardi and Hans-Peter Loock. Springer Berlin Heidelberg, (2014), pp. 163–209. DOI: 10.1007/978-3-642-40003-2_5.

[288] Gustavo Villares et al. “Dual-comb spectroscopy based on quantum-cascade-laser frequency combs”. *Nature Communications* 5.1 (2014), p. 5192. DOI: 10.1038/ncomms6192.

[289] Ian Coddington, Nathan Newbury, and William Swann. “Dual-comb spectroscopy”. *Optica* 3.4 (2016), p. 414. DOI: 10.1364/OPTICA.3.000414.

[290] Mengjie Yu et al. “Silicon-chip-based mid-infrared dual-comb spectroscopy”. *Nature Communications* 9.1 (2018), pp. 6–11. DOI: 10.1038/s41467-018-04350-1.

[291] Teemu Tomberg et al. “Sub-parts-per-trillion level sensitivity in trace gas detection by cantilever-enhanced photo-acoustic spectroscopy”. *Scientific Reports* (2018). DOI: 10.1038/s41598-018-20087-9.

[292] Wei Ren, Longqiang Luo, and Frank K. Tittel. “Sensitive detection of formaldehyde using an interband cascade laser near 3.6 μm”. *Sensors and Actuators, B: Chemical* 221 (2015), pp. 1062–1068. DOI: 10.1016/j.snb.2015.07.078.

[293] Lei Dong et al. “Compact TDLAS based sensor design using interband cascade lasers for mid-IR trace gas sensing”. *Optics Express* 24.6 (2016), pp. 528–535. DOI: 10.1364/OE.24.00A528.

[294] CISCO. “Cisco Visual Networking Index: Forecast and Trends, 2017–2022 White Paper”. (2019).

[295] Barry M. Leiner et al. “A brief history of the internet”. *ACM SIGCOMM Computer Communication Review* 39.5 (2009), pp. 22–31. DOI: 10.1145/1629607.1629613.

[296] René Jean Essiambre and Robert W. Tkach. “Capacity trends and limits of optical communication networks”. *Proceedings of the IEEE* 100.5 (2012), pp. 1035–1055. DOI: 10.1109/JPROC.2012.2182970.

[297] Georg Rademacher et al. “High capacity transmission with few-mode fibers”. *Journal of Lightwave Technology* 37.2 (2019), pp. 425–432. DOI: 10.1109/JLT.2018.2870038.

[298] Reinhold Noé. *Essentials of modern optical fiber communication, second edition*. (2016). DOI: 10.1007/978-3-662-49623-7.

[299] Nathan Blaunstein et al. *Fiber Optic and Atmospheric Optical Communication*. John Wiley & Sons, Inc., (2019). DOI: 10.1002/9781119602019.

[300] Kevin P. Scheibe et al. “Going the last mile: A spatial decision support system for wireless broadband communications”. *Decision Support Systems* 42.2 (2006), pp. 557–570. DOI: 10.1016/j.dss.2005.02.010.

[301] William C. Brown. “The History of Power Transmission by Radio Waves”. *IEEE Transactions on Microwave Theory and Techniques* (1984). DOI: 10.1109/TMTT.1984.1132833.

[302] Baris I. Erkmen, Bruce E. Moision, and Kevin M. Birnbaum. “A review of the information capacity of single-mode free-space optical communication”. *Free-Space Laser Communication Technologies XXII* 7587 (2010), 75870N. DOI: 10.1117/12.843542.

[303] Martin P. J. Lavery et al. “Free-space propagation of high-dimensional structured optical fields in an urban environment”. *Science Advances* 3.10 (2017), e–Location 1700552. DOI: 10.1126/sciadv.1700552.

[304] J. H. Taylor and H. W. Yates. “Atmospheric Transmission in the Infrared”. *Journal of the Optical Society of America* 47.3 (1957), p. 223. DOI: 10.1364/JOSA.47.000223.

[305] Carynelisa Erlick et al. “Atmospheric transmission in the ultraviolet and visible: Aerosols in cloudy atmospheres”. *Journal of Geophysical Research: Atmospheres* 103.D24 (1998), pp. 31541–31555. DOI: 10.1029/1998JD200053.

[306] Xiangyu He et al. “1 Gbps free-space deep-ultraviolet communications based on III-nitride micro-LEDs emitting at 262 nm”. *Photonics Research* 7.7 (2019), B41–B47. DOI: 10.1364/PRJ.7.000B41.

[307] Alexander Soibel et al. “Midinfrared interband cascade laser for free space optical communication”. *IEEE Photonics Technology Letters* 22.2 (2010), pp. 121–123. DOI: 10.1109/LPT.2009.2036449.

[308] Dave Kythe and Prem Kythe. “Hamming Codes”. *Algebraic and Stochastic Coding Theory*. Taylor & Francis Group, 6000 Broken Sound Parkway NW, Suite 300, Boca Raton, FL 33487-2742: CRC Press, (2017), pp. 75–94. DOI: 10.1201/b11707-5.

[309] Carl Stephen Clifton. “Error Detection and Correction”. *Data Communications*. CRC Press, (2020), pp. 65–77. DOI: 10.1201/9781003065586-5.

[310] R.D. Feldman et al. “An evaluation of architectures incorporating wavelength division multiplexing for broad-band fiber access”. *Journal of Lightwave Technology* 16.9 (1998), pp. 1546–1559. DOI: 10.1109/50.712236.

[311] Y. Hu et al. “Mid-infrared wavelength division (de)multiplexer using an interleaved angled multimode interferometer on the silicon-on-insulator platform”. *Optics Letters* 39.6 (2014), p. 1406. DOI: 10.1364/OL.39.001406.

[312] Ertuğrul Güvenkaya, Jehad M. Hamamreh, and Hüseyin Arslan. “On physical-layer concepts and metrics in secure signal transmission”. *Physical Communication* 25.114 (2017), pp. 14–25. DOI: 10.1016/j.phycom.2017.08.011.

[313] Matthias Geihs et al. *The Status of Quantum-Based Long-Term Secure Communication over the Internet*. Tech. rep. 2017.

[314] Markus Rosskopf, Till Mohr, and Wolfgang Elsäßer. “Ghost Polarization Communication”. *Physical Review Applied* 13.3 (2020), p. 034062. DOI: 10.1103/PhysRevApplied.13.034062.

[315] Sebastian Nauerth et al. “Air-to-ground quantum communication”. *Nature Photonics* 7.5 (2013), pp. 382–386. DOI: 10.1038/nphoton.2013.46.

[316] Juan Yin et al. “Satellite-based entanglement distribution over 1200 kilometers”. *Science* 356.6343 (2017), pp. 1140–1144. DOI: 10.1126/science.aan3211.

[317] Miao Er-long et al. “Background noise of satellite-to-ground quantum key distribution”. *New Journal of Physics* 7 (2005), pp. 215–215. DOI: 10.1088/1367-2630/7/1/215.

[318] Richard J. Hughes et al. “Practical free-space quantum key distribution over 10 km in daylight and at night”. *New Journal of Physics* 4 (2002), pp. 43–43. DOI: 10.1088/1367-2630/4/1/343.

[319] Eleni Diamanti et al. “Practical challenges in quantum key distribution”. *npj Quantum Information* 2.1 (2016), p. 16025. DOI: 10.1038/npjqi.2016.25.

[320] Sabine Euler. “Erzeugung und Charakterisierung von Einzelphotonen aus PDC in PPKTP für Anwendungen in der Quanteninformation”. PhD thesis. Technische Universität Darmstadt, 2017, p. 262.

[321] Patrick Janassek, Sébastien Blumenstein, and Wolfgang Elsäßer. “Recovering a hidden polarization by ghost polarimetry”. *Optics Letters* 43.4 (2018), p. 883. DOI: 10.1364/ol.43.000883.

[322] Olivier Spitz et al. “Private communications with quantum cascade laser photonic chaos”. *To Be Announced* (2021).

[323] Wei Li Zhang et al. “Chaos synchronization communication using extremely unsymmetrical bidirectional injections.” *Optics Lettersetters* 33.3 (2008), pp. 237–9. DOI: 149989[pii].

[324] Miguel C. Soriano et al. “Complex photonics: Dynamics and applications of delay-coupled semiconductors lasers”. *Reviews of Modern Physics* 85.1 (2013), pp. 421–470. DOI: 10.1103/RevModPhys.85.421.

Acknowledgement

In diesem Abschnitt möchte ich mich bei allen Personen bedanken, die zum Erfolg dieser Dissertation beigetragen haben.

Ein ganz besonderer Dank gilt meinem Doktorvater **Herrn Prof. Elsäßer**. Mit Ihrer freundlichen Art haben Sie mich in die Gruppe aufgenommen und mich an mein Thema herangetragen. Selbst bei größeren Schwierigkeiten konnten Sie mir stets behilflich sein und meine Experimente konnten trotz kleineren Rückschlägen stets weitergeführt werden. Danken möchte ich Ihnen insbesondere für die Erfahrungen, die ich während meiner Zeit als Promotionsstudent auf zahlreichen Konferenzen und Auslandsreisen sammeln durfte. Ich habe die Zeit während dieser Aufenthalte mehr als genossen und konnte dort meinen physikalischen Horizont themenübergreifend erweitern. Dabei habe ich viele neue Freunde gewonnen und konnte mich kulturell weiterbilden. Aber insbesondere muss ich mich bei Ihnen für die zahlreichen nicht-physikalischen Diskussionen bedanken. Es war mir immer eine Freude über Reiseziele, Wandersport und Radsport, insbesondere über das Piemont und Turin zu reden.

Neben der **Technischen Universität Darmstadt**, bedanke ich mich außerdem beim **Bundesministerium für Bildung und Forschung**, die das deutsch-griechische Forschungsprojekt ILLIAS finanziert hat. Den damit verbundenen Projektpartnern **nanoplus**, **die University of Athens**, der **hellenic public power company** "ΔΕΗ" und der **Knestel GmbH** danke ich für die gute Zusammenarbeit, sowie **Herrn Martin Sellhorst** und **Frau Martina Born** vom VDI für die gute Projektkoordination. **Adonis Bogris** meinem geschätzen griechischen Kollegen gebührt besonderer Dank für die schönen Diskussionen und Videokonferenzen.

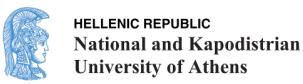

Großer Dank geht auch an **Daan Lenstra** dank dem ich große Erfahrungen im Bereich der Ratengleichungsmodelle und Steady-state Analyse sammeln konnte. Besonders bedanken möchte ich mich auch bei **Olivier Spitz** meinem geschätzen französischen Kollegen. Einer der internationalen Freunde, die ich auf dem Weg meiner Promotion sehr ins Herz geschlossen habe.

Till Mohr, der mit mir zu Beginn Büro und das Labor teilte, gebührt ebenso Dank. Bei physikalischen und technischen Fragestellungen warst Du für mich in jeder Hinsicht *der* Ansprechpartner in meiner Zeit als Masterstudent, die mich letztendlich zur Promotion geführt hat. Deine kritische Art Ergebnisse zu betrachten wird mir immer ein Vorbild sein. In unserem Büro herrschte eine warme Arbeitsatmosphäre nicht nur dann, wenn die Temperaturen im Winter auf $30\,^{\circ}\mathrm{C}$ stiegen, da die Heizkörper voll aufgedreht waren und die Sonne zudem durch die großen Fenster schien. Es war sehr schöne Zeit, da man sich mit Dir auch über unwichtigere Dinge unterhalten konnte und viel lachte. Mein Dank gilt auch **Sebastién Blumenstein und Robert Pawlus**, die ihr tiefgreifendes physikalisches Verständnis auf eine außergewöhnlich verständliche Weise vermitteln konnte. Ich habe sehr viel von Euch gelernt, man konnte aber auchmal tiefgreifende Gespräche abseits der Physik führen. Dem **Rest der AG Elsäßer** insbesondere **Christoph Weber, Dominik Auth und Markus Rosskopf** gilt Dank für die lustige Zeit und Gespräche im Büro und Labor. Vielen Dank auch an **Maria Musso** unserer temperamentvollen Sekretärin, deren italienische Wurzeln betont werden müssen. Auch **Pascal Sauer** danke ich für die außerordentlich tolle Hilfe beim Hochzeitsantrag. **Markus Weidmann** darf ebenfalls nicht vergessen werden - "mein erster Student". In ihm habe ich einen guten Freund gefunden, den ich immer wieder gerne sehe. Deine Art auf Leute zuzugehen und deinen Enthusiasmus sucht man bei anderen Leuten vergeblich.

Auch bedanke ich mich bei den **Kollegen der feinmechanischen Werkstatt** des Institutes für Angewandte Physik, insbesondere Herrn Fuchs ohne dessen feinmechanische Expertise meine Promotion nie hätte so gut gelingen können.

Meinem ehemaligen Mitbewohner **Moritz Reichert** und bestem Freund ist auch zu danken. Seit der Schule begleitetest Du mich mein ganzes Studium lang. Wenn man abends nochmal zusammen kochte oder man abfällig sich über die Fernsehsendung Galileo amüsierte, konnte man endlich mal abschalten. Ich werde immer an unsere extrem lustige Zeit zurückdenken - unter anderem dann wenn die Mischung des Cocktails *jetzt wirklich schmeckt*, dann wenn die Spülmaschine repariert werden muss und falls ich nachts mal jemanden vom Hallenbad abholen soll.

Bedanken möchte ich mich auch bei meinen Großeltern **Agnes und Gerd Gold**, die sehr verständig waren, wenn ich mal wieder keine Zeit hatte. Ich will das in Zukunft ändern, denn ich genieße die Momente mit Euch immer sehr.

Meiner Verlobten Pia gebührt außergewöhnlicher Dank, insbesondere in der Zeit in der die Dissertation entstand, die mich viele Nerven gekostet hat. Seitdem sich Ende 2014 unsere Wege kreuzten, gabst du meinem Leben einen tieferen Sinn und deshalb ist diese Arbeit auch unserem gemeinsamen Lebensweg gewidmet. Ich freue sehr mich auf unsere gemeinsame Zukunft, wenn Du willst gerne auch ohne Kücheninsel. *Ich liebe Dich*.

Der größte Dank aber gilt meiner **Mutter**, die mich während meines gesamten Studiums und der Promotion in jeder Situation bedingungslos unterstützt hat und mein Leben maßgeblich geprägt hat. Für mich endet jetzt der bisher wichtigste Teil meines Lebens, der ohne Dich in dieser Form nicht möglich gewesen wäre. Gerade in sehr schwierigen Zeiten warst Du für mich da, kümmertest Dich um mich, hast mir Trost gespendet, gingst mir voran. Die Fußstapfen sind unermesslich groß in die ich trete, wenn ich meinen zukünftigen Kindern genauso viel Liebe zukommen lassen will, wie Du sie mir gegeben hast.

"A mother is the truest friend we have, when trials heavy and sudden fall upon us; when adversity takes the place of prosperity; when friends desert us; when trouble thickens around us, still will she cling to us, and endeavor by her kind precepts and counsels to dissipate the clouds of darkness, and cause peace to return to our hearts."

Washington Irving

Appendix A

Publications (published)

A. Bogris, A. Herdt, D. Syvridis, and W. Elsäßer
"Mid-Infrared Gas Sensor Based on Mutually Injection Locked Quantum Cascade Lasers"
IEEE J. Sel. Top. Quant., Vol. 23, 1500107 (2017)
DOI: 10.1109/JSTQE.2016.2603341

A. Herdt, M. Weidmann, T. Mohr, D. Lenstra, and W. Elsäßer
"Theory of delay-coupled nonidentical quantum cascade lasers"
Proc. SPIE 10682, Semiconductor Lasers and Laser Dynamics VIII, 106820H (2018)
DOI: 10.1117/12.2305907

T. Mohr, A. Herdt, and W. Elsäßer
"2D tomographic terahertz imaging using a single pixel detector"
Opt. Express, Vol. 26(3), 3353-3367 (2018)
DOI: 10.1364/OE.26.003353

P. Janassek, A. Herdt, S. Blumenstein, and W. Elsäßer
"Ghost Spectroscopy with Classical Correlated Amplified Spontaneous Emission Photons Emitted by An Erbium-Doped Fiber Amplifier"
Appl. Sci., Vol. 8(10), 1896 (2018)
DOI: 10.3390/app8101896

O. Spitz, A. Herdt, J. Duan, M. Carras, W. Elsaesser, and F. Grillot
"Investigation of Chaotic and Spiking Dynamics in Mid-Infrared Quantum Cascade Lasers Operating Continuous-Waves and Under Current Modulation"
Proc. SPIE 10926, Quantum Sensing and Nano Electronics and Photonics XVI (2019)
DOI: 10.1117/12.2510502

O. Spitz, J. Wu, A. Herdt, M. Carras, W. Elsaesser, C.-W. Wong and F. Grillot
"Extensive study of the linewidth enhancement factor of a distributed feedback quantum cascade laser at ultra-low temperature"
IEEE J. Sel. Top. Quant. El., Vol. 25, 1200311 (2019)
DOI: 10.1109/JSTQE.2019.2937445

O. Spitz, A. Herdt, J. Wu, G. Maisons, M. Carras, C.-W. Wong, W. Elsaesser, and F. Grillot
"Peculiarities and predictions of rogue waves in mid-infrared quantum cascade lasers under conventional optical feedback"
Proc. SPIE 11288, Quantum Sensing and Nano Electronics and Photonics XVII, 112880A (2020)
DOI: 10.1117/12.2545217

O. Spitz, A. Herdt, J. Wu, G. Maisons, M. Carras, C.-W. Wong, W. Elsaesser, and F. Grillot
"Extreme events in quantum cascade lasers"
Advanced Photonics (Accepted late Sept. 2020)
DOI: 10.1117/1.AP.2.XX.XXXXXX (not known yet)

Publications (submitted)

O. Spitz, A. Herdt, J. Wu, G. Maisons, M. Carras, C. Wong, W. Elsäßer and F. Grillot
"Private communications with quantum cascade laser photonic chaos"
Submitted to Nature Photonics (Jul. 2020)

O. Spitz, A. Herdt, W. Elsäßer and F. Grillot
"Tunable all-optical modulation in mid-infrared quantum cascade lasers"
Submitted to SPIE Nanophotonics (Oct. 2020)

Publications in preparation

A. Herdt, M. Weidmann A. Bogris and W. Elsäßer
"Detector-free free-space bidirectional symmetric communication scheme based on compound states of two mutually coupled interband cascade lasers"
In preparation for Optica (early 2021)

A. Herdt, A. Bogris, M. v. Edlinger and W. Elsäßer
"Exploiting the optical injection locking mechanism for detection of mid-infrared radiation – The revival of the laser-as-detector approach"
In preparation for IEEE J. Sel. Top. Quant. El. (early 2021)

Supervised Theses

Master‘s Thesis of Markus Weidmann
"Opto-elektronische Eigenschaften eines gegenseitig gekoppelten Halbleiter-Lasersystems: Grundlagen und Anwendung für bidirektionale symmetrische Kommunikation"
Technische Universität Darmstadt (2018)

Bachelor‘s Thesis of Kenneth Jähner "Spektrale Analyse und Korrelations-Analyse von Superlumineszenzdioden" Technische Universität Darmstadt (2018)

Master‘s Thesis of Albert Demke "Opto-elektronische Eigenschaften eines MIR-Interbandkaskadenlasers: freilaufend und unter optischer Rückkopplung"
Technische Universität Darmstadt (2019)

Master‘s Thesis of Steffen Zienert "Erzeugung und Manipulation von super-pseudothermischem Licht" Technische Universität Darmstadt (2019)

Contributions to teaching

Head of the optics division of the basic physics lab course (“Grundpraktikum”) at Technische Universität Darmstadt
(2017 – 2020)

Exercise supervisor for the lecture "Konzepte und Methoden der Metrologie" at Technische Universität Darmstadt
(2017 – 2020)

Examination protocolist for the lecture "Messmethoden in der Optik (Spektroskopie)" at Technische Universität Darmstadt
(2016 – 2020)

Awards

Fraunhofer Green-Photonics Award 3rd rank in category Master’s degree (2017)

Nature Photonics Best presentation award at ISPALD (2019)

Conference Contributions

International Conference on Semiconductor Mid-IR Materials and Optics – SMMO
(international)
Poster - "Novel Mid-infrared Gas Sensor Based on Mutually Coupled Quantum Cascade Lasers"
21. – 25.03.2016 Lisbon, Portugal

Imaging and Applied Optics
(international)
Poster - "Novel Mid-infrared Gas Sensor Based on Mutually Coupled Quantum Cascade Lasers"
25. – 28.07.2016 Heidelberg, Germany

International Quantum Cascade Lasers School and Workshop – IQCLSW
(international)
Poster - "Novel Mid-infrared Gas Sensor Based on Mutually Coupled Quantum Cascade Lasers"
04. – 09.09.2016 Cambridge, United Kingdom

Conference on Lasers and Electro-Optics Europe – CLEO Europe
(international)
Talk - "A Novel Mid-infrared Gas Sensor Based On Mutually Coupled Quantum Cascade Lasers"
24. – 29.06.2017 Munich, Germany

International Symposium on Physics and Applications of Laser Dynamics – ISPALD
(international)
Talk - "Injection dynamics of mutually delay-coupled non-identical quantum cascade lasers"
15. – 17.11.2017 Paris, France

SPIE Photonics Europe
(international)
Talk - "Theory of delay-coupled non-identical quantum cascade lasers"
22. – 26.04.2018 Strasbourg, France

International Quantum Cascade Lasers School and Workshop – IQCLSW
(international)
Poster - "Locking mechanism of delay-coupled non-identical single-mode quantum cascade lasers"
03. – 07.09.2018 Cassis, France

European Semiconductor Laser Workshop – ESLW
(pan European)
Talk - "Detector free bidirectional symmetric communication scheme based on compound states of two mutually coupled diode lasers"
21. – 22.09.2018 Bari, Italy

Conference on Lasers and Electro-Optics Europe – CLEO Europe
(international)
Poster - "Detector free bidirectional symmetric communication scheme based on compound states of two mutually coupled diode lasers"
23. – 27.06.2019 Munich, Germany

International Symposium on Physics and Applications of Laser Dynamics – ISPALD
(international)
Talk - "Low-frequency fluctuations in an Interband Cascade Laser subject to optical feedback"
20. – 22.11.2019 Metz, France

Curriculum Vitae

Personal Data

Name	Andreas Herdt
Date of birth:	19.06.1991
Place of birth:	Wetzlar
Nationality:	German

Education

2017 - 2020

Technische Universität Darmstadt	**Promotion** Semiconductor Optics	Thesis Title: "The laser-as-detector approach exploiting mid-infrared emitting interband cascade lasers: A potential for spectroscopy and communication applications"

2014 - 2016

Technische Universität Darmstadt	**Master of Science (Physics)** Semiconductor Optics	Thesis Title: "Novel Mid-Infrared Gas Sensor Based On Mutually Coupled Quantum Cascade Lasers"

2010 - 2014

Technische Universität Darmstadt	**Bachelor of Science (Physics)** Experimental Condensed Matter Physics	Thesis Title: "Triplett-Solvatations-Dynamik an Dimethylsulfoxid-Wasser-Mischungen"

2010 - 2014

Weidigschule Butzbach	**Allgemeine Hochschulreife** Abitur	Leistungskurse Mathematik Physik

Appendix B

CAD drawings

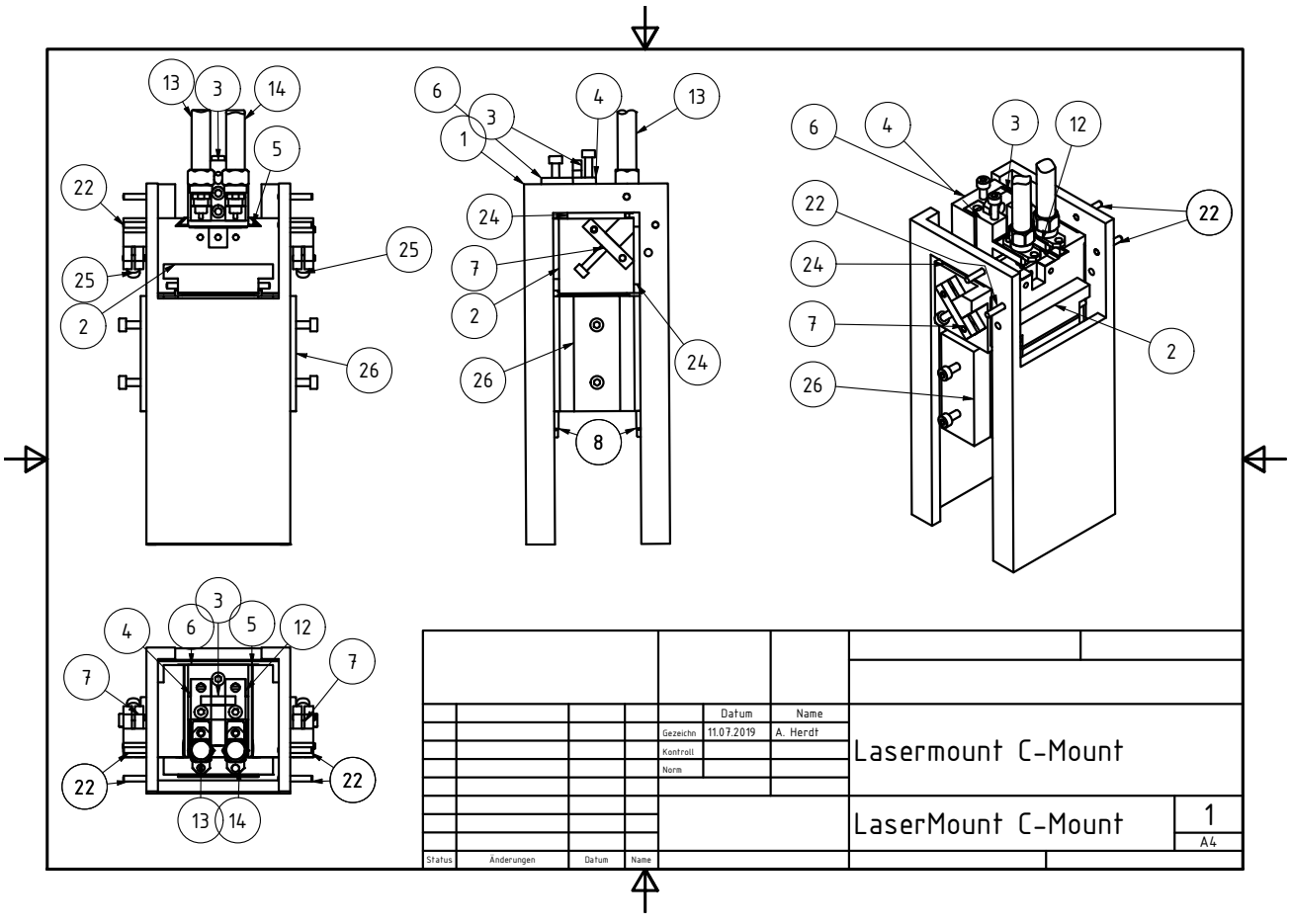

Figure 6.1: CAD drawing of the lasermount used for cmount ICLs. 1: shaft, 2: copper-heatsink, 3: electrical-connector-plate, 4: electrical-connector-arm, 5: sleight-base, 6: sleight-block, 7: spring-tensioner, 8: lower spring-tensioner,9: damper of spring-tensioner, 12: electrical-connector-arm right, 13: SMA-connector, 14: SMA-connector 2, 23: Peltier-module, 24: ceramic pins, 26: heatspreader. All other description numbers have been removed.

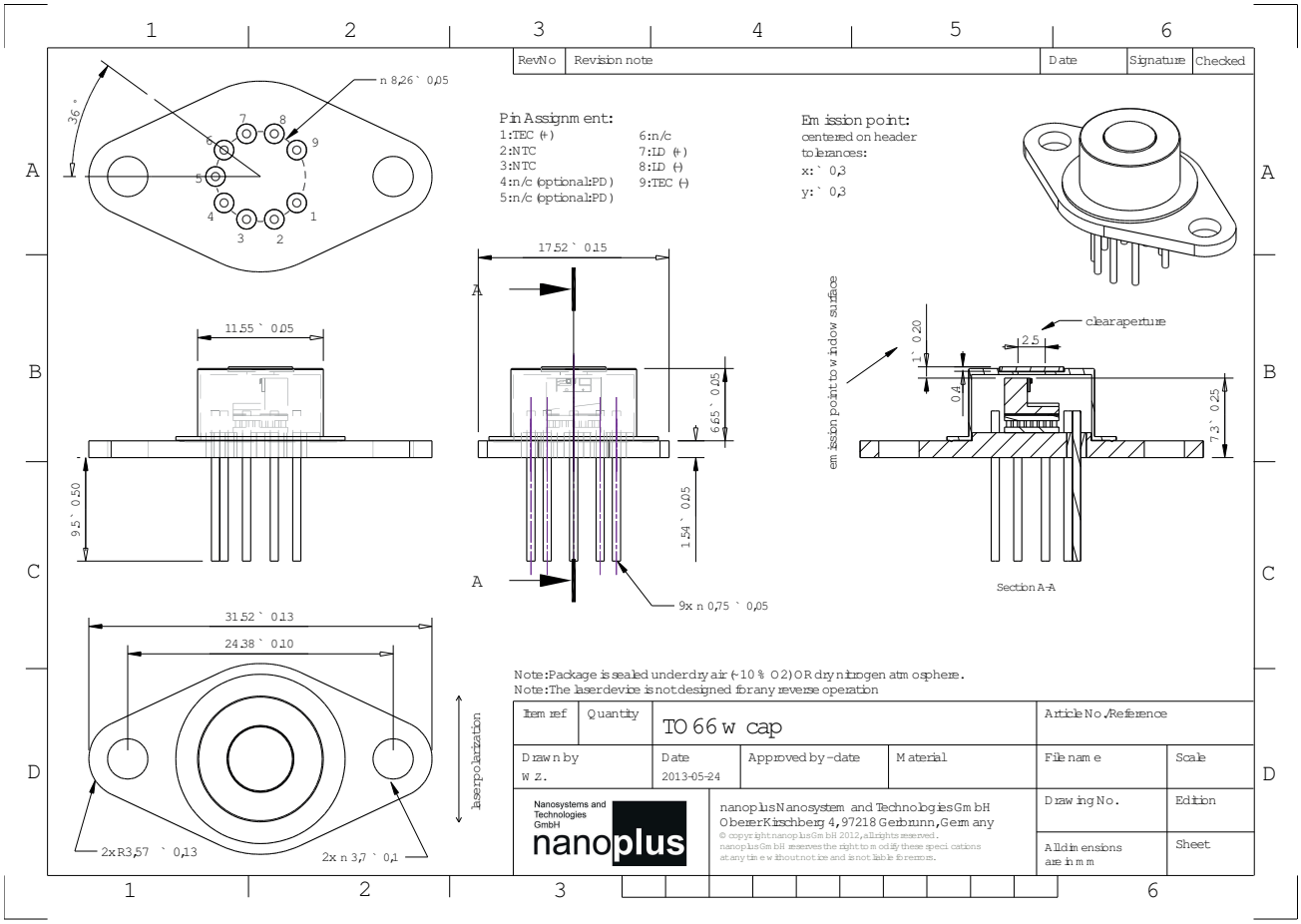

Figure 6.2: CAD drawing of the capped TO66-Can used for batch 2813 ICLSs. Copyright nanoplus.

Source code for numerical integration of the rate-equations for mutually coupled ICLs

```
clc
close all hidden
clear variables

%% Load Data %%


PreferencesObj  = Preference1;
LaserObj        = Lasers.ICL1;
CavityObj       = Cavities.Cavity1;


NumCavities =  numel(CavityObj);
NumLasers   =  numel(LaserObj);



parfor inner_i = 1:numel(CavityObj)
[TimeArray,E_1,E_2,NN_1,NN_2,Ith_f,slope_f] = main_NumIntegrate(PreferencesObj,LaserObj,CavityObj);
end


```

```
23
24
25          % Translation Electrical field -> optical power
26          if PreferencesObj.CalculatePower == true
27              P_1=abs(E_1(1, 1:end).^2);
28              P_2=abs(E_2(1, 1:end).^2);
29
30
31              P_1 = P_1(~isnan(P_1));
32              P_2 = P_2(~isnan(P_2));
33
34              NumInt = numel(P_1);
35
36
37              P_1=real(Filt.butterworth(P_1, NumInt, NumInt*PreferencesObj.SamplingTime, 20, 5e9, 0));
38              P_2=real(Filt.butterworth(P_2, NumInt, NumInt*PreferencesObj.SamplingTime, 20, 5e9, 0));
39
40              End1 = numel(P_1);
41              % ####### Create Outputs
42              Pout_1      = nanmean(P_1(max(1,End1-2^18):end))*factor; %Output Power Laser1
43              Pout_2      = nanmean(P_2((max(1,End1-2^18):end)))*factor;
44              Pout_1std   = nanstd(P_1((max(1,End1-2^18):end)))*factor;
45              Pout_2std   = nanstd(P_2((max(1,End1-2^18):end)))*factor;
46          end
47
48              NNout_1     = nanmean(NN_1((max(1,End1-2^18):end)));
49              NNout_2     = nanmean(NN_2((max(1,End1-2^18):end)));
50              NNout_1std  = nanstd(NN_1((max(1,End1-2^18):end)));
51              NNout_2std  = nanstd(NN_2((max(1,End1-2^18):end)));
52
53          % Calculate optical spectra
54          if PreferencesObj.CalculateSpectrum == true
55              Spectrum_1  = abs(fftshift(fft(E_1(2^18+1:end)))); % Optical frequency ############ Create frequency array
56              Spectrum_2 = abs(fftshift(fft(E_2(2^18+1:end)))); % Optical frequency ############ Create frequency array
57              Spectrum_1 = Spectrum_1/max(Spectrum_1); % Normalize Spectrum
58              Spectrum_2 = Spectrum_2/max(Spectrum_2); % Normalize Spectrum
59          else
60              Spectrum_1 = nan(1,1);
61              Spectrum_2 = nan(1,1);
62          end
63
64
65
66
67      if PreferencesObj.SaveCarrierNumberTrace == true
68      end
69
70      if PreferencesObj.SaveElectricalFieldTrace == true
71      end
72
73      end
74
75        if PreferencesObj.SaveFinalCarrierNumber == true
76      end
77      if PreferencesObj.SaveFinalPower == true
78      end
79
80      if PreferencesObj.SaveSpectrum == true
81      end
```